Genesis of quartz in Mediterranean soils

Génesis del cuarzo en suelos Mediterráneos

PhD Thesis - Tesis Doctoral

Alberto Molinero-García

Supervisors/Directores:

Rafael Delgado Calvo-Flores

Juan Manuel Martín-García

Department of Soil Science and Agricultural Chemistry

September/ Septiembre 2022

UNIVERSIDAD
DE GRANADA

Doctoral Programme in Earth Sciences

Programa Doctorado
Ciencias de la Tierra

Editor: Universidad de Granada. Tesis Doctorales
Autor: Alberto García Molinero
ISBN: 978-84-1117-643-9
URI: https://hdl.handle.net/10481/79631

La presente Tesis Doctoral ha sido financiada mediante un contrato predoctoral para el doctorando Alberto Molinero García, con referencia BES-2017-080078, y ha sido proporcionada por el Ministerio de Ciencia e Innovación y la Agencia Estatal de Investigación (MCIN/AEI /10.13039/ 501100011033).

MINISTERIO
DE CIENCIA
E INNOVACIÓN

UNIÓN EUROPEA
Fondo Social Europeo
El FSE invierte en tu futuro

AGENCIA
ESTATAL DE
INVESTIGACIÓN

Agradecimientos/Acknowledgements

Quiero expresar mi gratitud hacia mis directores de Tesis, Rafael Delgado Calvo-Flores y Juan Manuel Martín-García. Ellos han posibilitado el inicio de esta Tesis Doctoral y han contribuido, de forma decisiva, a su consecución. Su experiencia y profesionalidad, así como su calidad humana, han sido pilares fundamentales.

I would also like to thank my supervisors in the research stays abroad. Thanks to both Dr. Axel Bernd Müller (University of Oslo, Norway) and Dr. Pedro José Miranda da Costa (University of Coimbra, Portugal) for the welcome in the research centers, their valuable help, their experience and advice in the development of this PhD Thesis.

Gracias al personal de la Facultad de Farmacia, donde he desarrollado esta etapa de mi vida, por las múltiples ayudas recibidas. Gracias a los técnicos que integran el Centro de Instrumentación Científica de la Universidad de Granada, su ayuda ha sido fundamental en el desarrollo de esta Tesis Doctoral.

Gracias a mis compañeros del Departamento de Edafología y Química Agrícola, tanto de la Facultad de Farmacia como Ciencias, profesores, doctorandos, técnicos de laboratorio y personal de administración y servicios, siempre me han brindado su ayuda. En especial, a mi compañera de doctorado Ana Cervera, con ella he compartido este largo camino lleno de inquietudes, momentos complicados y también alegrías. Te deseo todo lo mejor, de corazón. Gracias, también, a todos los colaboradores científicos en esta Tesis Doctoral.

Gracias a mis amigos, que con café o charlas han sido decisivos para continuar motivado.

Por último, a mi familia, el verdadero soporte. Palabras especiales para mis padres, ellos son el pilar de lo que soy hoy día y el mejor ejemplo que he podido tener, siempre serán mi referencia. Mi agradecimiento y mi orgullo son eternos. Gracias a mi segunda familia, por haberme acompañado en este camino, por ser ayuda y apoyo absoluto. Por último, a Lourdes, mi compañera de vida, que ha soportado desde el primer día y hasta el último este proceso. Gracias por tu paciencia, tu alegría inagotable y tu sonrisa permanente. Estoy seguro, vienen tiempos buenos. Vosotros habéis sido esenciales, GRACIAS.

Table of contents

Abstract

The sand fraction of soil (50-2000 µm) is assumed to be inherited from the parent rock and has historically been considered useful for the provision of information about the type of parent material and its degree of alteration. However, there is a gap regarding the potential of this fraction in pedogenetic studies, since it has rarely been used as an object of study.

Quartz is an important component of soils and is concentrated in the sand fraction mainly due to inheritance, both as a clastic constituent from the parent rock by physical disintegration (fragmentation) or by dissolution (as occurs in carbonate rocks), as by aeolian inputs to the ground surface. Quartz is one of the chemically purest minerals in nature, after diamond and graphite. It contains, however, lattice bound trace elements in low concentrations due to atomic substitution of Si and interstitial elemental incorporation within the crystal structure. In addition, its high hardness and low solubility in water makes quartz a very stable mineral facilitating its enrichment in many sediments and clastic rocks. This enables it to collect and maintain features acquired by alteration (physical or chemical) and/or precipitation on its surface, which are used with great efficiency in environmental interpretations of sediments, soils and materials.

This PhD Thesis evaluates the sand fraction, and the quartz contained in that fraction, in materials from Mediterranean area. Our work is based on soils belonging to a chronosequence of the fluvial terraces of the Guadalquivir River, and on aeolian materials deposited in the south of the Iberian Peninsula. The main hypothesis is that the sand fraction and its main constituent, mineral quartz, are indicators of the genesis and origin of soil materials and atmospheric dust from the Mediterranean environment.

Mineralogical (X-ray diffraction -XRD-), elemental composition (major and minor including rare earth elements -REE-) (inductively coupled plasma atomic emission spectroscopy -ICP-AES-, inductively coupled mass spectrometry -ICP-MS-, laser ablation inductively coupled plasma mass spectrometry -LA-ICP-MS, scanning electron microscope backscattered electron -SEM-BSE-, scanning electron microscopy–energy dispersive X-ray spectroscopy -SEM-EDX-, variable pressure scanning electron microscope equipped with an EDX detector, and with

a structural and chemical analyzer by Raman spectroscopy -VP-SEM-EDX Raman-, high resolution transmission electron microscopy –HRTEM-) and morphological (SEM-EDX, SEM-BSE, scanning electron microscope cathodoluminescence -SEM-CL-, image anaysis –IA-, on mineral species, mainly quartz) studies are carried out.

Mineralogy and elemental composition (major and minor including REE, and also geochemical indices of alteration/evolution) studies have demonstrated the suitability of the soil sand fraction as a provider of pedogenetic information in Mediterranean environments, allowing: a discussion of the origin of the different minerals it contains and, therefore of the soil material; and knowledge of the pedogenetic alteration suffered by this granulometric fraction and the rate at which its properties and alteration evolve through the establishment of chronofunctions. In addition, the study of the quartz trace element content as well as its crystalline structure, in the soil sand fraction of a chronosequence of the Guadalquivir River, have made it possible to establish both its lithological origin (six types of quartz have been distinguished: metamorphic quartz, undeformed granitic quartz, strongly altered granitic quartz, recrystallised –deformed- granitic quartz, sandstone quartz and hydrothermal quartz) as its provenance (Iberian Massif, Betic Cordilleras or Cenozoic Guadalquivir Basin).

The granulometric and compositional characterization (mineralogy, major and minor chemical elements) of the atmospheric dust (and the iberulites contained in it) deposited in a Mediterranean environment provides information on its origin. Atmospheric dust samples were from both local and African sources. According to their mineralogy, the samples came from both the north-northwest of African and regional soil sources. Moreover, the morphology of the aeolian quartz grains is indicative of the origin and the alteration suffered in atmospheric transport. The quartz grains of African origin, with respect to those of local origin, have the following properties: a) greater presence of bulbous edges and upturned plates microtextures on the surface of quartz grains; and b) as regards the quartz shape parameters, minor values for area, perimeter, maximum feret, minimum feret, major axis, minor axis, and shape factor, and higher values for aspect ratio.

All the above demonstrate the potential of the sand granulometric fraction as a pedogenesis informant in Mediterranean soils. In addition, they demonstrate the suitability of mineral quartz as an indicator of origin and alteration both in soils and in aeolian materials, being able to provide (by itself) information of great interest for Earth Sciences.

Resumen

La fracción arena del suelo (50-2000 µm) se asume que es heredada de la roca madre y ha sido considerada históricamente útil para proporcionar información acerca del tipo de material parental y de su grado de alteración. Sin embargo, existe un gap de información sobre el potencial de esta fracción en los estudios pedogenéticos, ya que son pocos los trabajos que la han empleado como objeto de estudio.

El cuarzo es un constituyente importante de los suelos y se concentra en la fracción arena debido mayoritariamente a herencia, tanto como un constituyente clástico procedente de la roca madre por desintegración física (fragmentación) o por disolución (como ocurre en las rocas carbonatadas), como por aportes eólicos a la superficie del suelo. El cuarzo es uno de los minerales químicamente más puros de la naturaleza, después del diamante y el grafito. Sin embargo, contiene elementos traza en bajas concentraciones debido a sustituciones de Si y a incorporaciones intersticiales de elementos dentro de la estructura cristalina. Además, su alta dureza y baja solubilidad en agua hacen que el cuarzo sea un mineral muy estable facilitando su enriquecimiento en sedimentos y rocas clásticas. Esto posibilita que el cuarzo recoja y mantenga, en su superficie, rasgos adquiridos por alteración (física o química) y/o precipitación, los cuales son empleados con gran eficacia en interpretaciones medioambientales de sedimentos, suelos y materiales.

La presente Tesis Doctoral evalúa, en materiales del ámbito Mediterráneo, la fracción arena y el cuarzo contenido en ella. Se trabaja sobre suelos pertenecientes a una cronosecuencia de las terrazas fluviales del río Guadalquivir y sobre materiales eólicos depositados en el sur de la Península Ibérica. La principal hipótesis es que la fracción arena y su principal constituyente, el mineral cuarzo, son indicadores de la génesis y procedencia en los materiales de suelos y polvos eólicos del ambiente Mediterráneo.

Se realizan estudios mineralógicos (difracción de rayos-X –DRX-), de composición elemental (mayores y menores incluidas tierras raras, rare earth elements -REE-) (espectrometría de emisión por plasma de acoplamiento inductivo -ICP-OES-, espectrometría de masas de plasma acoplado por

inducción -ICP-MS-, espectrometría de masas de plasma acoplado por inducción con sistema de ablación láser -LA-ICP-MS-, microscopía electrónica de barrido de electrones retrodispersados -SEM-BSE-, microscopía electrónica de barrido con microanálisis por dispersión de energías de rayos-X -SEM-EDX-, microscopio electrónico de barrido de presión variable equipado con microanálisis EDX, y análisis químico-estructural por espectroscopía Raman -VP-SEM-EDX Raman-, microscopía electrónica de transmisión de alta resolución –HRTEM-) y morfológicos (SEM-EDX, SEM-BSE, microscopía electrónica de barrido con detector de catodoluminiscencia -SEM-CL-, análisis de imagen –IA-, sobre especies minerales, fundamentalmente cuarzo) para obtener información sobre la procedencia y génesis tanto de los materiales edáficos como eólicos.

El estudio de la mineralogía y composición elemental (mayores y menores incluidas REE, con la ayuda de los índices geoquímicos de alteración/evolución) han demostrado la idoneidad de la fracción arena, del suelo de ambientes Mediterráneos, como proveedora de información pedogenética, lo que permite: discutir el origen de los diferentes minerales que contiene y, por tanto, del material del suelo; y conocer la alteración pedogenética que sufre esta fracción granulométrica y la velocidad con que evolucionan sus propiedades y alteración mediante el establecimiento de cronofunciones. Además, el estudio del contenido de elementos traza del mineral cuarzo así como su estructura cristalina, en las arenas de los suelos de una cronosecuencia del río Guadalquivir, han permitido establecer tanto su origen litológico (se han distinguido seis tipos de cuarzos: cuarzo metamórfico, cuarzo granítico no deformado, cuarzo granítico fuertemente alterado, cuarzo granítico recristalizado -deformado-, cuarzo de arenisca y cuarzo hidrotermal) como su procedencia (Macizo Ibérico, Cordilleras Béticas y Cuenca Cenozoica del Guadalquivir).

La caracterización granulométrica y compositiva (mineralogía, elementos químicos mayores y menores) del polvo atmosférico (y de los iberulitos contenidos en él) depositado en un ambiente Mediterráneo aporta información sobre su procedencia. Las muestras de polvo atmosférico fueron originadas tanto en focos locales como africanos. De acuerdo con la mineralogía, proceden del norte-noreste de África y de suelos regionales. Además, la morfología de los granos de cuarzos eólicos es indicativa de procedencia y de la alteración sufrida en el transporte atmosférico. Los granos de cuarzo de origen africano, respecto a los de origen local, presentan las siguientes propiedades: a) mayor presencia de las microtexturas ‘bulbous edges’ y ‘upturned plates’ en su superficie; y b) para los parámetros de forma del cuarzo (shape parameters), menores valores de área, perímetro, feret máximo y mínimo, ‘major axis’, ‘minor axis’, y ‘shape fator’, y mayores valores para ‘aspect ratio’.

Todo ello ha demostrado la potencialidad de la fracción granulométrica arena como informadora de la pedogénesis en suelos Mediterráneos, así como la idoneidad del mineral cuarzo, tanto en suelos como en materiales eólicos, como indicador de procedencia y alteración, pudiendo por si sólo aportar información de gran interés para las Ciencias de la Tierra.

General approach of PhD Thesis

This PhD Thesis evaluates the sand granulometric fraction (50-2000 µm) of materials from the Mediterranean area. We work on soils belonging to a chronosequence of the fluvial terraces of the Guadalquivir River and on aeolian materials deposited in the south of the Iberian Peninsula.

Mineralogical, elemental composition (major and minor including rare earth elements-REE-) and morphological studies (on mineral species, fundamentally quartz) are carried out to obtain information on the origin and genesis of both soil and aeolian materials. The study of mineralogy, geochemical indices of alteration/evolution and REE contents, allow us to evaluate the suitability of the sand fraction as a provider of pedogenetic information. In addition, the study of trace elements content present in the quartz crystal lattice as well as the morphology and surface features of the quartz grains provide information on its origin and provenance. It is intended to evaluate the potential of the sand fraction as an informant of pedogenesis in Mediterranean soils, as well as to clarify the suitability of the quartz mineral as an indicator of origin and alteration, being able by itself to provide information of great interest for Earth Sciences.

This PhD Thesis is made up of seven chapters, five of which are scientific articles published in indexed journals (Journal Citation Reports). In the first chapter, general conceptual ideas are proposed to understand the development of the PhD Thesis. In addition, the hypothesis and objectives are established. In the second, third and fourth chapters, we work on the soils of the fluvial chronosequence of the Guadalquivir River. In the second chapter, titled "Pedogenetic information from fine sand: A study in Mediterranean soils", we studied the fine sand fraction and its results were published in the European Journal Soil Science in 2020. In the third chapter, titled "Provenance of quartz grains from soils over Quaternary terraces along the Guadalquivir River, Spain", published in the journal Geoderma in 2022, we study coarse sand-sized quartz grains. In the fourth chapter, “Lanthanides in granulometric fraction of Mediterranean soils. Can they be used as fingerprints of provenance”, we studied the content of lanthanides in different particle size fractions (including the sand fraction) and their results were published in the European Journal of Soil Science in 2019. In the fifth and sixth chapters, the aeolian materials deposited in the south of the Iberian Peninsula, specifically in the city of Granada, were studied.

Thus, in the fifth chapter, titled “Intrusions of dust and iberulites in Granada basin (Southern Iberian Peninsula). Genesis and formation of atmospheric iberulites”, we characterize the atmospheric dust deposited in the south of the Iberian Peninsula (Granada) during episodes of African intrusions and we study the genesis of iberulites. The results of this chapter were published in the journal Atmospheric Research in 2021. In the sixth chapter, entitled “Provenance fingerprints of atmospheric dust collected at Granada city (Southern Iberian Peninsula). Evidence from quartz grains”, we characterize the atmospheric dust, also deposited in the city of Granada, from three spring events where we study the morphoscopy of the atmospheric quartz mineral to be used as a fingerprint of provenance. The results of this chapter were published in the journal Catena in 2022. Finally, in the seventh chapter the general conclusions obtained in this PhD Thesis are shown.

Chapter 1: Introduction

1. Mediterranean soils

The term ‘Mediterranean’ is applied to a specific climate and kind of vegetation that is typical of areas surrounding the Mediterranean Sea but also found in five other world regions, namely California, central Chile, Southwest and South Australia, and the Cape region of South Africa. Although there is no consensus on the precise delineation of the Mediterranean region, the total area with a true Mediterranean climate is probably some 2×10^6 km^2 (Torrent, 2005). However, according to this author, the Mediterranean region sensu stricto occupies approximately 1.2×10^6 km^2.

Mediterranean region soils are of different ages, fragile and climatically vulnerable (Jones et al., 2012, Fedoroff and Courty, 2013; Lagacherie et al., 2018; Shukla et al., 2019), constituting an area susceptible to degradation and desertification (Ferreira et al., 2022). In addition, Mediterranean pedogenetic environments are extremely diverse, as well as the ecosystems to which they belong (Verheye and de la Rosa, 2005; Ferreira et al., 2022). However, they have common characteristics that make them unique and different from other soils (Torrent, 2005; Lagacherie et al., 2018). According to Yaalon (1997), they have at least four attributes of their own: specific climate, their mountains, the long-term effects of man and dust from the desert.

The climatic conditions under which these soils were formed vary from arid (with the absence of any precipitation) to hyper-humid (certain mountains receive more than 2000 mm of rain on average per year), and the mean values of precipitation range from 350 and 1000mm. Temperatures also vary greatly and average between 10 and 20 ºC (Torrent, 2005). Regarding the soil climate of the Soil Taxonomy (Soil Survey Staff, 2014), the moisture regimes are xeric, mountain xeric, udic and aridic, while temperature regimes are thermic, mesic and cryic. In winter, precipitation exceeds evapotranspiration and favors the processes of soil formation or erosion (increased when rainfall is torrential). Chemical weathering (fundamentally hydrolysis and dissolution) and the leaching of soluble compounds, as well as clay illuviation, find their optimum at this time of year. Hydrolytic alteration of silicate minerals gives rise to clay minerals (Yaalon, 1997; Weil and Brady, 2017). In soil profiles, clay illuviation and its deposition on grains, pores or ped forming coatings (cutans), can generate Bt argillic horizons, which is one of the characteristics of these soils (Fedoroff, 1997; Badía-Villas et al., 2022). Another significant soil development issue is the reprecipitation of calcium carbonate in the lower parts of the profile that gives rise to calcic horizons. Even the dynamics of carbonate dissolution-precipitation can be seasonal (Domínguez-Villar et at., 2022). In hot and dry summers, another specific alteration process occurs, which is rubefaction. The soil dries out, allowing the evolution of iron oxides, mainly hematite (also goethite and ferrihydrite), which are associated with clay particles (epitaxial growths). Another interesting process in Mediterranean environments is the alteration of the quartz mineral. Martin-Garcia et al. (2004, 2015) showed that this mineral is altered in the Mediterranean climate, so its use as an invariant mineral in isoquarcic balances was invalidated. Furthermore, Martin-Garcia et al. (2015) showed how surface alteration features in quartz grains (etch pits), in Sierra Nevada soils, increase to the same extent as soil evolution: Rock < Entisol < Inceptisol < Alfisol.

The Mediterranean region, between two crustal plates, has mountainous areas with steep slopes and high rates of erosion (Raab et al., 2019; Panagos et al., 2020). Altitude varies between over 3000 m and sea level. This orography has hindered the use and exploitation of the soil, which has led man to manage and modify the landscape, eliminating extensive areas of plant cover and thereby increasing soil erosion. Sedimentary rocks predominate, but plutonic, volcanic, and metamorphic rocks are well represented in most areas. Limestones and dolomites constitute a high proportion of the mountains. This variability of parent materials originates different types of soils (Da Silva et al., 2022).

Another defining aspect of soils in the Mediterranean region is the addition of atmospheric dust (Delgado et al., 2003; Fedoroff and Courty, 2013; Lucke et al., 2014, Vingiani et al., 2018; Amit et al., 2021; Tangari et al., 2021). Every year between 1 and 3 billion tons of dust are emitted into the atmosphere from arid and semi-arid areas, particularly from the Sahara and Sahel (North Africa), which are responsible for 50–70% of the global dust emissions. The Iberian Peninsula is frequently affected by air masses coming from Africa (Salvador et al., 2022).

In addition, wind erosion, which is considerable in arid or semi-arid regions of the Mediterranean area and on agricultural land (Tanner et al., 2016), increases this process of adding atmospheric dust. Thus, soils play a very important role in the production of atmospheric dust (Wang et al., 2021), since the dust present in the atmosphere will be determined by the mineralogy of the soils from which it comes (Journet et al., 2014).

Atmospheric dust undergoes mineral alteration processes throughout its transport. Baker et al. (2014) affirmed that atmospheric transport alters the chemical composition of mineral particles, generating layers on mineral dust particle surfaces. Other authors such as Díaz-Hernández and Párraga (2008) have shown the formation of iberulites in the atmosphere (by coalescence of particles) and the neoformation of minerals such as halite and gypsum. Zhang et al. (2022) affirmed that during the haze periods investigated in China, nitrate and mineral dust form a complex mixing state through heterogeneous reactions, which modify the aerosol properties.

Atmospheric mineral dust has become one of the most globally abundant aerosols and an essential component of the Earth's environmental system (Nickovic et al., 2012; Muhs et al., 2014; Schepanski, 2018; Beall et al., 2022). One of the main components of atmospheric dust is quartz (Shentil Kumar and Rajkumar, 2014; Menéndez et al., 2014; Blondet et al., 2019; Candeias et al., 2020). Thanks to their properties and characteristics, atmospheric dust quartz grains can be used as indicators of both the origin of the dust and the atmospheric processes that this mineral undergoes.

2. Soil chronosequences: terraces of the Guadalquivir River

Soils are not static elements of the ecosystem, but evolve continuously over time. The rhythm of its evolution and its evolutionary path are determined by the soil-forming factors (parental material –rock-, climate, relief or topography, biota –organisms- and time).

A very useful tool that can be applied to Mediterranean soils to quantify the action of pedogenic processes and their evolution is the study of soil chronosequences, which allows evaluating the effect of time (evolution) keeping the rest of the soil-forming factors constant. Harden (1982) defines soil chronosequence as a series of genetically related soils that evolve under similar conditions of vegetation, rock, topography, and climate. Furthermore, according to Schaetzl and Anderson (2005), chronosequences are considered as an irreplaceable tool for testing soil evolution models. The chronosequence study allows the comparison of the value of any soil property with respect to its value in parent material (Calero, 2005), which generates an idea of evolution in the set of these soils.

There are several types of soil chronosequence depending on the materials or geomorphic surfaces on which they develop: fluvial terraces, marine terraces, moraine deposits, volcanic rock deposits, etc. The establishment of chronosequences presents problems such as the inconstancy of soil-forming factors such as the parent rock, the climate or the vegetation. Time scales can be very diverse and in the case of very long ones, climatic variability, vegetation, etc., they could cause problems (Calero, 2005). For this reason, soil chronosequences located on Quaternary fluvial terraces constitute a particularly interesting case, since the only factor that varies significantly is the age of the terraces, a phenomenon caused by the fluvial dynamics.

In the Guadalquivir River´s basin (the most important fluvial system in the southern Iberian Peninsula), a system of four fluvial terraces and a floodplain constitute a soil chronosequence. It is a postincisive chronosequence in which there is a sequence of deposits of different ages, and the soils related to each deposit have formed from the end of the time of the deposition to the present (Birkeland, 1999). This is an ideal soil chronosequence: 1) Calero et al. (2008) found that Harden's Profile Development Index (PDI) and some important soil analytical properties of the fine earth fraction (<2 mm), and field morphological characteristics of soil quantified by optimal scaling, fit significant chronofunction equations; 2) some fabric morphometric attributes measured by scanning electron microscopy image-analysis (SEM-IA) also fit chronofunctions (Calero et al., 2009); 3) the transmission electron microscopy with analytical electron microscopy (TEM-AEM) and mineralogy (XRD) studies of mica and smectite in silt (2–50 μm) and clay (<2 μm) fractions (Calero et al., 2013) permitted nanoscale level determination, of statistically significant logarithmic chronofunctions of the crystallochemical parameters; and 4) Martín-García et al. (2016) studied some mineralogical (XRD), crystallochemical differential X-ray diffraction (DXRD), geochemical inductively coupled plasma mass spectrometry (ICP-MS) and inductively coupled plasma atomic emission spectroscopy (ICP-AES) and diffuse reflectance spectroscopy (DRS) colour parameters of the clay fraction of these soils, most of which showed logarithmic chronofunctions with asymptotes at 70–100 ka.

3. Origin of soil sand fraction

An important step in the formation of soil involves the weathering of the rock into smaller and/or chemically altered parts (Blum et al., 2018). It occurs due to rocks are unstable at the Earth´s surface conditions. This new environment is far different (temperature, pressure, oxygen and water concentration or biota) from the one in which they formed (Birkeland, 1999; Tuncay et al., 2019).

Weathering is the physical and chemical alteration of rocks and minerals at or near the Earth´s surface, produced by biological, chemical and physical agents or their combinations, as they adjust toward an equilibrium state in the surface environment (Pope et al., 2002; Weil and Brady, 2017). Physical weathering breaks rocks into smaller fragments down to sand and silt sized particles that are commonly made up of individual minerals. This increases the specific surface area of the material and its pore content (Schaetzl and Anderson, 2005), which facilitates that chemical weathering reactions occur on surfaces, and results in the rocks becoming increasingly fractured. The increase in porosity facilitates root invasion of these holes, which can cause physical breakage and even chemical weathering due to the root exudates and the acid conditions generated by the expulsion of CO_2.

Oxygen and water in contact with fractured rocks increase chemical weathering, releasing soluble materials and synthesizing new minerals, some of which are resistant end products. During the chemical changes, particle size continues to decrease, and constituents continue to dissolve in the aqueous weathering solution. The weathering solution constituents may recombine into new (secondary) minerals, may leave the profile in drainage water, keep in the soil exchange complex, or may be taken up by plant roots.

Geological processes have brought to the Earth’s surface numerous parent materials in which soils form. Inorganic parent materials can either be formed in place as residual material weathered from the rock below, furthermore, they can be also transported from one location and deposited at another. Even, in wet environments (such as swamps and marshes), incomplete decomposition may allow organic parent materials to accumulate from the residues of many generations of vegetation. Colluvial debris, alluvial deposits, coastal sediments, parent materials transported by glacial ice and meltwaters and organic deposit are also parent materials (Weil and Brady, 2017). Parent material can also be constituted by wind contributions, as is the case of soils developed on loess.

Mediterranean region mountains conditions an intense fluvial activity that erodes and transports materials along the rivers courses (Oliva et al., 2022). During flood events in a river course, the adjacent plain is inundated (floodplain) and heterometric sediments are deposited. The coarser materials settling closer to the river channel (where water flows deeper, faster, and with more flow turbulence) and the finer ones settle in calmer floods, far from the channel (Rhoads, 2020). Each flood episode establishes a distinctive layer of sediment size, creating the stratification that characterizes alluvial soils. These materials constitute a parental material from which the pedogenic processes act.

Soil particle size is conditioned by the mineral size in the original rock and their degree of alteration (Blum et al., 2018). Size study is important from the point of view of soil properties. In soil science, it is divided into particles ≥ 2mm (coarse fragment) and ≤ 2mm (fine earth). This last fraction, fine earth (≤ 2mm), is the most studied and is made up of sand (50-2000µm), silt (2-50µm) and clay (<2µm) subfractions. Sand and silt fractions are mainly formed by primary minerals, while secondary minerals abound in clay (formed from the alteration/transformation of primary minerals and neoformation from alteration products) (Figure 1). Each of these granulometric fractions imprints its character on the soil (Table 1) and their relative proportions will define textural class. Classically, sand fraction has been considered inert from the agronomic point of view due to its low potential for the production and development of crops. On the contrary, clay has the greatest agricultural capacities due to its high surface reactivity (Table 1).

Sand fraction is assumed to be inherited from the parent rock and has been considered historically useful for providing information about parent material type and its degree of alteration (Sulieman et al., 2015). However, there is a gap regarding the potential of sand fraction in pedogenetic studies, since few works have used it as an object of study (Delgado et al., 2003; Farragallah and Essa, 2011; Martín-García et al., 2015; Hernández-Hinojosa et al., 2018).

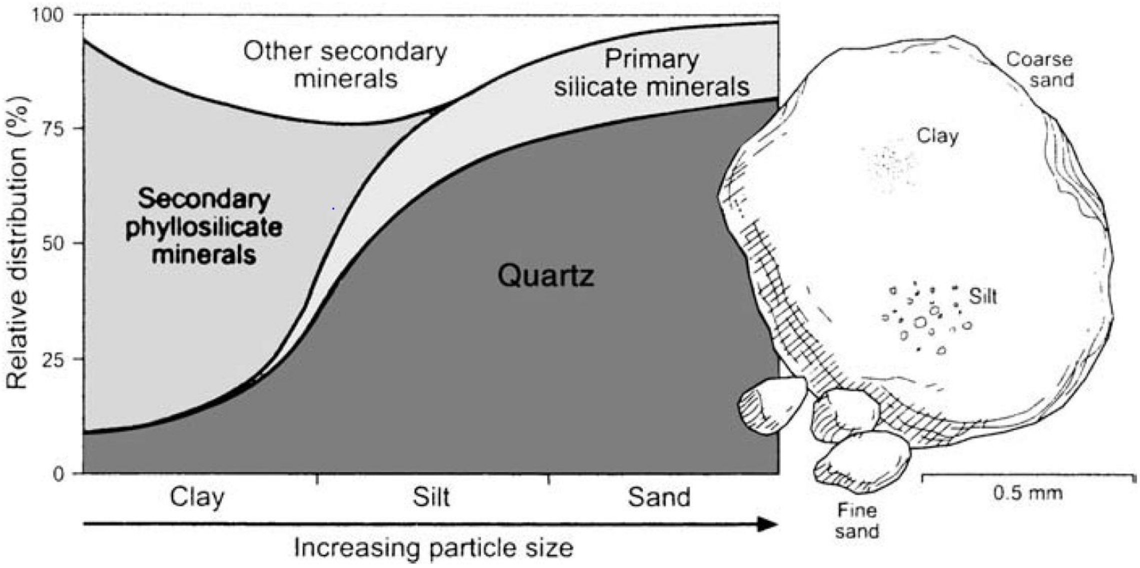

Figure 1. General relationship between particle size and particle mineralogy (source: Schaetzl and Anderson, 2005).

Table 1. Some general properties classically attributed on sand, silt and clay (adapted from: Weil and Brady, 2017).

Property	**Sand**	**Silt**	**Clay**
Size range (mm)	2.0-0.05	0.05-0.002	<0.002
Observation of particles	Naked eye	Light microscope	Electron microscope
Dominant mineral types	Primary	Primary/secondary	Mostly secondary
Attraction of particles for each other	Low	Medium	High
Attraction of particles for water	Low	Medium	High
Surface area	Very low	Low-medium	High-very high
Water-holding capacity	Low	Medium-high	High
Aeration	Good	Medium	poor
Potential to be compacted	Low	Medium	High
Resistant to pH change	Low	Medium	High
Ability to retain chemical and nutrients	Very low	Low	Medium-high
Susceptibility to wind erosion	Moderate (esp. fine sand)	High	Low
Susceptibility to water erosion	Low (unless fine sand)	High	Depends on degree of aggregation
Consistency when wet	Loose, gritty	Smooth	Sticky, malleable
Consistency when dry	Very loose, gritty	Powdery, some clods	Hard clods

4. Geochemistry of soil sand fraction

Geochemistry of the soil coarse granulometric fractions can provide relevant information on the provenance processes of the materials that form it (Garzanti and Resentini, 2016) and on the degree of soil weathering (Schaetzl and Thompson, 2015). Geochemical indices commonly consider the relationship between mobile chemical elements (alkaline and alkaline earth metals) and less mobile ones (Si, Al, Fe, Ti) (Garzanti and Resentini, 2016; Liu et al., 2016).

In addition, geochemistry of rare earth elements (REE) (lanthanoids: $_{57\text{-}71}$ Ln, scandium $_{21}$Sc and yttrium $_{39}$Y) is also used in the study of soils (Laveuf and Cornu, 2009). REE behave like a group that is closely related to parent materials during surface processes and exhibit passive behaviour during supergene processes resulting in their being an excellent tracer of the source area (Blundy and Wood, 2003). Even they are described as ideal tracers of origin in aeolian research (Wang et al., 2017). Therefore, the interest of REEs is due to their close relationship with the source area from which they come, which makes them ideal for using in paleoenvironmental studies of sedimentary origin (Chen et al., 2014; Och et al., 2014) and in soil studies as pedogenetic tracers (Laveuf and Cornu, 2009).

5. Quartz mineral in soil sand fraction

Sand fraction consist mainly of primary minerals, with quartz being the mineral par excellence (Figure 1) (Martín-García et al., 2015). This mineral is the second most abundant in the Earth's Crust (after feldspars), constituting 12.6% by weight of it (Strunz and Tennyson, 1982). Its chemical formula (SiO_2) is shared by 14 natural polymorphs (α-quartz, β-quartz, α-cristobalite, β-cristobalite, α-tridymite, β-tridymite, melanophlogite, fibrous SiO2, moganite, keatite, coesite, stishovite, seifertite and lechatelierite) among which the most abundant is α-quartz.

Quartz-α (hereinafter quartz) is a silicate of the tectosilicate subclass, in which the "bricks" to build its structure are SiO_4 tetrahedra where each oxygen has bonds with the silicon atoms of the adjacent tetrahedra forming a neutral three-dimensional network with general chemical formula SiO_2. It belongs to the trigonal crystal system, specifically to the symmetry point group 32 (enantiomorphic hemihedry). If we observe the structure parallel to the c axis, we appreciate a hexagonal or ditrigonal helical symmetry as well as relatively wide channels that run parallel to c axis (Rottier et al., 2017).

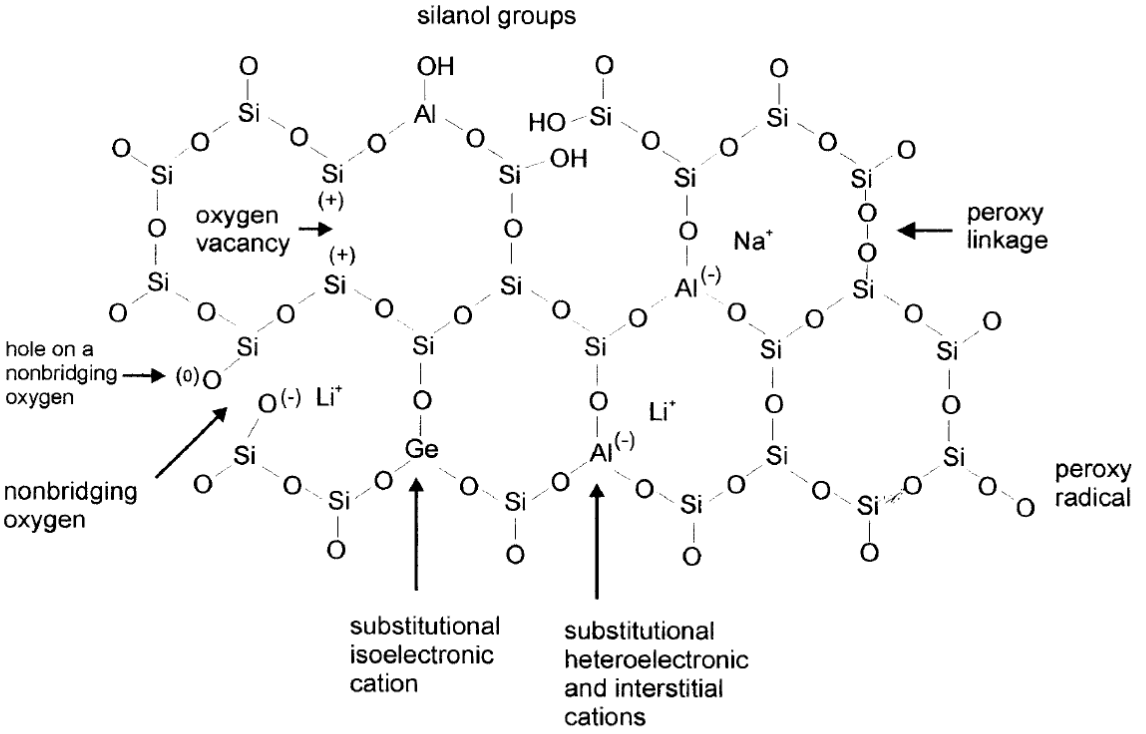

Figure 2. Schematic quartz structure showing the most common intrinsic and extrinsic lattice defects (source: Götze et al., 2001).

In addition, its high hardness (7) and low solubility in water (11.0 ± 1.1 mg kg^{-1}, at 25 ºC and 1 bar; Rimstidt, 1997) makes quartz a very stable mineral facilitating its enrichment in many sediments and clastic rocks (Blatt et al., 1980). This enables quartz to collect and maintain features acquired by weathering (physical or chemical) and/or precipitation on its surface. These are used with great efficiency in environmental interpretations of sediments, soils, and aeolian materials (e.g., Mahaney, 2002; Vos et al., 2014; Kemnitz and Lucke, 2019). The study by scanning electron microscopy (SEM) of these surface features and external morphology in quartz grains allows us to reconstruct their natural history.

Moreover, quartz is one of the chemically purest minerals in nature, after diamond and graphite (Drees et al., 1989). It contains, however, lattice bound trace elements in low concentrations due to atomic substitution of Si and interstitial elemental incorporation within the crystal structure (Figure 2). In addition, quartz may contain micro inclusions of solid, liquid or gaseous phases. Al, Ti, Li, Ge, H, Be, B, Mn, Rb, Sr, Na, P, K, Ca, and Fe are the most common trace elements in natural quartz (Götze et al., 2004; Müller and Koch-Müller, 2009).

Thanks to the chemical purity of this mineral, the content of trace elements is highly informative of its origin-formation. Trace element concentrations are directly determined with in situ micro-beam techniques, such as electron probe micro analysis (EPMA), laser ablation inductively coupled plasma mass spectrometry (LA-ICP-MS) and secondary ion mass spectrometry (SIMS) (Müller et al., 2003) or with spectrometric methods, such as FTIR spectrometry (Stalder et al., 2017) or cathodoluminescence (CL). This latter, is an imaging and spectroscopic technique, which reveals the relative abundance and distribution of lattice defects and impurity trace elements within quartz grains. CL visualises structures related to crystallisation, such as growth zoning and secondary processes (alteration, recrystallisation or radiation damage) (Götze, 2012; Sales de Oliveira et al., 2017). All of the above predisposes the quartz mineral as a possible origin/evolution fingerprint.

6. Hypothesis and objectives

The main hypothesis is that the sand granulometric fraction and its main constituent, the quartz mineral, are indicators of the genesis and origin of soil materials and atmospheric dust from the Mediterranean environment.

This hypothesis is developed as follows:

- Sand fraction provides pedogenetic information (genesis, origin and evolution) in Mediterranean environments.
- Quartz mineral is an indicator of origin and genesis in Mediterranean soils.
- Lanthanides geochemistry in soil fractions (including the sand fraction) provides information on provenance and evolution.
- The compositional characterization (mineralogy, major and minor chemical elements) of atmospheric dust (and the iberulites contained in it) deposited in a Mediterranean environment provides information on its provenance. In addition, the morphology of the aeolian quartz grains is indicative of the origin and the alteration suffered during atmospheric transport.

To address the above hypotheses, the following objectives are proposed:

- Evaluation through compositional (mineralogy and major and minor chemical elements) and morphology analyses, of the fine sand fraction, its capacity to be a fraction of pedogenetic interest in the Mediterranean area. It is intended to quantify the development of its properties over time (Chapter 2).
- To evaluate the provenance/origin of quartz grains (coarse sand) from soils over Guadalquivir River terraces by means of SEM-EDX, SEM-CL and LA-ICP-MS analyses (Chapter 3).
- To study lanthanide concentrations in fine sand, clay and free form of clay in soils over the Guadalquivir River terraces, in order to: 1) determine the effect of age; 2) determine correlations between concentrations of elements; 3) use lanthanides as fingerprints of provenance in comparison with geological materials (Chapter 4).
- To know the mineralogical and REE composition of atmospheric dust deposited in the south of the Iberian Peninsula, during African intrusion events, in order to identify the source area. Characterizing the iberulites (aggregates of particles formed in the atmosphere) collected in atmospheric dust to know its genesis (Chapter 5).
- To characterize the atmospheric dust, of three spring events, in the south of the Iberian Peninsula through its compositional analysis (mineralogical, major and minor chemical elements, including REE) to obtain conclusions about its provenance. Analyze the morphoscopy (microtextures and shape parameters) of atmospheric quartz mineral for its use as a fingerprint of provenance (Chapter 6).

7. References

Amit, R., Enzel, Y., Crouvi, O. (2021). Quaternary influx of proximal coarse-grained dust altered circum-Mediterranean soil productivity and impacted early human culture. Geology, 49(1), 61-65.

Badía-Villas, D., Poch, R. M., Longares, L. A., Yuste, A., Bauluz, B. (2022). Genesis and stability of textural pedofeatures along a soil transect in the siliceous Iberian Chain (NE Spain). Catena, 211, 105965.

Baker, A.R., Laskina, O., Grassian, V.H. (2014). Processing and Ageing in the Atmosphere. In: Knippertz, P., Stuut, J.B. (Eds.), Mineral Dust. Springer, Dordrecht, pp. 75–92.

Beall, C. M., Hill, T. C., DeMott, P. J., Köneman, T., Pikridas, M., Drewnick, F., Harder, H., Pöhlker, C., Lelieveld, J., Weber, B., Iakovides, M., Prokeš, R., Sciare, J., Andreae, M.O., Stokes, M.D., Prather, K. A. (2022). Ice-Nucleating Particles Near Two Major Dust Source Regions. Atmospheric Chemistry and Physics Discussions, 1-46.

Birkeland, P.W. (1999). Soils and Geomorphology. Oxford University Press, New York, 430p.

Blatt, H., Middleton, G.V., Murray, R.C. (1980). Origin of Sedimentary Rocks. Prentice-Hall Inc, Englewood Cliffs, NJ.

Blondet, I., Schreck, E., Viers, J., Casas, S., Jubany, I., Bahí, N., Zouiten, C., Dufréchou, G., Freydier, R., Galy-Lacaux, C., Martínez-Martínez, S., Faz, A., Soriano-Disla, M., Acosta, J.A., Darrozes, J. (2019). Atmospheric dust characterisation in the mining district of Cartagena-La Unión, Spain: air quality and health risks assessment. Sci. Total Environ., 693, 133496.

Blum, W.E.H., Schad, P., Nortcliff, S. (2018). Essentials of Soils Science. Soil formation, functions, use and classification (World reference Base, WRB). Borntraeger Science Publishers, Stuttgart.

Blundy, J. Wood, B. (2003). Partitioning of trace elements between crystals and melts. Earth and Planetary Science Letters, 210, 383–397.

Calero, J. (2005). Génesis de la Fracción Mineral y de la Ultramicrofábrica en una Cronosecuencia de Suelos sobre Terrazas del río Guadalquivir. Tesis Doctoral. Universidad de Granada.

Calero, J., Delgado, R., Delgado, G., Martín-García, J. M. (2009). SEM image analysis in the study of a soil chronosequence on fluvial terraces of the middle Guadalquivir (southern Spain). European Journal of Soil Science, 60, 465–480.

Calero, J., Delgado, R., Delgado, G., Martín-García, J.M. (2008). Transformation of categorical field soil morphological properties into numerical properties for the study of chronosequences. Geoderma 145 (3-4), 278–287.

Calero, J., Martín–García, J. M., Delgado, G., Aranda, V., Delgado, R. (2013). A nano-scale study in a soil chronosequence from southern Spain. European Journal of Soil Science, 64, 192–209.

Candeias, C., Vicente, E., Tomé, M., Rocha, F., Ávila, P., Alves, C. (2020). Geochemical, mineralogical and morphological characterisation of road dust and associated health risks. Int. J. Environ. Res. Public Health, 17 (5), 1563.

Chen, L.M., Zhang, G.L., Jin, Z.D. (2014). Rare earth elements of a 1000-year paddy soil chronosequence: implications for sediment provenances. Parent material uniformity and pedological changes. Geoderma, 230, 274–279.

Da Silva, R. J. A. B., da Silva, Y. J. A. B., van Straaten, P., do Nascimento, C. W. A., Biondi, C. M., da Silva, Y. J. A. B., de Araújo Filho, J. C. (2022). Influence of parent material on soil chemical characteristics in a semi-arid tropical region of Northeast Brazil. Environmental Monitoring and Assessment, 194(5), 1-21.

Delgado, R., Martín-García, J.M., Oyonarte, C. Delgado, G. (2003). Genesis of the *terrae rossae* of the Sierra Gádor (Andalusia, Spain). *European Journal of Soil Science*, 54, 1–16.

Díaz-Hernández, J.L., Párraga, J. (2008). The nature and tropospheric formation of iberulites: pinkish mineral microspherulites. Geochim. Cosmochim. Acta 72 (15), 3883–3906.

Domínguez-Villar, D., Bensa, A., Švob, M., Krklec, K. (2022). Causes and implications of the seasonal dissolution and precipitation of pedogenic carbonates in soils of karst regions–A thermodynamic model approach. Geoderma, 423, 115962.

Drees, L.R., Wilding, L.P., Smeck, N.E., Senkayi, A.L. (1989). Silica in soils: quartz and disordered silica polymorphs. In: Dixon, J.B., Weed, S.B.

(Eds.), Minerals in Soil Environments. Soil Science Society of America, Madison, WI, pp. 913–965.

Farragallah, M. A., Essa, M. A. (2011). Sand and clay mineralogical composition in relation to origin, sedimentation regime, uniformity, and weathering rate of Nile terrace soils at Assiut, Egypt. Australian Journal of Basic and Applied Sciences, 5, 239–256.

Fedoroff, N. (1997). Clay illuviation in Red Mediterranean soils. Catena, 28(3-4), 171-189.

Fedoroff, N., Courty, M. A. (2013). Revisiting the genesis of red Mediterranean soils. Turkish Journal of Earth Sciences, 22(3), 359-375.

Ferreira, C. S., Seifollahi-Aghmiuni, S., Destouni, G., Ghajarnia, N., Kalantari, Z. (2022). Soil degradation in the European Mediterranean region: Processes, status and consequences. Science of the Total Environment, 805, 150106.

Garzanti, E., Resentini, A. (2016). Provenance control on chemical indices of weathering (Taiwan river sands). Sedimentary Geology, 336, 81–95.

Götze, J. (2012). Mineralogy, geochemistry and cathodoluminescence of authigenic quartz from different sedimentary rocks. In: Götze, J., Möckel, R. (Eds.), Quartz: Deposits, Mineralogy and Analytics. Springer, Berlin, Heidelberg, pp. 287–306.

Götze, J., Plötze, M., Graupner, T., Hallbauer, D.K., Bray, C.J. (2004). Trace element incorporation into quartz: a combined study by ICP-MS, electron spin resonance, cathodoluminescence, capillary ion analysis, and gas chromatography. Geochim. Cosmochim. Acta 68 (18), 3741–3759.

Götze, J., Plötze, M., Habermann, D. (2001). Origin, spectral characteristics and practical applications of the cathodoluminescence (CL) of quartz–a review. Mineralogy and petrology, 71(3), 225-250.

Harden, J.W. (1982). A quantitative index of soil development from field descriptions: examples for a chronosecuence in central California. Geoderma 28, 1–28.

Hernández-Hinojosa, V., Montiel-García, P. C., Armstrong-Altrin, J. S., Nagarajan, R., Kasper-Zubillaga, J. J. (2018). Textural and geochemical characteristics of beach sands along the western Gulf of Mexico, Mexico. Carpathian Journal of Earth and Environmental Sciences, 13, 161–174.

Jones, A., Panagos, P., Barcelo, S.; Bouraoui, F.; Bosco, C.; Dewitte, O., Gardi, C., Erhard, M., Hervás, J., Hiederer, R. (2012). The State of Soil in Europe; A Contribution of the JRC to the European Environment Agency's Environment State and Outlook Report; European Commission: Luxembourg.

Journet, E., Balkanski, Y., Harrison, S.P. (2014). A new data set of soil mineralogy for dust-cycle modeling. Atmos. Chem. Phys. 14 (8), 3801–3816.

Kemnitz, H., Lucke, B. (2019). Quartz grain surfaces–A potential microarchive for sedimentation processes and parent material identification in soils of Jordan. Catena 176, 209–226.

Lagacherie, P., Alvaro-Fuentes, J., Annabi, M., Bernoux, M., Bouarfa, S., Douaoui, A., Grünberger, O., Hammani, A., Montanarella, L., Mrabet, R., Sabir, M., Raclot, D. (2018). Managing Mediterranean soil resources under global change: expected trends and mitigation strategies. Regional environmental change, 18(3), 663-675.

Laveuf, C., Cornu, S. (2009). A review on the potentiality of rare earth elements to trace pedogenetic processes. Geoderma, 154, 1–12.

Liu, B., Jin, H., Sun, Z., Zhao, S. (2016). Geochemical weathering of aeolian sand and its palaeoclimatic implications in the Mu Us Desert, northern China, since the Late Holocene. Journal of Arid Land, 8, 647–659.

Lucke, B., Kemnitz, H., Bäumler, R., Schmidt, M. (2014). Red Mediterranean Soils in Jordan: New insights in their origin, genesis, and role as environmental archives. Catena, 112, 4-24.

Mahaney, W.C. (2002). Atlas of sand grain surface textures and applications. Oxford University Press, New York.

Martín-García, J. M., Sánchez-Marañón, M., Calero, J., Aranda, V., Delgado, G., Delgado, R. (2016). Iron oxides and rare earth elements in the clay fractions of a soil chronosequence in southern Spain. European Journal of Soil Science, 67, 749–762.

Martín-García, J.M., Aranda, V., Gámiz, E., Bech, J., Delgado, R. (2004). Are Mediterranean mountains Entisols weakly developed? The case of Orthents from Sierra Nevada (Southern Spain). Geoderma 118, 115–131.

Martín-García, J.M., Márquez, R., Delgado, G., Sánchez-Marañón, M., Delgado, R. (2015). Relationships between quartz weathering and soil type (Entisol, Inceptisol and Alfisol) in Sierra Nevada (southeast Spain). Eur. J. Soil Sci. 66 (1), 179–193.

Menéndez, I., Pérez-Chacón, E., Mangas, J., Tauler, E., Engelbrecht, J.P., Derbyshire, E., Cana, L., Alonso, I. (2014). Dust deposits on La Graciosa Island (Canary Islands, Spain): texture, mineralogy and a case study of recent dust plume transport. Catena, 117, 133–144.

Muhs, D.R., Prospero, J.M., Baddock, M.C., Gill, T.E. (2014). Identifying Sources of Aeolian Mineral Dust: Present and Past. In: Knippertz, P., Stuut, J.B. (Eds.), Mineral Dust. Springer, Dordrecht, pp. 51–74.

Müller, A., Koch-Müller, M. (2009). Hydrogen speciation and trace element contents of igneous, hydrothermal and metamorphic quartz from Norway. Mineral. Mag. 73 (4), 569–583.

Müller, A., Wiedenbeck, M., van den Kerkhof, A.M., Kronz, A., Simon, K. (2003). Trace elements in quartz – a combined electron microprobe, secondary ion mass spectrometry, laser-ablation ICP-MS, and cathodoluminescence study. Eur. J. Mineral. 15 (4), 747–763.

Nickovic, S., Vukovic, A., Vujadinovic, M., Djurdjevic, V., Pejanovic, G. (2012). Highresolution mineralogical database of dust-productive soils for atmospheric dust modeling. Atmos. Chem. Phys. 12 (2), 845–855.

Och, L.M., Müller, B., Wichser, A., Ulrich, A., Vologina, E.G., Sturm, M. (2014). Rare earth elements in the sediments of Lake Baikal. Chemical Geology, 376, 61–75.

Oliva, M., Palacios, D., Fernández-Fernández, J. M. (2022). The Iberian Peninsula: from palaeoglaciers to the current glaciers. In Iberia, Land of Glaciers (pp. 55-60). Elsevier.

Panagos, P., Ballabio, C., Poesen, J., Lugato, E., Scarpa, S., Montanarella, L., Borrelli, P. (2020). A soil erosion indicator for supporting agricultural, environmental and climate policies in the European Union. Remote Sensing, 12(9), 1365.

Pope, G. A., Meierding, T. C., Paradise, T. R. (2002). Geomorphology's role in the study of weathering of cultural stone. Geomorphology, 47, 211–225.

Raab, G., Egli, M., Norton, K., Dahms, D., Brandová, D., Christl, M., Scarciglia, F. (2019). Climate and relief-induced controls on the temporal variability of denudation rates in a granitic upland. Earth Surface Processes and Landforms, 44(13), 2570-2586.

Rhoads, B.L. (2020). River Dynamics: Geomorphology to Support Management. Cambridge University Press.

Rimstidt, J.D. (1997). Quartz solubility at low temperatures. Geochim. Cosmochim. Acta 61 (13), 2553–2558.

Rottier, B., Rezeau, H., Casanova, V., Kouzmanov, K., Moritz, R., Schlöglova, K., Wälle, M., Fontboté, L. (2017). Trace element diffusion and incorporation in quartz during heating experiments. Contrib. to Mineral. Petrol. 172 (4), 23.

Sales de Oliveira, C.E., Pe-Piper, G., Piper, D.J.W., Zhang, Y., Corney, R. (2017). Integrated methodology for determining provenance of detrital quartz using optical petrographic microscopy and cathodoluminescence (CL) properties. Mar. Pet. Geol. 88, 41–53.

Salvador, P., Pey, J., Pérez, N., Querol, X., Artíñano, B. (2022). Increasing atmospheric dust transport towards the western Mediterranean over 1948–2020. npj Climate and Atmospheric Science, 5(1), 1-10.

Schaetzl, R. J., Thompson, M. L. (2015). Soil genesis and geomorphology. New York, NY: Cambridge University Press.

Schaetzl, R., Anderson, S. (2005). Soil Genesis and Geomorphology. Cambridge, University Press, UK.

Schepanski, K. (2018). Transport of mineral dust and its impact on climate. Geosciences, 8 (5), 151.

Senthil Kumar, R., Rajkumar, P. (2014). Characterization of minerals in air dust particles in the state of Tamilnadu, India through FTIR, XRD and SEM analyses. Infrared Phys. Technol. 67, 30–41.

Shukla, P.R., Skea, J., Slade, R., van Diemen, R., Haughey, E., Malley, J., Pathak, M., Pereira, J.P. (2019). Technical Summary In: P.R. Shukla, J. Skea, E. Calvo Buendia, V. Masson-Delmotte, H-O. Pörtner, D. C. Roberts, P. Zhai, R. Slade, S. Connors, R. van Diemen, M. Ferrat, E. Haughey, S. Luz, S. Neogi, M. Pathak, J. Petzold, J. Portugal Pereira, P. Vyas, E. Huntley, K. Kissick, M. Belkacemi, J. Malley, (Eds.). Climate Change and Land: an IPCC special report on climate change, desertification, land degradation, sustainable land management, food security, and greenhouse gas fluxes in terrestrial ecosystems. Geneva, Switzerland: The Intergovernmental Panel on Climate Change (IPCC).

Soil Survey Staff. (2014). Keys to soil taxonomy, 12th ed. Washington DC: Natural Resources Conservation Service, United States Department of Agriculture.

Stalder, R., Potrafke, A., Billström, K., Skogby, H., Meinhold, G., Gögele, C., Berberich, T. (2017). OH defects in quartz as monitor for igneous, metamorphic, and sedimentary processes. Am. Mineral. 102 (9), 1832–1842.

Strunz, H., Tennyson, C. (1982). Mineralogical Tables. Akademie-Verlaggesellschaft. Geest & Portig, Leipzig.

Sulieman, M. M., Ibrahim, I. S., Elfaki, J. T., Dafa-Allah, M. S. (2015). Origin and distribution of heavy minerals in the surficial and subsurficial sediments of the alluvial Nile River terraces. Open Journal of Soil Science, 5, 299–310.

Tangari, A. C., Le Pera, E., Andò, S., Garzanti, E., Piluso, E., Marinangeli, L., Scarciglia, F. (2021). Soil-formation in the central Mediterranean: Insight from heavy minerals. Catena, 197, 104998.

Tanner, S., Katra, I., Haim, A., Zaady, E. (2016). Short-term soil loss by eolian erosion in response to different rain-fed agricultural practices. Soil and Tillage Research, 155, 149-156.

Torrent, J. (2005). Mediterranean soils. In: Encyclopedia of Soils in the Environment (ed. D. Hillel), pp. 418– 427. Elsevier/Academic Press, Oxford.

Tuncay, T., Dengiz, O., Bayramin, I., Kilic, S., Baskan, O. (2019). Chemical weathering indices applied to soils developed on old lake sediments in a semi-arid region of Turkey. Eurasian Journal of Soil Science, 8, 60-72.

Verheyen, W., Rosa, D.d.l. (2005). Mediterranean soils in Land Use and Land Cover. Encyclopedia of Life Support Systems (EOLSS). EOLSS Publisheres, Oxford, UK.

Vingiani, S., Di Iorio, E., Colombo, C., Terribile, F. (2018). Integrated study of red Mediterranean soils from southern Italy. Catena, 168, 129-140.

Vos, K., Vandenberghe, N., Elsen, J. (2014). Surface textural analysis of quartz grains by scanning electron microscopy (SEM): From sample preparation to environmental interpretation. Earth-Sci. Rev. 128, 93–104.

Wang, G., Li, J., Ravi, S., Van Pelt, R.S., Costa, P.J.M. Dukes, D. (2017). Tracer techniques in aeolian research: approaches, applications, and challenges. Earth-Science Reviews, 170, 1–16.

Wang, R.D., Li, Q., Zhang, C.L., Wang, Z.T., Guo, Z.L., Chang, C.P., Li, J.F. (2021). Comparison of dust emission ability of sand desert, gravel desert (Gobi), and farmland in northern China. Catena, 201, 105215.

Weil, R.R., Brady, N.C. (2017). The Nature and Properties of Soils. Fifteenth Edition, Pearson, Columbus.

Yaalon, D. H. (1997). Soils in the Mediterranean region: what makes them different? Catena, 28(3-4), 157-169.

Zhang, X., Wei, H., Zou, S., Duan, J., Li, W., Dai, C. (2022). Effect of nitrate coatings on the optical properties of mineral dust particles during the haze aging process. Journal of Quantitative Spectroscopy and Radiative Transfer, 277, 107966.

Chapter 2:

Pedogenic information from fine-sand. A study in Mediterranean soils

Pedogenic information from fine-sand. A study in Mediterranean soils

J.M. Martín-García[a], A. Molinero-García[a], J. Calero[b], M. Sánchez-Marañón[a], M.V. Fernández-González[a], R. Delgado[a]

[a]Departamento de Edafología y Química Agrícola, Universidad de Granada, 18071 Granada, Spain

[b]Departamento de Geología, Universidad de Jaén, 23071 Jaén, Spain

*Author for correspondence: A. Molinero-García. E-mail: amolinerogarcia@ugr.es

Published on:

European Journal of Soil Science (2020), 71 (4), 580-597.
https://doi.org/10.1111/ejss.12935

Impact Factor (JCR):

Journal Impact Factor, JIF (2020): **4.949**; JIF Percentil in Category (Soil science - Scie): **77.03 (Q1)**

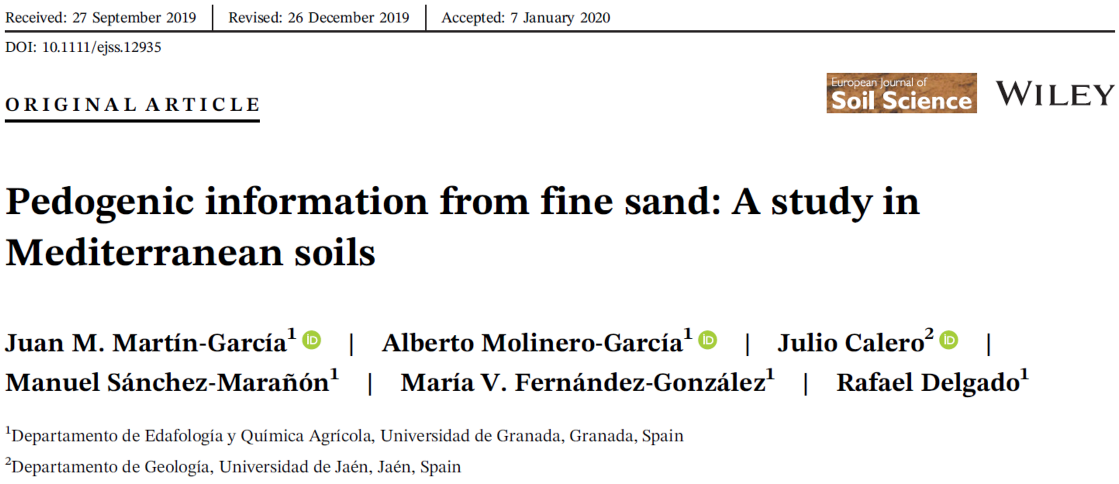

Received: 27 September 2019 | Revised: 26 December 2019 | Accepted: 7 January 2020
DOI: 10.1111/ejss.12935

ORIGINAL ARTICLE

European Journal of Soil Science WILEY

Pedogenic information from fine sand: A study in Mediterranean soils

Juan M. Martín-García[1] | Alberto Molinero-García[1] | Julio Calero[2] | Manuel Sánchez-Marañón[1] | María V. Fernández-González[1] | Rafael Delgado[1]

[1]Departamento de Edafología y Química Agrícola, Universidad de Granada, Granada, Spain
[2]Departamento de Geología, Universidad de Jaén, Jaén, Spain

Abstract

The fine sand fraction (50 – 250 µm) of Mediterranean soils from Southern Spain provides valuable information on soil genesis and the origin of their parent materials. This study considers the whole fine sand and heavy fine sand (ρ >2.82 g cm^{-3}) of Luvisols, Calcisols and Fluvisols which form a chronosequence (ages from 600 to 0.3 ka) of the River Guadalquivir terrace system. Advanced techniques (XRD, ICPms, ICP-AES, VPSEM with EDX system and Raman analysis) were employed. Inheritance is the principal pedogenic process. The whole fine sand consisted of carbonates (calcite and dolomite), tectosilicates (quartz, K-feldspar and plagioclases), phyllosilicates (illite/moscovite, biotite, Na-mica, chlorite, kaolinite, interstratified vermiculite-chlorite, vermiculite-illite and smectite-illite) and iron oxides (goethite and haematite). The minor minerals (rutile, anatase, ilmenite, zircon, staurolite, monacite, barite, apatite, andalusite, garnet and titanite) are concentrated, also through inheritance, in the heavy fine sand. However, there is also substantiated evidence for neoformation of rutile in these soils, never reported previously. In addition, we report that (1) the geochemical indices calculated in fine sand (SiO_2/CaO; Chemical Index of Weathering –CIW-; Weathering Index of Parker –WIP-; Weathering Index –WI-; Base Depletion Index –BDI-; Weathering Ratio –WR-; Sr/Zr) are closely related to soil age, allowing chronofunctions to be established; and (2) geochemical indices provide information on the origin of soils and permit the establishment of a ‘critical point’ corresponding to ‘time zero’, that is, the start of pedogenic alteration of the parent material.

Keywords: geochemical indices; Raman spectroscopy; rutile neoformation; heavy fine sand; soil chronofunction; Guadalquivir River.

Highlights:

- Mineralogy and geochemistry inform on the provenance of the fine sand
- Rutile is neoformed in the fine sand and co-exists with the polymorph anatase
- The properties of the fine sand including geochemical indexes fit chronofunctions

- Geochemical indices determine a ‘critical point’ related to the start of weathering

1. Introduction

The sand in soil (granulometric fraction 50-2000 µm) has been studied in the recent past (20th century) for a variety of reasons, including as a nutrient reserve in tropical soils (Tamm, 1937) or an indicator of the uniformity of the parent material (Arnold, 1968). More recently, it has been used to study specific pedogenic processes such as quartz dissolution (Martín-García *et al.*, 2004, 2015) and mica alteration (Martín-García *et al.*, 1998; Delgado *et al.*, 2003) and as an indicator of the provenance of materials and the degree of alteration in soil chronosequences (Tejan-Kella *et al.*, 1991a; Farragallah and Essa, 2011; Sulieman *et al.*, 2015). Nonetheless, relatively few studies have employed the sand in soils to investigate pedogenesis, and to a lesser extent in Mediterranean soils. This may be due to sand only being considered useful, historically, for providing information on parent material type and its degree of alteration, since it is assumed to be inherited from the parent material. By contrast, the sand fraction is frequently studied in sedimentology. For example, Hernández-Hinojosa *et al.* (2018) analyzed the mineralogy of sands along the Western Gulf of Mexico using X-Ray Diffraction (XRD) and Scanning Electron Microscopy-Energy Dispersive X-ray spectroscopy (SEM-EDX) and their geochemistry by X-ray fluorescence, to evaluate the intensity of chemical weathering, provenance, and tectonic environment.

The use of geochemical indices of evolution/alteration is another method employed in the study of the sand fraction (Garzanti & Resentini, 2016; Liu *et al.*, 2016). These indices generally consider the mobile chemical elements (mainly alkaline and alkaline earth metals) in relation to the least mobile elements (principally silica (Si), aluminium (Al) and iron (Fe)). The indices are primarily conditioned by the minerals containing these elements and the resistance of these minerals to alteration. Geochemical indices have been employed in soils to estimate the degree of evolution (Schaetzl and Thompson, 2015), as, during pedogenesis, unstable minerals are eliminated faster than those which are resistant. These indices are also useful in studies on the provenance of materials

(Garzanti & Resentini, 2016); nonetheless, there is a notable absence of soil studies with these objectives, particularly involving the sand fraction.

A soil chronosequence is a series of soils which differ in their profile development due to their differences in age, while the other soil-forming factors remain constant if possible. In the basin of the River Guadalquivir (the most important fluvial system in the Southern Iberian Peninsula) a system of four fluvial terraces and a floodplain, constitute an almost ideal soil chronosequence: Calero *et al.* (2008) found that Harden's Profile Development Index (PDI) and some important soil analytical properties of the fine earth fraction (<2 mm) and field morphological characteristics of soil quantified by optimal scaling fit significative chronofunction equations; furthermore, some fabric morphometric attributes measured by Scanning Electron Microscopy Image-Analysis (SEM-IA) also fit chronofunctions (Calero *et al.*, 2009). The Transmission Electron Microscopy with Analytical Electron Microscopy (TEM-AEM) and XRD studies of mica and smectite in silt (2 – 50 µm) and clay (<2 µm) fractions (Calero *et al.*, 2013) permitted determination, at nanoscale level, of statistically significant logarithmic chronofunctions of the crystallochemical parameters; Martín-García et al. (2016) studied some mineralogical (XRD), crystallochemical Differential X-ray Diffraction (DXRD), geochemical Inductively Coupled Plasma mass spectrometry (ICP-ms) and Inductively Coupled Plasma Atomic Emission Spectroscopy (ICP-AES) and Diffuse Reflectance Spectroscopy (DRS) colour parameters of the clay fraction of these soils, most of which showed logarithmic chronofunctions with asymptotes at 70-100 ka; and finally, Martín-García et al. (2019) established chronofunctions with the contents of lanthanides. However, the role of fine sand in this chronosequence, has not been studied.

Consequently, the aim of the present research, centred on the Mediterranean soils from the River Guadalquivir chronosequence, was to investigate the chemical and mineralogical compositions and morphology at the SEM scale of the soil fine sand fraction. Evolution/alteration indices of fine sand are calculated. An original aspect of this study is the investigation of chronofunctions with the properties measured in the fine sand. All of this is in order to elucidate the pedogenetic applications of fine sand. These themes have scarcely been studied to date.

2. Materials and Methods

2.1. Setting and soils

The alluvium of the River Guadalquivir (Figure 1a) consists of gravels with some stone-free sandy or silty layers derived from lithologically diverse rocks in the drainage basin: igneous rocks (acids, alkaline and intrusive rocks) and metamorphic rocks from the Iberian Massif (Larrea *et al.*, 1992, 1994, 1995, 1996; Carracedo *et al.*, 1997; Pin *et al.*, 2002; Martínez *et al.*, 2008; Pascual *et al.*, 2008); sedimentary rocks from the External Betic Zones of the Betic Cordilleras (Ortega-Huertas *et al.*, 1991; Martínez-Ruiz, 1994); metasedimentary rocks from the Internal Betic Zones of the Betic Cordilleras (Torres-Ruiz *et al.*, 2003); and quaternary sediments from the Guadalquivir Depression –Cenozoic Basin– (Martínez *et al.*, 2008; Jiménez-Espinosa *et al.*, 2016).

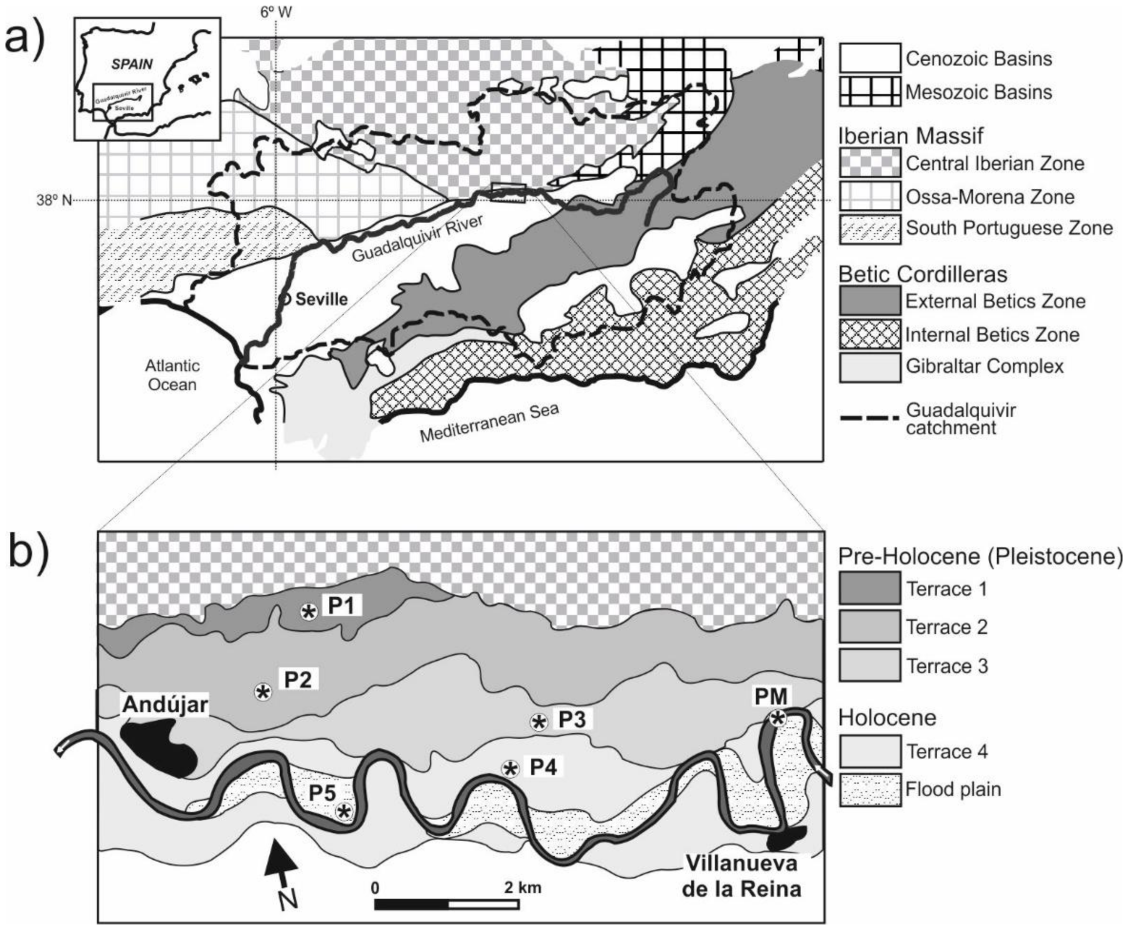

Figure 1. Study area: a) location and geology of the Guadalquivir catchment; b) position of fluvial terrace levels and soil sampling.

The study area is located between the towns of Andújar and Villanueva de la Reina (Figure 1b) in the middle reaches of the Guadalquivir River. Five representative soil profiles (P1 to P5) were selected from a postincisive soil chronosequence on fluvial terraces of the Guadalquivir River (Terrace 1 to Terrace 4 and Flood Plain) (Figure 1b; Table 1). The age of the surfaces ranges from 600 ka to 0.3 ka. Preholocenic terraces are Terrace 1 (600 ka), Terrace 2 (300 ka) and Terrace 3 (70 ka). Holocenic surfaces are Terrace 4 (7 ka) and the Flood Plain (0.3 ka). The soil surface ages were determined by Santos-García (1988), Santos-García *et al.* (1991) and Carral *et al.* (1998). Together with the soil profiles, fresh point bar sediments of the Guadalquivir River course were also sampled. The climate is Mediterranean (mean annual temperature of 18 ºC and total annual precipitation of 650 mm). Currently, the soils are mainly used for the cultivation of olives and other crops (mainly wheat and cotton).

2.2. Samples and soil-fine sand analyses

The bulk soil samples were air dried and sieved to <2 mm to obtain the fine earth. Subsequently, and after the removal of organic matter with H_2O_2, the fine sand fraction (50 – 250 µm) was separated by wet sieving and collected on quartered aliquots for later analysis (these samples are denoted as ‘whole fine sand’ in this study). For some analyses (such as XRD study and Variable Pressure Scanning Electron Microscope (VP-SEM) observations), the whole fine sand fraction was separated gravimetrically with bromoform ($\rho = 2.82$ g/cm^3) in order to concentrate the heavy fraction, denoted as ‘heavy fine sand’.

The quantitative mineralogical composition of whole fine sand was determined by XRD (powder method) with a Siemens D5000 X-ray diffractometer (Siemens, Karlsruhe, Germany) under the conditions: Cu *K*□ radiation, 35 kV, 15 mA, a step size of 0.05 º2θ. Mineral percentages were estimated by the intensity factor method (Martín-García *et al.*, 1997). For selected heavy fine sand samples, a qualitative study was carried out using XRD (same apparatus and conditions).

Selected samples of whole fine sand were examined morphologically and analytically using a VP-SEM, Zeiss SUPRA40VP equipment (Carl Zeiss SMT GmbH, Oberkochen, Germany), acceleration voltage at between 0.2 and 30 kV, in conventional mode, with a backscattered electron detector (AsB images), equipped with an EDX detector, and with a structural and chemical analyzer by Raman spectroscopy inside the measurement chamber of the SEM (SCA-Raman), with two laser excitation lines at 532 and 785 nm. The samples were mounted on aluminium sample holders on double-sided adhesive carbon paper and metallized with carbon. The use of the VP-SEM in backscattered electron images mode permitted the detection of minerals with elements of relatively high atomic mass, due to its greater luminosity. In the case of TiO_2 polymorphs, SCA-Raman allowed differentiation of rutile crystals (space group: $P4_2/mnm$) from those of anatase (space group: $I4_1/amd$). In the VP-SEM studies, at least 50 grains per sample were analyzed.

Chemical analyses of whole fine sand were carried out at the Natural History Museum laboratories (London, UK). Following a lithium metaborate fusion and nitric acid digestion, the following were determined: (a) Major oxides, by ICP-AES: SiO_2, Al_2O_3, CaO, Fe_2O_3, K_2O, MgO, Na_2O, P_2O_5, TiO_2; (b) trace elements by ICPms: Sc, V, Cr, Mn, Co, Ni, Cu, Zn, Ga, Rb, Sr, Y, Zr, Nb, Mo, Sn, Cs, Ba, Hf, Ta, W, Tl, Pb, Th, U. The sum of the lanthanide elements (ΣREE) was taken from Martín-García *et al.* (2019). Several weathering indices were used to estimate the extent of chemical alteration:

1) SiO_2/CaO
2) Chemical Index of Weathering (Harnois, 1988): CIW = $100×Al_2O_3/(Al_2O_3+CaO+Na_2O)$
3) Weathering Index of Parker (Parker, 1970): WIP = $100×(CaO_{MOLAR}/0.7+MgO_{MOLAR}/0.9+2Na_2O_{MOLAR}/0.35+2K_2O_{MOLAR}/0.25)$
4) Weathering Index (Vogel, 1975): WI = $100×(CaO+MgO+Na_2O+K_2O)/(SiO_2+Al_2O_3+Fe_2O_3+CaO+MgO+Na_2O+K_2O)$
5) Base Depletion Index (Jien et al., 2016): BDI = $(CaO+MgO+Na_2O+K_2O)/(Al_2O_3+Fe_2O_3+TiO_2)$
6) Weathering Ratio (Chittleborough, 1991): WR = $(CaO+MgO+Na_2O)/ZrO_2$
7) Sr/Zr (Muhs *et al.*, 2001)

Some of these weathering indices were calculated for the clay fraction of these soils by using Martín-García et al. (2016)'s data. Statistical analysis was carried out using the IBM SPSS v.22.0 software package.

Table 1. Characteristics of the soil chronosequence sampled in the Guadalquivir river terraces (SE Spain)[a].

Chronosequence Level	P1	P2	P3	P4	P5	PM
Altitude /m	250	230	215	206	200	200
Age /ka	600, pre-Holocene	300, pre-Holocene	70, pre-Holocene	7, Holocene	0.3, Holocene	0.001, Holocene
Soil[b]	Cutanic Luvisol	Lixic Calcisol	Cutanic Luvisol	Haplic Calcisol	Haplic Fluvisol	Alluvial[c]
Horizons (HDI[d])	Ap(0.38), Bt(0.52), Btg1(0.44), Btg2(0.44), 2BCtg(0.33), 3BCt(0.33), 4C(0.19)	Ap(0.44), Btg1(0.52), Btg2(0.54), Btk(0.51), Cmk/Btk(0.35)	Ap1(0.31), Ap2(0.28), Bt1(0.45), Bt2(0.46), Bt3(0.58), Bt4(0.56), Bt5(0.48), 2Bt6(0.35), 3Bt7(0.33)	Ap1(0.37), Ap2(0.31), Bwk1(0.33), 2Bwk2(0.35), 3C1(0.16), 4C2(0.09)	Ap(0.28), 2C1(0.16), 3C2(0.09), 4C3(0.20), 5C4(0.10), 6C5(0.17), 7C6(0.19)	Point-bar deposit (0.00)
PDI[d]	44.8	44.3	39.6	26.8	21.2	0
Solum thickness /m	1.65	>0.89	1.83	0.75	0.32	
Moist colour[e] (Munsell)	6.4YR 4.2/5.5	5.6YR 4.8/6.0	5.6YR 3.9/5.6	9.2YR 4.2/3.5	10YR 4/3	2.5Y 5/3
Clay[e] /%	32.3	42.4	31.3	29.7	23.0	16.3
Fine sand[e] /%	31.9	20.6	33.5	31.0	41.5	21.6
Organic C[e] /%	0.24	0.35	0.21	0.48	0.77	1.76
Carbonates[e] /%	0.8	16.2	0.0	26.0	38.4	23.5
pH[e]	7.3	7.9	7.6	8.1	7.9	8.4
CEC[e] /$\mathrm{cmol_{+}kg^{-1}}$	8.9	14.4	10.5	11.3	12.8	8.7

[a] Data summarized from Calero *et al.* (2008, 2009, 2013) and Martín-García *et al.* (2016)

[b] Soil classification (IUSS Working Group WRB).

[c] Current sediments

[d] HDI= Horizon Development Index; PDI= Profile Development Index (Martín-García *et al.*, 2016)

[e] Mean values of solum or sediment, measured in fine earth (<2 mm)

3. Results

3.1. XRD mineralogy

The following minerals were identified in the whole fine sand (Table S1, supplementary material): the phyllosilicates K-mica, Na-mica (paragonite), chlorite, kaolinite, and some 2:1 phyllosilicate phases with spacings between 1.23-1.53 nm and 1.0-1.22 nm (identified by Calero *et al.*, 2013 as smectite, chlorite and interstratified vermiculite-chlorite, vermiculite-illite and smectite-illite), tectosilicates quartz and feldspars (K-feldspar and plagioclases), iron (hydr)oxides (goethite and haematite) and carbonates (calcite and dolomite).

The XRD mineralogy of the heavy fine sand fraction of selected samples (Table S1, Figure S1, supplementary material; supported by Figures 2 and 3) revealed a range of mineral classes (and species): oxides (rutile, anatase, ilmenite, goethite and haematite), silicates (zircon, staurolite, quartz, K-mica, andalusite, garnet, chlorite and titanite) and carbonates (calcite and dolomite). This composition (Table S1) is different to that of the whole fine sand, although with a few coinciding mineral species: quartz, K-mica, chlorite, goethite, haematite, calcite and dolomite. The presence of light minerals in the heavy fine sand (Table S1, Figure S1), with densities close to or lower than that of bromoform, 2.82 g cm^{-3} (quartz, calcite, K-mica, chlorite), can be explained by: (1) the polymineral nature of many of the grains (Figure 2b, c, d, e, h, j, l), both heavy and light; (2) the presence of coverings of heavier minerals on the grains (e.g. iron oxides; Figure 2c); and (3) possible small differences in mineral composition (which change it to 'heavy') that were undetectable with the techniques used in this study.

3.2. VPSEM-EDX mineralogy of the whole fine sand

The VP-SEM-EDX images (Figure 2) have proved highly informative due to the following: 1) The mineralogy is confirmed for some of the major phases identified with XRD (Table S1): quartz, calcite, dolomite, K-feldspar and chlorite. 2) The mineral species of some of the phases identified with XRD are established: K-mica is both biotite (Figure 2f, i) and muscovite-illite (Figure 2b, c ,h ,i); plagioclase is predominantly albite-type (Na-plagioclase) (Figure 2e, l). 3) The mineralogical inventory is completed with minor species (mainly heavy minerals), which are difficult to detect with XRD due to their low contents. The presence of heavy atoms in the mineral composition is frequently shown in the backscattered electron images (BS in Figure 2) by bright tones close to white.

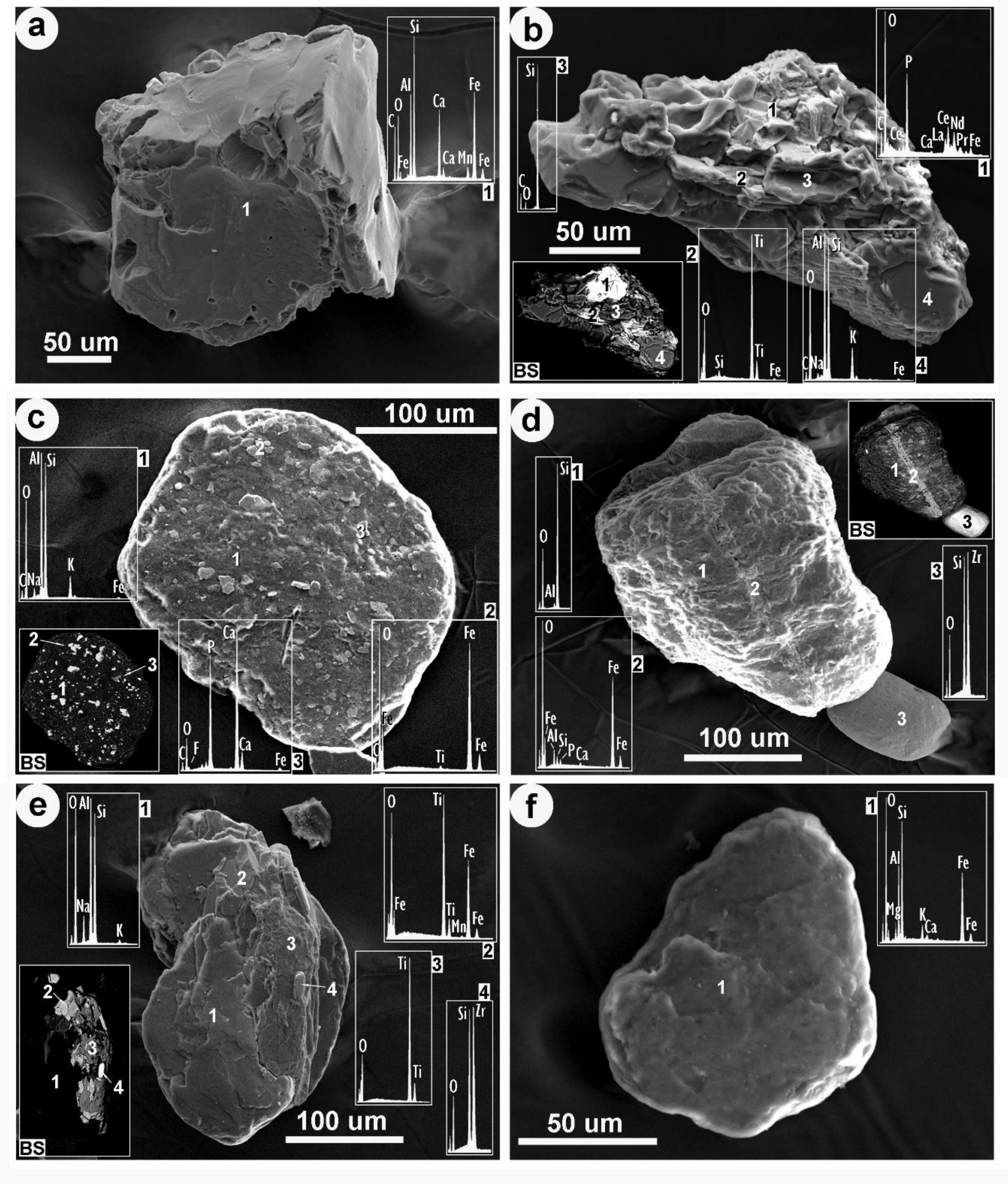

Figure 2. Conventional and backscattered (BS) VPSEM images and EDX microanalysis of fine sand-sized mineral grains. a) profile P4, horizon 4C2: monomineral grain of garnet (nesosilicate, variety andradite). b) profile P5, horizon 6C5: polymineral grain of monazite (1), titanium oxide (Tiox) (2), quartz (3) and K-mica (muscovite or illite) (4). c) profile P5, horizon 6C5: monomineral grain of K-mica (muscovite or illite) (1), although with iron

oxides adhering to surface (2) (goethite and/or haematite) and apatite (3). d) profile P1, horizon 2BCtg. Polymineral grain of quartz (1) with fissure filled with iron oxides (goethite and/or haematite) and apatite (2). Monomineral grain of zircon (3) of exceptional size (>100 µm), subrounded and polished by fluvial activity. e) profile P5, horizon 6C5: polymineral grain consisting of plagioclase (1) (probably albite), ilmenite (2), titanium oxide (Tiox) (3) and zircon (4). f) profile P3, horizon Bt2: monomineral grain of K-mica (biotite).

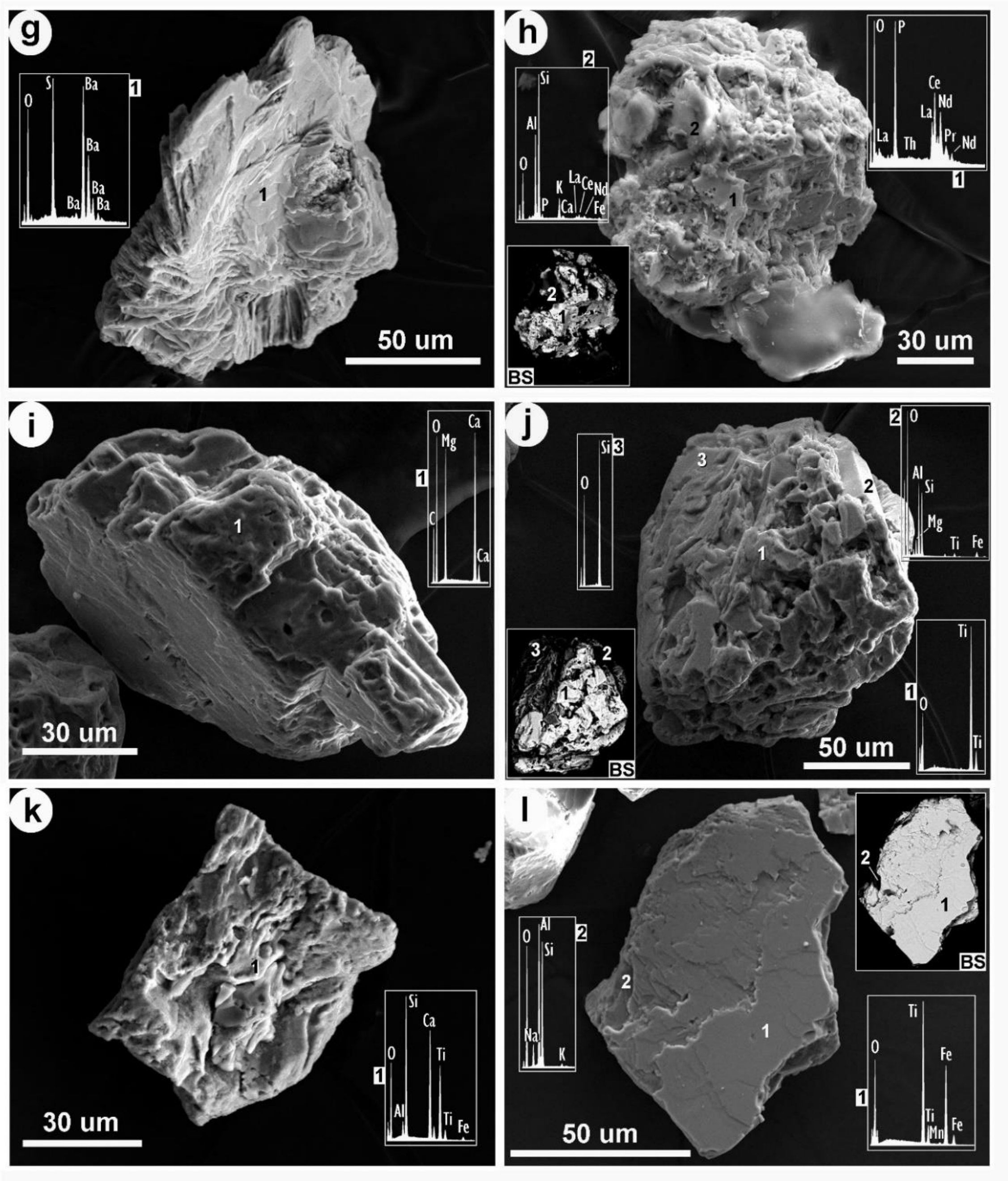

Figure 2 (continued). g) profile P1, horizon 2BCtg: monomineral grain of barite. h) profile P2, horizon Btg2: polymineral grain of K-mica (muscovite or illite) (1) and monazite (2).

i) profile P4, horizon 4C2; grain of dolomite. j) profile P4, horizon 4C2: polymineral grain composed of titanium oxide (Tiox) (1), staurolite (prism face {110} and pinacoid face {010}) (2) and quartz (3). k) profile P1, horizon 2BCtg: monomineral grain of titanite. l) profile P5, horizon 6C5: tabular polymineral grain, consisting mainly of ilmenite (1) with a plagioclase inclusion (albite) (2).

The following minority species were detected: garnet (nesosilicate, variety andradite - $Ca_3Fe_2(SiO_4)_3$- (Figure 2a), monazite -$(Ce,La,Nd,Pr)PO_4$- (Figure 2b, h), titanium oxide -rutile or anatase, TiO_2- (Figure 2b, e, j), apatite -$Ca_5(PO_4)_3(OH)$- (Figure 2c, d), zircon -$ZrSiO_4$- (Figure 2d, e), ilmenite -$FeTiO_3$- (Figure 2e, l), barite -$BaSO_4$- (Figure 2g), staurolite -$(Fe,Mg)_2Al_9(Si,Al)_4O_{20}(O,OH)_4$- (Figure 2j) and titanite -$CaTiSiO_5$- (Figure 2k). Iron oxides were also found in many of the grains (Figure 2c, d). Although VP-SEM-EDX does not permit mineral species identification, these were either goethite or haematite. The same occurred with the TiO_2 polymorphs, rutile and anatase. However, it was possible to identify these species of Fe and Ti using XRD (Figure S1). 4) Consideration of the mineralogical results derived from Figure 2 together with the XRD results (Table S1, Figure S1) confirms that the fine sand (both whole fine sand and heavy fine sand) is a complex of at least 25 different mineral species (20 in horizon 4C2 of P4 alone).

Another finding to confirm the usefulness of VP-SEM-EDX is the proof that many of the fine sand grains are polymineral (Figures 2b, c, d, e, h, j, l and 3 a) although some are monomineral (Figures 2a, f, g, i, k and 3 e).

3.3. VPSEM-EDX-Raman study of TiO_2 polymorphs in fine sand

Rutile and anatase (polymorphs of titanium dioxide) were found together in the soils using XRD (Table S1, Figure S1). Using VP-SEM-EDX, the presence of TiO_2 was described (Figure 2a, e, j) without being able to distinguish the grains of the two species, as this is not possible with EDX. Consequently, Raman spectroscopy was used (Figure 3d, f). Rutile showed maxima at 143, 236, 447, 612 and 826 cm^{-1} and anatase at 144, 197, 399, 516, 639 cm^{-1} (Arsov *et al.*, 1991). Rutile, more abundant than anatase, was found in polymineral or even monomineral grains, constituted internally by prismatic crystals. Rutile was also observed (Figure 3a, b, c, d) covering the faces of quartz grains as micrometric acicular and prismatic crystals, which appear to result from pedogenic recrystallization *in situ* (authigenic) of a colloid/gel of TiO_2. Two further observations are of interest: the tendency of the acicular and prismatic crystals to cross (Figure 3d), following the typical rutile-law twin (twinning on {011}), and that the crystal support is quartz (Figure 3b) due to the well-known quartz-rutile association (Klein & Dutrow, 2007).

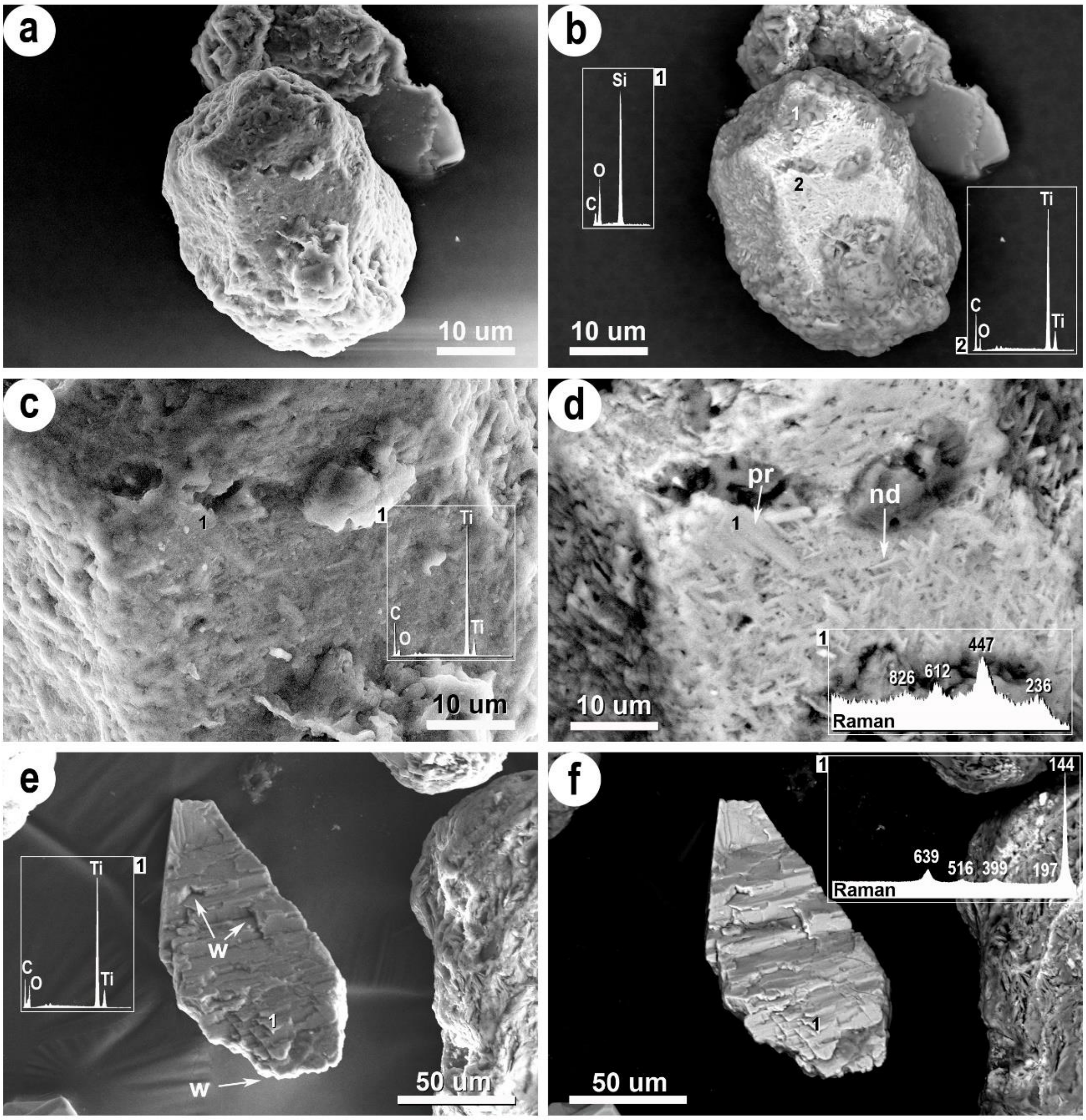

Figure 3. VP-SEM images with EDX and Raman spectra of the whole fine sand of horizon 2BCtg (P1). a, c and e are in conventional mode; b, d and f, in backscattered mode. a) and b): mineral grain of quartz (SiO_2) with “coating” of rutile (TiO_2) on one of its faces, visible in b as a light grey colour. c) and d): detail of a) and b) of rutile coating. c) shows TiO_2 composition, by EDX spectrum. In d) the Raman spectrum confirms the presence of rutile and also shows presence of rutile in a fabric, often interwoven, of acicular crystals

(nd) of 3×0.5 µm (approx.) with some larger prismatic crystals (pr) of 10×2 µm. e) and f) grain of anatase. In e), the EDX spectrum shows composition of TiO_2, while, in f), the Raman spectrum confirms the anatase and that the grain is weathered (w) physically and chemically.

3.4. Major and minor chemical elements

The content of SiO_2 varied between 51.68 and 90.36% (Table S2, supplementary material) and was more abundant in pre-Holocene soils (P1, P2, P3) than in Holocene soils (P4, P5) and point bar sediments. The content of CaO ranged from 0.06 and 23.60% decreasing dramatically in the pre-Holocene soils.

Minor elements (Table S3, supplementary material) exhibited variability between the different soils and terraces. Cr, Mn, Ni, Rb, Sr, Zr, Ba and ΣREE were the only elements to exceed 100 mg kg^{-1} in at least one sample (Cr and Ni only in Btg2 of P2, where their contents easily exceeded those of the other horizons). The concentrations (means per profile) of some minor elements such as Mn, Sr, Cs, Hf and W showed dependence with the age groups of the soils (pre-Holocene *versus* Holocene): Cs, Hf and W more abundant in pre-Holocene, Mn and Sr in Holocene. The maximum value of Zr (mean per profile) was that of P1.

4. Discussion

4.1. Mineralogy of fine sand

Quartz was the principal constituent in all horizons of the oldest soils, i.e. pre-Holocene P1, P2 and P3 (between 47 and 78%) (Table S1) so it can be assumed to be a resistant phase which is concentrated by inheritance during pedogenesis. In the most recent soils, i.e. Holocene- P4 and P5, the carbonates (calcite + dolomite) were the most abundant (>38%) in most of the horizons. However, in 2Bwk2 of P4 they accounted for only 1%, due to lithological discontinuity. Consequently, quartz and carbonates (calcite+dolomite) contents depend on soil age, and, as major components of these fine sands, their percentages are inversely related ($R^2 = 0.866$; n = 24).

The pronounced changes in XRD mineralogy (Table S1) confirm the presence of some of the lithological discontinuities already established morphologically and/or granulometrically. Of particular interest are those in horizons 2Bwk2 of P4, 2BCtg of P1 (with an increase in quartz and a decrease in K-feldspars) and 4C3 of P5 (with an increase in total phyllosilicates). In none of these examples can the mineralogical changes be explained by the action of pedogenic processes within the soil.

The dominant formation process of minerals from the heavy fine sand (Table S1) must be inheritance, since the majority are detrital species and thus originate from the geological materials of the zone. However, there are also other genetic possibilities (see section 'VP-SEM-EDX-Raman study of TiO_2 polymorphs in fine sand') since genesis by inheritance of the heavy minerals of the fine sand of the soils, and their subsequent use in chronosequences to study the provenance of materials and their degree of alteration, is not an indisputable paradigm. For example, Tejan-Kella *et al.* (1991a) found rutile and zircon grains with different degrees of alteration in the same profile, implying a complex environmental history (different provenances) in soils from a podzol chronosequence at Cooloola (Australia). Tejan-Kella *et al.* (1991b), in Psamments and Orthods from South Australia, developed in sandy sediments of various ages only found a weak tendency towards alteration over time in the heavy minerals. Farragallah & Essa (2011) found that the contents of relatively highly resistant minerals (sphene, rutile, garnet and zircon) followed an irregular distribution in both depth and time sequence in soils from different terraces of the River Nile near Assiut (Egypt). Sulieman *et al.* (2015) did not detect an increase in ultrastable heavy minerals (zircon, tourmaline, rutile) with increasing age of Nile terraces. In the present study, rutile or zircon were found in all profiles (Table S1).

The mineralogy of the heavy fine sand (Table S1, Figure S1) also reveals the decarbonatization undergone by the pre-Holocene profiles, since, unlike the Holocene soils and fresh point bar sediments of the Guadalquivir river course, they lack carbonate materials. In addition, the notable presence of anatase and rutile in the pre-Holocene soils is shown by the more intense reflections in the XRD diagrams (Figure S1). The high crystallinity, in some cases, of the rutile and anatase reflections could indicate that they are authigenic soil phases (see section 'VP-SEM-EDX-Raman study of TiO_2 polymorphs in fine sand').

The VP-SEM-EDX analysis of the whole fine sand permitted observation of the sub-rounded shape of some grains, with somewhat polished surfaces, mechanical marking and a degree of sedimentological maturity (Figure 2c, d, e, f, i, j), in accordance with the fluvial origin of the parent material. Superficial features of chemical alteration were also observed in grains of various mineral species (Figure 2b, h, i, j, k). Quartz showed alteration features, even in the fine sands of the less developed soils, such as P5 (Figure 2b), in agreement with our previous results (Martín-García *et al.*, 2004, 2015), which reported alteration features in quartz under Mediterranean climate, even in scarcely evolved soils. Alteration was also observed in the grains of K-mica (Figure 2h), dolomite (Figura 2i), titanium oxides (Figure 2j) or titanite (Figure 2k), from both pre-Holocene (P1, P3) and Holocene soils (P4, P5). These observations give rise to the hypothesis that the alteration features are not necessarily produced in the same soil as that where the grain is currently found, and may be (particularly in less evolved, that is, Holocene soils) inherited from fluvial sediments or from soils from before those giving rise to the sediment. This would, therefore, involve the discussion of aspects such as polycyclism, superimposed features and diverse origins, previously described in zircon by Tejan-Kella *et al.* (1991a), who stated that “the juxtaposition of euhedral, subeuhedral and unetched zircon and rutile grains with highly rounded and etched forms in the same profile indicates diverse provenance”. This genetic complexity would thus imply that the VP-SEM-EDX observations of any grain do not provide sufficiently robust information on the effects of the age of the terraces, where the soils are found, on the fine sand grains. This has resulted in further investigation into the problem of the alteration of our fine sands using complimentary geochemical methods (ICPms). Another interesting observation with VPSEM-EDX was the relatively greater presence of zircon grains in P1, the soil from the oldest terrace (600 ka, Table 1).

4.2. TiO_2 polimorphs

The VP-SEM-EDX-Raman study of TiO_2 polimorphs in fine sand (Figure 3) imply that pedogenic neoformation of rutile has taken place in the study soils. However, the possibility that some grains of this mineral species, present in our fine sands, may be inherited cannot be ruled out. In no case did the rutile grains show any sign of alteration. Anatase was present in fine sand-sized grains, with some signs of weathering (Figure 3e, f), suggesting possible inheritance from the parent material.

The coexistence of the two polymorphs of TiO_2 rutile (neoformed/inherited) and anatase (inherited), shown by VP-SEM-EDX-Raman, is an original finding, particularly in Mediterranean fluvial terrace soils. Fitzpatrick & Chittleborough (2002) reported that evidence from both laboratory synthesis and field studies indicated that rutile should not necessarily be attributed to high-temperature formation and could also crystallize from an intermediate anatase phase. Rutile neoformation in soils has been assumed by Sun *et al.* (2017), while Cornu *et al.* (1999) showed, in tropical soils, the mobility of Ti and the neoformation of anatase, but never of rutile.

4.3. Chemical composition

The SiO_2 contents (Table S2) was positively correlated with that of quartz (Table S1) ($R^2 = 0.851$; n = 24). The CaO contents decreased dramatically in the pre-Holocene soils due to decarbonation and was positively correlated with calcite+dolomite (carbonates) ($R^2 = 0.887$; n = 24), and calcite ($R^2 = 0.854$; n = 24); MgO was correlated with dolomite ($R^2 = 0.775$; n = 24), as well as CaO and MgO ($R^2 = 0.762$; n = 24). A horizon of interest is 2Bwk2 of P4, with the ‘k’ showing carbonate accumulation, which has very low percentages of CaO and MgO compared to the other horizons of the profile; the carbonates are found in the silt and clay fraction, as shown by the data of Calero (2005). All assert for CaO content confirm that, as in the case of SiO_2, the CaO amount of the fine sands in our soils contains valuable pedogenic information.

Major elements confirm the lithological discontinuity in 2Bwk2 (P4), shown by the XRD mineralogy (Table S1), with visibly higher values of SiO_2, Al_2O_3, Na_2O and K_2O, and lower values of CaO, Fe_2O_3 and MgO. In contrast, the lithological discontinuities of P5 were not accompanied by any notable change in chemical element composition.

The concentrations (means per profile) of some minor chemical elements such as Mn, Sr, Cs, Hf and W (Table S3) showed dependence with the age groups of the soils (pre-Holocene *versus* Holocene): Cs, Hf and W more abundant in pre-Holocene, Mn and Sr in Holocene. The maximum value of Zr (mean per profile) was that of P1. The Ba and Zr content can be related to the presence of barite -$BaSO_4$- and zircon -$ZrSiO_4$-, respectively (Figure 2d, e, g); as can ΣREE to that of monazite -(Ce,La,Nd,Pr)PO_4- (Figure 2h). The Mn content is related to the presence of ilmenite and andradite (garnet), since, although Mn does not belong to the ideal mineral formulae, it was detected in the VP-SEM-EDX spectra (Figure 2a, e, l). Furthermore, the positive correlations between Mn and Fe_2O_3 (R^2 = 0.777; n = 24) and TiO_2 (R^2 = 0.726; n = 24) suggest that, together with ilmenite and andradite, Mn may be linked to other Fe- and Ti-bearing minerals detected such as biotite, goethite or haematite.

The Rb content positively correlates with total feldspars (K-feldspar + plagioclases; Table S1) (R^2 = 0.717; n = 24) and consequently shows high relative values (>105 mg kg^{-1}) in the P3 horizons, with maximum values of these minerals (23–38% K-feldspar + plagioclase; Table S1). The Rb content also positively correlates with K_2O (R^2 = 0.908; n = 24). Hossain *et al.* (2014) showed that Rb isomorphically substitutes for K in feldspars, which would explain our findings. However, Donaire (1995) explained that the significant positive correlation between Rb and K_2O in granitic rocks of the Los Pedroches Batholith (zone of present study) is due to the substitution of Rb by K in the K-mica, as also reported by Feng & Kerrich (1990) and Varga *et al.* (2005). In our fine sands, Rb *vs.* K-mica showed a positive correlation, albeit low (R^2 = 0.167; n = 24) and much lower than that of Rb *vs.* total feldspars (R^2 = 0.717; n = 24), possibly due to the feldspars being more abundant than K-mica in most of our samples (Table S1).

The Sr content correlates with CaO (R^2 = 0.863; n = 24) and calcite (R^2 = 0.815; n = 24), which must be due to the well-known isomorphism between Sr and Ca. Cubillas *et al.* (2015) suggested that Sr can be incorporated into the structure of natural and laboratory calcites (and may be a good indicator of the relative supersaturations of Sr *versus* Ca at which the crystals grew).

The statistical relationship (R^2> 0.811; n = 24) between pairs of elements within groups such as Mn-Ti-Fe, Cr-Ni-Mo, Sr-Ca, Rb-K and Hf-Th-U-REE, must be due to isomorphism (ion substitution in the crystal lattices). This process is regulated by Goldschmidt's rules (Misra, 2012), which postulates ionic substitutions when Δr is small (<15% of the radius of the smallest). The case of the group Mn^{3+}, Fe^{3+}, Ti^{4+} can be considered paradigmatic, since their radii (0.064, 0.064 and 0.068 nm, respectively) have Δr between 0 and 0.004 (never exceeding 7% of the smallest).

The chemical element composition (mean values per profile) of the whole fine sand (Tables S2 and S3) differed from that of the clay (Martín-García *et al.*, 2019) in that the former contained lower quantities of major elements Al, Ca, Fe and K, and also lower quantities of most of the minor elements. This may be related, first, to the lower contents of phyllosilicates and, especially, of the (hydr)oxides goethite and haematite, in the fine sand, and, second, to the role of the clay fraction as a scavenger of heavy elements (Martín-García *et al.*, 2016). However, the higher content of Zr in the fine sand (except in point bar sediments), possibly due to the presence of zircon mineral (Table S1; Figures S1, 2d, e), should be noted. This mineral species, highly resistant to weathering, would tend to become concentrated through inheritance in the fine sand grains rather than the clay.

4.4. Geochemical indices

The SiO_2/CaO ratio of the whole fine sand (Table 2) showed mean values greater than 200 (up to 795) in the pre-Holocene soils (P1, P2, P3) and lower than 37 in the Holocene soils (P4, P5, point bar sediments), reflecting the effect of soil age on this geochemical index. The presence of these two populations of SiO_2/CaO can be attributed to the two pedogenic processes, which combine and intensify with age: the leaching of carbonates, reducing CaO content, and the relative accumulation of quartz (main source of SiO_2), a mineral with relatively high resistance to alteration. This explains the correlations 'SiO_2/CaO' *versus* 'calcite' ($R^2 = 0.775$, logarithmic) and 'SiO_2/CaO' *versus* 'quartz' ($R^2 = 0.777$, logarithmic).

The CIW and WIP values also depend on age, ranging from 16.20 (point bar sediments) to 92.58 (P1) for the former and 78.02 (P5) to 17.22 (P1) in the latter. These results are similar to those of Price & Velbel (2003), where CIW grew in parallel with alteration, fresh material being considered as that with CIW ≤50 (point bar sediments <20) and with maximum alteration at a value of 100 (P1 ≈ 93). For WIP, Price & Velbel (2003) considered fresh material to have a value >100 with maximum alteration at 0. In the present study, although none of the profiles reached these extreme values, they were within the range 100 – 0.

Table 2. Mean values of main geochemical indices for whole fine sand and clay fractions (weighted to horizon thickness). Standard deviation in parentheses.

	SiO_2/CaO	CIW[1]	WIP[2]	WI[3]	BDI[4]	WR[5]	Sr/Zr[6]
Fine sand							
P1	795.58 (402.00)	92.61 (1.98)	17.21 (2.16)	2.56 (0.39)	0.28 (0.03)	31.66 (11.25)	0.12 (0.07)
P2	631.86 (583.59)	73.83 (27.51)	26.11 (6.42)	5.96 (4.40)	0.87 (0.50)	147.25 (178.85)	0.31 (0.11)
P3	206.26 (41.10)	79.76 (0.98)	38.15 (4.37)	4.95 (0.50)	0.60 (0.04)	97.76 (19.26)	0.41 (0.05)
P4	36.70 (50.35)	38.59 (24.60)	56.27 (17.01)	19.42 (10.52)	2.20 (1.14)	895.54 (563.11)	0.87 (0.50)
P5	2.53 (0.12)	17.08 (2.57)	78.02 (5.34)	30.49 (1.14)	3.81 (0.69)	1287.03 (429.78)	2.21 (0.63)
PM	3.32	16.19	71.29	25.06	4.66	2446.46	6.02
Clay							
P1		75.66 (6.79)	49.16 (3.67)		0.38 (0.10)	374.40 (52.26)	
P2		69.26 (4.53)	53.47 (2.38)		0.50 (0.08)	584.14 (92.30)	
P3		67.31 (9.63)	51.95 (4.53)		0.55 (0.18)	532.52 (87.50)	
P4		37.79 (17.26)	70.33 (9.42)		1.81 (1.01)	1436.84 (561.84)	
P5		21.77 (7.03)	74.83 (5.19)		3.00 (1.11)	2060.88 (179.62)	
PM		14.84	77.17		4.00	1873.40	

[1] CIW: Chemical Index of Weathering (Harnois, 1988)

[2] WIP: Weathering Index of Parker (Parker, 1970)
[3] WI: Weathering Index (Vogel, 1975)
[4] BDI: Base Depletion Index (Jien *et al.*, 2016)
[5] WR: Weathering Ratio (Chittleborough, 1991)
[6] Muhs *et al.* (2001)

Ajmone *et al.* (1988) studied the WIP in fine sand of a soil chronosequence from Northwest Italy, where the youngest soil (aged between 10 – 50 ka) showed WIP of 41.7, and the oldest (500 – 750 ka), between 16.5 and 18.4, similar WIP and age values to the samples of the present study. Garzanti & Resentini (2016), studying fluvial point bar sands of Taiwanese rivers, reported values of CIW between 48 and 95 and WIP between 18 and 65, close to those of our fine sands.

The WI and BDI of our whole fine sand (Table 2) persistently showed values related to age. The WI decreased from P1 (2.56) to P5-point bar sediments (30.49-25.06, respectively); the BDI increased from P1 (0.28) to point bar sediments (4.66). The BDI was determined by Jien *et al.* (2016) in a soil chronosequence from Taiwan (Arenosol, Cambisol, Lixisol and Ferralsol), showing values in fine earth (<2 mm) from 0.25 (soils of 20 ka) to 0.05 (soils of 80 ka). This tendency of BDI to decrease with age coincided with our results, albeit with very different ranges of values. For example, our P3, with an age of 70 ka (Table 1), was comparable to the oldest Taiwanese soils studied by Jien *et al.* (2016), and showed a BDI of 0.59, while that of the equivalent Taiwanese soils was around 0.05. We believe that these divergences are due, in addition to our studying fine sand, to the lower intensity of pedogenic processes in the Mediterranean environment of our fluvial terraces (mean annual temperature 18ºC, total annual precipitation 650 mm; soil types Fluvisol, Calcisol and Luvisol) compared to that in the ferralitic soils with tropical oceanic climate of Taiwan (mean annual temperature 23.5 ºC, total annual precipitation 2500 mm, soil types Arenosol, Cambisol, Lixisol, Acrisol and Ferralsol).

The WR values (Table 2), from 31.66 (P1) to 2446.46 (point bar sediments), were also related to soil age. This wide range is due to both the relative abundance of Ca in the Holocene soils and point bar sediments and to the relative concentration of Zr in the pre-Holocene soils (particularly in P1) (Tables S2, S3). Consequently, the content of carbonates (calcite+dolomite), the main source of CaO, is positively correlated with WR ($R^2 = 0.761$; n = 24). Our values of WR are much higher than those of Chittleborough (1991), which were between 3 and 22, as they were estimated in fine sand of soils lacking calcium carbonates. In the present study, Sr/Zr showed similar tendencies to the other indices, and, since

Sr^{2+} is diadochic with Ca^{2+}, and Zr^{4+} increases in pre-Holocene soils, Sr/Zr decreased with age, from point bar sediments (6.02) to P1 (0.12) (Table 2).

Values of the geochemical indices for whole fine sand were generally similar to those of clay (Table 2). However, there were some cases with pronounced differences, such as WR, which showed lower values in the whole fine sand than in the corresponding clay. This may be due to the higher relative concentration of Zr in the whole fine sand. The trends in the values of the indices with soil age were similar in clay and whole fine sand.

4.5. Provenance of the soil materials

4.5.1. Mineralogical evidences

The most abundant mineral species in our fine sands (Table S1): phyllosilicates (muscovite/illite, biotite, paragonite, chlorite and interstratified minerals), quartz, feldspars (K-feldspar and plagioclases), iron oxides (goethite and haematite) and carbonates (calcite and dolomite) have been described in the rocks of the source area (Ortega-Huertas *et al.*, 1991; Larrea *et al.*, 1992, 1994, 1995, 1996; Martínez-Ruiz, 1994; Carracedo et al., 1997; Pin *et al.*, 2002; Torres-Ruiz *et al.*, 2003; Martínez *et al.*, 2008; Pascual *et al.*, 2008; Jiménez-Espinosa *et al.*, 2016). This suggests a potential provenance from the rocks/sediments through the process known as inheritance (Martín-García *et al.*, 1998). However, the idea of provenance through inheritance requires further explanation in some cases. For example, calcite may also originate from neoformation, in those horizons where it accumulates pedogenically (e.g., Cmk/Bt of P2). Goethite and haematite may be both neoformed and inherited. The process of transformation may be partly responsible, for example, for the presence of interstratified minerals (Calero *et al.*, 2013).

Because the mineral contents change over time due to soil evolution, the idea of provenance of soil materials (by comparison between soil materials and rocks of the source area) is only applicable to young soils and point bar sediments. The minor minerals are often used as indicators of provenance (von Eynatten & Dunkl, 2012). In the present study, most of the mineral species detected (Table S1, Figures 2 and 3) have also been cited as rock-forming minerals of the source area (river basin) materials of the fluvial terraces, and would be inherited from them towards our fine sands (see section ‘Minor elements’ in ‘Chemical composition’). However, some of these minor phases require further discussion since the type of rock from which they originate is clear. For example, garnet, staurolite and andalusite are of metamorphic origin in the Iberian Massif (Larrea *et al.*, 1992, 1994, 1995, 1996) or the Internal Betic Zone (Torres-Ruiz *et al.*, 2003). The variety of garnet found in P2 (horizons Btg1 and Btg2) and P4 (4C2) (Figure 2a) is andradite, typical of contact metamorphosed rocks when the wallrock is limestone (Klein & Dutrow, 2007), perfectly feasible in zones close to the Los Pedroches Batholith (Tornos & Chiaradia, 2004). The staurolite (Figure 2j) found in P4 (horizon 4C2) is a medium to high-grade metasedimentary mineral (regional metamorphism), and, in the source area, has been described in the metapelites of the Internal Zone of the Betic Cordillera (Díaz de Federico *et al.*, 1980). Rutile could also be employed as an indicator of provenance as it is present in most of the rocks of this zone. However, evidence that it may be neoformed (section ‘VP-SEM-EDX-Raman study of TiO_2 polymorphs in fine sand’) tends to invalidate this possibility.

4.5.2. Geochemical evidences

The spider diagrams of the chondrite-normalized chemical composition of selected elements in the whole fine sand (Figure S2, supplementary material), again show (sections ‘Chemical composition’ and Tables S2 and S3) that, due to the effect of time, composition differs between soils. Furthermore, its relationship with all the geological materials of the zone, potential providers of materials, is clear. However, the closest relationships (in all elements, from Fe to Ba) are with the sedimentary rocks (Ortega-Huertas *et al.*, 1991; Martínez-Ruiz, 1994) (Figure S2b). Figure S2 also shows the expected geochemical relationship between the whole fine sand and the clay (Martín-García *et al.*, 2016), although clay contained more Fe and V, and the former more Zr (except in point bar sediments).

The geochemical indices were used as fingerprints of provenance (Garzanti & Resentini, 2016) by comparing the values of the samples with those of the geological materials (Figure 4). According to CIW (Figure 4a), the fine sands and clays of the pre-Holocene soils (P1, P2, P3) would be related (similar range of values) to the igneous and metasedimentary rocks, while the fine sands and clays of the Holocene soils (P4, P5) and point bar sediments would be related to the sedimentary rocks. According to WIP (Figure 4a), the Holocene soils are in the middle of the range of all the rocks from the source area and the pre-Holocene soils would separate from them. The values of BDI (Figure 4b) reiterate the behaviour of CIW. This once again demonstrates that the values of these indices for our samples depend on age and that the indices are not decisive for determining provenance. However, the information obtained from Figures 4a and 4b overcame the simple use of geochemical indices as a provenance tool. First, through the possible predictive value between indices on showing that there are correlations with a high coefficient of determination between CIW *versus* WIP (negative) and WIP *versus* BDI (positive), for both the fine sand and clay fractions. Second, because they reveal that the lines of the two granulometric fractions intersect at a critical point (geometrical point common to both), after which they diverge (Figures 4a and 4b). This permits formulation of the hypothesis that the critical point are related to “time zero” for granulometric evolution, that is, when there is no size differentiation. It also supports the hypothesis that the critical point indicates “time zero” for pedogenic evolution. Both hypotheses are confirmed by Figures 4a and 4b, which show the critical point close to the least evolved materials studied: point bar sediments and Holocene soil P5. New evidence to support these hypotheses is the great similarity between the defining co-ordinates (values) of critical point (CP): $CP_{WIP\ (versus\ CIW)}$ = 80.76, very close to $CP_{WIP\ (versus\ BDI)}$ = 79.39. This value (≈80) is close to 100, the value of WIP for fresh material given by Price & Velbel (2003). The value of $CP_{CIW\ (versus\ WIP)}$ is 15.46, ≤50, attributed to the unaltered samples by Price & Velbel (2003).

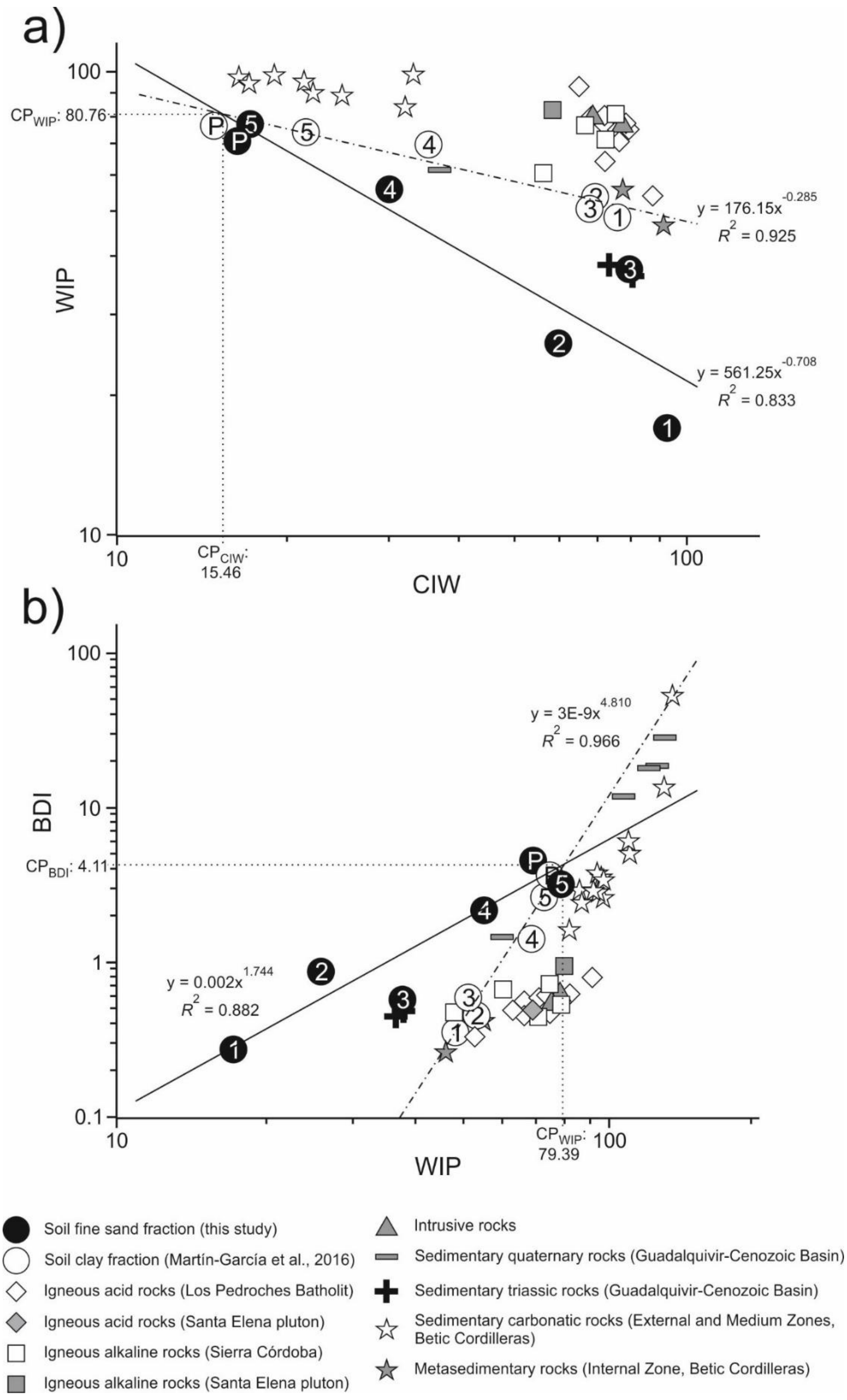

Figure 4. Relationships between geochemical indices CIW vs WIP (a) and WPI *vs* BDI (b) for soil whole fine sand and soil clay fractions (mean profile values) (Table 2). They include the values for rocks from the Guadalquivir catchment (igneous, sedimentary and metasedimentary). The numbers in the circles correspond to soil profiles, and P to point

bar sediment (point bar sediments). The lines (and adjacent equations) correspond to the straight lines of correlation for the population of samples of soil fine sand (continuous) and soil clay (dots and dashes) fractions. CP indicates the values of the indices at critical intersection points.

4.6. Soil fine sand chronofunctions

In order to better quantify the relationships of the different properties of the whole fine sand with age, chronofunctions were calculated (Table 3). Most were logarithmic ($y = a \cdot lnx+b$) and quadratic ($y = ax^2+bx+c$) and, to a lesser extent, linear ($y = ax+b$); this can be interpreted as these parameters will reach their steady-state (Schaeltz *et al.*, 1994) and prove the existence of an authentic soil chronosequence, previously demonstrated by other compositional and morphological properties of the soils of the chronosequence (Calero et al., 2008, 2009, 2013; Martín-García *et al.*, 2016, 2019). No previous studies of chronofunctions established using the soil fine sand have been found in the bibliography.

The equations obtained also provided other information. The curves which decreased with the age of calcite, CaO and Sr (CaO and Sr associated with the carbonates) quantify the process, detected previously, of loss of carbonates through dissolution/alteration over time. This is 0.057% every 1000 years for calcite. The opposite (curve increases with age) occurs in quartz, which accumulates through inheritance in the soil fine sand over time, at a rate of 0.065% every 1000 years, similar to the rate of calcite loss.

The Zr chronofunction also increases, in this case due to the Zr-bearing mineral zircon, which remains in the fine sand fraction (Figure 2d, e). The same also occurs in Hf, U and REE, which, as elements with low mobility, may be associated with the mineral monazite (Figure 2b, h). The positive chronofunction of the 1.23-1.53 nm phases, indicates the transformation of 2:1 phases, increasing with age, and which was demonstrated using chronofunctions of the nanoparameters of the clay fraction of our soils by Calero *et al.* (2013).

Table 3. Chronofunctions of mineralogical and chemical variables and geochemical indices (y) measured in the whole fine sand and clay (only geochemical indices) of soil horizons and averaged[a] ($n = 6$, $P<0.05$), x = ka.

	Linear equation	*r*	Logarithmic equation	*r*	Quadratic equation	*r*
Whole fine sand						
1.23-1.53 nm phases XRD /%	$y = 0.011x + 1.179$	0.853			$y = 4E\text{-}05x^2 - 0.012x + 1.864$	0.974
Quartz XRD /%			$y = 2.936\ln(x) + 41.083$	0.837		
Goethite XRD /%					$y = 2E\text{-}05x^2 - 0.008x + 1.812$	0.968
Calcite XRD /%			$y = -2.561\ln(x) + 17.940$	-0.930		
CaO /%			$y = -1.676\ln(x) + 12.016$	-0.887		
P_2O_5 /%			$y = -0.007\ln(x) + 0.0737$	-0.863		
Cr /mg kg^{-1}					$y = -0.001x^2 + 0.889x + 8.568$	-0.897
Ni /mg kg^{-1}					$y = -0.001x^2 + 0.412x + 3.844$	-0.897
Sr /mg kg^{-1}			$y = -30\ln(x) + 212.460$	-0.964		
Zr /mg kg^{-1}			$y = 9.897\ln(x) + 146.220$	0.852		
Mo /mg kg^{-1}					$y = -3E\text{-}05x^2 + 0.022x - 0.038$	-0.909
Hf /mg kg^{-1}	$y = 0.003x + 1.031$	0.907	$y = 0.136\ln(x) + 1.312$	0.815	$y = 2E\text{-}06x^2 + 0.002x + 1.073$	0.912
W /mg kg^{-1}	$y = 0.004x + 0.848$	0.840			$y = -2E\text{-}05x^2 + 0.013x + 0.563$	-0.982
U /mg kg^{-1}	$y = 0.002x + 1.0812$	0.850			$y = 5E\text{-}06x^2 - 0.001x + 1.161$	0.919
ΣREE /mg kg^{-1}	$y = 0.107x + 68.157$	0.873			$y = 2E\text{-}04x^2 - 0.008x + 71.653$	0.905
SiO_2/CaO	$y = 1.381x + 54.367$	0.964			$y = -0.0026x^2 + 2.869x + 9.189$	0.9998
CIW			$y = 5.939\ln(x) + 42.930$	0.897		
WIP	$y = -0.086x + 61.89$	-0.851	$y = -4.268\ln(x) + 55.088$	-0.874	$y = 2E\text{-}04x^2 - 0.227x + 66.152$	0.923
WI			$y = -1.972\ln(x) + 18.086$	-0.842		
BDI			$y = -0.348\ln(x) + 2.661$	-0.965		
WR			$y = -185.4\ln(x) + 1132.2$	-0.989		
Sr/Zr			$y = -0.434\ln(x) + 2.393$	-0.965		
Clay						
CIW			$y = 4.902\ln(x) + 39.453$	0.937		
WIP			$y = -2.248\ln(x) + 66.633$	-0.897		
BDI			$y = -0.295\ln(x) + 2.207$	-0.980		
WR			$y = -128.4\ln(x) + 1361.0$	-0.873		

[a] Mean profile values (from Tables 2, 3, 4 and 5) weighted to horizon thickness

The geochemical alteration indices SiO_2/CaO, CIW, WIP, WI, BDI, WR and Sr/Zr mainly exhibited logarithmic fitting in their chronofunction (Table 3), suggesting not only dependence on age but also that the alteration of the fine sands will attain steady state. The chronofunction BDI = -0.348 ln(age in ka) + 2.659 (Table 3) implies that, for an age of 600 ka (maximum investigated; Table 1) the BDI of the fine sand is 0.43. When this value is interpolated in the chronofunction for fine earth of Taiwanese soils reported by Jien *et al.* (2016): BDI = 1/(1 + 0.21×age in ka), the age required to attain this BDI is 6.2 ka. The great difference between 600 ka and 6.2 ka (~100 lower) is due to the Mediterranean climate of our chronosequence being much less pedogenically active than the tropical climate of Taiwan (section 'Geochemical indices'). Thus, environmental conditions (soil-forming factors) and soil classification must be considered when interpreting alteration indices in soil chronosequences.

The chronofunction equations obtained for the alteration indices (Table 3) also permit further discussion regarding the critical point (Figure 4) and the hypothesis that it represents "time zero" for soil formation or the start of alteration. When the equations are extrapolated to zero (or close to zero) for 0.001 ka (age attributed to point bar sediments; Table 1) WIP has a value (logarithmic) of 84.56, not only close to 71.34, the WIP value calculated for point bar sediments with the analytical data (Table 2) but also very close to those of CP_{WIP}, established in a completely different manner in Figures 4a and 4b: 80.76 and 79.39. This confirms an initial WIP of 70 – 80 in our soils and that critical point represents "time zero". Furthermore, the BDI values were: $\text{extrapolated}_{(0.001\text{ ka})}$ = 5.06, calculated in point bar sediments = 4.66, and CP_{BDI} = 4.11, which, due to their relative similarity, confirm an initial BDI value (without alteration) of between 4 and 5, and, once again, that CP represents "time zero".

5. Conclusion

Fine sands are suggested as a granulometric fraction of great pedogenic interest with the advantage of their easiness of extraction and analysis. Our results demonstrate the usefulness of fine sand to discuss the origin of the different minerals it owns, pedogenic alteration, the provenance of soil materials, even being able to establish chronosequences between properties of fine sand and soil age. Furthermore, pedogenetic rutile neoformation, never previously described, was reported, as was its coexistence with its polymorph, anatase. Finally, we think that our results may be useful in sedimentology, because these soils are a potential source of sediment.

Acknowledgements: Sample preparation and chemical analysis (ICPms and ICP-AES) were conducted by Emma Humphreys-Williams and Stanislav Strekopytov (Imaging and Analysis Centre, Natural History Museum, London). VPSEM images and EDX and Raman analysis was conducted by Isabel Guerra (Centro de Instrumentación Científica, Universidad de Granada, Spain). To Professor Dr. Gabriel Delgado for his invaluable advice on the analytical techniques to employ in this study. This work was supported by a grant from Ministerio de Economía, Industria y Competitividad de España ('Mediterranean Soil Typologies versus Quartz. At the frontier of pedogenic knowledge'; Ref. CGL2016-80308-P). We thank Robert Abrahams (Bsc) for revising the English language.

References

Ajmone-Marsan, F., Bain, D.C. & Duthie, D.M.L. (1988). Parent material uniformity and degree of weathering in a soil chronosequence, northwestern Italy. *Catena*, 15, 507–517.

Arnold, R.W. (1968). Pedological significance of lithologic discontinuities. *Trans. 9th international Congress of Soil Sci.*, 4, 595–603.

Arsov, Lj.D., Kormann, C. & Plieth, W. (1991). Electrochemical synthesis and in situ Raman spectroscopy of thin films of titanium dioxide. *Journal of Raman Spectroscopy*, 22, 573–575.

Birkeland, P.W. (1999). *Soils and Geomorphology*. Oxford University Press. New York.

Calero, J. (2005). *Génesis de la fracción mineral y de la ultramicrofábrica en una cronosecuencia de suelos sobre terrazas del río Guadalquivir*. Doctoral dissertation, Universidad de Granada, Granada.

Calero, J., Delgado, R., Delgado, G. & Martín-García, J.M. (2008). Transformation of categorical field soil morphological properties into numerical properties for the study of chronosequences. *Geoderma*, 145, 278–287.

Calero, J., Delgado, R., Delgado, G. & Martín-García, J.M. (2009). SEM image analysis in the study of a soil chronosequence on fluvial terraces of the middle Guadalquivir (southern Spain). *European Journal of Soil Science*, 60, 465–480.

Calero, J., Martín–García, J.M., Delgado, G., Aranda, V. & Delgado, R. (2013). A nano-scale study in a soil chronosequence from southern Spain. *European Journal of Soil Science*, 64, 192–209.

Carracedo, M., Larrea, F.J., Alonso-Olazabal, A. & Gil-Ibarguchi, J.I. (1997). The relationship between the plutonic intrusions and the dyke swarm in the Los Pedroches batholith (Iberian Massif, Spain): Dykes as a paleotectonic and paleostress indicators. *Caderno Lab. Xeolóxico de Laxe*, 22, 229–246.

Carral, M.P., Martín-Serrano, A., Sansteban, J.I., Guerra, A. & Jiménez-Ballesta, R. (1998). Los factores determinantes en la secuencia edáfica de la evolución morfodinámica del tramo medio del Guadalquivir (Jaén). *Revista de la Sociedad Geológica de España*, 11, 111-126.

Chittleborough, D.J. (1991). Indices of weathering in soils and palaeosols formed on silicate rocks. *Australian Journal of Earth Sciences*, 38, 115–120

Cornu, S., Lucas, Y., Lebon, E., Ambrosi, J.P., Luizao, F., Rouiller, J., Bonnay, M. & Neal, C. (1999). Evidence of titanium mobility in soil profiles, Manaus, central Amazonia. *Geoderma*, 91, 281–295.

Cubillas, P., Hu, X. & Higgins, S.R. (2015). Strontium incorporation during calcite growth: Implications for chemical mapping using friction force microscopy. *Chemical Geology*, 411, 274–282.

Delgado, R., Martín-García, J.M., Oyonarte, C. & Delgado, G. (2003). Genesis of the *terrae rossae* of the Sierra Gádor (Andalusia, Spain). *European Journal of Soil Science*, 54, 1–16.

Díaz de Federico, A., Puga, E., Burgos, J., Gallegos, J.A. & Sanz de Galdeano, C. (1980). *Mapa geológico de España a escala 1:50.000 (hoja 1027)*. Instituto Geológico y Minero de España (IGME), Madrid.

Donaire, T. (1995). *Petrología y geoquímica de las rocas granitoides y enclaves asociados del batolito de Los Pedroches (Macizo Ibérico)*. Doctoral dissertation, Universidad de Huelva, Huelva, Spain.

Farragallah, M.A. & Essa, M.A. (2011). Sand and Clay Mineralogical Composition in Relation to Origin, Sedimentation Regime, Uniformity, and Weathering Rate of Nile Terrace soils at Assiut, Egypt. *Australian Journal of Basic and Applied Sciences*, 5, 239–256.

Feng, R. & Kerrich, R. (1990). Geochemistry of fine-grained clastic sediments in the Archean Abitibi greenstone belt, Canada: Implications for provenance and tectonic setting. *Geochimica et Cosmochimica Acta*, 54, 1061–1081.

Fitzpatrick, R.W. & Chittleborough, D.J. (2002). Titanium and zirconium minerals. In: *Soil Mineralogy with Environmental Applications* (eds J.B. Dixon & D.G. Schulze), pp. 667-690. Soil Science Society of America Book Series No. 7, Madison, WI.

Garzanti, E. & Resentini, A. (2016). Provenance control on chemical indices of weathering (Taiwan river sands). *Sedimentary Geology*, 336, 81–95.

Harnois, L. (1988). The CIW index: a new chemical index of weathering. *Sedimentary Geology*, 55, 319–322.

Hernández-Hinojosa, V., Montiel-García, P.C., Armstrong-Altrin, J.S., Nagarajan, R. & Kasper-Zubillaga, J.J. (2018). Textural and geochemical characteristics of beach sands along the western Gulf Of Mexico, Mexico. *Carpathian Journal of Earth and Environmental Sciences*, 13, 161–174.

Hossain, I., Roy, K.K., Biswas, P.K., Alam, M., Moniruzzaman, M. & Deeba, F. (2014). Geochemical characteristics of Holocene sediments from Chuadanga district, Bangladesh: Implications for weathering, climate, redox conditions, provenance and tectonic setting. *Chinese Journal of Geochemistry*, 33, 336–350.

Jien, S.H., Baillie, I., Huang, W.S., Chen, Y.Y. & Chiu, C.Y. (2016). Incipient ferralization and weathering indices along a soil chronosequence in Taiwan. *European Journal of Soil Science*, 67, 583–596.

Jiménez-Espinosa, R., Jiménez-Millán, J. & García-Tortosa, F.J. (2016). Upper-Pleistocene terrace deposits in Mediterranean climate: geomorphological and source-rock control on mineral and geochemical signatures (Betic Cordillera, SE Spain). *Journal of Iberian Geology*, 42, 187–200.

Klein C., Dutrow B., 2007. *Mineral science*. Wiley, New York.

Larrea, F.J., Carracedo, M., Cueto, L.A., Quesada, C., Gil-Ibarguchi, J.I., Fernández, F.J. & Ortega, L.A. (1992). Petrology and geochemistry of Cardeña-Virgen de La Cabeza pluton (batholith of Los Pedroches). *Cuaderno Lab. Xeolóxico de Laxe*, 17, 209–222.

Larrea, F.J., Carracedo, M., Ortega, L.A. & Gil-Ibarguchi, J.I. (1994). The Linares granite (Jaén): cartography, petrology and geochemistry. *Cuaderno Lab. Xeolóxico de Laxe*, 19, 335–346.

Larrea, F.J., Carracedo, M., Ortega, L.A. & Gil-Ibarguchi, J.I. (1995). The Santa Elena stock (Jaén). An intrusion genetically independent from the magmatic association of the Los Pedroches Batolith. *Caderno Lab. Xeolóxico de Laxe*, 20, 151–166.

Larrea, F.J., Carracedo, M., Yusta, I., Ortega, L.A. & Gil-Ibarguchi J.I. (1996). Los diques traquiandesíticos asociados al plutón granodiorítico de Los Pedroches (batolito de Los Pedroches, España). *Geogaceta*, 20, 586–589.

Liu, B., Jin, H., Sun, Z. & Zhao, S. (2016). Geochemical weathering of aeolian sand and its palaeoclimatic implications in the Mu Us Desert, northern China, since the Late Holocene. *Journal of Arid Land*, 8, 647–659.

Martínez, J., Llamas-Borrajo, J., de Miguel-García, E., Rey-Arrans, J., Hidalgo-Estévez, M.C. & Sáez-Castillo, A.J. (2008). Multivariate analysis of contamination in the mining district of Linares (Jaén, Spain). *Applied Geochemistry*, 23, 2324–2336.

Martínez-Ruiz, F. (1994). *Geoquímica y mineralogía del tránsito Cretácico-Terciario en las Cordilleras Béticas y en la Cuenca Vasco-Cantábrica*. Doctoral dissertation, Universidad de Granada, Granada.

Martín-García, J.M., Delgado, G., Sánchez-Marañón, M., Párraga, J.F. & Delgado, R. (1997). Nature of dioctahedral micas in Spanish red soils. *Clay Minerals*, 32, 107–121.

Martín-García, J.M., Delgado, G., Párraga, J.F., Bech, J. & Delgado, R. (1998). Mineral formation in micaceous Mediterranean Red soils of Sierra Nevada, Granada, Spain. *European Journal of Soil Science*, 49, 253–268.

Martín-García, J.M., Aranda, V., Gámiz, E., Bech, J. & Delgado, R. (2004). Are Mediterranean mountains Entisols weakly developed? The case of Orthents from Sierra Nevada (Southern Spain). *Geoderma*, 118, 115–131.

Martín-García, J.M., Márquez, R., Delgado, G., Sánchez-Marañón, M. & Delgado, R. (2015). Relationships between quartz weathering and soil type (Entisol, Inceptisol and Alfisol) in Sierra Nevada (southeast Spain). *European Journal of Soil Science*, 66, 179–193.

Martín-García, J.M., Sánchez-Marañón, M., Calero, J., Aranda, V., Delgado, G. & Delgado, R. (2016). Iron oxides and rare earth elements in the clay fractions of a soil chronosequence in southern Spain. *European Journal of Soil Science*, 67, 749–762.

Martín-García, J.M., Molinero-García, A., Calero, J., Fernández-González, M. V., Párraga, J. & Delgado, R. (2019). Lanthanides in granulometric fractions of Mediterranean soils. Can they be used as fingerprints of provenance? *European Journal of Soil Science*, 70, 394–410.

McDonough, W.F. & Sun, S. (1995). The composition of the Earth. *Chemical Geology*, 120, 223–253.

Misra, K.C. (2012). *Introduction to Geochemistry. Principles and Applications*. Wiley-Blackwell, Oxford.

Muhs, D.R., Bettis, E.A., Been, J. & McGeehin, J.P. (2001). Impact of Climate and Parent Material on Chemical Weathering in Loess-derived Soils of the

Mississippi River Valley. *Soil Science Society of America Journal*, 65, 1761–1777.

Ortega-Huertas, M., Palomo, I., Moresi, M. & Oddone, M. (1991). A mineralogical and geochemical approach to establishing a sedimentary model in a passive continental margin (Subbetic zone, Betic Cordilleras, SE Spain). *Clay Minerals*, 26, 389–407.

Parker, A. (1970). An Index of Weathering for Silicate Rocks. *Geological Magazine*, 107, 501–504.

Pascual, E., Donaire, T. & Pin, C. (2008). The significance of microgranular enclaves in assessing the magmatic evolution of a high-level composite batholith: A case on the Los Pedroches Batholith, Iberian Massif, Spain. *Geochemical Journal*, 42, 177–198.

Pin, C., Liñán, E., Pascual, E., Donaire, T. & Valenzuela, A. (2002). Late Neoproterozoic crustal growth in the European Variscides: Nd isotope and geochemical evidence from the Sierra de Córdoba Andesites (Ossa-Morena Zone, Southern Spain). *Tectonophysics*, 352, 133–151.

Price, J.R. & Velbel, M.A. (2003). Chemical weathering indices applied to weathering profiles developed on heterogeneous felsic metamorphic parent rocks. *Chemical Geology*, 202, 397–416.

Santos-García, J.A. (1988). Informe sedimentológico sobre las terrazas del río Guadalquivir. In: Estudio geológico-hidrogeológico de la zona de Andujar (Jaén). Tomo IV-I: Estudio hidrogeológico de detalle 1:10000. ENRESA, Madrid. Technical report. Pp 56–72.

Santos-García, J.A., Jerez-Mir, F. & Saint-Aubin, J. (1991). Estudio sedimentológico de un sector del río Guadalquivir en las proximidades de Andújar (provincia de Jaén). Los depósitos de la terraza +6m (T4). *Estudios Geológicos*, 47, 43–55.

Schaeltz, R.J., Barrett, L.R. & Winkler, J.A. (1994). Choosing models for soil chronofunctions and fitting them to data. *European Journal of Soil Science*, 45, 219–232.

Schaetzl R.J., Thompson M.L. (2015). *Soil Genesis and Geomorphology*. Cambridge University Press. New York.

Sulieman, M.M., Ibrahim, I.S., Elfaki, J.T. & Dafa-Allah, M.S. (2015). Origin and Distribution of Heavy Minerals in the Surficial and Subsurficial Sediments of the Alluvial Nile River Terraces. *Open Journal of Soil Science*, 5, 299–310.

Sun, Z., Zhou, D., Du, J. & Xie, Y. (2017). Low temperature self-assembled growth of rutile TiO_2/manganese oxide nanocrystalline films. *Applied Surface Science*, 420, 489–495.

Tamm, O. (1937). Om de lagproduktiva sandmarkerna a Hökensas och i övre Lagadalen. *Meddelanden från Statens skogsförsöksanstalt*, 30, 1–66.

Tejan-Kella, M.S., Fitzpatrick, R.W. & Chittleborough, D.J. (1991a). Scanning electron microscope study of zircons and rutiles from a podzol chronosequence at Cooloola, Queensland, Australia. *Catena*, 18, 11–30.

Tejan-Kella, M.S., Chittleborough, D.J. & Fitzpatrick, R.W. (1991b). Weathering assessment of heavy minerals in age sequences of Australian sandy soils. *Soil Science Society of America Journal*, 55, 427–434.

Tornos, F. & Chiaradia, M. (2004). Plumbotectonic evolution of the Ossa Morena zone, Iberian Peninsula: Tracing the influence of mantle-crust interaction in ore-forming processes. *Economic Geology*, 99, 965–985.

Torres-Ruiz, J., Pesquera, A., Gil-Crespo, P.P. & Velilla, N. (2003). Origin and petrogenetic implication of turmaline-rich rocks in the Sierra Nevada (Betic Cordillera, southeastern Spain). *Chemical Geology*, 197, 55–86.

Varga, A.R., Szakmány, G., Raucsik, B. & Máthé, Z. (2005). Chemical composition, provenance and early diagenetic processes of playa lake deposits from the Boda Siltstone Formation (Upper Permian), SW Hungary. *Acta Geologica Hungarica*, 48, 49–68.

Vogel, D.E. (1975). Precambrian weathering in acid metavolcanic rocks from the Superior Province, Villebon Township, South-Central Quebec. *Canadian Journal of Earth Sciences*, 12, 2080–2085.

von Eynatten, H. & Dunkl, I. (2012). Assessing the sediment factory: The role of single grain analysis. *Earth-Science Reviews*, 115, 97–120.

Supplementary material

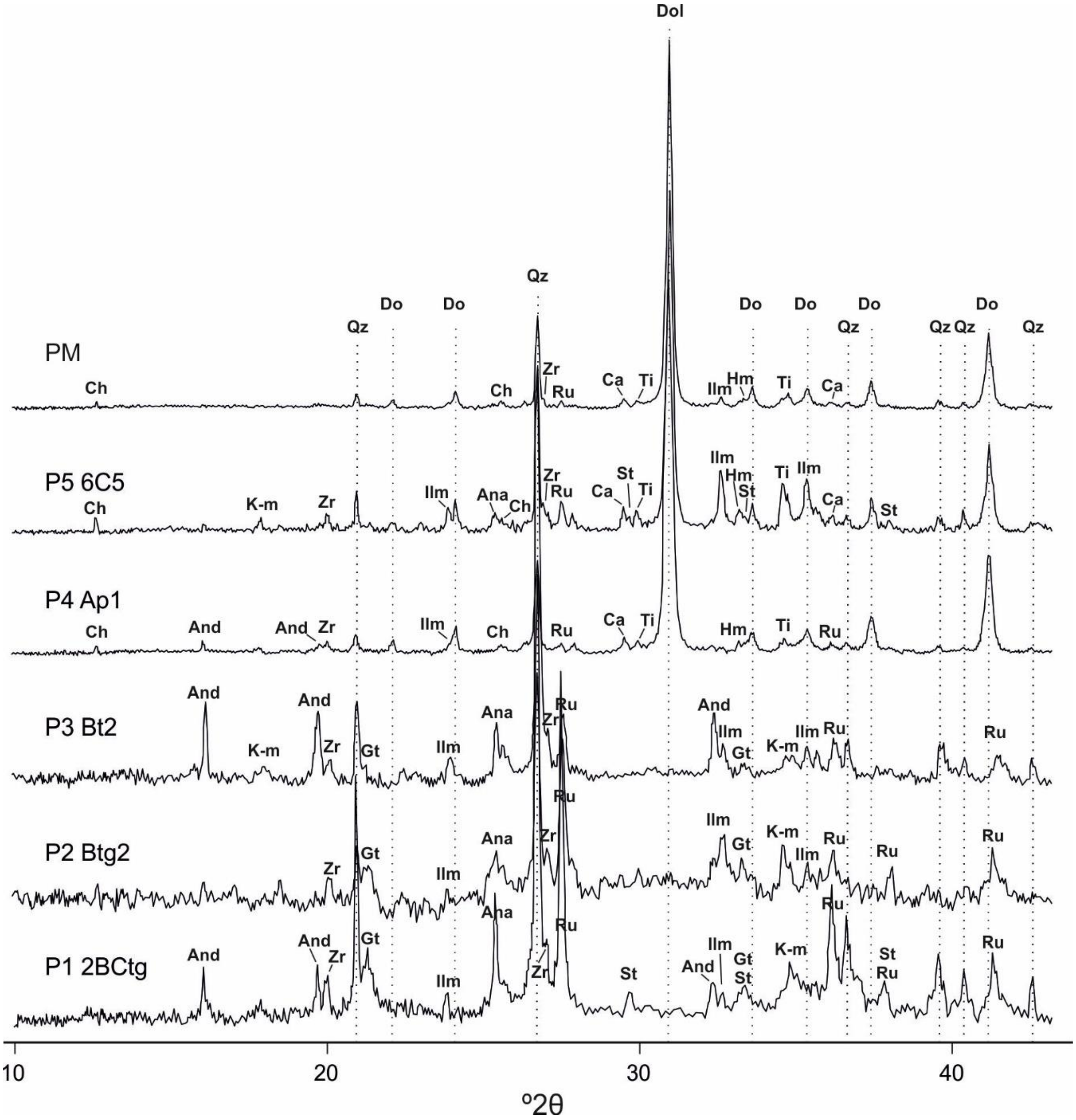

Figure S1. XRD profiles for selected heavy fine sand (ρ >2.82 g cm^{-3}) samples in the angular sector 10 – 43 °2θ. Abbreviations: K-m: K-mica; Ch: chlorite; Qz: quartz; Gt: goethite; Hm: haematite; Ca: calcite; Do: dolomite; Ti: titanite; Zr: zircon; Ru: rutile; Ilm: ilmenite; St: staurolite; Ana: anatase; And: Andalusite.

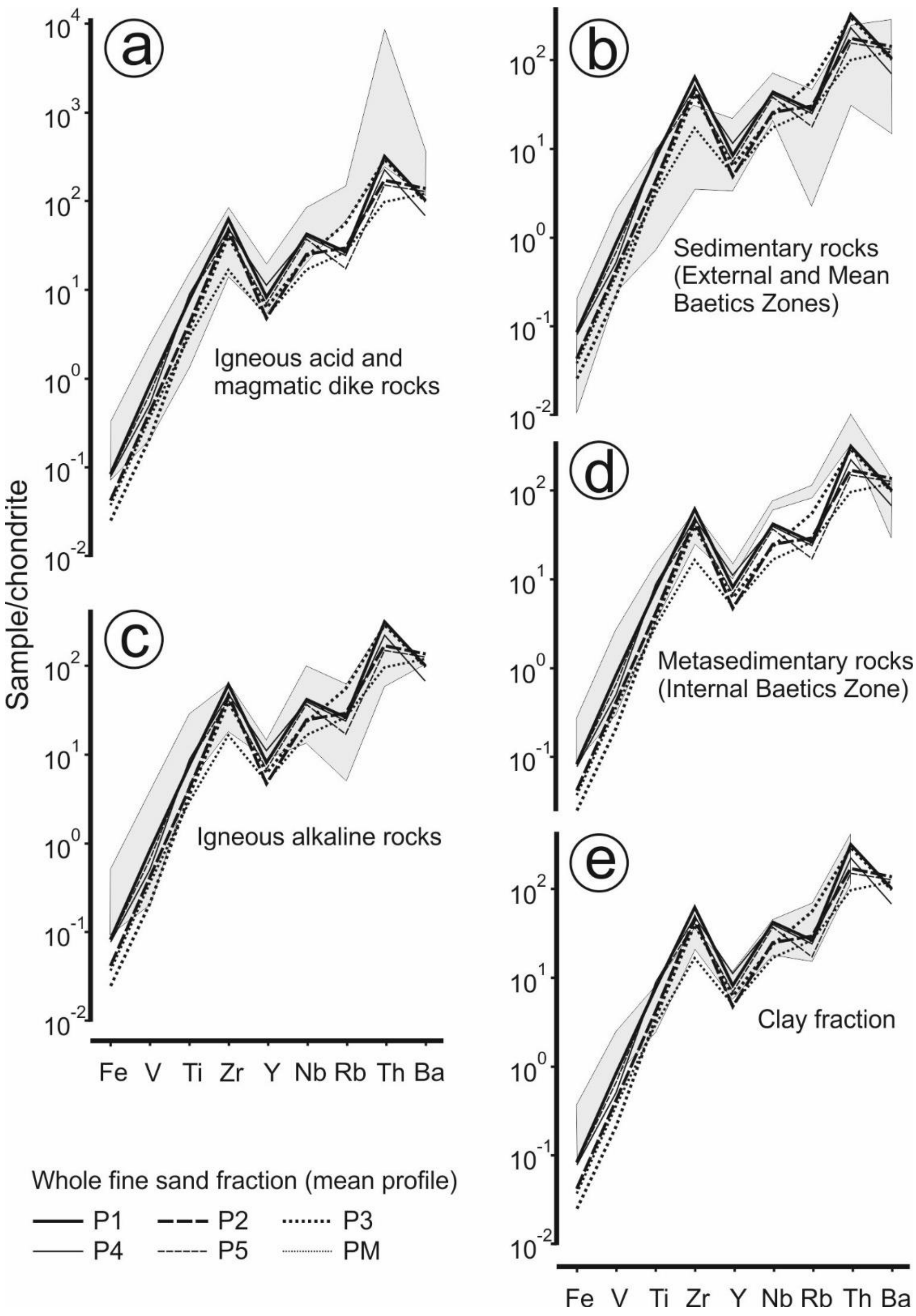

Figure S2. Spider diagrams of selected elements, normalized to the composition of chondritic meteorite of McDonough & Sun (1995) of whole fine sand (lines represent mean profiles) compared with (shaded area): (a) acid igneous and magmatic-dike rocks from Iberian Massiff, (b) sedimentary rocks from External and Mean Baetics Zones, (c) alkaline igneous rocks from Iberian Massiff, (d) metasedimentary rocks from Internal Baetics Zone and (e) soil clay fraction (<2 µm) from the studied soils (Martín-García *et al.,* 2016).

Table S1. X-ray diffraction (XRD) and VPSEM-EDX mineralogy (selected horizons) of whole fine sand (50 – 250 µm) and heavy fine sand (50 – 250 µm; ρ >2.82 g cm^{-3}) fractions.

		XRD																	VPSEM-EDX[b] (whole fine sand)
		Whole fine sand /%																Heavy fine sand (qualitative)[a]	
		Phyllosilicates																	
	horizon	1.23-1.53ph	1.0-1.22ph	K-m	Na-m	Ka	Ch	Total	Qz	KFd	Pl	Feld	Gt	Hm	Ca	Do	Carb		
P1	Ap	4	3	4	1	2	0	14	78	5	2	7	1	0	0	0	0		
	Bt	4	4	12	0	2	1	23	68	6	0	6	3	0	0	0	0		
	Btg2	11	8	12	1	3	3	38	48	8	1	9	5	0	0	0	0	Ru, Zr, Ilm, Ana, Gt, St, Qz, K-m	
	2BCtg	13	4	12	1	1	0	31	64	3	0	3	1	0	1	0	1	Ru, Gt, Zr, Ana, And, Ilm, St, Qz, K-m	Mo, Ti, Ba, Zr, Tiox
	4C	9	2	16	0	1	0	28	58	12	0	12	2	0	0	0	0		
	mean[c]	9 (4)	4 (2)	12 (3)	1 (0)	2 (1)	1 (1)	28 (7)	62 (9)	7 (3)	0 (1)	7 (3)	3 (2)	0 (0)	0 (0)	0 (0)	0 (0)		
P2	Ap	2	2	2	0	1	0	7	66	26	0	26	0	0	1	0	1		
	Btg1	5	2	9	2	2	0	20	67	5	0	5	3	0	5	0	5	Ilm, Gt, Ru, Ana, Zr, Hm, Qz	Mo, Tiox, Gr, Ilm
	Btg2	2	9	4	1	2	0	18	63	16	1	17	0	1	1	0	1	Ilm, Gt, Ru, Zr, Ana, Qz, K-m	Mo, Ilm, Tiox, Gr
	Cmk/Bt	1	2	13	1	4	1	22	47	2	2	4	1	1	25	0	25		
	mean[c]	2 (1)	4 (3)	7 (4)	1 (1)	2 (1)	0 (0)	17 (6)	60 (8)	13 (9)	1 (1)	14 (9)	1 (1)	1 (0)	8 (11)	0 (0)	8 (11)		
P3	Ap1	1	1	5	1	2	0	10	51	30	8	38	1	0	0	0	0		
	Bt1	0	1	2	0	1	1	5	70	13	10	23	2	0	0	0	0		
	Bt2	1	2	1	0	1	0	5	67	21	7	28	0	0	0	0	0	Ilm, Ru, Zr, And, Gt, Ana, Qz, K-m	Tiox, Ilm, Ba
	Bt3	0	1	1	0	1	1	4	67	10	15	25	2	1	1	0	1		
	Bt4	0	1	2	2	1	1	7	58	23	8	31	1	0	3	0	3		
	2Bt6	1	1	4	0	2	0	8	60	11	12	23	2	0	7	0	7	Ilm, Hm, Ru, Ti, Ana, And, K-m, Qz	
	mean[c]	0 (0)	1 (0)	2 (1)	0 (1)	1 (0)	1 (0)	5 (2)	64 (6)	16 (7)	11 (3)	27 (5)	1 (1)	0 (0)	2 (3)	0 (0)	2 (3)		
P4	Ap1	1	2	7	1	2	1	14	33	8	0	8	1	1	10	33	43	And, Zr, Ilm, Ti, Ru, Hm, Do, Ch, Ca, Qz	
	Bwk1	1	1	4	1	2	2	11	19	3	1	4	1	0	13	52	65		
	2Bwk2	1	3	3	2	4	1	14	59	11	13	24	2	0	0	1	1		
	4C2	3	9	1	2	4	1	20	31	5	1	6	2	2	15	24	39	Ilm, Zr, St, Ti, Ch, Do, Qz, K-m	Gr, Mo, Ilm, Tiox, Zr, Ti, St
	mean[c]	2 (1)	5 (3)	3 (2)	2 (0)	3 (1)	1 (0)	16 (3)	38 (15)	7 (3)	4 (6)	11 (8)	2 (0)	1 (1)	9 (6)	24 (18)	33 (23)		
P5	Ap	1	4	6	1	7	2	21	23	5	2	7	1	2	31	15	46		
	2C1	2	4	5	1	1	1	14	28	4	0	4	3	0	32	19	51		
	4C3	1	5	16	9	3	1	35	21	3	1	4	1	1	23	15	38		
	6C5	1	2	7	1	4	3	18	22	5	0	5	1	2	28	24	52	Hm, Ti, Zr, Ru, Ana, Ilm, St, Ch, Do, Qz, Ca, K-m	Mo, Tiox, Ilm, Zr, Ap, Ba
	mean[c]	1 (0)	4 (1)	8 (5)	3 (4)	4 (2)	2 (1)	22 (8)	24 (3)	4 (1)	1 (1)	5 (1)	2 (1)	1 (1)	29 (4)	18 (3)	47 (5)		
PM		3	9	3	2	0	0	17	30	10	0	10	2	1	33	7	40	Ru, Ti, Zr, Hm, Ilm, Ch, Ca, Do, Qz	

[a] Selected samples; [b] Selected samples. Only showing minor minerals; [c] Weighted to horizon thickness (standard deviation in parentheses).

Abbreviations: 1.23-1.53ph: 1.23 to 1.53 nm phases: 1.0-1.22ph: 1.0 to 1.22 nm phases; K-m: K-mica (muscovite/illite and biotite); Na-m: Na-mica (paragonite); Ka: kaolinite; Ch: chlorite; Qz: quartz; KFd: K-feldspar; Pl: plagioclase; Feld: total feldspars = KFd+Pl; Gt: goethite; Hm: haematite; Ca: calcite; Do: dolomite; Carb: total carbonates = Ca+Do; Mo: monazite; Ti: titanite; Ba: barite; Zr: zircon; Ru: rutile; Ana: anatase; Tiox: titanium oxide (rutile or anatase); Ilm: ilmenite; Gr: garnet (andradite); Ap: apatite; St: staurolite; And: andalusite

Table S2. Chemical compositions of major elements (%) in whole fine sand fraction of soil horizons and PM.

		SiO_2	Al_2O_3	Fe_2O_3	TiO_2	CaO	MgO	Na_2O	K_2O	P_2O_5
P1	Ap	90.36	3.49	1.18	0.45	0.06	0.22	0.22	0.94	
	Bt	85.16	6.42	2.47	0.63	0.1	0.53	0.38	1.34	0.03
	Btg2	84.16	6.69	2.44	0.62	0.09	0.53	0.32	1.59	0.04
	2BCtg	84	6.4	2.1	0.55	0.49	0.47	0.27	1.62	0.03
	4C	84.7	5.97	1.82	0.52	0.08	0.4	0.27	1.65	0.02
	mean [a]	85.02 (1.73)	6.13 (0.86)	2.13 (0.39)	0.57 (0.06)	0.19 (0.18)	0.46 (0.09)	0.30 (0.05)	1.49 (0.21)	0.03 (0.01)
P2	Ap	89.06	4.07	0.49	0.18	0.06	0.09		2.65	0.03
	Btg1	81.75	3.82	1.13	0.44	1.98	0.27	0.35	1.04	0.02
	Btg2	83.87	4.39	1.17	0.21	0.11	0.15	0.20	2.47	0.06
	Cmk/Bt	64.01	4.51	1.32	0.42	8.46	0.40	0.40	1.13	0.05
	mean [a]	79.29 (9.88)	4.27 (0.24)	1.04 (0.32)	0.29 (0.11)	2.68 (3.68)	0.22 (0.12)	0.23 (0.15)	1.95 (0.72)	0.04 (0.01)
P3	Ap1	82.22	5.85	0.48	0.24	0.33	0.09	1.03	2.61	0.03
	Bt1	82.67	6.46	0.32	0.20	0.33	0.05	1.29	2.87	
	Bt2	78.82	6.83	0.40	0.19	0.37	0.08	1.36	2.76	
	Bt3	85.01	7.15	0.51	0.22	0.40	0.12	1.40	2.62	
	Bt4	85.91	7.25	0.80	0.29	0.44	0.18	1.27	2.49	
	2Bt6	85.49	8.88	1.23	0.32	0.64	0.32	1.86	3.15	0.04
	mean [a]	83.48 (2.40)	7.19 (0.94)	0.63 (0.33)	0.24 (0.05)	0.42 (0.11)	0.14 (0.10)	1.41 (0.25)	2.79 (0.22)	0.01 (0.02)
P4	Ap1	64.15	4.25	1.24	0.44	10.16	3.57	0.53	1.33	0.11
	Bwk1	54.62	4.20	1.45	0.46	17.05	4.67	0.45	1.14	0.08
	2Bwk2	90.33	6.10	0.63	0.41	0.80	0.22	1.17	2.25	0.04
	4C2	52.81	4.84	3.78	0.98	17.00	5.81	0.40	0.94	0.08
	mean [a]	66.22 (16.38)	5.01 (0.76)	2.01 (1.37)	0.63 (0.27)	11.06 (7.19)	3.57 (2.34)	0.66 (0.34)	1.43 (0.56)	0.07 (0.02)
P5	Ap	56.31	4.16	1.74	0.53	23.60	3.91	0.36	1.33	0.14
	2C1	51.68	3.75	1.78	0.51	20.39	3.53	0.30	1.13	0.09
	4C3	53.82	5.62	2.53	0.64	20.86	3.40	0.36	1.44	0.09
	6C5	52.63	4.35	2.62	0.86	19.20	3.35	0.34	1.15	0.10
	mean [a]	53.74 (1.84)	4.45 (0.73)	2.09 (0.40)	0.60 (0.12)	21.28 (1.58)	3.58 (0.22)	0.34 (0.03)	1.27 (0.13)	0.11 (0.02)
PM		64.30	3.82	0.92	0.22	19.39	1.71	0.38	1.61	0.11

[a] weighted to horizon thickness (standard deviation in parentheses)

Table S3. Chemical compositions of minor elements (mg kg^{-1}) in fine sand fraction of soil horizons and PM

		Sc	V	Cr	Mn	Co	Ni	Cu	Zn	Ga	Rb	Sr	Y	Zr	Nb	Mo	Sn	Cs	Ba	Hf	Ta	W	Tl	Pb	Th	U	ΣREE
P1	Ap	2.79	24.13	30.45	71.97	3.19	20.57	21.27	22.05	4.41	39.83	18.71	8.49	172.93	8.03	0.49	44.51	2.82	136.72	2.56	0.62	1.82	0.25	33.81	6.88	1.63	120.47
	Bt	5.47	47.72	43.3	214.28	7.48	30.33	23.62	35.91	8.08	54.16	23.15	13.48	302.44	10.87	0.64	4.74	4.07	227.73	3.31	0.85	2.83	0.33	7.15	10.03	2.35	147.19
	Btg2	6.23	50.48	45.77	288.04	9.16	30.21	22.77	41.49	9.2	65.79	24.9	14.38	301.97	11.08	1.05	5.14	4.97	267.26	3.36	0.88	2.93	0.4	7.61	11.08	2.6	154.68
	2BCtg	5.8	47.08	39.79	269.29	8.05	26.83	19.92	34.91	8.72	67.97	28.41	11.23	271.09	9.96	0.94	2.83	4.89	295.71	2.77	0.79	2.63	0.41	8.96	8.6	2.18	128.37
	4C	5.26	42.48	36.68	142.9	5.52	19.21	17.32	32.38	8.00	69.40	27.66	11.31	104.46	9.73	0.54	2.29	4.85	247.58	2.88	0.77	2.46	0.42	8.44	8.93	2.08	141.02
	mean [a]	5.44 (0.89)	45.10 (7.03)	40.58 (4.47)	218.36 (68.68)	7.24 (1.74)	26.47 (4.47)	21.11 (2.30)	35.00 (5.07)	8.15 (1.25)	61.81 (9.04)	25.32 (2.93)	12.27 (1.75)	245.69 (77.05)	10.22 (0.87)	0.77 (0.21)	7.39 (11.63)	4.51 (0.64)	249.26 (43.11)	3.04 (0.29)	0.81 (0.07)	2.65 (0.31)	0.37 (0.05)	10.30 (7.36)	9.42 (1.22)	2.25 (0.27)	140.59 (11.35)
P2	Ap	1.19	10.68	8.89	41.97	0.84	2.91	9.49	20.23	3.80	77.79	39.09	3.92	280.44	3.55	0.12	1.63	3.66	406.71	1.00	0.32	1.80	0.51	15.14	2.69	0.77	49.19
	Btg1	3.18	27.27	25.20	168.52	4.56	14.65	14.20	21.03	5.08	41.93	32.04	9.12	146.24	8.40	0.27	2.51	2.31	180.60	1.92	0.64	1.51	0.26	7.97	5.81	1.36	89.34
	Btg2	1.86	20.67	453.60	165.35	4.99	214.46	14.06	18.77	5.20	85.62	49.03	6.11	121.56	4.46	11.03	2.39	5.17	429.31	1.47	0.40	6.16	0.57	53.08	4.10	1.03	74.58
	Cmk/Bt	4.49	36.77	34.43	165.49	4.87	18.22	21.32	27.73	6.65	51.13	62.93	11.02	161.01	8.82	0.37	2.33	2.93	227.70	2.21	0.62	1.72	0.31	7.63	7.67	1.67	115.34
	mean [a]	2.61 (1.32)	23.62 (9.74)	171.96 (205.93)	135.82 (53.43)	3.89 (1.74)	81.89 (97.00)	15.00 (4.38)	21.93 (3.72)	5.25 (1.04)	68.33 (17.38)	48.29 (10.79)	7.35 (2.77)	174.45 (62.35)	5.98 (2.30)	3.98 (5.15)	2.20 (0.33)	3.80 (1.08)	334.75 (103.79)	1.62 (0.46)	0.48 (0.13)	3.25 (2.13)	0.45 (0.13)	25.22 (20.56)	4.98 (1.92)	1.19 (0.35)	81.77 (24.60)
P3	Ap1	1.18	8.82	10.21	81.67	1.14	4.42	24.12	14.44	6.42	105.14	47.24	5.84	165.66	4.66	0.14	4.20	3.09	204.86	1.42	0.45	0.79	0.64	21.68	4.84	0.92	55.19
	Bt1	1.11	7.68	9.95	45.09	0.68	3.65	4.51	19.67	8.18	135.03	58.92	10.36	155.93	4.30	0.09	2.76	3.81	241.51	1.52	0.43	0.88	0.81	22.48	7.74	1.19	78.58
	Bt2	1.24	8.87	12.09	56.43	1.24	4.41	33.88	10.29	7.87	117.80	54.98	6.98	134.20	4.57	0.11	3.95	3.58	217.84	1.40	0.47	0.84	0.71	20.44	6.36	1.02	68.53
	Bt3	1.72	11.99	12.18	54.04	1.18	4.47	51.60	14.81	8.92	123.44	65.64	9.67	141.72	5.28	0.13	5.57	4.41	242.45	1.63	0.56	1.03	0.75	20.80	9.81	1.38	90.82
	Bt4	2.33	16.10	15.15	80.75	1.96	5.77	52.82	18.98	8.75	113.03	60.92	7.43	143.74	6.70	0.14	5.73	4.81	235.55	1.54	0.65	1.16	0.70	18.29	7.10	1.12	82.09
	2Bt6	3.04	15.48	14.12	210.54	3.21	7.21	36.38	27.40	11.12	143.96	70.83	14.36	162.13	8.16	0.18	5.82	7.27	250.58	2.17	0.95	1.34	0.90	21.89	11.44	1.91	111.04
	mean [a]	1.80 (0.73)	11.48 (3.28)	12.25 (1.81)	89.60 (61.94)	1.58 (0.89)	4.99 (1.26)	33.28 (17.54)	18.13 (5.59)	8.78 (1.36)	126.18 (12.48)	61.28 (6.96)	9.71 (2.77)	150.13 (10.92)	5.65 (1.45)	0.13 (0.03)	4.66 (1.21)	4.65 (1.40)	235.68 (14.18)	1.65 (0.27)	0.60 (0.19)	1.02 (0.19)	0.77 (0.08)	21.10 (1.27)	8.36 (2.11)	1.32 (0.33)	84.37 (16.72)
P4	Ap1	2.86	21.47	15.56	219.29	2.50	7.33	96.71	27.51	4.45	44.52	110.15	7.49	94.54	6.82	0.21	4.88	1.92	162.02	0.63	0.54	0.79	0.27	19.53	3.13	0.88	53.82
	Bwk1	3.67	28.68	19.44	279.25	3.84	8.71	14.76	26.50	5.01	40.84	188.32	7.93	120.28	7.94	0.31	1.78	1.87	165.42	0.64	0.61	0.70	0.24	10.87	3.49	1.06	59.16
	2Bwk2	1.94	13.56	14.33	132.84	2.98	5.81	67.44	14.02	7.20	95.09	60.46	12.34	323.27	7.75	0.20	7.86	3.08	219.25	2.94	0.70	1.14	0.59	19.23	13.28	1.79	124.84
	4C2	12.34	38.42	34.23	796.32	4.19	11.33	11.37	42.95	5.00	33.10	131.91	29.40	135.33	13.33	0.44	33.12	1.70	128.09	0.97	0.92	0.78	0.19	8.74	4.38	1.33	74.90
	mean [a]	6.15 (4.72)	26.52 (10.39)	22.64 (8.95)	412.65 (294.80)	3.50 (0.66)	8.57 (2.31)	42.24 (33.92)	28.84 (11.88)	5.58 (1.09)	54.96 (26.82)	117.17 (44.65)	16.95 (9.61)	182.83 (93.76)	9.66 (2.80)	0.31 (0.11)	15.43 (13.55)	2.18 (0.60)	167.61 (37.29)	1.45 (0.99)	0.74 (0.15)	0.88 (0.18)	0.33 (0.17)	13.98 (5.01)	6.70 (4.37)	1.35 (0.33)	83.80 (28.21)
P5	Ap	4.25	32.33	26.08	376.20	4.37	13.14	13.99	33.09	4.95	38.66	378.39	11.17	167.25	8.52	0.33	21.66	1.86	334.23	1.08	0.61	0.65	0.22	25.12	4.60	1.26	77.79
	2C1	4.24	29.36	22.22	358.48	4.05	11.27	10.76	28.84	4.42	33.42	288.43	9.27	94.10	7.53	0.27	11.49	1.68	265.12	0.56	0.56	0.54	0.19	25.80	3.12	0.94	61.18
	4C3	5.54	44.52	35.34	405.15	6.14	16.89	12.49	38.52	6.78	45.05	321.75	11.09	209.13	9.56	0.43	6.94	2.74	318.51	0.99	0.69	0.75	0.25	21.15	5.05	1.21	81.71
	6C5	5.47	40.20	33.03	449.43	5.34	14.92	13.41	38.79	5.60	37.56	303.16	11.25	190.26	12.83	0.44	24.54	2.02	353.14	0.74	0.92	0.78	0.22	18.51	5.01	1.11	73.62

mean [a]	4.77 (0.63)	35.82 (6.26)	28.40 (5.39)	389.31 (30.59)	4.88 (0.86)	13.84 (2.19)	12.55 (1.30)	34.10 (4.13)	5.37 (0.93)	38.64 (4.40)	325.70 (36.25)	10.60 (0.87)	159.99 (45.79)	9.13 (1.72)	0.36 (0.07)	15.16 (6.89)	2.06 (0.42)	312.32 (32.63)	0.85 (0.22)	0.66 (0.12)	0.66 (0.09)	0.22 (0.02)	23.30 (2.73)	4.34 (0.82)	1.13 (0.13)	73.29 (8.30)
PM	2.54	19.24	16.45	234.30	2.73	8.89	12.03	23.67	4.44	61.81	391.46	7.91	65.00	4.06	0.20	6.58	2.57	290.82	0.65	0.34	0.52	0.38	19.31	2.83	0.87	49.92
Mean whole sand	3,89 (1.80)	26,96 (11.98)	48,71 (61.19)	246,67 (131.00)	3,97 (1.95)	24,11 (29.29)	22,70 (12.43)	26,95 (6.83)	6,26 (1.76)	68,62 (29.97)	161,54 (156.98)	10,80 (3.51)	163,02 (58.55)	7,45 (2.54)	0,96 (1.50)	8,57 (5.51)	3,30 (1.17)	265,07 (60.60)	1,54 (0.84)	0,61 (0.17)	1,50 (1.15)	0,42 (0.19)	18,87 (5.70)	6,11 (2.51)	1,35 (0.47)	85,62 (29.89)
Mean clay		87.47 (39.44)	65.13 (29.54)	404.68 (43.18)	12.67 (3.47)	38.17 (11.58)		88.51 (16.29)	18.10 (7.82)	99.40 (47.83)		12.53 (3.28)	116.72 (21.37)	6.87 (2.34)	0.77 (0.72)	45.38 (40.63)			3.12 (0.66)			0.55 (0.26)		7.69 (3.53)	2.41 (1.38)	92.22 (31.68)

[a] weighted to horizon thickness (standard deviation in parentheses)

Chapter 3:

Provenance of quartz grains from soils over Quaternary terraces along the Guadalquivir River, Spain

Provenance of quartz grains from soils over Quaternary terraces along the Guadalquivir River, Spain

Molinero-García, A.[1], Müller, A.[2,3], Martín-García, J. M.[1]*, Simonsen, S.L.[4], Delgado, R.[1]

[1]Departamento de Edafología y Química Agrícola (Facultad de Farmacia), Universidad de Granada

[2]Natural History Museum, University of Oslo, P.O. Box 1172 Blindern, 0318 Oslo, Norway

[3]Natural History Museum, Cromwell Road, London SW7 5BD, United Kingdom

[4]Department of Geosciences, University of Oslo, PO Box 1047 Blindern, N-0316 Oslo, Norway

*Author for correspondence. Email: jmmartingarcia@ugr.es

Published on:

GEODERMA, 414 (2022), 115769. https://doi.org/10.1016/j.geoderma.2022.115769

Impact Factor (JCR):

Journal Impact Factor, JIF (2021): **7.422**; JIF Percentil in Category (Soil science - Scie): **91.03 (Q1-D1)**

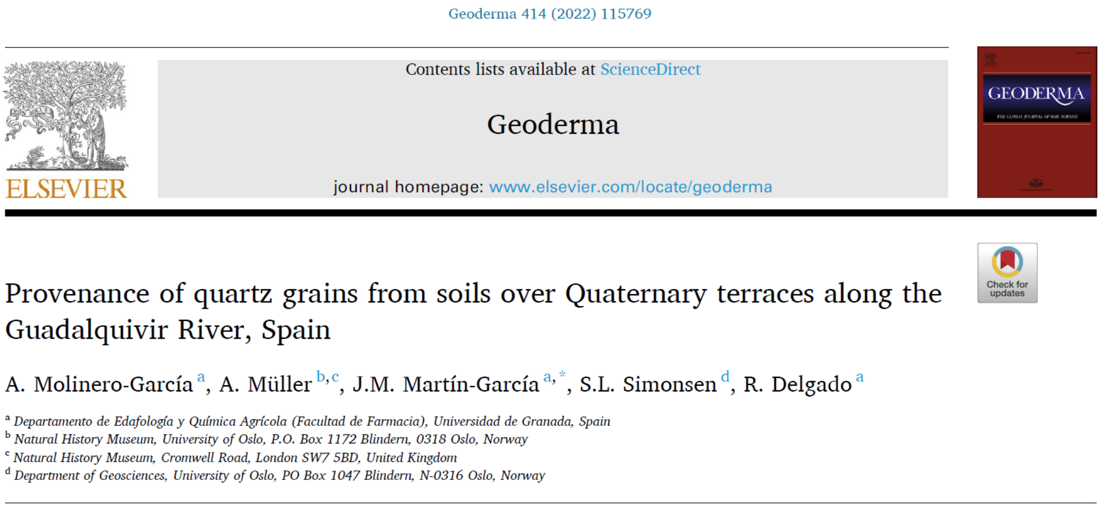

Geoderma 414 (2022) 115769

Contents lists available at ScienceDirect

Geoderma

journal homepage: www.elsevier.com/locate/geoderma

Provenance of quartz grains from soils over Quaternary terraces along the Guadalquivir River, Spain

A. Molinero-García [a], A. Müller [b,c], J.M. Martín-García [a,*], S.L. Simonsen [d], R. Delgado [a]

[a] *Departamento de Edafología y Química Agrícola (Facultad de Farmacia), Universidad de Granada, Spain*
[b] *Natural History Museum, University of Oslo, P.O. Box 1172 Blindern, 0318 Oslo, Norway*
[c] *Natural History Museum, Cromwell Road, London SW7 5BD, United Kingdom*
[d] *Department of Geosciences, University of Oslo, PO Box 1047 Blindern, N-0316 Oslo, Norway*

Abstract

The characterisation of quartz grains’ chemical and mineralogical properties in sediments and sedimentary rocks is widely used in provenance studies. This paper analyses quartz grains from the coarse sand fraction in soils in Quaternary fluvial terraces (Guadalquivir River, southern Spain). The tentative soil ages are 0.3 ka (Haplic Fluvisol), 7 ka (Haplic Calcisol), 70 ka (Cutanic Luvisol), 300 ka (Lixic Calcisol) and 600 ka (Cutanic Luvisol). The quartz grains analyses shed light on the sedimentological history of these terraces. Scanning electron microscope cathodoluminescence (SEM-CL) characteristics, micro inclusion inventory established by Energy-dispersive X-ray spectroscopy (SEM-EDX) and trace element contents determined with laser ablation inductively coupled plasma mass spectrometry (LA-ICP-MS) of quartz grains permitted distinguishing six types of grains in the soils studied: metamorphic quartz (type 1), undeformed granitic quartz (type 2), strongly altered granitic quartz (type 3), recrystallised (deformed) granitic quartz (type 4), sandstone-derived quartz (type 5) and hydrothermal quartz grains (type 6).

Metamorphic quartz grains (type 1) come from the Sierra Morena (Iberian Massif) and Sierra Nevada (Internal Betic Zone). Granitic quartz grains (types 2 to 4) come from Los Pedroches batholith and its associated plutons (Santa Elena and Linares). The sandstone-derived quartz type 5 comes from the numerous sandstone outcrops scattered in the central catchment area of the Guadalquivir River. Finally, hydrothermal quartz grains (type 6) originate from hydrothermal veins associated with subvolcanic rocks of the Los Pedroches batholith.

Variations were noted in the proportions of quartz types in soils of different ages, attributed to spatial and temporal changes in the catchment area. The most remarkable change occurred between 500-240 ka ago when the catchment area extended into Sierra Nevada´s metamorphic rocks, well reflected in type 1 content (lower in P2, P4, P5 and PM) and their characteristics (quartz with less healed fractures, less Al content, bigger mica microinclusions, smaller Al/Ti ratio) in the post-500-240 ka soils.

Our study shows that the combined study of SEM-CL characteristics, micro inclusions (SEM-EDX), and trace element contents (LA-ICP-MS) of quartz grains

is an efficient approach for characterising the provenance of quartz grains in the sand fraction of soils.

Graphical Abstract

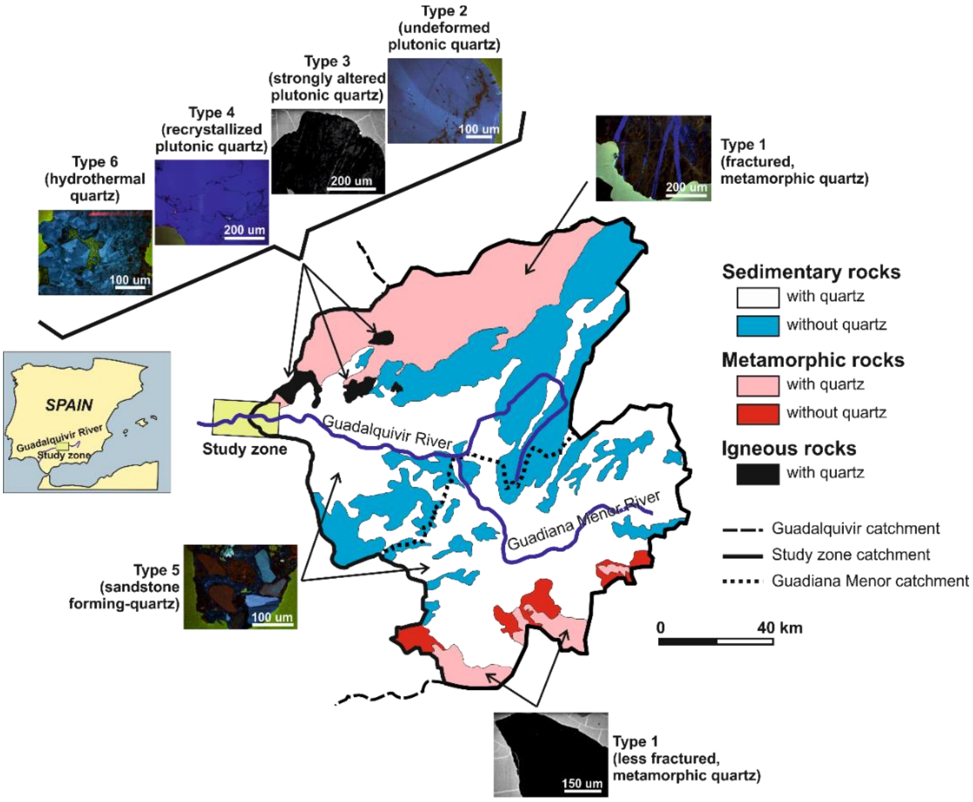

Provenance of quartz grains in soils of Guadalquivir River terraces

Keyword: provenance study; quartz cathodoluminescence; quartz trace elements; quartz microinclusions; soil; Guadalquivir valley.

Highlights:

- SEM-CL, SEM-EDX and LA-ICP-MS characterize the provenance of quartz grains in soils
- Six genetic quartz types identified in soil terraces of the Guadalquivir River
- Quartz grains reveal the sedimentological history of the terraces
- Changes in soil's quartz types record changes in the Guadalquivir catchment area

1. Introduction

Quartz is a major component of the soils (Drees et al., 1989) and is present in most sedimentary, metamorphic and igneous rocks. It is a tectosilicate with the formula SiO_2, in which silicon tetrahedrons share their oxygens in a three-dimensional structure, forming small channels that run parallel to the c axis (e.g. Rottier et al., 2017). In addition, its high hardness (7) and low solubility in water (11.0 ±1.1 mg kg^{-1}, at 25 ºC and 1 bar; Rimstidt, 1997) makes quartz a very stable mineral facilitating its enrichment in many sediments and clastic rocks (Blatt et al., 1980). In soils, it concentrates as pebble, sand and silt fractions (Calero et al., 2013; Martín-García et al., 2015).

Quartz is one of the chemically purest minerals in nature, after diamond and graphite (Drees et al., 1989). It contains, however, lattice-bound trace elements in low concentrations due to atomic substitution of Si and interstitial elemental incorporation within the crystal structure. In addition, quartz may contain micro inclusions of solid, liquid or gaseous phases.

Al, Ti, Li, Ge, H, Be, B, Mn, Rb, Sr, Na, P, K, Ca, and Fe are the most common trace elements in natural quartz (e.g. Bambauer, 1961; Kats, 1962; Weil 1984, 1993; Perny et al., 1992; Larsen et al., 2000; Götze et al., 2004; Müller and Koch-Müller, 2009). Concentrations of these elements are directly determined with *in situ* micro-beam techniques, such as electron probe micro analysis (EPMA), laser ablation inductively coupled plasma mass spectrometry (LA-ICP-MS) and secondary ion mass spectrometry (SIMS) (e.g. Müller et al., 2003) or with spectrometric methods, such as FTIR spectrometry (e.g. Stalder et al. 2017). Cathodoluminescence (CL) is an imaging and spectroscopic technique, which reveals the relative abundance and distribution of lattice defects and impurity trace elements within quartz grains. As such, CL visualises structures related to crystallisation, such as growth zoning and secondary processes (alteration, recrystallisation or radiation damage) (Ramseyer and Mullis, 1990; Götze et al., 2001; Richter et al., 2003; Götze, 2012; Sales de Oliveira et al., 2017).

Physicochemical conditions strongly control the incorporation of trace elements in quartz and the formation of lattice defects during its crystallisation (e.g. Götze, 2009 and references therein). Thus, the trace element and lattice defect diversity and abundance detected along with the micro inclusion inventory are genetic fingerprints. The combination of quartz CL imaging and spectrometry with results of *in situ* micro-beam techniques (EPMA, LA-ICP-MS, SIMS) permits reconstructing the crystallisation and alteration processes using compositional and defect variations to estimate formation pressure, temperature and fluid or melt composition. Because quartz is relatively resistant to alteration and weathering compared to other minerals, it is increasingly used in provenance surface environment studies (Müller and Knies, 2013; Ackerson et al., 2015; Sales de Oliveira et al., 2017). However, there are no studies that apply these techniques to quartz grains in soils.

There are a few microchemical studies of quartz from granulometric fractions of soil. For example, Martín-García et al. (2004, 2015) obtained evidence of quartz alteration in the fine sand fraction (50 – 250 µm) of soils, developed on mica schist formations in Sierra Nevada, southern Spain, by scanning electron microscope backscattered electron (SEM-BSE) imaging, EPMA, high-resolution transmission electron microscopy (HRTEM) and selected area electron diffraction (SAED). They detected an increase of the trace element content on the edges of quartz grains in the Parent Rock<Entisol<Inceptisol<Alfisol evolution sequence.

This paper studies the quartz grains of the sand fraction from Quaternary soils forming terraces along the Guadalquivir River. The tentative ages of the terraces range between 0.3 and 600 ka (Calero et al., 2008). The bedrocks exposed in the river catchment area have a wide lithological variety (igneous, metamorphic and sedimentary rocks) belonging to the Iberian Massif, Internal Betic Zone and External Betic Zone. The sand fraction of these soils, which has been studied before by Martín-García et al. (2020), consists of a great mineral variety, including mainly quartz, K-feldspar, plagioclases, muscovite, illite, biotite, paragonite, chlorite, mixed-layered clay minerals, goethite, hematite, calcite and dolomite. These authors suggested the provenance of some of these minerals: 1) garnet (pyralspite group) and andalusite originate from metamorphic rocks of the Iberian Massif or the Internal Betic Zone; 2) andradite (garnet) is a typical constitute of calcareous, contact metamorphic rocks, found close to the Los Pedroches batholith (Iberian Massif – External Betic Zone contact); 3) staurolite, as a medium- to high-grade metasedimentary mineral (regional metamorphism), possibly comes from metapelites of the Internal Zone of the Betic Cordilleras; and 4) rutile, which is ubiquitous, was evidently neoformed in these soils, invalidating the possibility of using it as a mineral index in the provenance studies.

The great abundance of quartz grains in the sand fraction of the soil chronosequence from the Guadalquivir River (Calero et al., 2009; Martín-García et al., 2020) makes it an ideal provenance pathfinder. Therefore, the main objective is to determine the provenance of the quartz grains that constitute the soils of the Guadalquivir River's chronosequence between 0.3 and 600 ka. To do so, we combined SEM-CL and LA-ICP-MS on quartz grains of the sand fraction (500 - 2000 µm). This is the first time this method combination is applied to quartz grains in soils. Finally, the results are compared and discussed regarding the provenance of other mineral soil grain suggested by Martín-García et al. (2020).

2. Geological setting and sample origin

The study area is located in the Cenozoic Guadalquivir Basin, drained by the Guadalquivir River, the largest river system in the southern Iberian Peninsula. Along the Guadalquivir River shores, a complex fluvial terrace system has developed during Quaternary. Soil sampling has been carried out on terraces of different ages located between the cities of Andújar and Villanueva de la Reina, along a 3.7 km long transect of the river between 3º 50' – 4º 3' W and 38º 0' – 38º 2' N (Figure 1c).

The Cenozoic Guadalquivir Basin developed between the Iberian Massif to the north and the Betic Cordilleras to the south (Figure 1a). The Quaternary fluvial alluvium of the Guadalquivir Basin consists of gravels with some stone-free sandy, silty layers originating from remarkably diverse lithology (Figure 1). According to Martín-García et al. (2020), these rocks comprise: igneous rocks (granite, granodiorite, rhyolite, tonalite, andesite, and gabbro) and metamorphic rocks (schists, quartzites) from the Iberian Massif; sedimentary rocks (clays, sands, gravels, breccias, sandstones, limestones, marly limestones, marls and dolostones) from the External Betic Zone of the Betic Cordilleras; and sedimentary (limestones and dolostones) and metasedimentary rocks (schist, quartzites, shales, phyllites, marble and gneiss) from the Internal Betic Zone of the Betic Cordilleras.

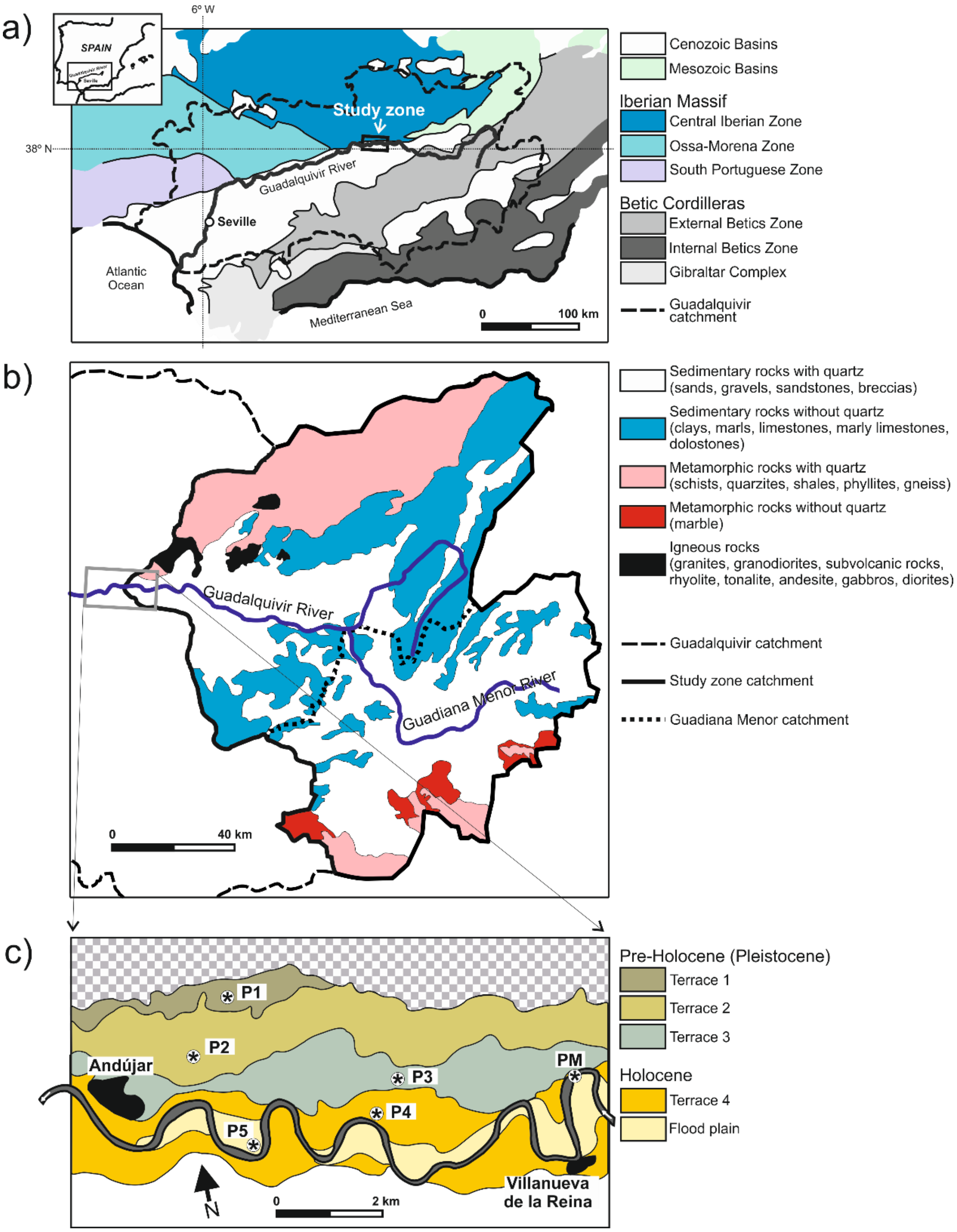

Figure 1. Geology of the study area. a) Location of the study area in relation to the Iberian Massif and Betic Cordilleras; b) Simplified lithology of the Guadalquivir river catchment area; c) Detailed map of the sampling area with indicated positions of fluvial terraces and soil sampling sites.

The mineralogical diversity observed in the fluvial alluvium is related to the complex history of the catchment area of the Guadalquivir River, which has changed over time (Figure 1b). The catchment of the sampling area is currently 17700 km^2**,** but 500-240 ka ago, it was much smaller (approx. 10420 km^2). Until then, there was an endorheic lake, the Guadix-Baza basin, into which the Guadiana Menor river drained (Demuro et al., 2015; García-Tortosa et al., 2019). Guadiana Menor river is a side stream of the Guadalquivir River in the eastern part of its current catchment area. Between 500-240 ka ago, due to Alpine tectonics and erosion, the Guadix-Baza basin drainage was strongly modified, and the endorheic lake became an exorheic lake, which started to drain towards the Atlantic Ocean via the Guadalquivir River (Ortiz et al., 2000). As a result, the catchment area became as twice as large, and for the first time, material from the Internal Betic Zone contributed to the formation of the terraces and floodplain of the Guadalquivir River in the study zone.

The soils studied in this paper developed on the surfaces of four Quaternary terraces and the floodplains (Table 1). These sequences have the following tentatives ages (Calero et al., 2008): 600 ka (P1; Terrace 1), 300 ka (P2; Terrace 2), 70 ka (P3; Terrace 3), 7 ka (P4; Terrace 4) and 0.3 ka (P5; floodplain). Samples were taken from all five environments. In addition, fresh point bar sediments (PM) were collected in the Guadalquivir River from an active bar of streams. Soil typologies are as follows (IUSS Working Group WRB, 2015): P1, Cutanic Luvisol; P2, Lixic Calcisol; P3, Cutanic Luvisol; P4, Haplic Calcisol; P5, Haplic Fluvisol.

The transformation of the ancient endorheic lake of the Guadix-Baza basin into an exorheic lake and the related catchment extension of the Guadalquivir River between 500-240 ka ago caused the sediments from the Internal Betic Zone rocks to become part of the material deposited on terraces (2, depending on the age of the catchment extension), 3 and 4 (affecting profiles (P2), P3, and P4), on the floodplain (profile P5) and the current riverbed point bar (PM).

Table 1. Main characteristics of investigated soil samples according to Calero et al. (2008, 2009, 2013) and Martín-García et al. (2016).

Chronosequence level (soil profile)	P1	P2	P3	P4	P5	PM
Age (ka)	600, pre-Holocene	300, pre-Holocene	70, pre-Holocene	7, Holocene	0.3, Holocene	0.001, Holocene
Soil classification[a]	Cutanic Luvisol/Palexeralf	Lixic Calcisol/Haploxeralf	Cutanic Luvisol/ Haploxeralf	Haplic Calcisol/Calcixerept	Haplic Fluvisol/Xerofluvent	Alluvial[b]
PDI	44.8	44.3	39.6	26.8	21.2	0
Horizons sequence	Ap, Bt, Btg1, Btg2, 2BCtg, 3BCt, 4C	Ap, Btg1, Btg2, Btk, Cmk/Btk	Ap1, Ap2, Bt1, Bt2, Bt3, Bt4, Bt5, 2Bt6, 3Bt7	Ap1, Ap2, Bwk1, 2Bwk2, 3C1, 4C2	Ap, 2C1, 3C2, 4C3, 5C4, 6C5, 7C6	Point-bar deposit
Horizonte selected (sample name)	Btg2 (QAG04)	Btg2 (QAG10)	Bt4 (QAG18)	Bwk1 (QAG24)	Ap (QAG29)	(QAG38)
Moist colour (Munsell)	5YR 4/6	7.5YR 4/6	5YR 4/4	10YR 5/4	10YR 4/3	2.5Y 5/3
Clay (%)	27.4	41.7	42.0	30.1	23.0	16.3
Coarse sand (0.5-2 mm) (%)	26.5	1.9	18.8	22.8	3.5	45.3
Organic carbon (%)	0.15	0.40	0.27	0.30	0.77	1.76
Carbonates (%)	0.0	4.4	0.0	36.0	38.4	23.5
pH	7.2	7.8	7.4	8.1	7.9	8.4
CEC ($cmol_+kg^{-1}$)	6.9	14.7	29.1	12.2	12.8	8.7

[a] Word Reference Base for Soil Resources/Soil Taxonomy

[b] Recent sediments

Abbreviations: PM - Parent material (current river sediments); PDI - Profile Development Index (according to Harden, 1982); CEC - Cation Exchange Capacity.

The climate is currently hot Mediterranean with 500 mm total annual rainfall and a mean annual temperature of 18 ºC. The vegetation is mainly anthropogenic because the flat surfaces are used, from time immemorial, as farmland (nowadays, olive groves, wheat and cotton).

The solum of the older terraces (pre-Holocene soils: P1, P2, and P3) shows Bt horizons (with clay illuviation features such as clay cutans), red munsell colours, relatively deep thickness, clayey texture (>30% clay) and evidence of carbonates leaching (and accumulation, in P2). Thus, the older soils have the greatest Harden's Profile Development Indexes (between 44.8 of P1 and 39.6 of P3; Table 1). In the Holocene soil P4, brunification (Fe oxide precipitation) and some leaching/accumulation of carbonates has also been detected. P5 have no pedogenic evolution features.

The processes of weathering, leaching and carbonate accumulation, clay illuviation, reddening and soil structuration have affected the morphological, analytical and mineralogical properties of these soils which vary over time, establishing an ideal chronosequence (Calero et al., 2008, 2009) also evidenced in the clay fraction formed (Calero et al., 2013; Martín-García et al., 2016) and fine sand fraction of these soils (Martín-García et al., 2020).

3. Material and methods

3.1. Sample preparation

Coarse sand grains (500 – 2000 µm) of five soil samples (one horizon per terrace was selected, choosing the one of greatest pedogenic evolution; Martín-García et al., 2020) and the point bar sediment of the Guadalquivir riverbed were separated (Table 1). First, the bulk soil samples and sediment PM were air-dried and sieved to <2 mm to obtain the fine earth fraction (<2 mm). Then and after removing organic matter with H_2O_2, the coarse sand fraction (500–2000 µm) was separated by wet sieving and collected on quartered aliquots to extract the quartz grains. A total of 1011 grains (between 131 and 217 grains in each sample) were hand-picked from the coarse sand fraction. Finally, the grains were embedded in epoxy resin on petrological standard glass slides (4.8 × 2.8 × 0.5 mm) and polished down half grain size for SEM, SEM-CL and LA-ICP-MS analysis.

3.2. Analytical methods

All 1011 quartz grains were first examined at the SEM, a Hitachi S–3600 N equipped with an energy-dispersive X-ray spectroscopy detector (EDX) from Bruker XFlash® 5030. The instrument is based at the Natural History Museum of Oslo. BSE imaging was used to map the grains, and EDX was applied to identify micro inclusions in quartz. BSE-SEM imaging and EDX semi-qualitative analyses of micro inclusions were performed on 160 representative quartz grains, in which 275 micro inclusions were identified with EDX.

A total of 297 grains out of 1011 were randomly selected (sample by sample) for SEM-CL study (Table 2). At least 20 grains were studied (in each sample) in order to obtain a number of grains statistically representative (Mahaney, 2002). The CL images were acquired with a Delmic Sparc Advanced CL System attached to a Hitachi SU5000 FE-SEM based at the University of Oslo. The instrument settings of SEM-CL imaging were a dwell time of 50 µs and a gain of 650 mV. The settings for CL spectrum acquisition were a voltage of 12 kV, an exposure time of 200 ms and a beam input slit of 500 µm. This way, grain-specific, intra-granular features such as growth zoning or alteration patterns were mapped, and CL spectra were recorded to identify the wavelengths of emission bands causing the different CL colours of the examined quartz grains. The criteria established by Müller (2000), Götze et al. (2001), Bernet and Basset (2005), Müller et al. (2010) and Sales de Oliveira et al. (2017) were used for identifying the quartz origin. This approach utilizes CL-SEM features of quartz grains and quartz CL emission characteristics, which provide information about the type and distribution of lattice defects, which in turn reflect the physico-chemical conditions of crystal growth.

From the 297 grains, 51 grains were selected for LA-ICP-MS analysis. In addition to SEM-BSE and SEM-CL observations, the selection was based on examination at the petrological microscope. Only grains without visible micro inclusions were chosen. The ICP-MS used in this study was a double-focusing sector field instrument of the ELEMENT-1 Finnigan MAT type combined with a New Wave UP-193 nm excimer laser probe. Continuous raster ablation was carried out, resulting in ablated rasters of approximately 150×100 µm with depths of 20 to 30 µm. Element concentrations were calculated by multi-standard calibration.

The analysed elements and their detection limits (in ppm, in parentheses) were Al (9.46), Li (0.41), Be (0.08), B (1.29), Mn (0.07), Ge (0.10), Rb (0.09), Sr (0.01), Sb (0.01), U (0.01), Na (46.6), P (1.60), K (8.16), Ca (21.60), Ti (0.75), Fe (1.29), Zn (1.42) and Ga (0.06). The isotope ^{29}Si was used as the internal standard applying the stoichiometric concentration of Si in SiO_2. External multistandard calibration was performed using three silicate glass reference materials produced by the National Institute of Standards and Technology, USA (NIST SRM 610, 612, and 614). In addition, the applied standards included the NIST SRM 1830 soda-lime float glass (0.1% m/m Al_2O_3), the certified reference material BAM No. 1 amorphous SiO_2 glass from the Federal Institute for Material Research and Testing in Germany, and the Qz-Tu synthetic pure quartz monocrystal provided by Andreas Kronz from the Geowissenschaftliches Zentrum Göttingen (GZG), Germany. Certified, recommended, and proposed values for these reference materials were taken from Jochum et al. (2011) and from the certificates of analysis where available. For the calculation of P concentrations, the procedure of Müller et al. (2008) was applied. An Ar blank was run before each reference material and sample measurement to determine the background signal. The background was subtracted from the instrumental response of the reference material/sample before normalization against the internal standard in order to avoid effects of instrumental drift. This was carried out to avoid memory effects between samples. A weighted least squares regression model, including several measurements of the six reference materials, was used to define the calibration curve for each element. Ten sequential measurements on the BAM No.1 SiO_2 quartz glass were used to estimate the limits of detection (LOD) which were based on 3× standard deviation (3σ) of the 10 measurements. Occasionally individual solid or fluid inclusions were hit by the laser. These analyses were recognisable from concentration spikes in the time-resolved analytical spectra; these data were not considered.

Table 2. Frequency (and percentage) of quartz grains from coarse sand by quartz types.

			Quartz type[a] (percentage in parenthesis)					
Profile	Soil Horizon	Total grains	Type 1	Type 2	Type 3	Type 4	Type 5	Type 6
P1	Btg2	38	23 (60)	4 (11)	6 (16)	3 (8)	0 (0)	2 (5)
P2	Btg2	47	9 (19)	18 (38)	4 (9)	1 (2)	15 (32)	0 (0)
P3	Bt4	55	0 (0)	52 (94)	1 (2)	2 (4)	0 (0)	0 (0)
P4	Bwk1	60	17 (28)	34 (57)	3 (5)	4 (7)	2 (3)	0 (0)
P5	Ap	53	14 (26)	26 (49)	4 (8)	7 (13)	2 (4)	0 (0)
PM		44	4 (9)	26 (60)	1 (2)	11 (25)	1 (2)	1 (2)
TOTAL		297	67 (23)	160 (54)	19 (6)	28 (9)	20 (7)	3 (1)

[a] Type 1: metamorphic quartz; Type 2: undeformed plutonic quartz; Type 3: strongly altered plutonic quartz; Type 4: recrystallised plutonic quartz originating from metamorphic rocks; Type 5: sandstone quartz; Type 6: hydrothermal quartz

4. Results

Based on SEM-BSE and SEM-CL imaging, six types of quartz grains are distinguished. In addition, the trace elements contents, determined by LA-ICP-MS, are considered in the discrimination of quartz grain types.

4.1. Grain type 1: Metamorphic quartz

The type 1 population, comprising 67 (23%) out of 297 grains, is characterised by a monocrystalline structure and subangular-rounded grain shape (Table 2). The grains show one characteristic red emission band at ~650 nm in CL spectra (Figure 2) and a homogeneous dull red-brown CL (Figure 3). The spectra are uncommon because natural quartz usually has two broad emission bands, besides the red one also a blue band at ~450 nm (e.g. Götze et al., 2001). Type 1 is present in all profiles except P3. The P1 sample had the highest frequency of type 1, more than half of the grains studied (Table 2). Only a few mineral inclusions with little variety were detected (Table 3): mica, feldspar, zircon and rutile. The abundance and type of these micro inclusions is a specific feature of grain type 1.

In SEM-CL, some type 1 grains are cross-cut by thin, healed, brightly luminescent fractures and mostly with preferred orientation (Figures 3a and b) and others type 1 grains do not show fractures (Figure 3c). The CL spectrum of quartz healing these fractures exhibits both emission bands whereby the blue band dominates over the red one. The number of grains exhibiting these fractures varies in each sample depending on whether the soil is pre-Holocene or Holocene: in P1 and P2 (pre-Holocene), these fractures appear in most grains (68 and 56%, respectively), whereas in P4, P5 and PM (Holocene) grains, these fractures are scarce or absent (24, 0 and 0%, respectively).

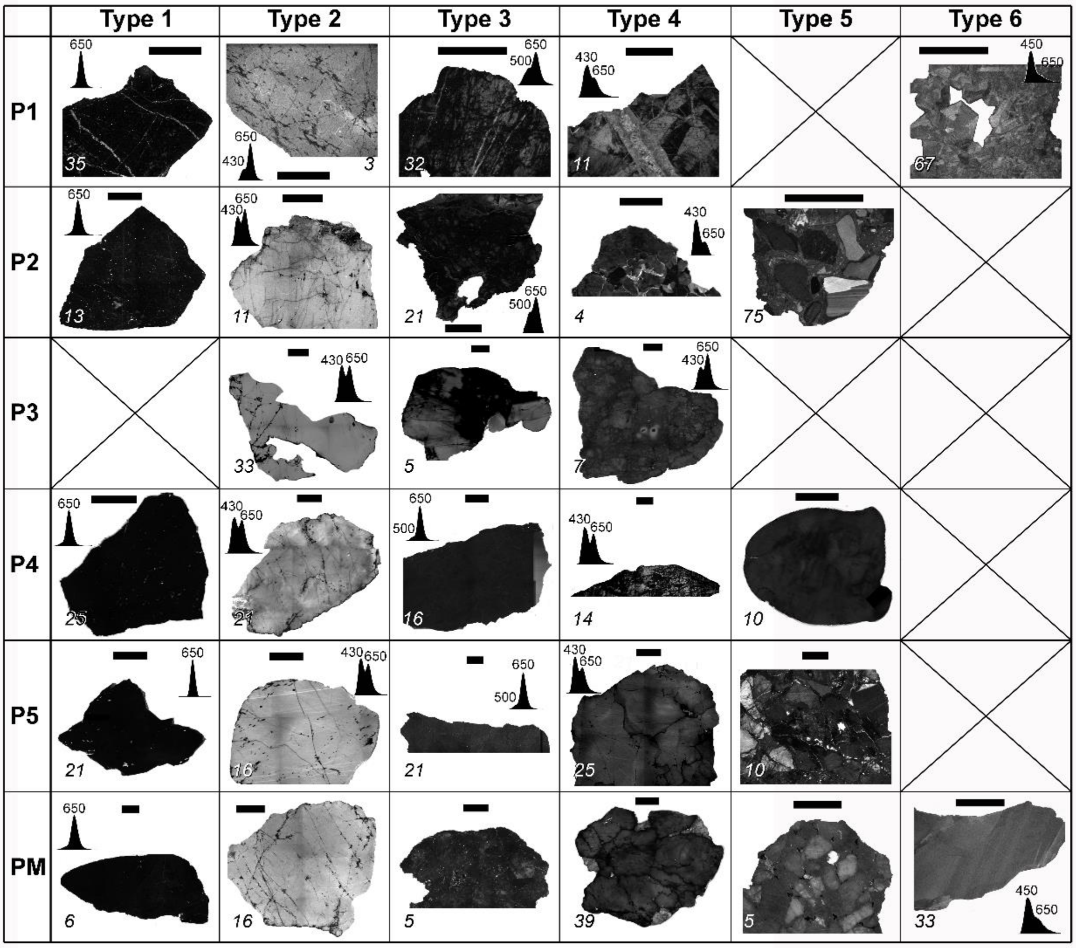

Figure 2. Classification of quartz grains of soil sand fraction (>500 µm) based on CL characteristics. One representative SEM-CL image of each quartz grain type in each sample is shown. The number in the lower left of the cells indicate the grain abundance (in percent) in respect to the total number of identified grains of this type. The scale bar length correspond to 200 µm. Representative CL spectra with indicated peak maximum wavelength numbers (in nm) are provided for grains. Type 1: Metamorphic quartz grains; Type 2: Undeformed quartz grains originating from plutonic rocks; Type 3: Strongly altered plutonic quartz grains; Type 4: Recrystallised quartz grains from deformed plutonic rocks; Type 5: Sandstone quartz grains; Type 6: Hydrothermal quartz grains.

The metamorphic origin of these quartz grains is suggested because of their weak reddish-brown CL, the absence of growth zoning and healed fluid pathways (typical of igneous quartz) and deformation lamellae characteristic of high-grade metamorphic quartz (Müller, 2000; Bernet and Basset, 2005; Sales de Oliveira et al., 2017).

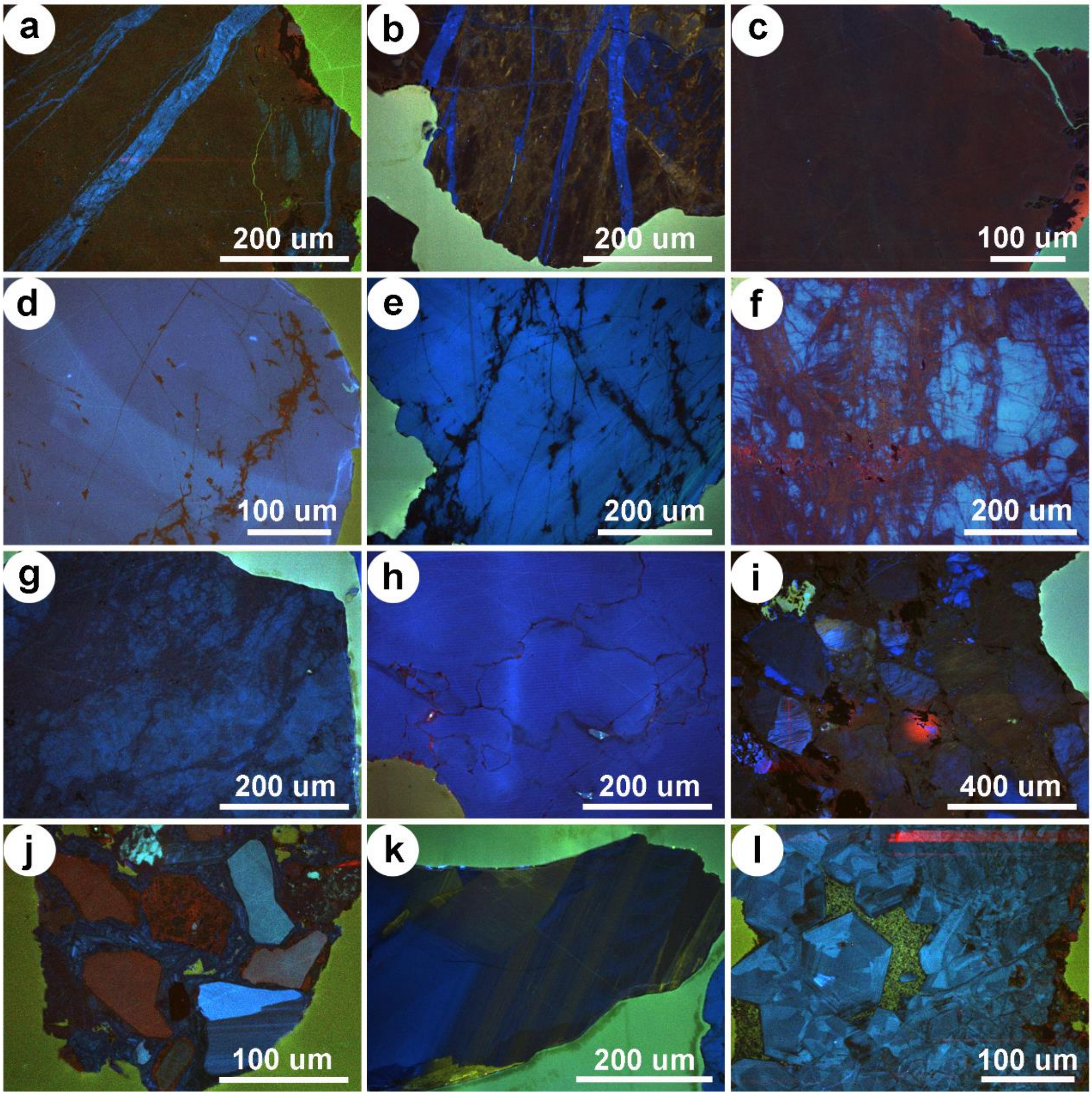

Figure 3. SEM-CL color images of quartz sand grains. a) type 1 (from P1); b) type 1 (P4); c) type 1 without fractures (P2); d) type 2 (P1); e) type 2 (PM); f) type 3 (P2); g) type 4 (P5); h) type 4 (PM); i) type 5 (P5); j) type 5 (P2); k) type 6 (PM); l) type 6 (P1).

The most abundant trace element is Al (192 ± 164 ppm), followed by Fe (95 ± 144 ppm) and K (61 ± 51 ppm). Mean element concentrations show high standard deviation values due to the variability among grains. Al/Ti values have a wide range and vary from 1.6 to 375.8. There are poor correlations between the contents of Al and K ($R^2 = 0.014$, n = 10) and Al and Li ($R^2 = 0.342$; n = 10) (Figure SM1).

Type 1 grains differ from the other types described below. They have lower Ti than types 2, 4 and 5 (except for grains in sample P2), contain little Li compared to types 2 and 4 (except two cases) and in Holocene samples, are rich in Mn compared to the other types.

4.2. Quartz type 2: Undeformed plutonic quartz

Most of the grains studied (160 out of 297 = 54%) belong to type 2 (Table 2). This group comprises monocrystalline and subangular-angular quartz grains. Some grains are very angular. These grains have a relatively bright, violet to blue CL, and the CL spectra show two broad emission bands at ~430 and ~650 nm (Figures 2 and 3). In most cases, the intensities of both emissions are similar. Occasionally, patches of dull CL and weakly contrasted growth zoning are developed (Figure 3e). Randomly oriented fractures, which are healed with non-luminescent quartz, are common. These features are typical of plutonic quartz (Müller et al., 2010; Sales de Oliveira et al., 2017). Grains, which exhibit magmatic growth zoning (Figure 3e), originate typically from subvolcanic or volcanic granitic rocks, such as rhyolites.

Type 2 is present in all samples in very variable abundance (Table 2, Figure 2). Type 2 has the highest amount and variety of micro inclusions comprising mainly feldspar, mica, zircon and monazite. These are typical minerals of granitic rocks (Table 5).

The most abundant trace elements are Al, Ti and Li (>30 ppm usually) (Table 4). In type 2, no correlation has been detected between the Al and other elements.

Comparing the chondrite-normalised trace element values of type 2 and type 1 (Figure 4), the following differences are noticed: Type 2 has more consistent compositions (closer lines), higher average concentrations of Li and Ti, and is depleted of Sb, Sr and Ge compared to type 1.

Table 3. Mineral micro inclusions identified in the studied quartz grains.

	P1 (N=37)		P2 (N=25)		P3 (N=22)		P4 (N=23)		P5 (N=22)		PM (N=31)		TOTAL (N=160)		
	n	mean size (µm)	n	mean size (µm)	n	mean size (µm)	n	mean size (µm)	n	mean size (µm)	n	mean size (µm)	n	mean size (µm)	%
Feldspar[a]	10	111± 87	11	209 ± 62	13	250 ± 225	5	254 ± 203	5	141 ± 77	13	268 ± 185	57	206	36
Muscovite[b]	18	29 ± 23	5	154 ± 129	5	103 ± 102	6	205 ± 199	5	137 ± 83	4	143 ± 43	43	128	27
Zircon	3	45 ± 13	2	38 ± 18	4	45 ± 37	2	18 ± 11	2	15 ± 14	5	52 ± 19	18	35	11
Iron Oxides[c]	5	46 ± 27	2	38 ± 18	2	13 ± 4	2	10 ± 0	1	20			14	25	9
Monazite	1	20			5	42 ± 36	3	42 ± 8	3	15 ± 9			12	30	8
Rutile	3	82 ± 59	4	58 ± 30					3	50 ± 36	1	45	11	59	7
Ilmenite	3	28 ± 19	4	34 ± 11			1	100	2	20 ± 21	1	100	11	56	7
Apatite	1	40	1	60	1	100	1	150					4	88	3
Gypsum									4	38 ± 15	1	50	5	44	3
Xenotime					2	45 ± 7	1	50					3	48	2
Cassiterite			1	90									1	90	1
Pyrite									1	5			1	5	1
Barite									2	45 ± 7			2	45	1
Antimony	1	5											1	5	1
TOTAL	45		30		32		21		28		25		183		

N = number of analysed quartz grains (among the grains that show micro inclusions); n = number of analysed micro inclusions by profile.

[a] The feldspar found was either K-feldspar or albite. Ca-bearing plagioclases (anorthite) has not been found

[b] Muscovite and/or biotite

[c] Goethite, hematite and/or magnetite

Table 4. Mean values (and standard deviation) of trace elements contents (ppm) and Al/Ti ratio in quartz grains (LA-ICP-MS) from coarse sand.

	Profile	n	Al	Li	Be	B	Mn	Ge	Rb	Sr	Sb	U	Na	P	K	Ca	Ti	Fe	Zn	Ga	Al/Ti
	LOD		9.46	0.41	0.08	1.29	0.07	0.10	0.09	0.01	0.01	0.01	46.60	1.60	8.16	21.60	0.75	1.29	1.42	0.06	
type 1	P1	5	269.39 ±143.17	8.39 ±12.99	0.13 ±0.06	3.55 ±0.88	0.91 ±0.51	1.62 ±0.31	0.39 ±0.27	1.21 ±0.68	1.41 ±0.82	<0.01	<46.6	2.09 ±2.89	46.25 ±28.19	<21.6	1.67 ±0.46	37.25 ±46.53	2.25 ±1.41	0.13 ±0.06	172.07 ±120.74
	P2	1	393.68	34.05	0.20	5.33	1.21	1.05	0.39	0.12	1.17	<0.01	<46.6	3.86	92.08	<21.6	42.47	445.93	9.24	0.32	9.27
	P4	2	40.24 ±41.08	1.62 ±0.75	0.03 ±0.02	2.08 ±0.58	17.17 ±18.01	1.36 ±0.40	0.10 ±0.09	3.10 ±3.42	1.58 ±0.25	0.03 ±0.02	606.58 ±824.88	8.79 ±7.21	92.38 ±125.61	214.85 ±226.49	5.51 ±1.92	24.42 ±28.64	11.25 ±5.98	0.43 ±0.20	9.16 ±10.65
	P5	2	49.19 ±35.20	1.67 ±0.85	0.09 ±0.07	1.90 ±0.34	25.24 ±27.56	1.30 ±0.38	0.52 ±0.52	4.25 ±0.91	1.13 ±0.54	<0.01	155.53 ±186.99	1.57 ±1.09	52.30 ±16.55	86.15 ±21.43	2.88 ±0.02	134.70 ±155.77	16.45 ±15.06	0.11 ±0.02	17.07 ±12.11
	Mean	10	191.95 ±164.11	8.26 ±12.98	0.11 ±0.07	3.10 ±1.27	9.06 ±15.39	1.45 ±0.34	0.36 ±0.29	2.09 ±1.93	1.36 ±0.60	0.01 ±0.01	166.40 ±369.08	3.50 ±4.22	61.27 ±51.00	69.12 ±111.89	6.76 ±12.66	95.04 ±144.02	7.59 ±8.16	0.21 ±0.15	92.21 ±116,63
type 2	P1	2	183.81 ±47.30	21.21 ±20.43	0.17 ±0.13	3.98 ±1.22	0.91 ±0.62	0.94 ±0.10	0.25 ±0.27	0.57 ±0.74	1.04 ±1.39	<0.01	<46.6	<1.60	23.71 ±24.49	<21.26	34.53 ±23.08	14.01 ±14.00	1.51 ±1.12	0.12 ±0.01	6.27 ±2.82
	P2	6	228.97 ±76.23	37.14 ±20.14	0.18 ±0.05	3.57 ±1.19	1.07 ±0.30	0.70 ±0.06	0.17 ±0.18	0.16 ±0.17	1.41 ±2.99	<0.01	<46.6	<1.60	41.43 ±48.70	<21.6	54.86 ±18.35	16.95 ±9.79	2.95 ±1.89	0.20 ±0.14	4.44 ±1.43
	P3	10	219.97 ±82.09	38.05 ±14.98	0.30 ±0.36	2.22 ±0.90	1.12 ±1.44	0.90 ±0.33	0.18 ±0.20	0.06 ±0.03	0.15 ±0.17	<0.01	<46.6	8.33 ±18.10	13.67 ±13.19	29.03 ±45.21	40.57 ±14.95	14.68 ±19.05	2.91 ±1.34	0.18 ±0.10	5.90 ±2.56
	P4	5	310.63 ±79.51	41.33 ±18.03	0.27 ±0.27	4.16 ±3.18	1.82 ±1.77	0.81 ±0.20	0.37 ±0.28	0.21 ±0.16	0.22 ±0.22	0.02 ±0.02	54.56 ±42.83	8.94 ±6.40	24.19 ±8.71	40.02 ±39.48	37.50 ±15.80	9.25 ±4.36	6.50 ±4.06	0.31 ±0.25	8.85 ±2.25
	P5	3	223.86 ±28.96	28.98 ±16.42	0.17 ±0.01	4.74 ±2.84	1.43 ±0.81	0.78 ±0.08	0.66 ±0.53	0.08 ±0.07	0.22 ±0.12	<0.01	188.89 ±286.80	4.51 ±3.26	97.07 ±62.95	68.87 ±27.21	79.08 ±24.17	6.60 ±4.60	3.75 ±2.22	0.30 ±0.09	3.04 ±1.11
	PM	6	265.54 ±54.65	51.50 ±8.78	0.15 ±0.18	3.63 ±1.23	1.11 ±0.57	0.75 ±010	0.16 ±0.07	0.09 ±0.04	0.17 ±0.14	<0.01	<46.6	3.11 ±1.58	14.22 ±13.13	24.77 ±20.91	60.61 ±21.54	27.79 ±26.02	4.02 ±1.48	0.25 ±0.06	4.90 ±2.02
	Mean	32	242.47 ±74.99	39.01 ±16.67	0.22 ±0.24	3.39 ±1.83	1.23 ±1.10	0.81 ±0.22	0.25 ±0.27	0.14 ±0.20	0.47 ±1.34	<0.01	<46.6	5.28 ±10.59	29.07 ±36.71	29.62 ±34.12	49.76 ±21.41	15.91 ±16.85	3.68 ±2.42	0.22 ±0.14	5.65 ±2.58
type 3	P1	1	99.25	0.79	<0.08	6.36	2.28	1.50	0.40	0.12	1.03	<0.01	88.18	<1.60	29.97	<21.6	0.83	6.29	2.01	0.12	119.58
	P5	1	305.76	2.98	0.38	5.87	7.33	1.64	31.02	8.24	2.82	<0.01	156.71	<1.60	74.63	50.20	5.44	181.52	19.17	0.22	56.21
	Mean	2	202.51 ±146.02	1.89 ±1.55	0.21 ±0.24	6.12 ±0.35	4.81 ±3.57	1.57 ±0.10	15.71 ±21.65	4.18 ±5.74	1.92 ±1.27	<0.01	122.44 ±48.46	<1.60	52.30 ±31.58	30.50 ±27.86	3.13 ±3.26	93.91 ±123.91	10.59 ±12.13	0.17 ±0.07	87.90 ±44.81
type 4	P5	1	161.67	16.73	0.45	2.76	0.15	0.26	0.61	<0.01	0.12	<0.01	334.34	36.29	48.54	156.28	44.20	1.63	16.30	1.62	3.66

	PM	4	320.37 ±149.31	15.60 ±10.98	0.19 ±0.13	6.04 ±4.76	1.31 ±0.56	0.70 ±0.12	0.23 ±0.10	0.48 ±0.43	0.28 ±0.17	0.03 ±0.03	<46.6	6.15 ±2.38	68.95 ±58.48	51.35 ±54.35	67.72 ±21.10	170.72 ±248.44	3.97 ±1.15	0.41 ±0.30	4.65 ±1.03
	Mean	5	288.63 ±147.50	15.83 ±9.52	0.24 ±0.16	5.38 ±4.37	1.07 ±0.71	0.61 ±0.22	0.30 ±0.19	0.39 ±0.43	0.24 ±0.16	0.03 ±0.03	<46.6	12.18 ±13.64	64.87 ±51.46	72.34 ±66.47	63.02 ±21.08	136.90 ±228.06	6.43 ±5.60	0.65 ±0.60	5.65 ±1.03
type 5	P4	1	196.74	0.37	4.27	3.85	1.28	0.52	<0.09	1614.84	<0.03	0.02	<46.6	5.95	20.61	<21.6	62.42	13.58	2.55	0.40	3.15
type 6	P1	1	837.98	2.22	0.09	5.76	0.28	2.10	0.59	1.08	0.58	<0.01	<46.6	1.61	208.73	39.3	1.97	43.39	2.39	0.16	425.37
Mean all types		51	236.20 ±135.68	12.96 ±20.88	0.28 ±0.61	3.69 ±2.15	3.33 ±7.33	1.00 ±0.42	0.89 ±4.31	0.74 ±1.58	0.67 ±1.19	0.01 ±0.01	74.15 ±183.12	5.37 ±9.70	48.30 ±48.34	41.41 ±60.88	36.93 ±27.88	46.84 ±101.86	4.94 ±5.02	0.33 ±025	33.91 ±83.49

n - number of analyzed quartz grains. Mean values were calculated considering the mean value of the range for data above detection limit. LOD: Limit of detection

Table 5. Frequency of micro inclusions in quartz grains sorted by quartz type[a].

	Grouped profiles by age	n	Fd	m	Pb-m	Ru	Il	Sb	Zr	Fe-ox	Mo	Ca	Ap	Xe	Py	Gy
Type 1	Preholocenic (P1)	7	1[b]	4	4				1							
	Holocenic (P5)	2			1	1										
Type 2	Preholocenic (P2. P3)	13	6[c]	4	7				3	1	4	1	1	2		
	Holocenic (P4. P5. PM)	21	8[c]	7	14	1	2	1	6	1	3		1	1		
Type 3	Preholocenic (P1. P2)	4		1	2	3	1		1	1						
Type 4	Preholocenic (P1. P3)	3	1	3	3				1	1	1					
	Holocenic (P5. PM)	4	1[c]		2				1	2						1
Type 5	Preholocenic (P2)	4	2[c]			1	2		1	1						
	Holocenic (P5. PM)	2			1	1	1				1				1	
TOTAL		60	19	19	34	7	6	1	14	7	9	1	2	3	1	1

[a] Micro inclusion in type 6 grains have not been studied; [b] K-feldspar; [c] Albite and K-feldspar.

Abbreviations: n = number of analyzed quartz grains; Fd = feldspars; m = micas: biotite, muscovite or illite; Ru = rutile. Il = ilmenite; Sb = Sb-bearing mineral (unspecified); Zr = zircon; Fe-ox = iron(hydr)oxides: goethite, hematite or magnetite; Mo = monazite; Ca = Cassiterite; Ap = Apatite; Xe = xenotime; Py = pyrite; Gy = gypsum.

4.3. Quartz type 3: Strongly altered plutonic quartz

Type 3 represents a less abundant quartz population, comprising 19 (6%) out of 297 grains studied, although it is present in all samples (Table 2). This type comprises monocrystalline and mainly subangular-angular to subangular-rounded grains with a patchy CL (Figures 2 and 3f). The CL spectra show two emission bands at 500 and 650 nm, of which the 500 nm band is less pronounced. This grain population is interpreted as strongly altered plutonic quartz, which presumably originates from similar plutonic rocks as type 2, with the difference that the quartz was altered post-crystallisation by late magmatic or hydrothermal fluids.

Mineral inclusions are common and include rutile, mica, zircon, iron oxides and ilmenite (Table 5).

Two LA-ICP-MS analysis were performed only on this grain type. The grains are from samples P1 and P5. Both analyses differ considerably in their abundance of trace elements compared to other types (Table 4), with low Ti and exceptionally low Li.

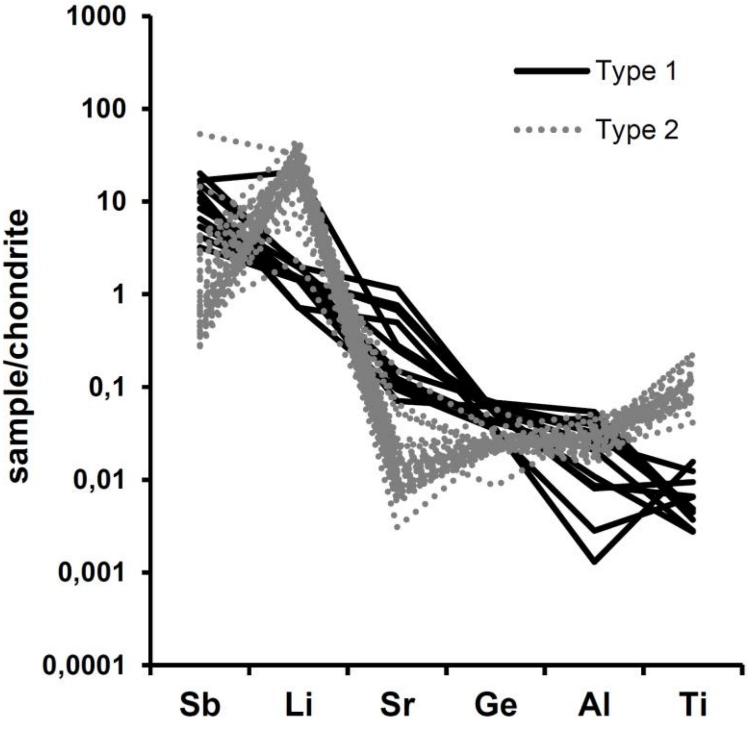

Figure 4. Spider diagram depicting some trace element contents detected in type 1 and type 2 quartz grains normalized to carbonaceous chondrite (McDonough and Sun, 1995).

4.4. Quartz type 4: Recrystallised (deformed) plutonic quartz

Type 4 quartz population comprises 28 (9%) out of 297 grains studied with SEM-CL. The group is characterised by polycrystalline clusters of recrystallised quartz grains, typical of quartz in deformed rocks. They have a heterogeneous morphology from subangular-angular to subangular-rounded grains. Frequently, they appear dark grey or black in panchromatic SEM-CL due to low CL intensities (Figure 2). The CL spectra show two bands at 430 and 650 nm, similar to spectra of type 2 grains. Micro inclusions are common and comprise mainly mica and subordinate feldspar, zircon, iron oxides, monazite and gypsum (or anhydrite) (Table 5). Based on the observations, this population is interpreted as recrystallised (deformed) plutonic quartz. However, gypsum inclusions in some grains indicate that the originally plutonic quartz grains were deposited in sediments after their deformation before they ended up in the river terraces.

The highest number of type 4 grains was found in sample PM, followed by Holocene and pre-Holocene soil samples (Table 2).

Five microanalyses of this type (from P5 and PM) show that the most abundant elements are Al (289 ± 148 ppm), K (65 ± 52 ppm) and Ti (63 ± 21 ppm). Once again, the high standard deviation values reflect the variability among grains. Some samples have elevated values of Na, Fe, P, and Ca (Table 4). The Li content is lower than in type 2 but higher than in the other types. Al and K contents are very well correlated ($R^2 = 0.895$), which indicates that substitutional is charge-compensated partially by K^+ ($Si^{4+} \rightarrow Al^{3+} + K^+$; e.g. Müller and Koch-Müller 2009). Another noticeable correlation is detected in the Al and Ti relationship ($R^2 = 0.817$).

4.5. Quartz type 5: Sandstone-derived quartz

Type 5 quartz grains comprise 20 (7%) out of 297 grains studied with CL (Table 2). Most type 5 grains (15) were identified in sample P2. Samples P1 and P3 do not contain this type. The grains are characterised either by clusters of well-rounded grains with variable CL cemented by non-luminescent authigenic quartz or by well-rounded single grains with remains of authigenic quartz overgrowths (Figures 2 and 3). Based on these observations, type 5 grains originate from sandstone or arkose. However, the variable CL of the “primary”, authigenic-quartz-embedded grains indicate different origins, such as metamorphic or plutonic rocks.

These grains show a diversity of mineral inclusions, including ilmenite, feldspar, zircon, rutile, monazite and pyrite (Table 5).

Microanalysis of type 5 (only of one grain from sample P4) show the following abundance: Al (197 ppm) >Ti (62 ppm) > K (21 ppm) (Table 4). The remaining elements have concentrations <20 ppm.

4.6. Quartz type 6: Hydrothermal quartz

The sixth grain type identified exhibits oscillatory growth zoning typical for hydrothermal quartz (Götze et al., 2001; Bernet and Basset, 2005; Sales de Oliveira et al., 2017; Figures 2 and 3). This quartz population is rare and comprised only 3 (1%) out of 297 grains (Table 2). The CL spectrum shows two emission bands, one high-intensity band at ~450 nm and a weak band at ~650 nm.

Due to their small grain size, trace element data were only acquired from one of the three grains. This grain has the highest Al of all quartz of 838 ppm studied, confirming the supposed hydrothermal origin of the grain (e.g. Rusk et al., 2008). The Al content is followed by K (209 ppm)>Fe (43 ppm)>Ca (39 ppm) (Table 4). Concentrations of the other elements are below 10 ppm. The high Ge content of 2.1 ppm is also characteristic of hydrothermal quartz (e.g. Götze et al., 2004).

5. Discussion

The provenance of the six types of quartz grains (previously defined and summarized in Table 6) and the approximate extension and change of the catchment area over time are discussed considering the following: 1) types of quartz, their relative abundance in the individual samples and change of the abundance over time; 2) micro inclusion inventory of quartz grains; 3) trace element content of the different quartz types, and 4) Ti content as an indicator of the quartz crystallisation temperature by applying the Ti-in-quartz geothermobarometer by Huang and Audétat (2012).

Table 6. Features of quartz grains types from the study area.

	Type 1	Type 2	Type 3	Type 4	Type 5	Type 6
Structure and morphology	monocrystalline and subangular-rounded	monocrystalline and subangular-angular (even very angular)	monocrystalline and subangular-angular to subangular-rounded	polycrystalline cluster of recrystallised quartz and subangular-angular to subangular-rounded	cluster of grains or well-rounded single grain	not applicable
CL appearance	homogeneous dull red-brown	bright, violet to blue	patchy	dark grey or black (panchromatic SEM-CL)	variable with non-luminescent authigenic quartz	oscillatory growth zoning
CL-SEM emission bands	650 nm	430 and 650 nm	500 and 650 nm	430 and 650 nm	variable	450 and 650 nm
Presence of fractures	thin, healed, brightly luminescent with mostly preferred orientation	randomly oriented, healed with non-luminescent quartz	not applicable	not applicable	not applicable	not applicable
Trace elements	abundant Al, Fe, K	abundant Al, Ti, Li	low Ti, Li	abundant Al, Ti, K	abundant Al, Ti, K	high Al, Ge
Al/Ti	1.6 to 375.1	1.6 to 11.6	56.2 to 119.6	3.7 to 5.9	3.15	425.4
Mineral micro inclusions	low variety	high variety	medium variety	medium variety	medium-high variety	
Lithological origin	metamorphic	undeformed plutonic	strongly altered plutonic	recrystallised (deformed) plutonic	sandstone-derived	hydrothermal
Provencance	Sierra Morena (Iberian Massif) and Sierra Nevada (Betic Cordilleras)	Los Pedroches batholith and associated plutons (Iberian Massif)	Los Pedroches batholith and associated plutons (Iberian Massif)	Los Pedroches batholith and associated plutons (Iberian Massif)	outcrops of Mesozoic and Cenozoic sandstones (Betic Cordilleras)	veins associated to Los Pedroches batholith and associated plutons (Iberian Massif)

5.1. Quartz types and provenance

First, we checked if the corresponding rocks of the identified genetic quartz types (plutonic, metamorphic, sedimentary and subvolcanic rocks) occur in the current and historic river catchment areas (Figure 1).

In today's catchment area, several plutons (Santa Elena and Linares) belonging to the Los Pedroches batholith are exposed (Figure 1b). Although the pluton exposures are relatively small compared to other rock types, they are close to the sampling area and, thus, most likely the protoliths of the most common quartz type of our study, type 2 and of the other plutonic quartz types 3 and 4. All three types appear in all samples studied.

Besides plutonic rocks, there are abundant metamorphic rocks in the catchment area, both in Sierra Morena (Iberian Massif) to the north and Sierra Nevada (Internal Betic Zone) to the south (Figure 1b). These rocks are most likely the source of our metamorphic quartz type 1. It is the second most common quartz type in our samples. Based on SEM-CL characteristics, type 1 grains are subdivided into two groups: grains of the pre-Holocene samples (P1 and P2) commonly exhibit quartz-healed, luminescent micro-fractures, whereas these fractures are rare or absent in the Holocene ones (P4, P5 and PM), which suggests type 1 grains originate presumably from two metamorphic sequences. This is supported by there being two large massifs of metamorphic rocks of different ages and metamorphic history in the catchment area: the Sierra Morena mountains (Variscan orogeny; peak metamorphic age ~380 Ma) to the north and the Sierra Nevada mountains (Alpine orogeny; peak metamorphic age 30-15 Ma) to the south. During the long-lasting and much older Variscan orogeny, quartz of the metamorphic rock was exposed to multiple events of deformation and fracturing compared to quartz in rocks formed during the younger Alpine orogeny. Based on the different geological histories, type 1 quartz grains with healed fractures most likely originate from Variscan rocks, whereas the more homogenous (in SEM-CL) type 1 grains are from Alpine rocks.

The pre-Holocene samples (P1 and P2) contain more type 1 grains with healed fractures (Variscan protoliths) than Holocene samples (P4, P5 and PM). In turn, Holocene samples have more homogenous type 1 grains (Alpine protoliths). This change of the subgroups abundance could be related to the increase of the catchment area between 500-240 ka ago (Demuro et al., 2015; García-Tortosa et al., 2019) when Guadiana Menor (a side stream of Guadalquivir River) drained the endorheic lake in the Guadix-Baza basin. According to the presence of these subgroups, this event that took place after P2 (300 ka) was formed, extended the catchment area to Sierra Nevada (Alpine orogeny) and, for the first time, material from there could be transported and deposited in P3, P4 and P5 formations and PM.

The sedimentary type 5 quartz, rare and not present in all samples, most likely originates from the numerous outcrops of Mesozoic and Cenozoic sandstones scattered in the catchment area (Figure 1b). It is, in fact surprising, that so few type 5 grains are preserved in the soils since sandstones are very common rocks in the centre of the catchment area. The primary origin of quartz grains constituting the eroded sandstones are both plutonic and metamorphic rocks.

The very distinctive type 6 grains originate from hydrothermal mineralisation. Abundant hydrothermal veins are associated with subvolcanic rocks of the Los Pedroches batholith and associated plutons. According to the classification of hydrothermal quartz by Rusk (2012) based on Ti and Al contents, type 6 quartz has Al and Ti values corresponding to epithermal and orogenic Au quartz.

There are differences in quartz grain populations among pre-Holocene samples (P1, P2 and P3): 1) P1 contains mostly metamorphic (type 1) and plutonic quartz of the strongly altered type (type 3); 2) in P2 mostly plutonic quartz (type 2) and 75% (15 out of 20 described) of the sandstone-derived quartz (type 5) were found; and 3) in P3 only plutonic quartz almost exclusively of the unaltered type (type 2) occurs. These differences could point to successive changes in the source area (P1 to P2, P2 to P3). The quartz population changes from P1 to P2 and P2 to P3 could be due to the increase of the catchment area, that took place between 500-240 ka (Demuro et al., 2015; García-Tortosa et al., 2019). Moreover, grains of easily erodible sandstone likely ended up in the soil during the initial stages of the extended catchment area. Later on, when the river had cut into the sandstone, quartz grains transported from further distances were deposited in the soils.

In contrast, the Holocene samples (P4, P5 and PM) are relatively similar in the abundance of quartz types. In all Holocene soils, undeformed plutonic quartz dominates (type 2). The source area appears stable throughout Holocene but is different from pre-Holocene times (change from P3 to P4).

5.2. Implications of mineral micro inclusions in quartz

Mineral micro inclusion species detected with SEM-EDX in quartz grains are typical minerals (Tables 3 and 5), described as rock-forming minerals in lithologies of the catchment area (Azcárate et al., 1977; Larrea et al., 2013). Thus, the micro inclusions identified in quartz can be used as an additional indicator of grain provenance. Most of the identified minerals (feldspar, mica, zircon, iron oxides, monazite, rutile, ilmenite, apatite, barite) were described as the fine sand fraction constituents of these same soil samples (Martín-García et al., 2020).

Considering the mineralogical variety of micro inclusions by quartz type (Table 5), type 2 (undeformed plutonic quartz) has the greatest diversity, followed by type 5 (sandstone-derived quartz). It is not only the diversity but also the type of inclusions that are similar. The similarity between type 2 and type 5 grains could be because the grain cluster forming the sandstone fragments consists predominantly of plutonic quartz (type 2). It is noteworthy that Holocene type 2 samples (P4, P5 and PM) have more micro inclusions than pre-Holocene ones (P2 and P3), which is another indication of the change of the source area.

The identified feldspar micro inclusions (found in 36% of the grains) were K-feldspar or albite. Anorthite, Ca-bearing feldspar, was not found. This indicates that the plutonic source rocks represent fractionated granitic rocks, which crystallised K-feldspar and Ca-free or -poor plagioclase (albite). Mica micro inclusions (found in 27% of the grains) are generally smaller (mean 29 µm) in P1 quartz compared to other samples (103 to 205 µm). Although the mica inclusion size has high standard deviation values (Table 3), this difference in mica inclusion size could indicate different protoliths and, thus, changes in the catchment area between the deposition of the P1 and P2 terraces, as outlined above.

5.3. Trace element contents in the quartz types

Another approach to reveal the provenance of quartz grains and their change over time is comparing the trace element content of quartz grains in soils of different ages with quartz trace element contents of rocks in the catchment area (Table 4). However, no quartz trace element data are available for rocks exposed in the catchment area. Gárate-Olave et al. (2017) performed the closest quartz trace element study on igneous rocks of the Variscan Nisa-Alburquerque batholith about 315 km northwest of the study zone. However, the general trace element signature of quartz formed in different geological environments are well-known and, thus, can be used to determine the general protolith formation setting of quartz grains (e.g. Schrön et al., 1988; Götze et al. 2004; Jacamon and Larsen, 2009; Müller and Koch-Müller, 2009; Rusk, 2012).

The low Al, Ti and Li contents in grains of type 1 confirm the metamorphic formation conditions of this grain population (e.g. Müller et al., 2007; Müller and Koch-Müller, 2009). The detected trace elements contents are similar, for example, to those of sand quartz grains from soils of Sierra Nevada (Martín-García et al., 2004, 2015). The grains found in the Sierra Nevada soils were interpreted as weathering products of the underlying metamorphic rocks. The similarities in the trace element contents again support our statement that type 1 grains are derived from metamorphic rocks. The Al/Ti ratio of type 1 grains is higher in P1 samples (range 77 – 376) compared to grains in samples P2, P4 and P5 (<26). Although there are few analyses, the low Al/Ti values of grains from P2, P4 and P5 are similar to those of the Sierra Nevada quartz described by Martín-García et al. (2015) (23 ± 35). Low Al/Ti ratios indicate high formation temperatures (as discussed below) and, thus, the grains in P1 and the Sierra Nevada originate from low- to medium-grade metamorphic rocks and grains in P2, P4 and P5 from high-grade metamorphic rocks. This, in turn, could point to a significant change in the catchment area between 600 ka (P1) and the other terraces (P2, P3, P4, P5 and PM). There are other differences between pre-Holocene and Holocene samples in type 1. In pre-Holocene samples, there are higher contents of Al and B (in most cases). In addition, Na is always below the detection limit (<46.6 ppm), and Ca usually as well (<21.6 ppm) (Table SM1). In

Holocene samples, however, concentrations of Na (frequently) and Ca (always) were above detection limits.

Concentrations of trace elements in type 2 grains are more homogeneous than type 1. However, differences between pre-Holocene and Holocene samples are observed for Na, Ca, Zn and Ga contents. Similar to type 1 grains, concentrations of Na in pre-Holocene samples are below the detection limit (<46.6 ppm) and that of Ca (<21.6 ppm) for the majority of results as well (Table 4). Trace element signature in type 2 agree with that of the quartz from Variscan granitic rocks in general (e.g. Müller et al. 2000, 2010; Breiter and Müller, 2009; Breiter et al. 2012, 2013, 2020). As mentioned above, Gárate-Olave et al. (2017) performed quartz trace element analyses on granitic rocks of the Variscan Nisa-Alburquerque batholith, the closest quartz chemistry study to our area. For comparison, our data of the igneous type 2 and type 3 grains were plotted with the data from the Nisa-Alburquerque batholith in the binary Al/Ti versus Ge/Ti plot (Figure 5). The chemistries of our type 2 and 3 grains are within the range of the Variscan samples studied by Gárate-Olave et al. (2017).

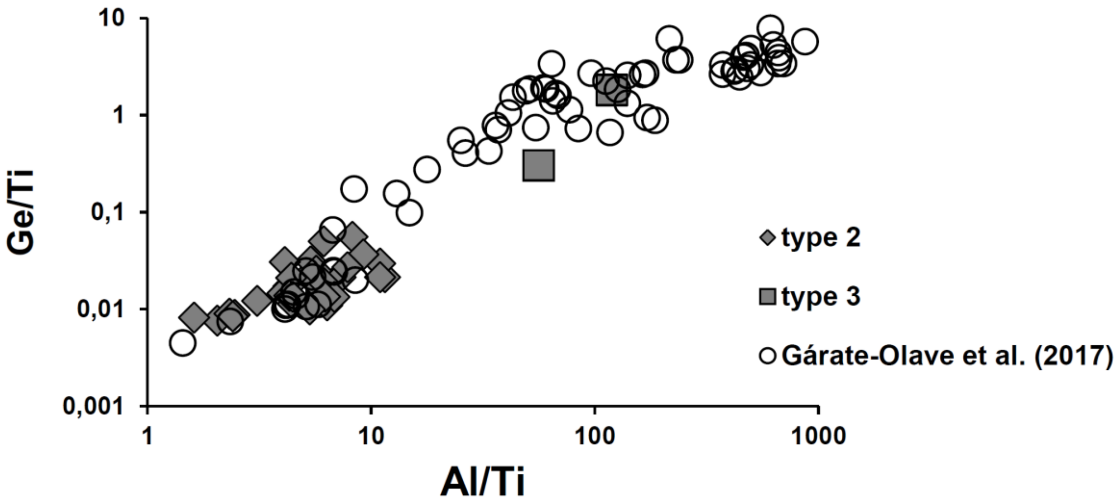

Figure 5. Binary Al/Ti versus Ge/Ti plot showing the chemical variation of the type 2 and type 3 quartz grains from soil samples compared to quartz chemistries of the Variscan Nisa-Alburquerque batholith (open circles).

According to Müller et al. (2002), Jacamon and Larsen (2009), and Breiter et al. (2013), increasing Al/Ti and Ge/Ti ratios in quartz indicate an increasing degree of fractionation of granitic magmas. Type 3 grains have significantly higher Al/Ti and Ge/Ti ratios than type 2 grains, indicating that the protolith of type 3 grains is a highly fractionated granite. The grains may even originate from pegmatite since ratios are in the range of the aplite-pegmatites of the Nisa-Alburquerque batholith (Gárate-Olave et al., 2017). That would also explain the strong alteration of type 3 grains: highly fractionated granites and pegmatites are enriched in volatiles, which react with and overprint already crystallised minerals during the late stage of melt crystallisation. The relative low Al/Ti and Ge/Ti ratios of type 3 grains indicate relative primitive granite compositions comparable to the monzogranites of the Nisa-Alburquerque batholith (Gárate-Olave et al., 2017).

The composite type 5 sandstone fragments contain plutonic and metamorphic quartz grains cemented by authigenic quartz. The Al/Ti ratio of the one analysed crystal is exceptionally low (~3), which suggest that the grain comes originally (before sandstone formation) from a chemical primitive pluton of the Iberian Massif pluton or high-grade metamorphic rocks of the Internal Betic Zones.

Based on the identified trace element correlations of type 1 grains in pre-Holocene (P1, P2, P3) and Holocene (P4, P5 and PM) samples, differences in trace element incorporation are observed (Figure SM1): the combined substitution of Al^{3+} + K^{+} for Si^{4+} seems to be the prevailing process in pre-Holocene grains ($R^2 = 0.535$; $n = 6$) whereas the Al^{3+} + Li^{+} substitution for Si^{4+} is the dominant one for the Al^{3+} defect charge compensation in Holocene grains ($R^2 = 0.967$, $n = 4$). This conclusion bases on the observed correlation between Al and K, and Al and Li, respectively.

Figure 6 shows the compositional differences between the different grain types and confirms their genetic attributions. In the ternary Ti - 10*Ge - Al/50 plot, according to Schrön et al. (1988), type 2 grains (undeformed plutonic quartz) show a relative homogenous composition dominated by the Ti content. According to the Ti - 10*Ge - Al/50 discrimination, the type 2 grains originate from granites of primitive chemical (little fractionated) composition. The Al-Ge-Ti chemistries of type 4 (recrystallised plutonic quartz) and 5 (sandstone quartz) grains are in the same range as type 2 grains, which confirms, first, that type 4 grains were of plutonic origin before deformation and, second, that the one analysed type 5 grain from the sandstone fragment is also of plutonic origin. Type 1 (metamorphic quartz), 3 (strongly altered plutonic quartz) and 6 (hydrothermal quartz) grains plot close to the 10*Ge corner, indicating either that the grains originate from highly fractionated granitic rocks or hydrothermal mineralisation (e.g. Müller et al., 2018; Breiter et al., 2020).

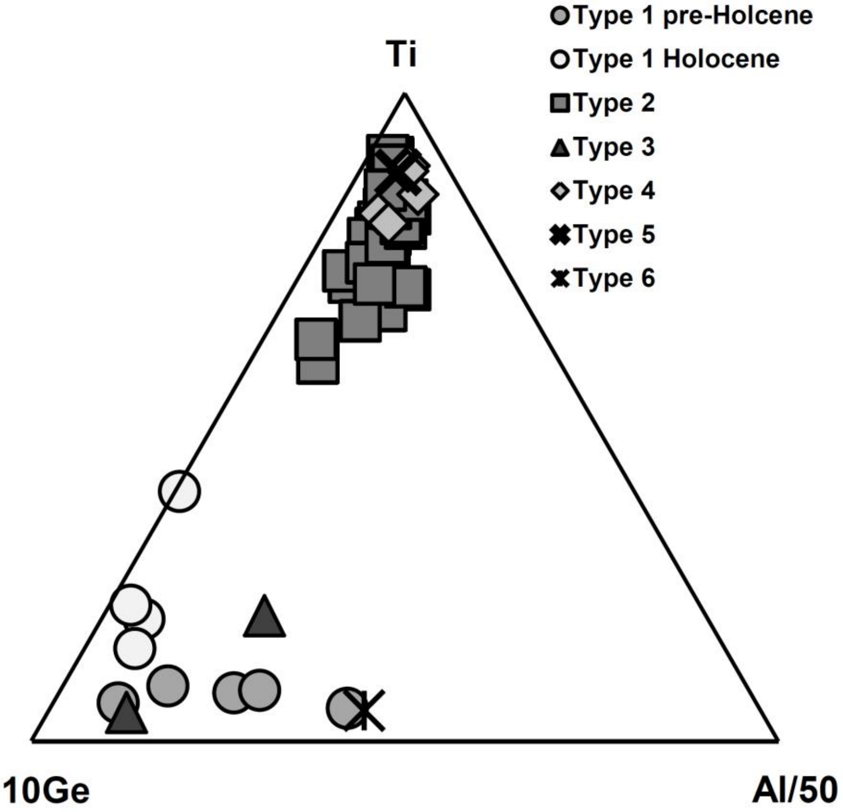

Figure 6. Ternary Ti - 10*Ge - Al/50 plot according to Schrön et al. (1988) for trace elements in quartz showing the chemical variation of type 1 to 6 grains from sand fraction of soils.

5.4. Ti content in quartz as a geothermobarometer

Huang and Audétat (2012) modified the original Ti-in-quartz geothermometer by Wark and Watson (2006) to the TitaniQ geothermobarometer. The adjustment was based on the observation that the incorporation of Ti in the quartz lattice is controlled by temperature and, to a minor extent, by pressure. Thus, to calculate quartz crystallisation temperature, the approximate formation pressure and the Ti saturation of the fluid or melt from which the quartz crystallised must be known. In the catchment area, rock pressure and temperature conditions are highly variable. The metamorphic rocks of the Variscan Iberian Massif underwent multiple regional metamorphisms ranging from low (<2 kbar and 190-360 ºC; Aparicio et al., 1997) to medium grades (green schist facies, 3.5-4 kbar and 350-400 ºC; Larrea et al., 2013). Contact metamorphism occurred in the vicinity of the Los Pedroches batholith and its associated plutons (Linares and Santa Elena) with recorded pressures of <3 kbar and temperatures of 700 ºC (Larrea, 1998). However, compared to the regional metamorphic rocks, the contact metamorphic rocks are exposed in small areas only. Igneous rocks of the Variscan Los Pedroches batholith were generated at 3 kbar and <750 ºC, and associated subvolcanic rocks formed at <3 kbar and <750 ºC (Larrea, 1998; Larrea et al., 2013). Metamorphic rocks of the Internal Zone of the Betic Cordilleras underwent medium-grade regional metamorphism with pressures of 3-9 kbar and temperatures of 430-540 ºC for the Veleta Unit and 3.5-10 kbar and 480-630 ºC for the Mulhacen Unit (Puga et al., 2007).

Subsequently, the known approximate pressures were applied to calculate the minimum crystallisation temperature of the analysed quartz grains using the equation of Huang and Audétat (2012). The resulting values are minimum crystallisation temperatures because the Ti saturation of the quartz-forming melts and fluids are unknown.

Type 1 quartz grains originate from metamorphic rocks either from the Iberian Massif with formation pressures between 3.5 and 4 kbar or from the Betic Cordilleras with pressure from 3 to 10 kbar. As suggested above, type 1 quartz in sample P1 is from the Iberian Massif while those from P2, P4 and P5 samples from both the Iberian Massif and Betic Cordilleras. This statement is supported by the findings of Demuro et al. (2015) and García-Tortosa et al. (2019), who suggested that the Internal Betic Zone that became the sediment source area about 500-240 ka ago caused a change in the grain population of samples P2, P4 and P5. The calculated formation temperatures of the type 1 grains in P1 are generally lower (404 - 454 ºC) than those of type 1 grains in P2, P4 and P5 (452 - 791 ºC) (Figure 7). The calculated formation temperatures of all type 1 quartz are higher than the temperatures of the regional metamorphism of the Variscan rocks but agree with the metamorphic temperatures of the Betic Cordilleras rocks (Internal Zone; Puga et al., 2007). It is unlikely that the high-temperature type 1 quartz originated from Variscan contact metamorphic because these rocks occur in small outcrops only. The high crystallisation temperature of type 1 grain of sample P2 (791 ºC) suggests this particular grain originates from a plutonic rock and not from metamorphic rock, as the SEM-CL observations imply.

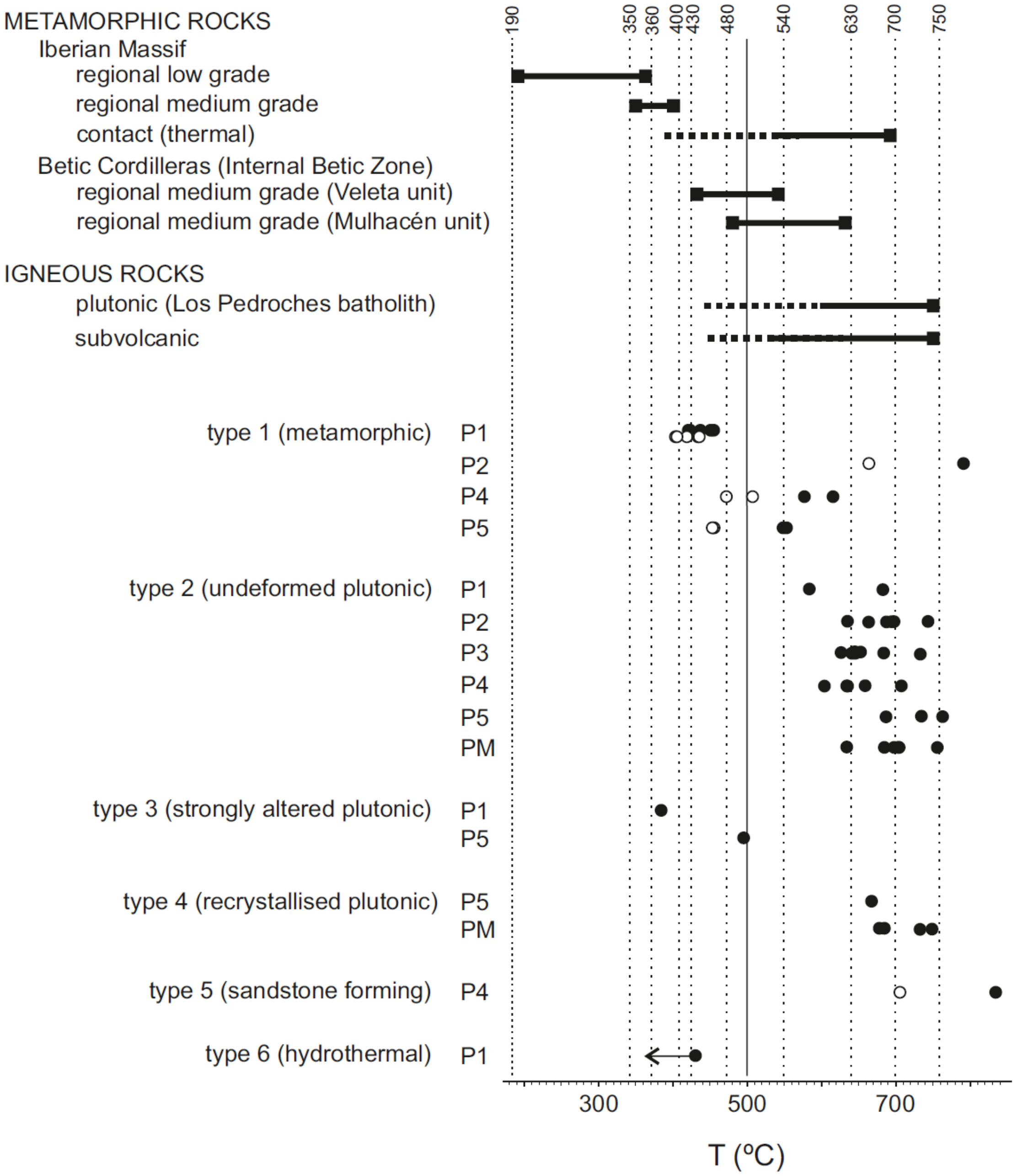

Figure 7. Calculated minimum crystallization temperatures of analysed quartz grains in soil samples according to the TitaniQ thermobarometer for quartz. For comparison, literature data of formation temperatures of metamorphic and igneous rocks of the Variscan Iberian Massif and the Alpine Betic Cordilleras located in the catchment area of the Guadalquivir River are provided. Open circles are values applying the minimum pressure scenario and black circles the maximum pressure scenario.

Crystallisation temperatures of type 2 grains (plutonic quartz) are between 585 and 761 ºC, which is, in general, the crystallisation range of granitic magmas. Larrea et al. (2013) stated that the crystallisation temperature of the Los Pedroches batholith was in the range of 700 to 750 ºC. These temperatures are consistent with our type 2 crystallisation temperatures considering that the calculated values are minimum temperatures.

Temperatures calculated for type 3 grains (strongly altered plutonic quartz) are 384 to 494 ºC. The low temperatures imply that the quartz alteration, presumably hydrothermal alteration, caused a release of Ti from the quartz lattice. Lillo (1992), for example, described widespread hydrothermal alteration affecting the granodiorites of the Santa Elena pluton (Los Pedroches batholith).

Type 4 grains (recrystallised plutonic quartz) have crystallisation temperatures between 668 and 748 ºC, which is in the range of the solidus temperature of granitic rocks. Thus, the deformation did not affect the quartz's Ti content, implying that type 4 quartz was exposed to low-temperature shear stress rather than regional medium- or high-grade metamorphism.

The plutonic crystal of the type 5 sandstone fragment had a crystallisation temperature of 705 ºC (assuming about 3 kbar for magma crystallisation), confirming the igneous nature of the grain.

The hydrothermal type 6 quartz was formed at 431 ºC, which is compatible with formation temperatures of granite-related magmatic-hydrothermal mineralisation commonly found in the Variscan plutons of the southern Iberian Massif (e.g. Chicharro et al., 2016).

5.5. Quartz in soil chronosequence

In a soil chronosequence, which is defined as a series of genetically related soils that evolve under similar conditions of vegetation, parent rock, topography and climate (Harden, 1982), both soil properties and constituents can be statistically related to the soil age, and thus constitute chronofunctions. The samples used in this study belong to a genuine soils chronosequence where chronofunctions have been established using morphological, analytical and compositional properties (Calero et al., 2008, 2009, 2013; Martín-García et al., 2016, 2020).

However, using the sand fraction (500-2000 µm) of the same soils in this study, no chronofunctions have been detected for the quartz trace elements compositions or the quartz type abundance, except for the abundance of type 4 per profile ($R^2 = 0.864$). Nevertheless, differences are observed in pre-Holocene and Holocene samples, mainly due to changes in the source area rather than soil-forming processes.

Martín-García et al. (2015) found in the fine sand of soil from Sierra Nevada (Guadalquivir catchment) a relative enrichment in trace elements by comparing the edges of grains with their centres attributed to the pedological evolution. These authors demonstrated an increase in the content of trace elements on the edge of the quartz grain following the evolutionary sequence of the soil: parent rock < Entisol < Inceptisol < Alfisol; this was corroborated by the SEM study of the surface of these grains (W of Marcelino et al., 1999) in which signs of alteration increased with the evolution of the soil. However, the absence of these differences in this study could be due to: 1) different fractions were used to carry out the study: fine sand (Martín-García et al., 2004, 2015) *vs* coarse sand (this study); 2) fine sand is a granulometric fraction more weathered than coarse sand (similar to parent rock); 3) different methods of study and equipment were used: in the fine sand studied by Martín-García et al. (2004, 2015), the centre and edge of quartz grains were analysed with EMPA with an analytical spot of about 10 µm, while in this study, only the centres of quartz grains were analysed by LA-ICP-MS, applying a raster ablation of about 150x100 µm. However, the SEM-CL research of our study shows that there are no differences in CL between the core and the crystal rim, suggesting that the trace element contents are more or less consistent across the grain (e.g. Götze et al., 2001).

Concluding, the compositional changes of the surface of fine sand-sized quartz grains observed by Martín-García et al. (2004, 2015) is related to surface alteration processes related to the soil formation, while the analysis of the composition of the interior of coarse sand quartz grains (this study) and SEM-CL analysis, allows obtaining information about the lithological origin and infer their source area.

6. Conclusions

Based on SEM-CL characteristics, micro inclusion inventory and trace element contents of quartz grains from soil sand fraction of Guadalquivir River terraces, six types of grains have been distinguished: metamorphic quartz (type 1), undeformed granitic quartz (type 2), strongly altered granitic quartz (type 3), recrystallised (deformed) granitic quartz (type 4), sandstone quartz (type 5) and hydrothermal quartz (type 6).

The major quartz grain types (76% of the grains) are undeformed granitic quartz (type 2) and metamorphic quartz (type 1). All quartz grains of granitic origin (types 2, 3 and 4) are interpreted to come from the Los Pedroches batholith and its associated plutons (Santa Elena and Linares plutons). Metamorphic quartz grains (type 1) have two possible sources: Sierra Morena (Iberian Massif) to the north or Sierra Nevada (Betic Cordilleras) to the south. The metamorphic quartz grains of terrace P1 originate exclusively from the Iberian Massif. Grains of the younger P4 and P5 terraces come from both source areas. However, the origin of P2 grains is dubious due to the uncertainty about when the extension of the catchment area took place. The sandstone-derived quartz grains (type 5) most likely originate from the numerous outcrops of Mesozoic and Cenozoic sandstones scattered in the central catchment area. The sandstone-derived grains comprise quartz crystals, the primary origin of those are both granitic and metamorphic rocks. Hydrothermal quartz grains (type 6) come from hydrothermal quartz veins associated with subvolcanic rocks of the Los Pedroches batholith.

The quartz type contents in pre-Holocene soils (P1, P2 and P3) are more variable than in Holocene soils (P4 and P5), which are more homogeneous. This difference could be attributed to changes in the source area over time, which affected the materials that form the soils.

Our study shows that the characterisation of quartz grains by applying SEM-CL, SEM-EDX and LA-ICP-MS is an effective methodological approach to characterise the provenance of quartz grains in the sand fraction of soils and substantially improves the knowledge of the sedimentological history of the Guadalquivir River terraces.

Acknowledgements

This work was supported by a grant from the Ministerio de Economía, Industria y Competitividad de España ("Mediterranean Soil Typologies versus Quartz. At the frontier of pedogenic knowledge"; Ref. CGL2016-80308-P). Alberto Molinero-García acknowledges the PhD funding (BES-2017-080078) provided by MCIN/AEI /10.13039/501100011033 and FSE "El FSE invierte en tu futuro". This work is part of the Doctoral Dissertation of Alberto Molinero-García. We thank Dr. Mathieu Duval and an anonymous reviewer for their constructive criticism of the script and their valuable suggestions. We also acknowledge Tanya Shew for English proofreading. Funding for open access charge: Universidad de Granada / CBUA.

References

Ackerson, M.R., Tailby, N.D., Watson, E. B., 2015. Trace elements in quartz shed light on sediment provenance. Geochem. Geophys. Geosyst. 16 (6), 1894–1904.

Aparicio, A., García, R., Brell, J.M., 1997. El metamorfismo de bajo y muy bajo grado de los materiales carboníferos del área hercinica de Sierra Morena. Boletín geológico y minero 108 (2), 171–184.

Azcárate, J.E., Esnaola, J.M., Maldonado, M., del Pan T., Perconig, E., Moreno, E., Argüelles, A., Martínez, J.U., Fernández, Luanco, M.C., Solar, J.B., 1977. Mapa geológico y memoria de la hoja nº 905 (Linares). Mapa Geológico de España E. 1:50.000 (MAGNA). Segunda Serie, Primera edición. IGME. Depósito Legal: M-18.924 -1977.

Bambauer, H.U., 1961. Spurenelementgehalte und γ-Farbzentren in Quarzen aus Zerrklüften der Schweizer Alpen. Schweizerische Mineralogische und Petrographische Mitteilungen 41, 335–369.

Bernet, M., Bassett, K., 2005. Provenance analysis by single-quartz-grain SEM-CL/optical microscopy. J. Sediment. Res. 75 (3), 492–500.

Blatt, H., Middleton, G.V., Murray, R.C., 1980. Origin of Sedimentary Rocks. Prentice-Hall, Inc., Englewood Cliffs, NJ.

Breiter, K., Müller, A., 2009. Evolution of rare-metal granitic magmas documented by quartz chemistry. Eur. J. Mineral. 21, 335–346.

Breiter, K., Svojtka, M., Ackerman, L., Švecová, K., 2012. Trace element composition of quartz from the Variscan Teplice caldera (Krušné Hory/Erzgebirge Mts., Czech Republic/Germany): insights into the volcano-plutonic complex evolution. Chemical Geology 326–327, 36–50.

Breiter, K., Ackerman, L., Svojtka, M., Müller, A., 2013. Behavior of trace elements in quartz from plutons of different geochemical signature: A case study from the Bohemian Massif, Czech Republic. Lithos 175, 54-67.

Breiter, K., Ďurišová, J., Dosbaba, M., 2020. Chemical signature of quartz from S- and A-type rare-metal granites – A summary. Ore Geol. Rev. 125, 103674.

Calero, J., Delgado, R., Delgado, G., Martín-García, J.M., 2008. Transformation of categorical field soil morphological properties into numerical properties for the study of chronosequences. Geoderma, 145 (3-4), 278-287.

Calero, J., Delgado, R., Delgado, G., Martín-García, J.M., 2009. SEM image analysis in the study of a soil chronosequence on fluvial terraces of the middle Guadalquivir (southern Spain). Eur. J. Soil Sci. 60 (3), 465-480.

Calero, J., Martín-García, J.M., Delgado, G., Aranda, V., Delgado, R., 2013. A nano-scale study in a soil chronosequence from southern Spain. Eur. J. Soil Sci. 64 (2), 192-209.

Chicharro, E., Boiron, M.C., López-García, J.Á., Barfod, D.N., Villaseca, C., 2016. Origin, ore forming fluid evolution and timing of the Logrosán Sn–(W) ore deposits (Central Iberian Zone, Spain). Ore Geol. Rev. 72, 896-913.

Demuro, M., Arnold, L.J., Parés, J.M., Sala, R., 2015. Extended-range luminescence chronologies suggest potentially complex bone accumulation histories at the Early-to-Middle Pleistocene palaeontological site of Huéscar-1 (Guadix-Baza basin, Spain). Quat. Int. 389, 191-212.

Drees, L.R., Wilding, L.P., Smeck, N.E., Senkayi, A.L., 1989. Silica in soils: quartz and disordered silica polymorphs. In: Dixon, J.B., Weed, S.B. (Eds) Minerals in Soil Environments. Soil Science Society of America, Madison, WI. pp. 913–965.

Gárate-Olave, I., Müller, A., Roda-Robles, E., Gil-Crespo, P.P., Pesquera, A., 2017. Extreme fractionation in a granite–pegmatite system documented by quartz chemistry: The case study of Tres Arroyos (Central Iberian Zone, Spain). Lithos 286, 162-174.

García-Tortosa, F.J., García, P.A., Giralt, S., Medina, I., Herrera, A.A., Rojas, I.M., 2019. Edad de la captura de la cuenca de Guadix-Baza. In XV Reunión Nacional de Cuaternario Bizkaia Aretoa-Bilbao, 1-5 julio 2019 libro de resúmenes (pp. 273-276). Universidad del País Vasco/Euskal Herriko Unibertsitatea.

Götze, J., 2009. Chemistry, textures and physical properties of quartz – geological interpretation and technical application. Mineral. Mag. 73, 645–671.

Götze, J., 2012. Mineralogy, geochemistry and cathodoluminescence of authigenic quartz from different sedimentary rocks. In Götze, J., Möckel, R. (Eds.), Quartz: Deposits, Mineralogy and Analytics. Springer, Berlin, Heidelberg. pp. 287–306.

Götze, J., Plötze, M., Habermann, D., 2001. Origin, spectral characteristics and practical applications of the cathodoluminescence (CL) of quartz–a review. Mineral. Petrol. 71 (3–4), 225-250.

Götze, J., Plötze, M., Graupner, T., Hallbauer, D.K., Bray, C.J., 2004. Trace element incorporation into quartz: a combined study by ICP-MS, electron spin resonance, cathodoluminescence, capillary ion analysis, and gas chromatography. Geochim. Cosmochim. Acta 68 (18), 3741–3759.

Harden, J.W., 1982. A quantitative index of soil development from field descriptions: examples for a chronosecuence in central California. Geoderma 28, 1–28.

Huang, R., Audétat, A., 2012. The titanium-in-quartz (TitaniQ) thermobarometer: a critical examination and re-calibration. Geochim. Cosmochim. Acta 84, 75–89.

IUSS Working Group WRB. 2015. World Reference Base for Soil Resources 2014, update 2015 International soil classification system for naming soils and creating legends for soil maps. World Soil Resources Reports No. 106. FAO, Rome.

Jacamon, F., Larsen, R., 2009. Trace element evolution of quartz in the charnockitic Kleivan granite, SW-Norway: the Ge/Ti ratio of quartz as an index of igneous differentiation. Lithos 107, 281–291.

Jochum, K.P., Weis, U., Stoll, B., Kuzmin, D., Yang, Q., Raczek, I., Jacob, D.E., Stracke, A., Birbaum, K., Frick, D.A., Günther, D., Enzweiler, J., 2011. Determination of reference values for NIST SRM 610-617 glasses following ISO guidelines: Geostand. Geoanalyt. Res. 35, 397–429.

Kats, A., 1962. Hydrogen in alpha quartz. Philips Research Reports, 17, 133–279.

Larrea, F. J., 1998. Caracterización petrológica y geoquímica del sector oriental del batolito de Los Pedroches. Tesis Doctoral, Universidad del Pais Vasco.

Larrea, F.J., Santisteban, J.I., Cueto, L.A., Quesada, C., Fernández, F.J., Martín-Serrano, Á., La Moneda, E., Bea Barredo, F., González, A., Matas, J., Martín, L.M., Vallejo, J., López, M.A., 2013. Mapa geológico y memoria de la hoja nº 904 (Andújar). Mapa Geológico de España E. 1:50.000 (MAGNA). Segunda Serie, Primera edición. IGME. Depósito legal: M–34940–2013.

Larsen, R.B., Polvè, M., Juve, G., 2000. Granite pegmatite quartz from Evje-Iveland: Trace element chemistry and implications for the formation of high-purity quartz: Norges Geologiske Undersøkelse Bulletin 436, 57–65.

Lillo-Ramos, F.J., 1992. Geology and geochemistry of Linares-La Carolina Pb-ore field (Southeastern border of the Hesperian Massif). Doctoral dissertation, University of Leeds.

Mahaney, W.C., 2002. Atlas of Sand Grain Surface Textures and Applications. Oxford University Press. Oxford, UK.

Marcelino, V., Mussche, G., Stoops, G., 1999. Surface morphology of quartz grains from tropical soils and its significance for assessing soil weathering. Eur. J. Soil Sci. 50, 1–8.

Martín-García, J.M., Aranda, V., Gámiz, E., Bech, J., Delgado, R., 2004. Are mediterranean mountains entisols weakly developed? The case of orthents from Sierra Nevada (southern Spain). Geoderma 118 (1–2), 115–131.

Martín-García, J.M., Márquez, R., Delgado, G., Sánchez-Marañón, M., Delgado, R., 2015. Relationships between quartz weathering and soil type (Entisol, Inceptisol and Alfisol) in Sierra Nevada (southeast Spain). Eur. J. Soil Sci. 66 (1), 179–193.

Martín-García, J.M., Molinero-García, A., Calero, J., Sánchez-Marañón, M., Fernández-González, M.V., & Delgado, R., 2020. Pedogenic information from fine sand: A study in Mediterranean soils. Eur. J. Soil Sci. 71(4), 580–597.

Martín-García, J.M., Sánchez-Marañón, M., Calero, J., Aranda, V., Delgado, G., Delgado, R., 2016. Iron oxides and rare earth elements in the clay fractions of a soil chronosequence in southern Spain. Eur. J. Soil Sci. 67 (6), 749–762.

McDonough, W.F., Sun, S., 1995. The composition of the Earth. Chemical Geology 120, 223–253.

Müller, A., 2000. Cathodoluminescence and characterisation of defect structures in quartz with applications to the study of granitic rocks (Doctoral dissertation, Niedersächsische Staats-und Universitätsbibliothek Göttingen).

Müller, A., Seltmann, R., Behr, H.J., 2000. Application of cathodoluminescence to magmatic quartz in a tin granite – case study from the Schellerhau Granite Complex. Miner. Depos. 35, 169–189.

Müller, A., Wiedenbeck, M., van den Kerkhof, A.M., Kronz, A., Simon, K., 2003. Trace elements in quartz – a combined electron microprobe, secondary ion mass spectrometry, laser-ablation ICP-MS, and cathodoluminescence study. Eur. J. Mineral. 15, 747–763.

Müller, A., Ihlen, P.M., Wanvik, J.E., Flem, B., 2007. High-purity quartz mineralisation in kyanite quartzites, Norway. Miner. Depos. 42, 523–535.

Müller, A., Koch-Müller, M., 2009. Hydrogen speciation and trace element contents of igneous, hydrothermal and metamorphic quartz from Norway. Mineral. Mag. 73, 569–584.

Müller, A., Wiedenbeck, M., Flem, B., Schiellerup, H., 2008. Refinement of phosphorus determination in quartz by LA-ICP-MS through defining new reference material values: Geostand. Geoanalyt. Res. 32, 361–376.

Müller, A, Herrington, R., Armstrong, R., Seltmann, R., Kirwin, D.J., Stenina, N.G., Kronz, A., 2010. Trace elements and cathodoluminescence of quartz in stockwork veins of Mongolian porphyry-style deposits. Miner. Depos. 45, 707–727.

Müller, A., Kronz, A., Breiter, K., 2002. Trace elements and growth patterns in quartz: a fingerprint of the evolution of the subvolcanic Podlesí Granite System (Krušné hory Mts., Czech Republic). Bull. Czech Geol. Surv. 77, 135–145.

Müller, A., Knies, J., 2013. Trace elements and cathodoluminescence of detrital quartz in Arctic marine sediments–a new ice-rafted debris provenance proxy. Clim. Past 9 (6), 2615–2630.

Müller, A., Herklotz, G., Giegling, H., 2018. Chemistry of quartz related to the Zinnwald/Cínovec Sn-W-Li greisen-type deposit, Eastern Erzgebirge, Germany. J. Geochem. Explor. 190, 357–373.

Ortiz, J.E., Torres, T., Llamas, J.F., Canoira, L., García-Alonso, P., García de la Morena, M.A., Lucini, M., 2000. Dataciones de algunos yacimientos paleontológicos de la cuenca de Guadix-Baza (sector de Cúllar-Baza, Granada, España) y primera estimación de edad de la apertura de la cuenca mediante el método de racemización de aminoácidos. Geogaceta 28, 109–112.

Perny, B., Eberhardt, P., Ramseyer, K., Mullis, J., Pankrath, R., 1992. Microdistribution of Al, Li, and Na in α quartz: Possible causes and correlation with short-lived cathodoluminescence. Am. Mineral. 77, 534–544.

Puga, E., de Federico, A.D., Nieto, J.M., Puga, M.D., 2007. Petrología, evolución geodinámica y georrecursos del Espacio Natural de Sierra Nevada. Estud. Geol. 63 (2), 19–40.

Ramseyer, K., Mullis, J., 1990. Factors influencing short-lived blue cathodoluminescence of alpha-quartz. Am. Mineral. 75 (7-8), 791–800.

Richter, D.K., Götte, T., Götze, J., Neuser, R.D., 2003. Progress in application of cathodoluminescence (CL) in sedimentary geology. Mineral. Petrol. 79, 127–166.

Rimstidt, J.D., 1997. Quartz solubility at low temperatures. Geochim. Cosmochim. Acta 61, 2553– 2558.

Rottier, B., Rezeau, H., Casanova, V., Kouzmanov, K., Moritz, R., Schlöglova, K., Wälle, M., Fontboté, L., 2017. Trace element diffusion and incorporation in quartz during heating experiments. Contrib. to Mineral. Petrol., 172 (4), 23.

Rusk, B.G., Lowers, H.A., Reed, M.H., 2008. Trace elements in hydrothermal quartz: Relationships to cathodoluminescent textures and insights into vein formation. Geology 36, 547–550.

Rusk, B., 2012. Cathodoluminescent Textures and Trace Elements in Hydrothermal Quartz. In: Götze J., Möckel R. (Eds), Quartz: Deposits, Mineralogy and Analytics. Springer Geology. Springer, Berlin, Heidelberg, pp. 307–329.

Sales de Oliveira, C.E., Pe-Piper, G., Piper, D.J., Zhang, Y., Corney, R., 2017. Integrated methodology for determining provenance of detrital quartz using optical petrographic microscopy and cathodoluminescence (CL) properties. Mar. Pet. Geol. 88, 41–53.

Schrön, W., Schmädicke, E., Thomas, R., Schmidt, W., 1988. Geochemische Untersuchungen an Pegmatitquarzen. Zeitschrift für Geologische Wissenschaften 16, 229–244.

Stalder, R., Potrafke, A., Billström, K., Skogby, H., Meinhold, G., Gögele, C., Berberich, T., 2017. OH defects in quartz as monitor for igneous, metamorphic, and sedimentary processes. Am. Mineral. 102, 1832–1842.

Wark, D.A., Watson, E.B., 2006. TitaniQ: a titanium-in-quartz geothermometer. Contrib. to Mineral. Petrol. 152 (6), 743–754.

Weil, J.A., 1984. A review of electron spin spectroscopy and its application to the study of paramagnetic defects in crystalline quartz. Phys. Chem. Miner. 10, 149–165.

Weil, J.A., 1993. A review of the EPR spectroscopy of the point defects in α-quartz: the decade 1982-1992. In: Helms, C.R., Deal, B.E. (Eds), Physics and Chemsitry of SiO2 and the Si-SiO interface 2. Plenum Press, New York, pp. 131-144.

Supplementary material

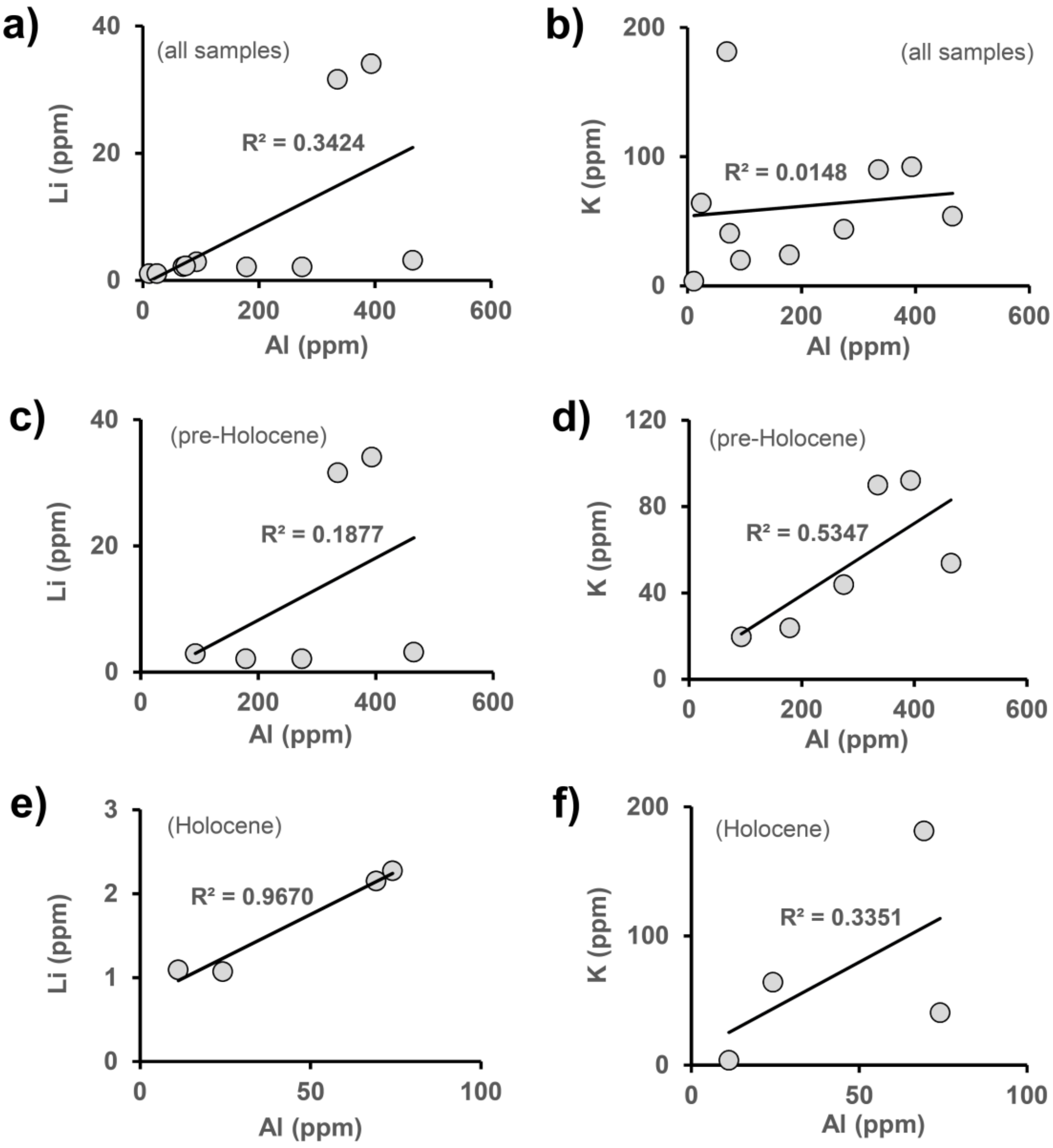

Figure SM1. Al vs Li and Al vs K plots in all samples (a and b), pre-Holocene samples (c and d) and Holocene samples (e and f).

Table SM1. Trace elements contents (ppm) in of LA-ICP-MS analysis of individual quartz grains (LA-ICP-MS) from coarse sand. Outstanding concentration spikes of Na (>46.6 ppm), Fe (>60 ppm), Ca (>21.6 ppm), P (>10 ppm) and Sr (>5 ppm) and caused by micro fluid or mineral inclusion.

Quartz type	Profile	Quartz grain	Al	Li	Be	B	Mn	Ge	Rb	Sr	Sb	U	Na	P	K	Ca	Ti	Fe	Zn	Ga	Al/Ti
1	P1	QAG04-015	335.37	31.60	0.19	4.53	0.91	1.93	0.60	2.05	2.37	<0.01	<46.6	<1.60	89.96	23.6	2.15	14.71	4.53	0.23	155.99
		QAG04-042	92.97	2.92	0.11	3.82	1.60	1.68	0.10	1.82	1.17	<0.01	<46.6	<1.60	19.72	<21.6	1.21	0.99	<1.42	0.07	76.83
		QAG04-057	465.10	3.17	0.16	4.06	0.38	1.28	0.17	0.79	2.13	<0.01	<46.6	<1.60	53.86	<21.6	1.24	1.40	1.95	0.11	375.08
		QAG04-131	178.90	2.12	0.13	3.03	1.21	1.88	0.73	0.51	0.92	0.01	<46.6	<1.60	23.87	<21.6	2.13	61.43	1.70	0.13	83.99
		QAG04-151	274.61	2.12	<0.08	2.31	0.46	1.32	0.37	0.89	0.45	<0.01	<46.6	7.26	43.83	22.4	1.63	107.72	2.34	0.13	168.47
	P2	QAG10-054	393.68	34.05	0.20	5.33	1.21	1.05	0.39	0.12	1.17	<0.01	<46.6	3.86	92.08	<21.6	42.47	445.93	9.24	0.32	9.27
	P4	QAG24-080	69.28	2.15	<0.08	2.49	4.43	1.64	0.16	5.52	1.40	0.01	1189.85	3.69	181.20	375.0	4.15	44.67	15.47	0.29	16.69
		QAG24-161	11.19	1.09	0.01	1.67	29.90	1.07	0.03	0.68	1.75	0.04	<46.6	13.89	3.56	54.7	6.86	4.17	7.02	0.57	1.63
	P5	QAG29-009	74.08	2.27	<0.08	1.66	5.75	1.57	0.15	4.89	0.75	0.01	<46.6	2.34	40.59	101.3	2.89	24.55	5.80	0.09	25.63
		QAG29-093	24.30	1.07	0.14	2.14	44.72	1.03	0.88	3.61	1.51	<0.01	287.75	<1.60	64.00	71.0	2.86	244.84	27.10	0.12	8.50
2	P1	QAG04-074	217.26	35.66	0.26	3.12	0.47	0.87	0.06	0.05	0.06	<0.01	<46.6	<1.60	6.40	<21.6	50.85	4.11	<1.42	0.13	4.27
		QAG04-178	150.37	6.77	0.08	4.84	1.34	1.01	0.44	1.09	2.02	<0.01	<46.6	<1.60	41.03	26.5	18.21	23.91	2.30	0.11	8.26
	P2	QAG10-023	176.27	31.63	0.26	3.78	1.18	0.65	0.21	0.48	0.53	0.01	<46.6	1.85	50.61	<21.6	85.90	31.64	6.16	0.47	2.05
		QAG10-030	190.08	35.00	0.18	4.85	1.36	0.78	<0.09	0.07	0.11	<0.01	<46.6	<1.60	14.63	<21.6	42.90	11.14	<1.42	0.14	4.43
		QAG10-077	210.40	48.30	0.10	2.86	1.42	0.76	0.09	0.20	7.51	<0.01	<46.6	<1.60	13.67	<21.6	52.37	27.26	2.49	0.17	4.02
		QAG10-099	368.05	3.61	0.19	4.87	0.66	0.63	0.52	0.11	0.09	<0.01	<46.6	<1.60	135.35	<21.6	57.88	10.84	1.83	0.13	6.36
		QAG10-110	166.24	40.02	0.17	3.29	0.93	0.71	0.13	0.06	0.20	<0.01	<46.6	<1.60	5.23	<21.6	31.47	10.41	2.59	0.09	5.28
		QAG10-114	262.77	64.26	0.17	1.79	0.85	0.66	<0.09	0.05	0.05	<0.01	<46.6	2.06	29.11	<21.6	58.62	10.39	3.92	0.18	4.48
	P3	QAG18-003	221.32	70.35	1.23	3.40	0.91	1.79	0.23	0.10	0.56	0.02	<46.6	<1.60	7.89	<21.6	36.02	10.23	<1.42	0.15	6.14
		QAG18-005	157.80	26.18	0.17	2.38	0.48	0.91	<0.09	0.04	0.08	<0.01	<46.6	3.08	3.47	<21.6	29.34	3.71	1.93	0.08	5.38
		QAG18-011	261.54	49.36	0.14	2.03	0.46	0.73	0.16	0.02	0.09	<0.01	<46.6	3.38	46.77	<21.6	38.24	7.83	3.09	0.31	6.84
		QAG18-013	140.57	34.65	<0.08	2.26	1.50	1.04	0.14	0.04	0.08	<0.01	<46.6	<1.60	14.87	<21.6	34.17	1.51	3.28	0.16	4.11

		QAG18-018	149.29	31.82	0.40	3.62	0.50	0.71	0.13	0.08	0.07	<0.01	<46.6	<1.60	5.10	29.1	33.93	<1.29	1.78	0.07	4.40
		QAG18-019	253.53	28.52	<0.08	2.74	1.05	0.74	0.25	0.06	0.09	<0.01	<46.6	2.03	21.18	<21.6	34.73	16.28	2.80	0.22	7.30
		QAG18-021	302.07	51.90	0.18	<1.29	5.09	0.85	0.72	0.10	0.10	0.01	<46.6	59.38	12.82	29.8	50.97	58.41	5.59	0.38	5.93
	P3	QAG18-029	199.09	25.30	0.23	2.13	0.39	0.87	<0.09	0.06	0.04	<0.01	<46.6	<1.60	2.49	<21.6	35.03	5.40	3.38	0.10	5.68
		QAG18-068	385.03	23.52	0.09	1.50	0.45	0.71	<0.09	0.09	0.39	<0.01	<46.6	8.59	16.61	155.8	33.31	38.95	2.46	0.13	11.56
		QAG18-104	129.42	38.86	0.50	1.49	0.37	0.65	<0.09	0.05	0.05	<0.01	<46.6	3.59	5.52	<21.6	79.91	3.84	4.05	0.23	1.62
	P4	QAG24-021	250.14	33.63	<0.08	8.99	4.87	0.67	0.43	0.39	0.61	0.05	<46.6	16.94	20.55	106.8	22.78	8.31	9.35	0.69	10.98
		QAG24-023	334.80	24.17	0.18	5.56	1.47	0.65	0.81	0.37	0.21	0.02	<46.6	9.45	28.17	31.9	30.49	15.07	12.13	0.41	10.98
		QAG24-046	244.22	28.94	<0.08	2.81	0.67	0.73	0.09	0.12	0.09	0.01	103.36	12.83	36.68	<21.6	39.54	8.37	3.38	0.16	6.18
		QAG24-083	286.65	52.89	0.65	0.86	0.48	1.13	0.17	0.06	0.15	<0.01	99.55	4.68	22.01	39.8	31.00	3.21	2.80	0.19	9.25
		QAG24-107	437.35	67.02	0.46	2.57	1.63	0.85	0.34	0.12	0.06	0.01	<46.6	<1.60	13.53	<21.6	63.69	11.27	4.85	0.08	6.87
	P5	QAG29-011	192.13	12.00	0.16	2.23	0.52	0.74	0.20	0.09	0.10	<0.01	<46.6	1.66	59.83	99.9	82.51	2.75	1.95	0.20	2.33
		QAG29-076	230.57	30.16	0.18	7.82	1.69	0.73	0.53	0.14	0.24	<0.01	<46.6	3.82	61.63	49.1	53.38	5.35	3.06	0.31	4.32
		QAG29-121	248.87	44.77	0.16	4.18	2.07	0.88	1.24	<0.01	0.33	<0.01	520.06	8.06	169.75	57.6	101.35	11.70	6.23	0.38	2.46
	PM	QAG38-005	320.57	44.79	<0.08	5.19	1.37	0.69	0.17	0.17	0.41	<0.01	<46.6	2.99	6.26	<21.6	51.42	20.37	2.42	0.30	6.23
		QAG38-007	236.26	62.03	<0.08	3.06	1.36	0.82	0.23	0.07	0.13	<0.01	<46.6	3.61	13.10	<21.6	97.86	16.32	4.66	0.22	2.41
		QAG38-024	248.15	58.21	<0.08	3.87	1.01	0.85	0.12	0.07	0.06	<0.01	<46.6	<1.60	14.30	64.3	31.55	44.67	6.21	0.18	7.87
		QAG38-104	276.88	57.59	0.24	1.76	1.93	0.83	0.13	0.09	0.11	0.01	<46.6	4.45	7.60	<21.6	61.99	12.75	4.93	0.19	4.47
		QAG38-126	327.88	45.44	<0.08	3.22	0.35	0.61	<0.09	0.11	0.04	0.01	<46.6	4.97	39.80	30.1	61.50	71.96	2.80	0.32	5.33
		QAG38-137	183.50	40.96	0.47	4.67	0.61	0.72	0.24	0.05	0.25	<0.01	<46.6	1.81	4.25	21.8	59.32	<1.29	3.08	0.31	3.09
3	P1	QAG04-164	99.25	0.79	<0.08	6.36	2.28	1.50	0.40	0.12	1.03	<0.01	88.18	<1.60	29.97	<21.6	0.83	6.29	2.01	0.12	119.58
	P5	QAG29-099	305.76	2.98	0.38	5.87	7.33	1.64	31.02	8.24	2.82	<0.01	156.71	<1.60	74.63	50.2	5.44	181.52	19.17	0.22	56.21
4	P5	QAG29-086	161.67	16.73	0.45	2.76	0.15	0.26	0.61	<0.01	0.12	<0.01	334.34	36.29	48.54	156.3	44.20	1.63	16.30	1.62	3.66
	PM	QAG38-016	533.09	10.06	<0.08	2.63	1.15	0.68	0.20	0.89	0.30	0.05	<46.6	6.17	153.58	125.7	91.02	529.82	4.39	0.86	5.86
		QAG38-026	306.91	2.83	0.31	4.47	1.49	0.53	0.13	0.17	0.50	0.06	<46.6	9.41	57.82	58.1	80.08	144.94	5.41	0.27	3.83
		QAG38-058	192.48	25.02	0.12	13.08	1.95	0.82	0.36	0.06	0.20	<0.01	<46.6	3.80	20.53	<21.6	51.31	3.85	3.13	0.20	3.75
		QAG38-123	249.01	24.49	0.28	3.97	0.62	0.75	0.21	0.81	0.10	0.01	<46.6	5.21	43.86	<21.6	48.48	4.27	2.95	0.30	5.14

5	P4	QAG24-165	196.74	0.37	4.27	3.85	1.28	0.52	<0.09	1614.84	<0.03	0.02	<46.6	5.95	20.61	<21.6	62.42	13.58	2.55	0.40	3.15
6	P1	QAG04-048	837.98	2.22	0.09	5.76	0.28	2.10	0.59	1.08	0.58	<0.01	<46.6	1.61	208.73	39.3	1.97	43.39	2.39	0.16	425.37
	Mean all grains (n=51)		246.30	27.77	0.36	3.75	2.87	0.96	1.04	33.71	0.68	0.02	347.48	8.08	43.16	75.84	40.11	48.73	5.30	0.26	33.91

Chapter 4:

Lanthanides in granulometric fractions of Mediterranean soils. Can they be used as fingerprints of provenance?

Lanthanides in granulometric fractions of Mediterranean soils. Can they be used as fingerprints of provenance?

J. M. Martín-García[a], A. Molinero-García[a], J. Calero[b], M. V. Fernández-González[a], J. Párraga[a] & R. Delgado[a]

[a]Departamento de Edafología y Química Agrícola, Universidad de Granada, 18071 Granada, Spain

[b]Departamento de Geología, Universidad de Jaén, 23071 Jaén, Spain

*Author for correspondence: R. Delgado. *E-mail address*: rdelgado@ugr.es

Published on:

European Journal of Soil Science (2019), 70 (2), 394-410.
https://doi.org/10.1111/ejss.12730

Impact Factor (JCR):

Journal Impact Factor, JIF (2019): **3.742**; JIF Percentil in Category (Soil science - Scie): **80.26 (Q1)**

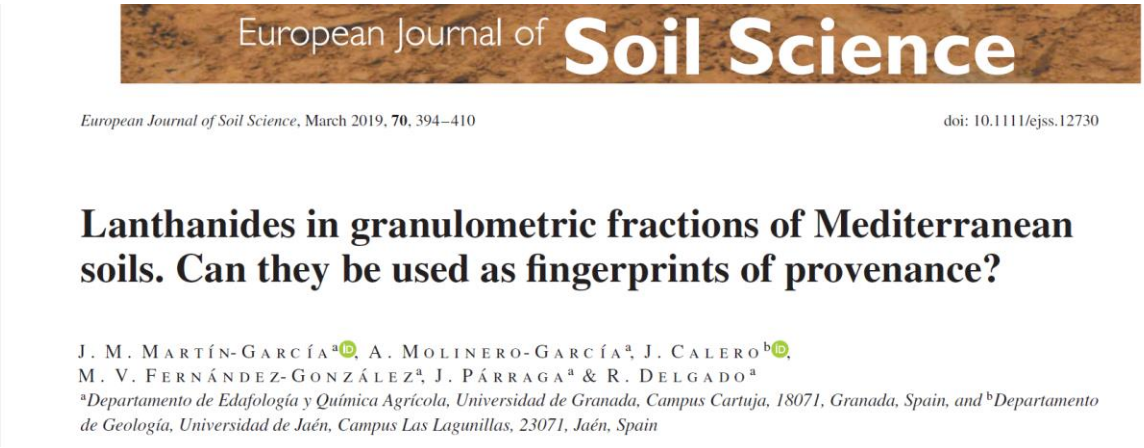

European Journal of Soil Science

European Journal of Soil Science, March 2019, **70**, 394–410 doi: 10.1111/ejss.12730

Lanthanides in granulometric fractions of Mediterranean soils. Can they be used as fingerprints of provenance?

J. M. Martín-García[a], A. Molinero-García[a], J. Calero[b],
M. V. Fernández-González[a], J. Párraga[a] & R. Delgado[a]
[a]*Departamento de Edafología y Química Agrícola, Universidad de Granada, Campus Cartuja, 18071, Granada, Spain, and* [b]*Departamento de Geología, Universidad de Jaén, Campus Las Lagunillas, 23071, Jaén, Spain*

Abstract

There is geochemical interest in the lanthanides because they behave like a group that is closely related to the parent materials during surface processes, although they also undergo fractionation as a result of supergene dynamics. We analysed lanthanide concentrations (ICPms) in the granulometric fractions fine sand, clay and free forms of clay ($FF_{clay-CDB}$ and $FF_{clay-Ox}$: extracted with citrate-dithionite-sodium bicarbonate and with ammonium oxalate, respectively) from a soil chronosequence of Mediterranean soils. There was a relative enrichment of heavy rare earth elements (HREE) in the clay fraction and its free forms with respect to fine sand. The clay free forms behaved as scavengers of lanthanides, while oxidative scavenging of cerium (Ce) in $FF_{clay-CDB}$ was also detected. Lanthanide concentrations (lanthanum to gadolinium in fine sand; terbium to lutetium in clay) varied with soil age, and chronofunctions were established. There was a strong positive collinearity between most of the lanthanide concentrations. Furthermore, the value of the correlation index (Pearson's *r*) of the concentrations between couples of lanthanides (r_{CLC}) decreased significantly with increasing separation between the elements in the Periodic Table; this has never been described in soils. Several geochemical properties and indices in the fine sand and clay soil fractions and in the geological materials of the Guadalquivir catchment showed, on the one hand, a genetic relation between them all, enabling the lanthanides to be used as fingerprints of provenance and, on the other, fractionation between fine sand and clay showed these latter are actively involved in soil lanthanide dynamics.

Keywords: soil chronosequence, correlation matrix, rare earth elements, geochemical indices, soil chronofunction.

Highlights:

- Were lanthanides from fine sand and clay genetically related to the geological materials?
- Lanthanide concentrations of fine sand and clay fit chronofunctions
- Pearson's *r* of lanthanide couples decreases when separation increases in the Periodic Table

- Free forms of clay are scavengers of lanthanides and concentrate HREE and cerium

1. Introduction

Quantities of rare earth elements (REE) (lanthanoids: $_{57\text{-}71}$Ln, and scandium $_{21}$Sc and yttrium $_{39}$Y) in the Earth's crust are of the order mg kg^{-1}, and show some characteristic periodic behaviour such as: (i) light REE (LREE), low atomic weight (A_r) (lanthanum La to samarium Sm), are more abundant than heavy REE (HREE) (holmium Ho to lutetium Lu) (British Geological Survey, 2011) (medium REE, MREE: samarium Sm to dysprosium Dy, has an intermediate A_r; Rollinson, 1993) and (ii) strong linear correlation between their concentrations has been reported; in European soils, $r > 0.7$ (Salminen *et al.*, 2005).

The chemical signatures of the parent rock assemblages in a tectonic province can persist in the daughter sediments produced, and are thus preserved in the corresponding sedimentary deposits (Rollinson, 1993). It has been suggested (Blundy & Wood, 2003) that the trace elements (<0.1% by weight, as in the case of lanthanides) exhibit passive behaviour during supergene processes, resulting in their being excellent tracers of the source area of sediments and soil materials. Wang *et al.* (2017) described them as ideal tracers of origin in aeolian research. Consequently, the geochemical interest in the lanthanides is due to their close relation with the source area. This feature can be used in paleoenvironmental studies of sedimentary origin and tectonic setting (Chen *et al*., 2014; Och *et al.*, 2014), and in soil studies such as pedogenic tracers (Laveuf & Cornu, 2009). The concentrations of REE in soil have been shown to depend not only on the lithology over which they develop, but also there are soil processes that induce internal fractionation or anomalies (Laveuf & Cornu, 2009). The Ln patterns, where the abundance of each Ln relative to that of a chondrite or shale is plotted on a logarithmic scale against the atomic number, or the geochemical ratios between lanthanides (e.g. HREE/LREE, lanthanum/ytterbium (La/Yb), samarium/ytterbium (Sm/Yb), and so on, or the cerium and europium anomalies (Ce/Ce* and Eu/Eu*, respectively)) are used for studying both the provenance of geological materials (as fingerprints) and for analysing pedogenic intensity (Rollinson, 1993; Moreno *et al.*, 2006; Mongelli *et al.*, 2014). In soil lanthanide dynamics, another process to add to inheritance and pedogenic action is aeolian contribution. Aeolian processes are common in Mediterranean soils (Delgado *et al.*, 2003).

Relatively little is known about lanthanide behaviour in soil (Chen *et al.*, 2014), therefore, their dynamics in different soil environments need to be analysed (Laveuf *et al.*, 2012). Studies of REE concentrations of granulometric fractions of soils, including sands (2000–50 µm) (Aide & Smith-Aide, 2003; Marques *et al.*, 2011) or in free forms, or in soil chronosequences are even more scarce (Chang *et al.*, 2016; Martín-García *et al*., 2016).

The aim of the present study was to examine lanthanide concentrations in the fine sand and clay fractions and the free forms of clay from a soil chronosequence from the River Guadalquivir (southern Spain) (a soil chronosequence is a series of soils that differ in their degree of profile development because of differences in age, while other soil-forming factors remained relatively constant). Other novel aspects investigated in this study are: (i) the effect of soil age, including the formulation of chronofunctions, (ii) the correlations between concentrations, (iii) the use of lanthanides as fingerprints of provenance compared to geological samples from the same soil zone and (iv) the contribution to the soil of lanthanides from aeolian materials.

In previous studies we have shown how the soils of the Guadalquivir behave like an ideal chronosequence, in which a considerable number of components and properties fitted significantly to chronofunction equations (Calero *et al.*, 2008, 2009, 2013). In addition, Martín-García *et al.* (2016) have studied the geochemistry of the clay fraction (including some aspects of lanthanides).

The present study can be included in the collection of soil chronofunction studies, which, at present, are few.

2. Materials and methods

2.1 Setting and soils

Geographically, the Guadalquivir River (640-km long) drains an area of 68 300 km^2. It rises in the Baetic Cordillera at a height of 1400 m before flowing into the Atlantic Ocean. It is the most important fluvial system in the Southern Iberian

Peninsula. From a geological point of view, the Guadalquivir-Cenozoic Basin was developed between the Iberian Massif (passive margin) to the north and the Baetic Cordillera (active margin) to the south (Figure 1). From a sedimentological point of view their fluvial alluvia are gravels with some stone-free sandy silt layers. The source rocks for this alluvium are lithologically diverse and include: to the north, igneous rocks (such as granite, granodiorite, rhyolite, tonalite, andesite, gabbro and intrusive rocks) and metamorphic rocks (mainly shales) from the Iberian Massif (Central Iberian Zone, mainly *Los Pedroches* batholith and *Santa Elena* pluton, and Iberian Massif) (Larrea *et al.*, 1992, 1994, 1995; Carracedo *et al.*, 1997; Pin *et al.*, 2002; Pascual *et al.*, 2008); to the south and west, sedimentary materials such as limestones, marly limestones, marls and dolomites from the External Baetics Zone of the Baetic Cordillera (Martínez-Ruiz, 1994); metasedimentary rocks (schist and gneiss) from the Internal Baetics Zone (Torres-Ruiz *et al.*, 2003) and Quaternary sediments from the Guadalquivir Depression, a Cenozoic Basin (Jiménez-Espinosa *et al.*, 2016).

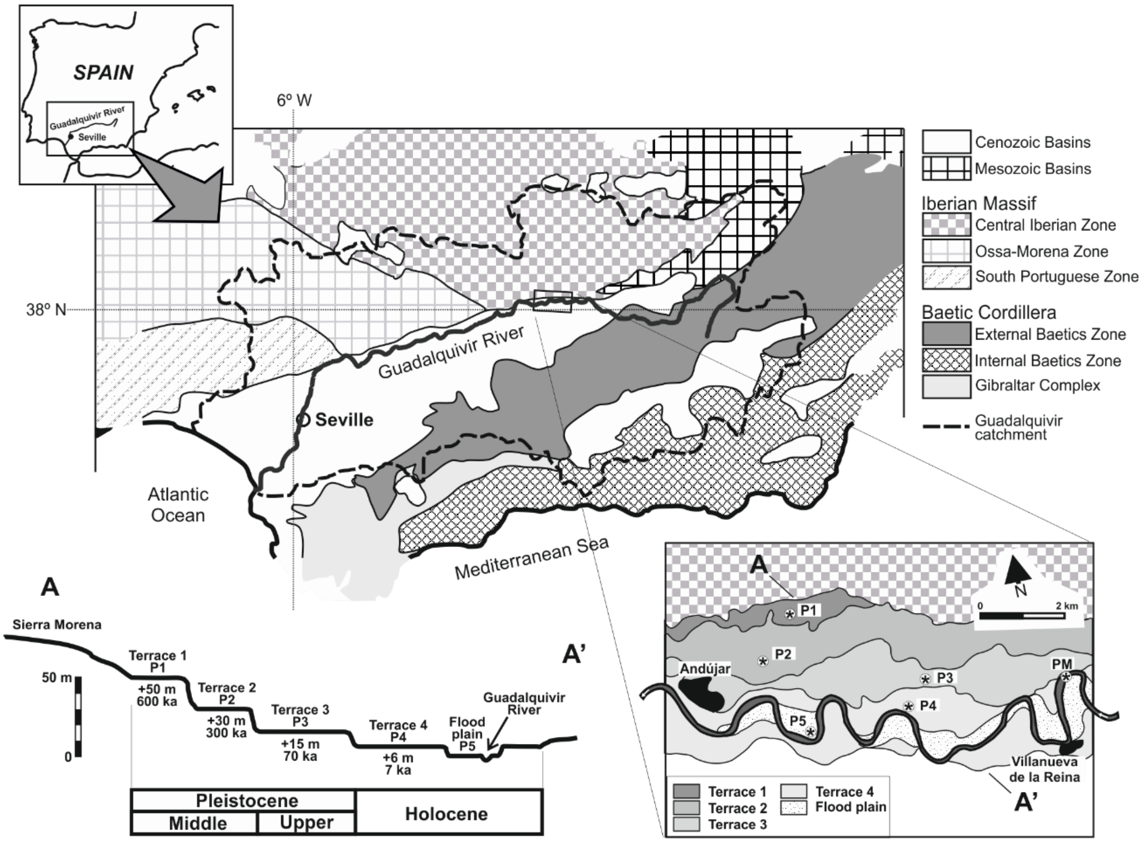

Figure 1. Location of the study area, geology of the Guadalquivir catchment, position of fluvial terrace levels (Terraces 1 to 4 and flood plain), topographic profile (A-A′) and soil sampling (P1 to P5 and PM).

Table 1. Soil characteristics[1]. Mean values and standard deviation (in parentheses).

Profile (Terrace no)	Soil classification[2]	Age /ka	PDI	Fine earth fraction (<2 mm)							Clay fraction (<2 µm)		Mineralogy (XRD) /%										
													Fine sand (50 – 250 µm)						Clay (<2 µm)				
				Clay /%	Fine sand /%	OC /%	pH	CEC /cmol$_+$·kg^{-1}	FF$_{CDB}$ /%	CaCO$_3$ eq /%	FF$_{clay\text{-}CDB}$ /%	FF$_{clay\text{-}Ox}$ /%	phy	qz	fd	feox	ca	do	phy	qz	fd	feox	ca
P1 (Terrace 1)	Cutanic Luvisol/ Palexeralf	600[3]	44.8	29.4 (7.2)	35.8 (9.6)	0.24 (0.14)	7.4 (0.4)	8.5 (1.8)	3.64 (0.44)	0.5 (0.9)	5.61 (0.83)	0.38 (0.06)	29 (9)	61 (10)	6 (3)	3 (1)	1 (0)		86 (1)	8 (1)	1 (1)	5 (1)	0 (0)
P2 (Terrace 2)	Lixic Calcisol/ Haploxeralf	300[3]	44.3	42.9 (5.5)	21.4 (13.4)	0.32 (0.23)	7.9 (0.1)	15.1 (2.8)	3.24 (0.36)	16.9 (19.4)	3.66 (0.35)	0.38 (0.06)	18 (6)	58 (8)	12 (10)	3 (1)	9 (10)		87 (1)	5 (1)	2 (1)	4 (1)	2 (1)
P3 (Terrace 3)	Cutanic Luvisol/ Haploxeralf	70[3]	39.6	30.7 (7.5)	36.4 (9.2)	0.22 (0.09)	7.6 (0.2)	10.7 (7.7)	1.90 (0.34)	0.0 (0.0)	3.06 (0.28)	0.53 (0.10)	6 (2)	58 (10)	31 (10)	2 (1)	3 (3)		89 (2)	6 (1)	2 (1)	3 (1)	0 (1)
P4 (Terrace 4)	Haplic Calcisol/ Calcixerept	7[4]	26.8	24.5 (8.5)	29.9 (6.8)	0.37 (0.25)	8.2 (0.4)	8.9 (6.1)	1.80 (0.48)	24.2 (7.1)	1.60 (0.43)	0.33 (0.05)	14 (5)	30 (15)	9 (7)	3 (1)	14 (5)	30 (18)	87 (3)	3 (1)	2 (1)	2 (1)	6 (3)
P5 Flood plain	Haplic Fluvisol/ Xerofluvent	0.3[4]	21.2	17.5 (3.4)	43.0 (8.2)	0.41 (0.19)	8.0 (0.1)	6.9 (3.3)	1.27 (0.11)	39.0 (1.9)	1.15 (0.15)	0.45 (0.11)	20 (8)	26 (5)	6 (3)	2 (1)	29 (3)	17 (5)	88 (1)	3 (2)	1 (0)	1 (1)	7 (0)
PM[5]			0	16.3	21.6	1.76	8.4	8.7	0.78	23.5	1.06	0.60	17	30	10	3	33	7	85	3	2	1	9

PDI, Profile development index (Harden, 1982); OC, organic carbon; CEC, cation exchange capacity; FF$_{CDB}$, citrate-ditionite-bicarbonate extractable free forms in fine earth fraction (Fe_2O_3+Al_2O_3); FF$_{clay\text{-}CDB}$, citrate-dithionite-bicarbonate extractable free forms in clay fraction (Fe_2O_3+Al_2O_3+TiO_2); FF$_{clay\text{-}Ox}$, ammonium oxalate extractable free forms in clay fraction (Fe_2O_3+Al_2O_3+TiO_2); $CaCO_3$ eq, calcium carbonate equivalent; phy, phyllosilicates (illite, smectite, mixed-layer phases, kaolinite, chlorite, brammallite); qz, quartz; fd, feldspar; feox, iron (hydr)oxides (goethite, hematite); ca, calcite; do, dolomite.

[1] From Calero *et al.* (2009) and Martin-Garcia *et al.* (2016)

[2] World Reference Base for Soil Resources/ Soil Taxonomy

[3] Preholocene

[4] Holocene

[5] Parent Material: Fluvial sediment ‘point bar’

The study area is in the middle reaches of the Guadalquivir River, near the town of Andújar on a transect of 3.7 km along the river between 3º 50’–4º 3’ W and 38º 0’–38º 2’ N (Figure 1). The soils selected (Table 1) developed on four Quaternary terrace surfaces (P1, P2, P3 and P4: Luvisols and Calcisols) and a floodplain (P5: Fluvisol) with ages ranging from 600 ka to 0.3 ka (Calero *et al.*, 2008). Fresh point bar sediments (PM) in the river were also selected. Currently, the climate is hot the Mediterranean with mean annual rainfall of 650 mm and a mean annual temperature of 18 ºC. The vegetation is mainly anthropogenic because the flat surfaces have been cultivated since time immemorial (nowadays olive groves, wheat and cotton).

The solum of the older terrace soils (pre-Holocene soils: P1, P2, and P3) (Table 1) shows Bt horizons (with clay illuviation features such as clay cutans), red Munsell colours, relatively deep thickness, clayey textures (>30% clay) and evidence of leaching of carbonates (and accumulation, in P2). Thus, the older soils have the largest values of Harden’s profile development index (between 44.8 for P1 and 39.6 for P3; Table 1). In the Holocene soil P4, brunification and some leaching and accumulation of carbonates has also been detected. The soil P5 had no evident evolution features. In the fine sand fraction (Table 1), quartz was the main mineralogical component in P1, P2 and P3 (≥58%, mean value), whereas the carbonates, calcite and dolomite, were the main components in P4 and P5 (≥44%, mean value of total carbonates). Other phases present were phyllosilicates (illite, brammallite, chlorite, kaolinite and various mixed-layer phases), feldspars (potassium feldspar and plagioclases, both abundant in P3) and iron (hydr)oxides (goethite and haematite). The point bar sediment PM showed a more balanced composition of quartz and carbonates (30 and 40%, respectively).

2.2. Materials and lanthanide analyses

Lanthanide concentrations of the fine sand fraction (50–250 µm) of 24 samples (belonging to soil horizons and point bar sediment, PM) were determined by inductively coupled plasma–mass spectrometry (ICP–MS) using an Agilent 7700x (Santa Clara, CA, United States) instrument at the Natural History Museum (London) after lithium metaborate fusion in a Pt–Au crucible, and the resulting flux was dissolved in 10% HNO_3. Calibration was performed using certified reference materials (CRM) prepared in the same way. Further analytical details are given in Gregory *et al.* (2017). As study material, we also used the concentrations of lanthanides from the clay fraction and the free forms of clay after extraction with citrate-dithionite-bicarbonate ($FF_{clay\text{-}CDB}$) or with ammonium oxalate ($FF_{clay\text{-}Ox}$), measured previously by Martín-García *et al.* (2016). The $FF_{clay\text{-}CDB}$ is conventionally assumed to be a measure of the total pedogenic free forms (crystalline and poorly crystalline forms), whereas $FF_{clay\text{-}Ox}$ is a measure of poorly crystalline forms; mainly iron, but with appreciable quantities of Al and Ti.

We grouped lanthanides following Rollinson (1993) into light (LREE: La to Nd), medium (MREE: Sm to Dy) and heavy rare earth elements (HREE: Ho to Lu). Lanthanide concentrations were normalized to (i.e. divided by) the CI chondrite, considered to represent the bulk earth composition, of McDonough & Sun (1995), and then the Ce/Ce* and Eu/Eu* anomalies were calculated ($Ce/Ce^* = Ce_N/(La_N \times Pr_N)^{1/2}$; $Eu/Eu^* = Eu_N/(Sm_N \times Gd_N)^{1/2}$; the subscript $_N$ shows that the value was normalized by the chondrite used. It makes sense to calculate both anomalies because Eu^{3+} and Ce^{3+} might be in another valency (Eu^{2+} and Ce^{4+}) and thus be involved in different reactions from the rest of the trivalent lanthanides (Ln^{3+}), i.e. separate from the group behaviour. The ratios La_N/Yb_N, Sm_N/Yb_N, $HREE_N/LREE_N$ and $MREE_N/LREE_N$ were also calculated; all establish the degree of fractionation of LREE from MREE and HREE (La is a representative of LREE, Sm of MREE, and Yb of HREE) during geochemical processes.

2.3. Statistical analysis

The statistical analysis was carried out using the IBM SPSS v.22.0 software package. The Kolmogorov–Smirnov and Shapiro–Wilk tests were used to determine the normality of data; and the results was considered statistically significant if P was less than 0.05. Statistical analyses were carried out after data were log transformed if this was necessary. The matrix of Pearson's product-moment correlation coefficients (r) and, in some cases, the coefficients of determination (R^2) were obtained. The coefficient of determination (R^2) was obtained to determine the fit of least squares regressions.

3. Results and discussion

3.1. Lanthanides in fine sand fraction

The series of lanthanides in fine sand showed very variable values, ranging from around 0.06 to 66.5 mg kg^{-1} (Table 2). The order of abundance was Ce > La > Nd > Pr > Sm > Gd > Dy > Er > Yb > Eu > Ho > Tb > Tm > Lu, identical to that of the mean of the Earth's crust (Rollinson, 1993; British Geological Survey, 2011), so that ΣLREE > ΣMREE > ΣHREE (Table 3). Lanthanide concentration increased with depth in the profile (Table 2). The P1 horizons contained most ΣLn (Table 3). The ΣLREE increased with age (P1>P2>P3>P4>P5>PM) and profile P4 was the richest in ΣHREE and Dy (e.g. horizon 4C2 had the largest concentration). The ratios $MREE_N/LREE_N$ and $HREE_N/LREE_N$ were smaller in preHolocene than Holocene soils and PM (Table 3).

The concentrations of lanthanides (ΣLn) were related to that of phyllosilicates, as proposed by Mongelli *et al*. (2014). In the fine sand of the present study, this is determined as:

$$\Sigma Ln\ (mg\ kg^{-1}) = 1.85 \times Phyllosilicates\ (\%) + 59.08 \qquad (n = 24;\ r = 0.538;\ P < 0.01).$$

In addition, the abnormally large concentrations of Dy and HREE in 4C2 of profile P4 (Table 2) reaffirm the presence of the lithological discontinuity detected morphologically by Calero *et al.* (2008, 2009). A possible explanation might be a change in the mineralogical composition of the major species (phyllosilicates, quartz, feldspars, iron oxides, calcite and dolomite) compared to the other horizons of the profile. However, this mineralogical change was not detected (table 4 on page 471 of Calero *et al.*, 2009). Therefore, it must be assumed that the change is in the minority mineral phases (<1%), which are those having an important role in lanthanide concentration (Kerr & Rafuse, 2012). Thus, the excess of Dy and HREE in geologic materials might be due to the presence of minerals such as thortveitite, with the formula $(Sc,Y)Si_2O_7$, which can show detectable concentrations of Dy, Ho, Er, Tm, Yb and Lu (Guastoni *et al.*, 2012) or xenotime, with the formula $(HREE,Y)PO_4$. However, verification of this would be beyond the scope of the present study.

Table 2. Lanthanide content (mg kg^{-1}) in the soil fine sand fraction (50–250 µm).

	La	Ce	Pr	Nd	Sm	Eu	Gd	Tb	Dy	Ho	Er	Tm	Yb	Lu
P1														
Ap	24.93	53.69	6.37	23.03	4.14	0.66	2.92	0.35	1.87	0.32	0.97	0.14	0.93	0.15
Bt	29.55	64.30	7.58	28.09	5.29	0.93	4.03	0.52	2.97	0.51	1.49	0.21	1.50	0.22
Btg2	31.78	66.50	7.97	29.82	5.66	1.05	4.22	0.53	3.05	0.53	1.56	0.23	1.56	0.22
2BCtg	26.21	54.91	6.69	25.06	4.91	0.95	3.51	0.42	2.37	0.40	1.29	0.17	1.29	0.19
4C	29.86	61.30	7.32	26.78	5.11	0.93	3.54	0.44	2.46	0.41	1.23	0.18	1.27	0.19
mean[1]	28.85 (2.81)	60.92 (5.66)	7.29 (0.65)	27.02 (2.63)	5.14 (0.57)	0.94 (0.15)	3.75 (0.51)	0.47 (0.07)	2.64 (0.48)	0.45 (0.09)	1.36 (0.23)	0.19 (0.04)	1.37 (0.25)	0.20 (0.03)
P2														
Ap	10.79	21.59	2.51	9.08	1.66	0.34	1.13	0.14	0.8	0.15	0.42	0.06	0.45	0.07
Btg1	18.82	37.44	4.66	17.06	3.18	0.64	2.53	0.34	1.95	0.38	1.05	0.15	0.99	0.15
Btg2	17.09	32.75	3.73	13.26	2.35	0.50	1.67	0.21	1.23	0.23	0.67	0.11	0.68	0.10
Cmk/Bt	23.76	48.96	6.04	22.56	4.28	0.80	3.20	0.40	2.25	0.46	1.19	0.17	1.09	0.18
mean[1]	17.66 (5.36)	35.20 (11.34)	4.20 (1.49)	15.35 (5.73)	2.83 (1.13)	0.56 (0.20)	2.08 (0.92)	0.26 (0.12)	1.51 (0.66)	0.29 (0.14)	0.80 (0.35)	0.12 (0.05)	0.78 (0.29)	0.12 (0.05)
P3														
Ap1	11.97	22.72	2.96	10.72	2.06	0.37	1.47	0.19	1.12	0.21	0.63	0.09	0.59	0.09
Bt1	17.30	32.51	4.16	15.06	2.95	0.45	1.99	0.27	1.56	0.30	0.94	0.13	0.83	0.13
Bt2	15.00	28.97	3.65	12.75	2.46	0.42	1.77	0.23	1.33	0.25	0.77	0.11	0.71	0.11
Bt3	18.86	38.83	4.75	17.31	3.37	0.47	2.43	0.31	1.83	0.36	1.09	0.15	0.92	0.14
Bt4	17.50	35.79	4.26	15.35	2.87	0.50	2.01	0.27	1.46	0.28	0.82	0.12	0.74	0.11
2Bt6	23.32	47.41	5.69	20.24	3.86	0.51	2.94	0.44	2.70	0.53	1.54	0.23	1.41	0.22
mean[1]	18.01 (3.81)	35.78 (8.49)	4.41 (0.93)	15.85 (3.35)	3.05 (0.64)	0.46 (0.05)	2.19 (0.52)	0.30 (0.09)	1.76 (0.56)	0.34 (0.11)	1.02 (0.32)	0.15 (0.05)	0.91 (0.29)	0.14 (0.05)
P4														
Ap1	11.21	21.74	2.80	10.43	2.10	0.45	1.63	0.22	1.34	0.26	0.78	0.11	0.65	0.10
Bwk1	12.53	24.01	3.06	11.32	2.23	0.47	1.76	0.24	1.47	0.29	0.84	0.12	0.71	0.11
2Bwk2	26.43	54.91	6.47	23.59	4.38	0.54	3.02	0.37	2.11	0.38	1.17	0.19	1.11	0.17
4C2	13.33	26.26	3.26	12.25	2.52	0.54	2.76	0.54	4.41	1.01	3.50	0.53	3.45	0.54
mean[1]	16.80 (7.09)	33.77 (15.56)	4.12 (1.73)	15.21 (6.17)	2.96 (1.06)	0.51 (0.05)	2.48 (0.70)	0.38 (0.15)	2.71 (1.43)	0.57 (0.35)	1.89 (1.30)	0.29 (0.20)	1.81 (1.33)	0.28 (0.21)
P5														
Ap	16.03	31.08	4.02	15.25	3.03	0.61	2.57	0.34	2.09	0.38	1.13	0.15	0.94	0.17
2C1	12.51	24.40	3.13	11.98	2.38	0.51	1.96	0.26	1.70	0.32	0.97	0.13	0.81	0.12
4C3	16.78	34.21	4.07	15.26	2.99	0.58	2.54	0.34	2.03	0.39	1.17	0.16	1.03	0.16
6C5	15.39	29.65	3.74	13.95	2.72	0.53	2.40	0.33	2.04	0.39	1.16	0.16	1.01	0.15
mean[1]	15.09 (1.87)	29.72 (4.09)	3.73 (0.43)	14.09 (1.55)	2.78 (0.30)	0.56 (0.05)	2.36 (0.28)	0.31 (0.04)	1.95 (0.18)	0.37 (0.03)	1.10 (0.09)	0.15 (0.01)	0.94 (0.10)	0.15 (0.02)
PM	10.41	19.98	2.58	9.76	2.01	0.43	1.56	0.20	1.23	0.24	0.72	0.10	0.61	0.09

[1] weighted to horizon thickness (standard deviation in parentheses)

Table 3. Total content and selected geochemical ratios of lanthanides. Mean profile values and standard deviation (in parentheses). Soil fine sand and soil clay fractions and free forms of soil clay fraction extracted with citrate-dithionite-bicarbonate ($FF_{clay-CDB}$) and oxalate ($FF_{clay-Ox}$).

	ΣLn /mg kg^{-1}	ΣLREE /mg kg^{-1}	ΣMREE /mg kg^{-1}	ΣHREE /mg kg^{-1}	$MREE_N/LREE_N$	$HREE_N/LREE_N$	Eu/Eu*	Ce/Ce*
Soil fine sand (50–250 µm) (*n* = 24)								
P1	140.59 (12.87)	124.08(11.65)	12.94 (1.75)	3.57 (0.63)	0.26 (0.02)	0.12 (0.01)	0.65 (0.05)	1.02 (0.02)
P2	81.77 (15.34)	72.40 (23.85)	7.24 (3.01)	2.12 (0.88)	0.25 (0.02)	0.12 (0.02)	0.73 (0.06)	0.99 (0.02)
P3	84.37 (14.15)	74.04 (16.54)	7.76 (1.82)	2.56 (0.82)	0.26 (0.01)	0.14 (0.02)	0.55 (0.07)	0.97 (0.04)
P4	83.80 (35.71)	69.91 (30.55)	9.05 (2.69)	4.85 (3.39)	0.31 (0.10)	0.28 (0.26)	0.61(0.13)	0.97 (0.04)
P5	73.29 (9.86)	62.63 (7.86)	7.96 (0.83)	2.70 (0.26)	0.31 (0.01)	0.17 (0.01)	0.67 (0.04)	0.96 (0.03)
PM	49.92	42.73	5.43	1.76	0.32	0.16	0.74	0.93
Soil clay (<2 µm) (*n* = 35)								
P1	86.99 (12.31)	71.75 (10.71)	11.10 (1.25)	4.14 (0.37)	0.39 (0.01)	0.24 (0.02)	0.67 (0.02)	0.94 (0.01)
P2	105.23 (15.80)	90.73 (13.20)	10.50 (2.08)	4.00 (0.53)	0.30 (0.01)	0.19 (0.01)	0.66 (0.01)	1.15 (0.08)
P3	143.01 (26.60)	123.25 (23.61)	14.86 (2.42)	4.90 (0.69)	0.30 (0.01)	0.16 (0.01)	0.65 (0.01)	1.00 (0.05)
P4	97.84 (34.20)	83.67 (29.50)	10.68 (3.67)	3.49 (1.05)	0.32 (0.01)	0.17 (0.01)	0.63 (0.04)	1.04 (0.03)
P5	68.81 (17.10)	58.63 (14.79)	7.58 (1.75)	2.60 (0.56)	0.33 (0.01)	0.18 (0.01)	0.69 (0.01)	0.98 (0.01)
PM	51.46	43.72	5.74	2.00	0.33	0.19	0.71	0.99
$FF_{clay-CDB}$ (*n* = 35)								
P1	39.82 (10.08)	31.07 (8.49)	6.92 (1.33)	1.83 (0.27)	0.58 (0.07)	0.25 (0.04)	0.75 (0.02)	1.09 (0.11)
P2	45.74 (13.45)	38.10 (10.92)	5.87 (2.00)	1.77 (0.54)	0.44 (0.01)	0.21 (0.01)	0.71 (0.03)	1.74 (0.33)
P3	67.41 (12.30)	54.91 (10.20)	9.45 (1.64)	3.05 (0.41)	0.47 (0.04)	0.24 (0.02)	0.71 (0.01)	1.39 (0.07)
P4	13.64 (3.09)	10.83 (2.62)	2.05 (0.36)	0.76 (0.13)	0.53 (0.04)	0.31 (0.02)	0.74 (0.03)	1.50 (0.19)
P5	14.66 (6.03)	11.58 (4.97)	2.29 (0.84)	0.79 (0.23)	0.51 (0.04)	0.29 (0.05)	0.75 (0.04)	1.05 (0.03)
PM	9.60	7.66	1.44	0.50	0.49	0.27	0.75	1.03
$FF_{clay-Ox}$ (*n* = 35)								
P1	1.76 (0.86)	0.92 (0.54)	0.55 (0.22)	0.29 (0.11)	1.39 (0.46)	1.34 (0.43)	0.65 (0.35)	0.86 (0.09)
P2	1.22 (0.84)	0.61 (0.53)	0.36 (0.20)	0.25 (0.11)	1.58 (1.30)	1.91 (2.21)	0.88 (0.36)	1.83 (1.09)
P3	3.93 (1.12)	2.26 (0.74)	0.98 (0.26)	0.69 (0.18)	1.09 (0.20)	1.35 (0.18)	0.55 (0.06)	1.40 (0.36)
P4	1.02 (0.37)	0.66 (0.25)	0.24 (0.10)	0.13 (0.06)	0.83 (0.31)	0.84 (0.58)	0.24 (0.09)	1.24 (0.46)
P5	0.61 (0.23)	0.28 (0.14)	0.17 (0.06)	0.16 (0.05)	1.41 (0.32)	2.35 (1.65)	1.08 (0.43)	0.92 (0.56)
PM	0.58	0.25	0.20	0.13	2.11	2.89	0.34	2.22

Ln, La to Lu; LREE, La to Nd; MREE, Sm to Dy; HREE, Ho to Lu; the suffix “N” shows that the value normalized to chondrite was used; $Eu/Eu^* = Eu_N/(Sm_N \times Gd_N)^{1/2}$; $Ce/Ce^* = Ce_N/(La_N \times Pr_N)^{1/2}$; $FF_{clay-CDB}$, citrate-dithionite-bicarbonate extractable free forms in clay fraction; $FF_{clay-Ox}$, ammonium oxalate extractable free forms in clay fraction

The chondrite-normalized profiles (Figure 2a) always had values >1, i.e. larger quantities than in the reference meteorite, a common tendency in soil materials (Hu *et al.*, 2006). Figure 2(a) also indicates a pronounced relative abundance of LREE, shown by a steep slope which flattens out in such a way that after Ho (region of the HREE) it is almost horizontal. The P1 horizons, with more lanthanides, occupy the highest positions on the graph and the 4C2 horizon of P4 is V-shaped because of its large Dy and HREE concentrations.

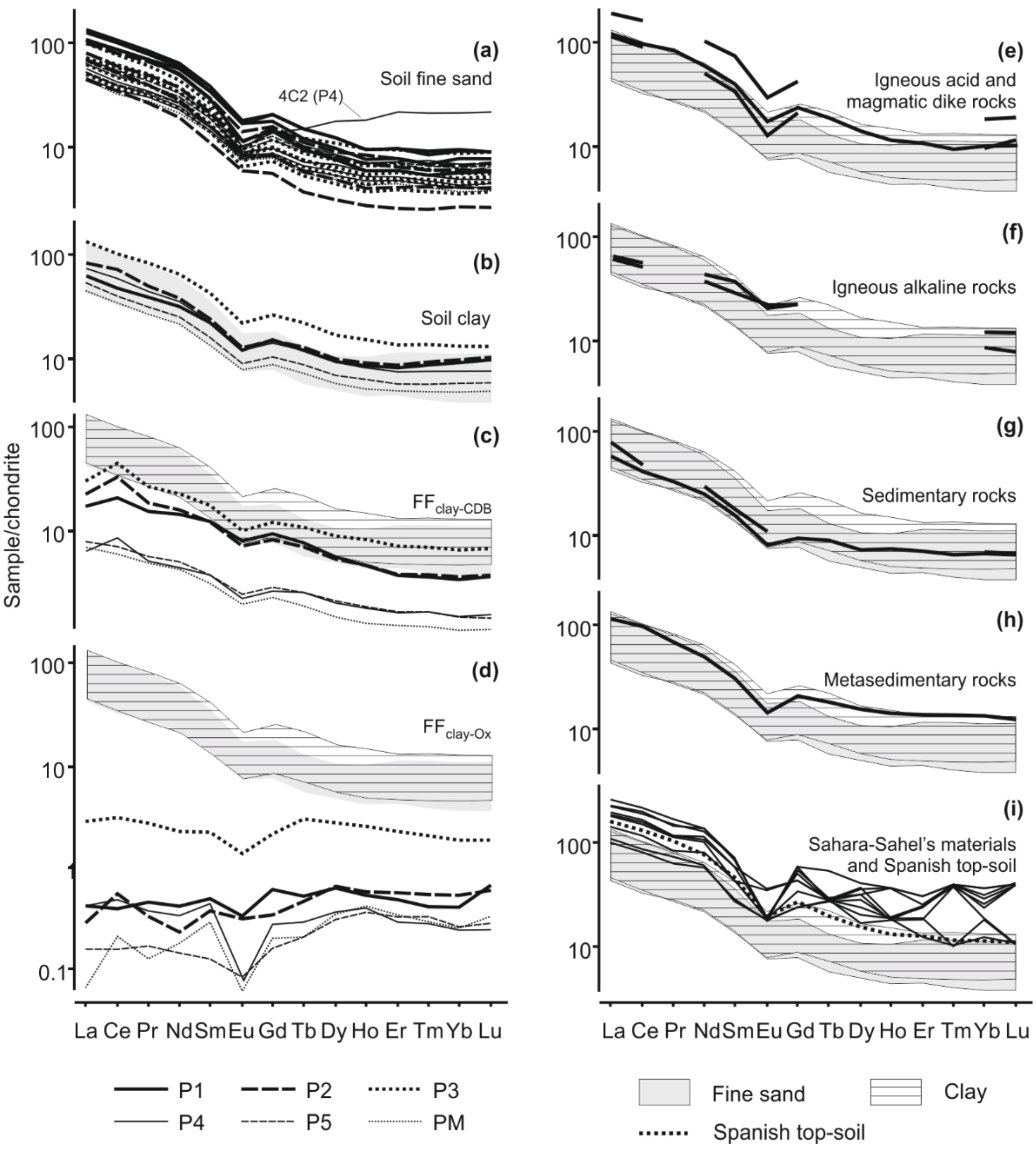

Figure 2. Chondrite-normalized concentrations of lanthanides (logarithmic scale) in: (a) soil fine sand fraction (50–250 µm) (all horizons; this study), (b) soil clay fraction (<2 µm) (mean profile, this study), (c) free forms from soil clay fraction (mean profile, this study) extracted with citrate-dithionite-bicarbonate ($FF_{clay-CDB}$), (d) free forms from soil clay fraction (mean profile, this study) extracted with oxalate ($FF_{clay-Ox}$), (e) acid igneous and

magmatic-like rocks from the Guadalquivir catchment (Larrea *et al.*, 1992, 1994, 1995; Carracedo *et al.*, 1997; Pascual *et al.*, 2008), (f) alkaline igneous rocks from Guadalquivir catchment (Larrea *et al.*, 1995; Pin *et al.*, 2002), (g) sedimentary rocks from Guadalquivir catchment (Martínez-Ruiz, 1994; Jiménez-Espinosa *et al.*, 2016), (h) metasedimentary rocks from Guadalquivir catchment (Torres-Ruiz *et al.*, 2003) and (i) Sahara–Sahel materials (Moreno *et al.*, 2006) and Spanish topsoil (Locutura *et al.*, 2012). The shaded area (b to i) and the area with horizontal lines (c to i) enclose the upper and lower margins of the mean values per profile of the fine sand and clays (a and b).

No notable Ce/Ce* anomaly was detectable (Figure 2a, Table 3), with values very close to unity (all horizons between 0.93 and 1.04). The mean values of Ce/Ce* per profile increased with soil age, probably resulting from alteration processes in the soil material (Huang & Gong, 2001). In the present study, the alteration could be related to decarbonation of the fine sand (decrease in calcite and dolomite content through leaching) (Table 1), as shown by the moderate negative correlation in fine sand between Ce/Ce* and the sum of calcite + dolomite, % ($r = –0.530$; $n = 22$; $P< 0.01$), which accords with the results of Wen *et al.* (2014), in their case with $r = –0.403$ and $P< 0.01$.

According to its lanthanides, the fine sand fraction has evolved geochemically rather than being inert.

3.2. Lanthanides in the clay fraction and clay free forms

In the clay fraction, the order of abundance of ΣLn (mean values per profile in mg kg^{-1}) is: P3>P2>P4>P1>P5>PM (Table 3), with no obvious trend regarding age or when compared with the respective fine sand (Table 3). Aide & Smith-Aide (2003) and Marques *et al.* (2011) reported that the lanthanides are concentrated in the fine fractions, <50 µm (silt and clay); in the present study, this was not clear in P1 and P5. This might be due to the differences in phyllosilicate content because these were always larger in the clay (Table 1), and in P1 and P5 this would suggest searching for the presence of lanthanide-rich minerals (e.g. zircon) in fine sand; again, beyond the scope of the present study. Moreover, in the clay fraction, as occurred in the fine sand, a relation between ΣLn and phyllosilicates was found ($n = 35$; $r = 0.566$; $P< 0.001$). Considering the complete population (clay + fine sand), this correlation was not significant.

The clay of the pre-Holocene soils (P1, P2, P3) contained more ΣHREE than the two of the Holocene (P4, P5) and PM. Furthermore, the clay of these pre-Holocene soils also had more ΣHREE than the corresponding fine sand (Table 3).

The clay free forms ($FF_{clay\text{-}CDB}$ and $FF_{clay\text{-}Ox}$) generally contained fewer lanthanides (ΣLn) than the fine sand and clay fractions (Table 3). However, calculation of ΣLn in $FF_{clay\text{-}CDB}$, assuming that all proceed from the mineral phases which constitute the free forms (in $FF_{clay\text{-}CDB}$ it was mainly goethite, haematite and poorly crystalline forms of Fe; in $Fe_{clay\text{-}Ox}$ it was poorly crystalline iron, mostly ferrihydrite, Martín-García *et al.*, 2016) provided striking new evidence of REE accumulation in iron free forms. Thus, $FF_{clay\text{-}CDB}$ of P1, with ΣLn of 39.82 mg kg^{-1} attributable to 5.61% of $FF_{clay\text{-}CDB}$ (Fe_2O_3+Al_2O_3+TiO_2; Table 1) suggests that iron (hydr)oxides ($FF_{clay\text{-}CDB}$) had ΣLn of 709.8 mg kg^{-1}. When the calculation was carried out with PM (1.06% $FF_{clay\text{-}CDB}$ (Fe_2O_3+Al_2O_3+TiO_2; Table 1) and 9.60 mg kg^{-1} of ΣLn) the goethite+haematite had 905.7 mg kg^{-1}. These values of ΣLn can be attributed to the special characteristics of these iron (hydr)oxides: small particle size and neoformed in the soil, absorbing Ln at their surface, which might even have been buried during the growth of the iron (hydr)oxide. This proves that iron (hydr)oxides act as lanthanide scavengers. Our figures were small considering that Onac *et al.* (1997) reported Σ(La, Ce, Sm, Nd) greater than 2000 mg kg^{-1} in coatings of ferromanganese (hydr)oxides.

The ΣLn in the clay free forms ($FF_{clay\text{-}CDB}$ and $FF_{clay\text{-}Ox}$) tended to increase with soil age because they were more abundant in pre-Holocene soils than in Holocene soils and PM (Table 3).

The chondrite-normalized patterns (Figure 2b) showed that in most cases the clay was within the range of concentrations of fine sand. The profiles of $FF_{clay\text{-}CDB}$ (Figure 2c) differentiate clearly between the pre-Holocene soils (P1, P2, P3) and the Holocene soils (P4, P5) and PM, which had smaller concentrations.

The ratio $HREE_N/LREE_N$ in the clay fraction (Table 3) was greater than in the fine sand (except in P4). Laveuf & Cornu (2009) stated that during pedogenesis the LREE are less readily complexed by fluids than the HREE and that the latter accumulate in alteration products such as phyllosilicates, which are more abundant in the clays than in the fine sand. Furthemore, the $HREE_N/LREE_N$ index was greater in $FF_{clay\text{-}CDB}$ and $FF_{clay\text{-}Ox}$ (neoformed iron (hydr)oxides) than in fine sand or clay, which was in accord with Pédrot *et al.* (2015) who reported that the iron (hydr)oxides precipitated during alteration have a greater affinity for HREE than for LREE. This all suggests fractionation of the Ln by granulometric fractions (and mineralogy), with the HREE being concentrated in the clay, $FF_{clay\text{-}CDB}$ and $FF_{clay\text{-}Ox}$.

The values of the Ce/Ce* anomaly of the clay fraction (0.94–1.15) (Table 3, Figure 2a) were also similar to those of the fine sand. In $FF_{clay\text{-}CDB}$ all these values were positive (1.03–1.62) indicating a relative accumulation of Ce in the iron (hydr)oxides also reported by Pédrot *et al.* (2015); in $FF_{clay\text{-}Ox}$ the range was wider (0.86–2.22) and erratic again.

3.3. Behaviour of lanthanides in relation to soil horizon evolution and time

The lanthanide concentrations exhibited very different behaviour in the fine sand and clay fractions with regard to the morphological evolution of the soil horizons, measured with the horizon development index (HDI) (Harden, 1982) (Table 4). Positive linear correlations with $P< 0.01$ were typical of the clay fraction, whereas there was no significant correlation with the fine sand. Thus, lanthanide concentration in clay increases with horizon evolution; particularly in HREE, which are those with the strongest correlations ($P< 0.001$; $r = 0.656, 0.705, 0.727$ and 0.656 for Tm, Yb, Lu and ΣHREE, respectively). The clay free forms $FF_{clay\text{-}CDB}$ showed the same behaviour as the clay fraction with the correlations being even more significant (with $P< 0.001$), possibly because of the previously mentioned role of iron (hydr)oxides (goethite and haematite, principal constituents of the $FF_{clay\text{-}CDB}$) as scavengers of the lanthanides liberated during alteration of the soil minerals. The ratio Ce/ΣLn (Pédrot *et al.*, 2015) in $FF_{clay\text{-}CDB}$ was correlated ($P< 0.05$) with HDI ($r = 0.416$; $n = 35$), suggesting the relative enrichment of Ce in $FF_{clay\text{-}CDB}$ in the most morphologically evolved horizons.

Evidence has already been provided to illustrate the dependence of the lanthanides in the present study (properties ΣLn, ΣLREE, ΣHREE, Ce/Ce*, $MREE_N/LREE_N$ and $HREE_N/LREE_N$) with age groups of soils: pre-Holocene (P1, P2, P3) and Holocene (P4, P5 and PM). To quantify these relations better, we calculated the correlation matrix of lanthanide concentration with soil age (Table 5). Behaviour was different: the fine sand showed a linear relation with time ($y = ax+b$) and a quadratic relation with time ($y = ax^2+bx+c$) in LREE and part of MREE (La to Gd), and ΣLn; while the clay fraction fitted significant logarithmic functions ($y = a\ln x+b$) in HREE and another part of MREE (Tb to Lu) and ΣHREE. For the fine sand this suggests that the concentrations of lanthanides from La to Gd did not attain a stable state (identified by the logarithmic model). On the other hand, the concentrations in clay of lanthanides from Tb to Lu did attain a stable state. Furthermore, the chronofunctions with strong correlations spanned from La to Gd in fine sand and were present from Gd (not included) in the clay suggesting the 'gadolinium breaking effect' (Chi *et al.*, 2006). The latter the infringement of the monotonic change of properties of lanthanide compounds according to the atomic number, attributed to a variation in the electron configuration of the lanthanides occurring in the gadolinium.

Table 4. Matrix of linear correlation (Pearson's *r*) between lanthanides content and horizon development index (HDI)[1].

Lanthanide content	Soil fine sand[2] (*n* = 24)	Soil clay[1] (*n* = 35)	$FF_{\text{clay-CDB}}$[1] (*n* = 35)	$FF_{\text{clay-Ox}}$[1] (*n* = 35)
La	0.314	***0.557***	***0.718***	*0.367*
Ce	0.317	***0.579***	***0.765***	**0.483**
Pr	0.297	***0.565***	***0.745***	**0.442**
Nd	0.257	***0.551***	***0.746***	*0.409*
Sm	0.192	***0.572***	***0.766***	**0.503**
Eu	0.031	**0.526**	***0.745***	**0.467**
Gd	0.020	***0.567***	***0.741***	**0.516**
Tb	–0.077	***0.564***	***0.746***	**0.454**
Dy	–0.203	***0.589***	***0.745***	**0.527**
Ho	–0.227	***0.594***	***0.740***	*0.373*
Er	–0.267	***0.614***	***0.730***	*0.403*
Tm	–0.227	***0.656***	***0.724***	**0.431**
Yb	–0.213	***0.705***	***0.746***	**0.484**
Lu	–0.219	***0.727***	***0.741***	**0.517**
ΣLn	0.252	***0.575***	***0.762***	***0.537***
ΣLREE	0.304	***0.569***	***0.761***	**0.461**
ΣMREE	0.007	***0.571***	***0.753***	**0.519**
ΣHREE	–0.240	***0.656***	***0.739***	**0.454**

$FF_{\text{clay-CDB}}$, citrate-dithionite-bicarbonate extractable free forms in clay fraction; $FF_{\text{clay-Ox}}$, ammonium oxalate extractable free forms in clay fraction

Statistical significance: *P*< *0.05*; ***P*< 0.01**; ***P< 0.001***

[1] HDI and lanthanides values from Martín-García *et al.* (2016)

[2] Lanthanides values from Table 2.

Table 5. Correlation (R^2, coefficient of determination) between lanthanide contents and geochemical ratio with soil age (n = 6). Selected chronofunctions (s).

Lanthanide properties	Soil fine sand$^{1.2}$			Soil clay$^{1.3}$			$FF_{clay\text{-}CDB}$$^{1.3}$			$FF_{clay\text{-}Ox}$$^{1.3}$		
	Linear	Logarithmic (ln)	Quadratic	Linear	Logarithmic (ln)	Quadratic	Linear	Logarithmic (ln)	Quadratic	Linear	Logarithmic (ln)	Quadratic
La	*0.794*(s)	0.643	*0.824*	0.005	0.469	0.241	0.211	0.526	0.429	0.032	0.338	0.049
Ce	*0.801*(s)	0.616	*0.841*	0.004	0.486	0.391	0.106	0.494	0.524	0.000	0.234	0.102
Pr	*0.785*(s)	0.593	*0.835*	0.011	0.496	0.229	0.183	0.501	0.381	0.033	0.309	0.046
Nd	*0.787*(s)	0.555	*0.854*	0.014	0.506	0.194	0.215	0.523	0.389	0.040	0.278	0.046
Sm	*0.752*(s)	0.494	*0.859*	0.058	0.607	0.192	0.251	0.563	0.410	0.064	0.276	0.077
Eu	*0.823*(s)	0.323	*0.945*	0.083	0.624	0.188	0.324	0.593	0.444	0.227	0.436	0.324
Gd	0.613	0.416	*0.796*	0.092	0.645	0.168	0.329	0.588	0.440	0.138	0.358	0.147
Tb	0.365	0.389	0.578	0.086	*0.664*	0.208	0.241	0.554	0.378	0.052	0.279	0.111
Dy	0.127	0.237	0.372	0.102	*0.676*	0.224	0.195	0.546	0.364	0.032	0.275	0.150
Ho	0.016	0.155	0.176	0.099	*0.674*	0.230	0.171	0.520	0.326	0.005	0.184	0.067
Er	0.001	0.094	0.189	0.153	*0.743*	0.300	0.130	0.490	0.298	0.023	0.250	0.115
Tm	0.000	0.100	0.134	0.207	*0.764*	0.365	0.122	0.471	0.314	0.012	0.164	0.020
Yb	0.025	0.154	0.181	0.314	**0.865**	0.493	0.126	0.491	0.329	0.006	0.219	0.129
Lu	0.010	0.144	0.142	0.411	**0.893**	0.500	0.163	0.510	0.364	0.043	0.308	0.222
ΣLn	*0.762*(s)	0.596	*0.819*	0.013	0.523	0.285	0.165	0.526	0.446	0.020	0.277	0.078
ΣLREE	*0.796*(s)	0.608	*0.841*	0.006	0.493	0.301	0.150	0.516	0.464	0.009	0.269	0.060
ΣMREE	0.582	0.438	0.760	0.080	0.638	0.191	0.265	0.570	0.407	0.072	0.315	0.124
ΣHREE	0.010	0.126	0.176	0.222	*0.805*	0.386	0.136	0.496	0.317	0.013	0.228	0.108
$HREE_N/LREE_N$	0.324	0.070	0.462	*0.752*	0.068	*0.906*	0.293	0.255	*0.830*	0.082	0.551	0.083
La_N/Yb_N	0.533	0.412	*0.870*	**0.850**	0.171	*0.865*	0.300	0.003	0.325	0.027	0.226	0.108

s: Selected linear chronofunction[3] from fine sand fraction:

La (mg kg^{-1}) = 0.022×age (ka) + 14.17; Ce (mg kg^{-1}) = 0.050×age (ka) + 27.75; Pr (mg kg^{-1}) = 0.006×age (ka) + 3.46; Nd (mg kg^{-1}) = 0.021×age (ka) + 12.80; Sm (mg kg^{-1}) = 0.004×age (ka) + 2.52; Eu (mg kg^{-1}) = 0.001×age (ka) + 0.47; ΣLn (mg kg^{-1}) = 0.107×age (ka) + 68.15; ΣLREE (mg kg^{-1}) = 0.099×age (ka) + 58.19

$FF_{clay\text{-}CDB}$, citrate-dithionite-bicarbonate extractable free forms in clay fraction; $FF_{clay\text{-}Ox}$, ammonium oxalate extractable free forms in clay fraction

Statistical significance: *P< 0.05*; ***P< 0.01***

[1] Soil age values from Table 1; [2] Lanthanide values from Table 2; [3] Lanthanide values from Table 3 and Martín-García *et al.* (2016)

When the problem of soil age is considered from the point of view of LREE and HREE fractionation, estimated by the indices $HREE_N/LREE_N$ and La_N/Yb_N (Table 5), it can appear that this process depends markedly on age with the HREE concentration increasing with time (e.g. in soil clay:

$La_N/Yb_N = –5.2×10^{-3}×$ age(ka) + 10.39; $n = 6$; $R^2 = 0.870$; $P< 0.01$).

However, a stable state was not attained for either fine sand or clay because the correlations never fitted the logarithmic functions.

3.4. Relations between lanthanide quantities

Although concentrations of elements of the lanthanide series were different in all the fractions analysed (Tables 2 and 3, Figure 2a–d), many changed in a parallel way in the samples showing a strong positive collinearity (large r_{CLC}; where r_{CLC} are the correlation coefficients between ‘couples of lanthanide concentrations’) (Figure 3). In the fine sand, the r_{CLC} varied between 0.998 ($P< 0.001$) and 0.477 ($P< 0.001$). In the clay fractions (total clay, $FF_{clay-CDB}$ and $FF_{clay-Ox}$) r_{CLC} was even larger, ranging from 0.998 to 0.896 (both with $P< 0.001$). Salminen *et al.* (2005) stated that in European soils “all REE in soil are strongly correlated among themselves, with all correlation coefficients higher than 0.7”. However, in the present study, more than a third of the r_{CLC} of the fine sand were below 0.7.

Furthermore, r_{CLC} had (Figure 3) the largest values between couples of adjacent lanthanides in the Periodic Table (e.g. $_{60}$Nd vs. $_{61}$Pr: 0.998 in fine sand, >0.945 in clay, $FF_{clay-CDB}$ or $FF_{clay-Ox}$). This fact was previously reported for igneous materials (Kerr & Rafuse, 2012) and shales (Noack *et al.*, 2015), but never demonstrated for soil.

In addition, r_{CLC} became progressively weaker with increasing separation between the elements in the Periodic Table: e.g, in fine sand, r_{CLC} of $_{57}$La with the adjacent $_{58}$Ce was 0.997, with $_{66}$Dy, 0.622 and with $_{71}$Lu, at the other extreme, 0.524. This behaviour has never been described previously in geologic materials, and is related to chemical periodicity (adjacent Ln have similar ionic radii, atomic mass and a +3 valence, and will behave similarly in the crystal structure of the minerals). This behaviour of r_{CLC} enables a bivariate diagram to be produced (Figure 4) showing the r_{CLC} of any couple of lanthanides with their differences in standard atomic weight (ΔA_r) with a negative collinearity ($P < 0.001$). The A_r (expressed in decimals) was used because it differentiates more precisely between couples than Z (expressed in units) and is more independent of valency than effective ionic radii (IR). However, A_r, Z and IR are equivalent magnitudes, with strong collinearity (Table 6).

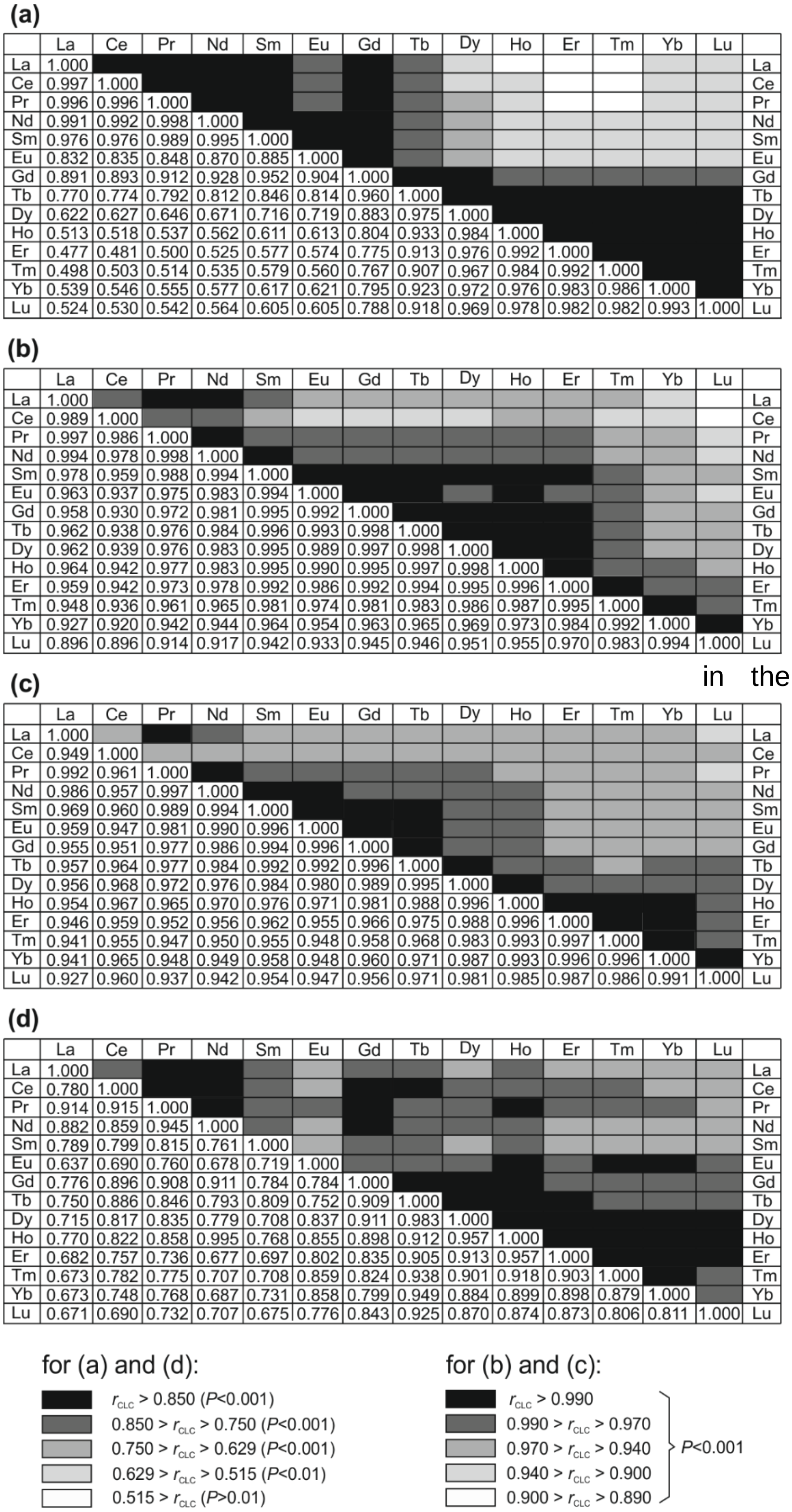

(a)

	La	Ce	Pr	Nd	Sm	Eu	Gd	Tb	Dy	Ho	Er	Tm	Yb	Lu	
La	1.000	█	█	█	█	▓	█	▓	░				░	░	La
Ce	0.997	1.000	█	█	█	▓	█	▓	░	░			░	░	Ce
Pr	0.996	0.996	1.000	█	█	▓	█	▓	▒	░			░	░	Pr
Nd	0.991	0.992	0.998	1.000	█	█	█	▓	▒	░	░	░	░	░	Nd
Sm	0.976	0.976	0.989	0.995	1.000	█	█	▓	▒	░	░	░	░	░	Sm
Eu	0.832	0.835	0.848	0.870	0.885	1.000	█	▓	▒	░	░	░	░	░	Eu
Gd	0.891	0.893	0.912	0.928	0.952	0.904	1.000	█	█	▓	▓	▓	▓	▓	Gd
Tb	0.770	0.774	0.792	0.812	0.846	0.814	0.960	1.000	█	█	█	█	█	█	Tb
Dy	0.622	0.627	0.646	0.671	0.716	0.719	0.883	0.975	1.000	█	█	█	█	█	Dy
Ho	0.513	0.518	0.537	0.562	0.611	0.613	0.804	0.933	0.984	1.000	█	█	█	█	Ho
Er	0.477	0.481	0.500	0.525	0.577	0.574	0.775	0.913	0.976	0.992	1.000	█	█	█	Er
Tm	0.498	0.503	0.514	0.535	0.579	0.560	0.767	0.907	0.967	0.984	0.992	1.000	█	█	Tm
Yb	0.539	0.546	0.555	0.577	0.617	0.621	0.795	0.923	0.972	0.976	0.983	0.986	1.000	█	Yb
Lu	0.524	0.530	0.542	0.564	0.605	0.605	0.788	0.918	0.969	0.978	0.982	0.982	0.993	1.000	Lu

(b)

	La	Ce	Pr	Nd	Sm	Eu	Gd	Tb	Dy	Ho	Er	Tm	Yb	Lu	
La	1.000	▓	█	█	▓	▒	▒	▒	▒	▒	▒	▒	░		La
Ce	0.989	1.000	▓	▓	▒	░	░	░	░	▒	▒	░	░		Ce
Pr	0.997	0.986	1.000	█	▓	▓	▓	▓	▓	▓	▓	▒	▒	░	Pr
Nd	0.994	0.978	0.998	1.000	█	▓	▓	▓	▓	▓	▓	▒	▒	░	Nd
Sm	0.978	0.959	0.988	0.994	1.000	█	█	█	█	█	█	▓	▒	▒	Sm
Eu	0.963	0.937	0.975	0.983	0.994	1.000	█	█	▓	█	▓	▓	▒	░	Eu
Gd	0.958	0.930	0.972	0.981	0.995	0.992	1.000	█	█	█	█	▓	▒	▒	Gd
Tb	0.962	0.938	0.976	0.984	0.996	0.993	0.998	1.000	█	█	█	▓	▒	▒	Tb
Dy	0.962	0.939	0.976	0.983	0.995	0.989	0.997	0.998	1.000	█	█	▓	▒	▒	Dy
Ho	0.964	0.942	0.977	0.983	0.995	0.990	0.995	0.997	0.998	1.000	█	▓	▓	▒	Ho
Er	0.959	0.942	0.973	0.978	0.992	0.986	0.992	0.994	0.995	0.996	1.000	█	▓	▓	Er
Tm	0.948	0.936	0.961	0.965	0.981	0.974	0.981	0.983	0.986	0.987	0.995	1.000	█	▓	Tm
Yb	0.927	0.920	0.942	0.944	0.964	0.954	0.963	0.965	0.969	0.973	0.984	0.992	1.000	█	Yb
Lu	0.896	0.896	0.914	0.917	0.942	0.933	0.945	0.946	0.951	0.955	0.970	0.983	0.994	1.000	Lu

(c)

	La	Ce	Pr	Nd	Sm	Eu	Gd	Tb	Dy	Ho	Er	Tm	Yb	Lu	
La	1.000	▒	█	▓	▒	▒	▒	▒	▒	▒	▒	▒	▒	░	La
Ce	0.949	1.000	▒	▒	▒	▒	▒	▒	▒	▒	▒	▒	▒	▒	Ce
Pr	0.992	0.961	1.000	█	▓	▓	▓	▓	▓	▒	▒	▒	▒	░	Pr
Nd	0.986	0.957	0.997	1.000	█	█	▓	▓	▓	▓	▒	▒	▒	▒	Nd
Sm	0.969	0.960	0.989	0.994	1.000	█	█	█	▓	▓	▒	▒	▒	▒	Sm
Eu	0.959	0.947	0.981	0.990	0.996	1.000	█	█	▓	▓	▒	▒	▒	▒	Eu
Gd	0.955	0.951	0.977	0.986	0.994	0.996	1.000	█	▓	▓	▒	▒	▒	▒	Gd
Tb	0.957	0.964	0.977	0.984	0.992	0.992	0.996	1.000	█	▓	▓	▒	▓	▓	Tb
Dy	0.956	0.968	0.972	0.976	0.984	0.980	0.989	0.995	1.000	█	▓	▓	▓	▓	Dy
Ho	0.954	0.967	0.965	0.970	0.976	0.971	0.981	0.988	0.996	1.000	█	█	█	▓	Ho
Er	0.946	0.959	0.952	0.956	0.962	0.955	0.966	0.975	0.988	0.996	1.000	█	█	▓	Er
Tm	0.941	0.955	0.947	0.950	0.955	0.948	0.958	0.968	0.983	0.993	0.997	1.000	█	▓	Tm
Yb	0.941	0.965	0.948	0.949	0.958	0.948	0.960	0.971	0.987	0.993	0.996	0.996	1.000	█	Yb
Lu	0.927	0.960	0.937	0.942	0.954	0.947	0.956	0.971	0.981	0.985	0.987	0.986	0.991	1.000	Lu

(d)

	La	Ce	Pr	Nd	Sm	Eu	Gd	Tb	Dy	Ho	Er	Tm	Yb	Lu	
La	1.000	▓	█	█	▓	▒	▓	▓	▒	▓	▒	▒	▒	▒	La
Ce	0.780	1.000	█	█	▓	▒	█	█	▓	▓	▓	▓	▒	▒	Ce
Pr	0.914	0.915	1.000	█	▓	▓	█	▓	▓	█	▓	▓	▓	▒	Pr
Nd	0.882	0.859	0.945	1.000	▓	▒	█	▓	▓	▓	▒	▒	▒	▒	Nd
Sm	0.789	0.799	0.815	0.761	1.000	▒	▓	▓	▒	▓	▒	▒	▒	▒	Sm
Eu	0.637	0.690	0.760	0.678	0.719	1.000	▓	▓	▓	█	▓	█	█	▓	Eu
Gd	0.776	0.896	0.908	0.911	0.784	0.784	1.000	█	█	█	▓	▓	▓	▓	Gd
Tb	0.750	0.886	0.846	0.793	0.809	0.752	0.909	1.000	█	█	█	▓	▓	▓	Tb
Dy	0.715	0.817	0.835	0.779	0.708	0.837	0.911	0.983	1.000	█	█	█	█	█	Dy
Ho	0.770	0.822	0.858	0.995	0.768	0.855	0.898	0.912	0.957	1.000	█	█	█	█	Ho
Er	0.682	0.757	0.736	0.677	0.697	0.802	0.835	0.905	0.913	0.957	1.000	█	█	█	Er
Tm	0.673	0.782	0.775	0.707	0.708	0.859	0.824	0.938	0.901	0.918	0.903	1.000	█	▓	Tm
Yb	0.673	0.748	0.768	0.687	0.731	0.858	0.799	0.949	0.884	0.899	0.898	0.879	1.000	▓	Yb
Lu	0.671	0.690	0.732	0.707	0.675	0.776	0.843	0.925	0.870	0.874	0.873	0.806	0.811	1.000	Lu

for (a) and (d):

█ $r_{CLC} > 0.850$ ($P<0.001$)
▓ $0.850 > r_{CLC} > 0.750$ ($P<0.001$)
▒ $0.750 > r_{CLC} > 0.629$ ($P<0.001$)
░ $0.629 > r_{CLC} > 0.515$ ($P<0.01$)
☐ $0.515 > r_{CLC}$ ($P>0.01$)

for (b) and (c):

█ $r_{CLC} > 0.990$
▓ $0.990 > r_{CLC} > 0.970$
▒ $0.970 > r_{CLC} > 0.940$
░ $0.940 > r_{CLC} > 0.900$
☐ $0.900 > r_{CLC} > 0.890$
} $P<0.001$

Figure 3. Matrix of Pearson correlation coefficients of couples of lanthanides concentrations (r_{CLC}) in the Mediterranean soils studied: (a) soil fine sand fraction (50–250 µm), (b) soil clay fraction (<2 µm), (c) free forms extracted from the soil clay fraction with citrate-dithionite-bicarbonate extract ($FF_{clay\text{-}CDB}$) and (d) free forms extracted from the soil clay fraction with oxalate ($FF_{clay\text{-}Ox}$).

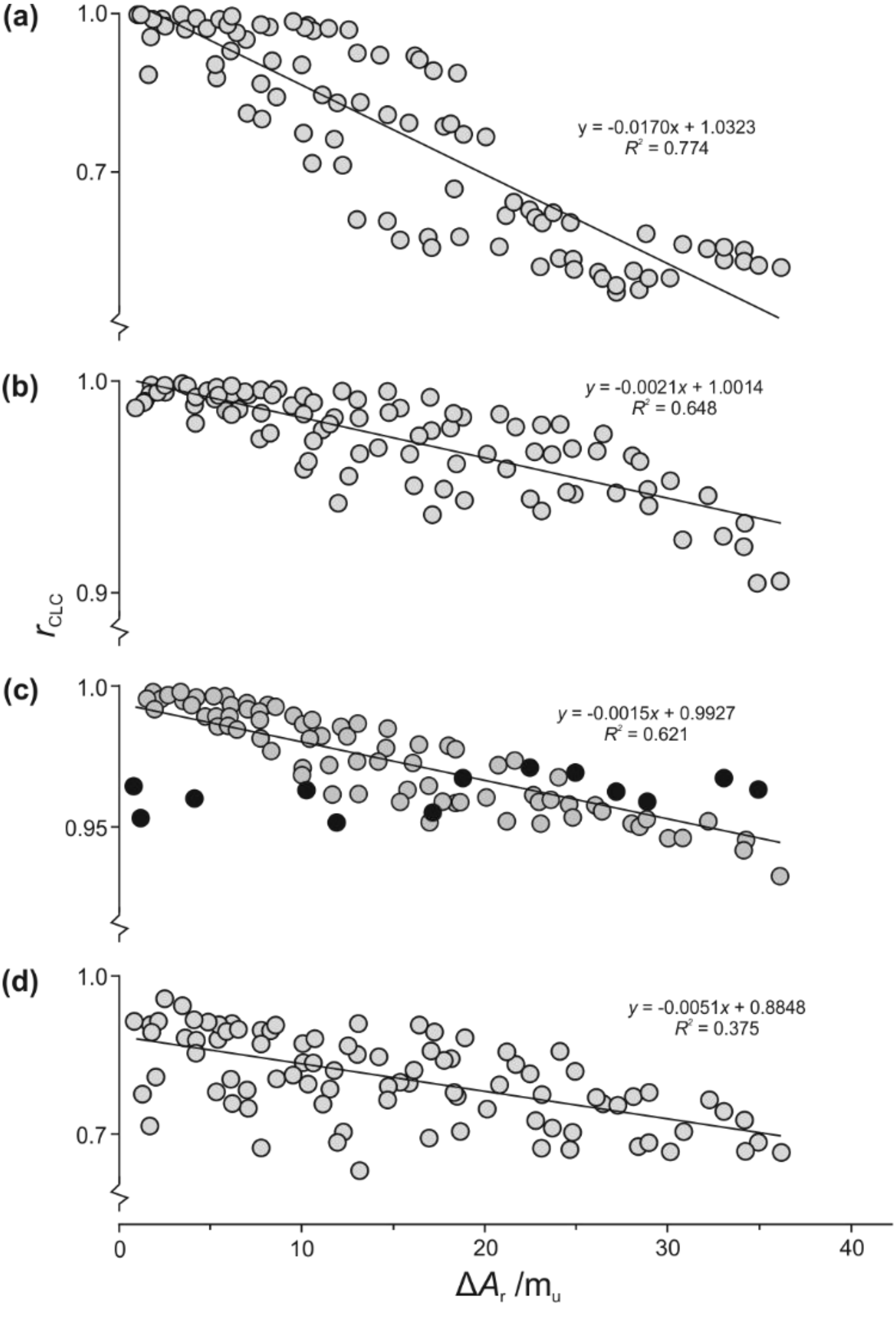

Figure 4. Relations between differences in atomic weight (ΔA_r) and Pearson correlation coefficients of couples of lanthanides concentrations (r_{CLC}) in: (a) soil fine sand fraction (50–250 µm), (b) soil clay fraction (<2 µm), (c) free forms extracted from the soil clay fraction with citrate-dithionite-bicarbonate ($FF_{clay\text{-}CDB}$). The black circles represent correlations with Ce and (d) free forms extracted from the soil clay fraction with oxalate ($FF_{clay\text{-}Ox}$). In all cases: *n* = 91; *P*< 0.001.

Table 6. Chemical and physical properties of lanthanides.

Name	Chemical symbol	Atomic number (Z)[1]	A_r /m_u[1,2]	Valency[3]	Effective ionic radii (IR) /pm[1,3]
Lanthanum	La	57	138.9	3	116.0
Cerium	Ce	58	140.1	3, 4	114.3
Praseodymium	Pr	59	140.9	3	112.6
Neodymium	Nd	60	144.2	3	110.9
Promethium[4]	Pm	61	-	3	-
Samarium	Sm	62	150.4	2, 3	107.9
Europium	Eu	63	152.0	2, 3	106.6
Gadolinium	Gd	64	157.3	3	105.3
Terbium	Tb	65	158.9	3, 4	104.0
Dysprosium	Dy	66	162.5	3	102.7
Holmium	Ho	67	164.9	3	101.5
Erbium	Er	68	167.3	3	100.4
Thulium	Tm	69	168.9	3	99.4
Ytterbium	Yb	70	173.1	2, 3	98.5
Lutetium	Lu	71	175.0	3	97.7

[1] There is strong collinearity between A_r and Z and IR: $Z = 0.3640 \cdot A_r + 7.1654$, $r = 0.997$; IR $= -0.4787 \cdot A_r + 180.6$, $r = 0.991$; ($n = 14$, $P< 0.001$). In the case of IR, the equivalence is due to the periodic rule known as 'lanthanide contraction'.

[2] A_r is the standard atomic weight (Meija *et al.*, 2016).

[3] Valency and effective ionic radii for $^{VIII}Ln^{+3}$ (Shannon, 1976).

[4] Pm has no stable isotopes

The equation of the straight line ΔA_r against r_{CLC} shows different values from its slope (m), depending on the granulometric fraction: (i) fine sand, $m = -0.0170$ and (ii) clay, –0.0021, $FF_{clay\text{-}CDB}$ –0.0015 and $FF_{clay\text{-}Ox}$, –0.0051. Thus, m becomes a granulometric differentiating characteristic.

In Figure 4(c), $FF_{clay\text{-}CDB}$, the behaviour of Ce is interesting because it shows slightly stronger correlation with the elements furthest from A_r (Ce against Tb to Lu: $0.955<r_{CLC}<0.968$; mean = 0.963; $\sigma_{n\text{-}1} = 0.005$) than with those nearest (Ce against La to Gd: $0.947<r_{CLC}<0.960$; mean = 0.954; $\sigma_{n\text{-}1} = 0.006$), and thus related better with the HREE than LREE. This is due to $FF_{clay\text{-}CDB}$ being free from forms of iron (goethite and haematite) where the process of oxidative scavenging of Ce takes place: part of the Ce^{3+} adsorbed on to Fe (hydr)oxides oxidizes to Ce^{4+}, producing a preferential desorption of the remaining Ce^{3+} (Bau, 1999; Pédrot *et al.*, 2015), and the Ce^{4+} accumulated in the $FF_{clay\text{-}CDB}$ behaves similarly to the HREE (Pédrot *et al.*, 2015). Further evidence for this is the preferential fractionation of Ce and HREE in $FF_{clay\text{-}CDB}$ described in the samples. Furthermore, Figure 3(c) shows a change in tendency of the r_{CLC} values in the correlations between Ce and Gd (0.951) and Ce with Tb (0.964), once again suggesting the gadolinium breaking effect (Chi *et al.*, 2006).

3.5. Evidence for fractionation and fingerprints of provenance

The La – 5×Sm – 10×Yb triangle (Figure 5) shows the population of the fine sand and clay plotted close together as a cluster (except for the fine sand of 4C2 of P4). As La represents the LREE, Sm the MREE and Yb the HREE, the fractionation of LREE and of HREE in fine sand compared with clay is demonstrated by proximity of the points of the former to the vertex of La and the points of the latter to 10×Yb. Figure 5 also shows that the cluster of samples includes the parent rocks of soils such as acidic igneous rocks, quaternary sediments and carbonate and metamorphic rocks, slightly separated from the alkaline igneous rocks. Initial interpretation could be that: (i) fine sand and clay are related genetically and (ii) the lanthanides in the soil originate from these parent rocks and could potentially be used as fingerprints of provenance. The point for the Spanish soils is close to the cluster; the Sahara–Sahel materials are also close, even coinciding with our clays.

The chondrite-normalized profiles of lanthanide concentration (Figure 2) also appear to show the genetic relation ‘fine-sand with clay’ and ‘fine-sand+clay with parent rock’. Fine sand and clay (Figure 2a,b) have profiles that are close together and the profiles of igneous (Figure 2e,f), sedimentary (Figure 2g) and metasedimentary (Figure 2h) rocks are included in the shaded area representing our samples.

Similarly, mean values of fine sand and clay of Σ(La, Ce, Nd, Sm, Eu, Yb, Lu) (only these seven Ln were analysed in all the studies on the geological materials of the Guadalquivir basin) (Figure 6) are within the mean values of the rocks of the Guadalquivir catchment area, although closer in value to those of the sedimentary and alkaline igneous rocks than to the others. The ratio of La_N/Yb_N (Figure 6) further emphasizes this tendency; the values for our samples form a cluster with a range of 7.2–15.7, within the range of the geological materials of the source area (range 3.3–20.4). The fine sand (range 9.8–15.7) had larger values than the clays (range 7.2–11.0) and would be closer to acidic igneous than sedimentary rocks. Notwithstanding this difference between fine sand and clay, it seems more likely that the fractionation of the lanthanides, rather than different source areas for the two fractions, resulted in the fine sand having a larger concentration of La than Yb. The Σ(La, Ce, Nd, Sm, Eu, Yb, Lu) (Figure 6) also shows that our samples have smaller values than the Sahara–Sahel materials or even the Spanish soils (both possible aeolian source areas). In contrast, La_N/Yb_N values do not explain the differences between our samples and the Sahara–Sahel materials or the Spanish soils as they are all between 6.9 and 14.3 (except clay of P1 and fine sand of P2, which are close).

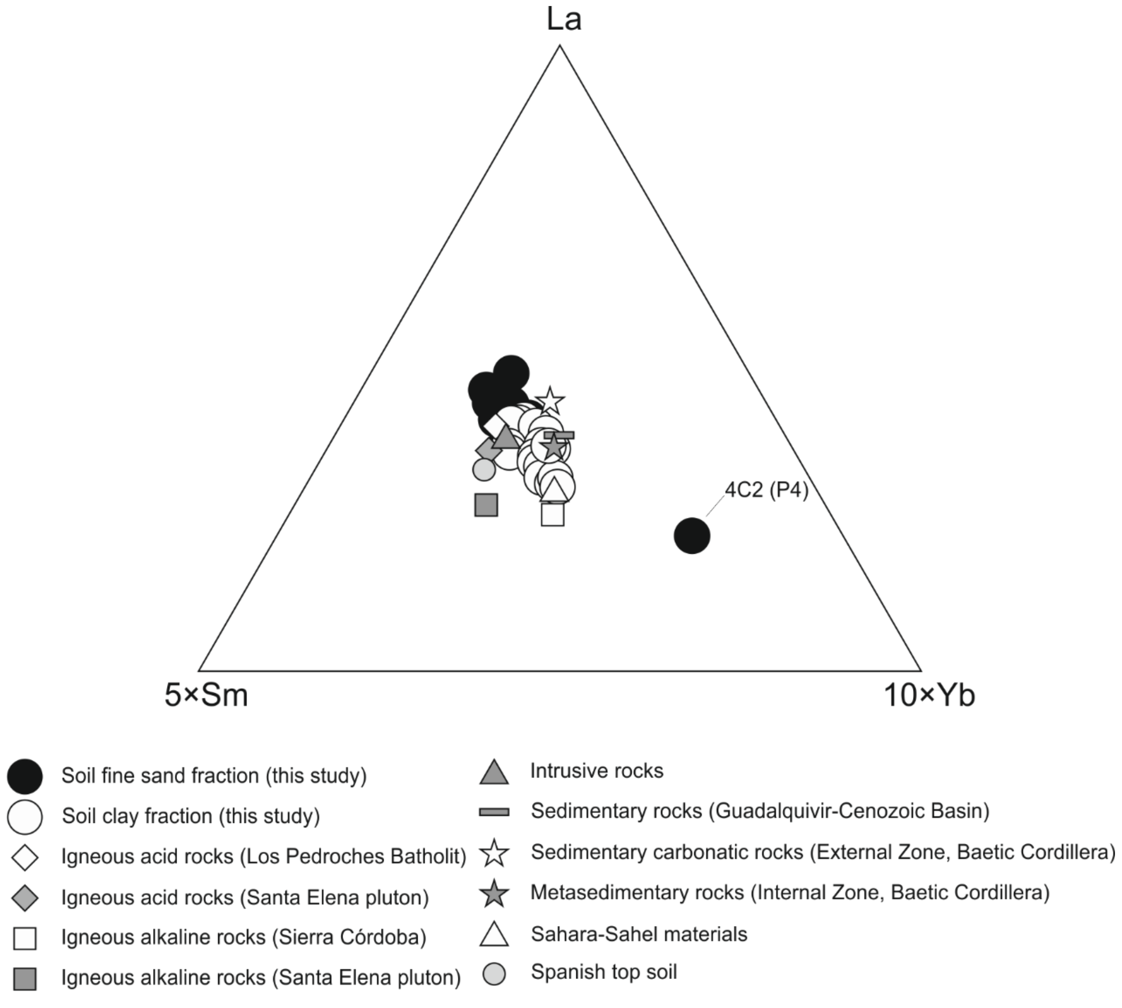

Figure 5. Triangular diagram of La–5Sm–10Yb for soil fine sand and clay fractions (all samples) and mean values of parent rocks of soils from the Guadalquivir catchment (igneous, sedimentary and metasedimentary rocks; Larrea *et al.*, 1992, 1994, 1995; Martínez-Ruiz, 1994; Carracedo *et al.*, 1997; Pin *et al.*, 2002; Pascual *et al.*, 2008; Jiménez-Espinosa *et al.*, 2016), Sahara–Sahel materials (Moreno *et al.*, 2006) and Spanish topsoil (Locutura *et al.*, 2012).

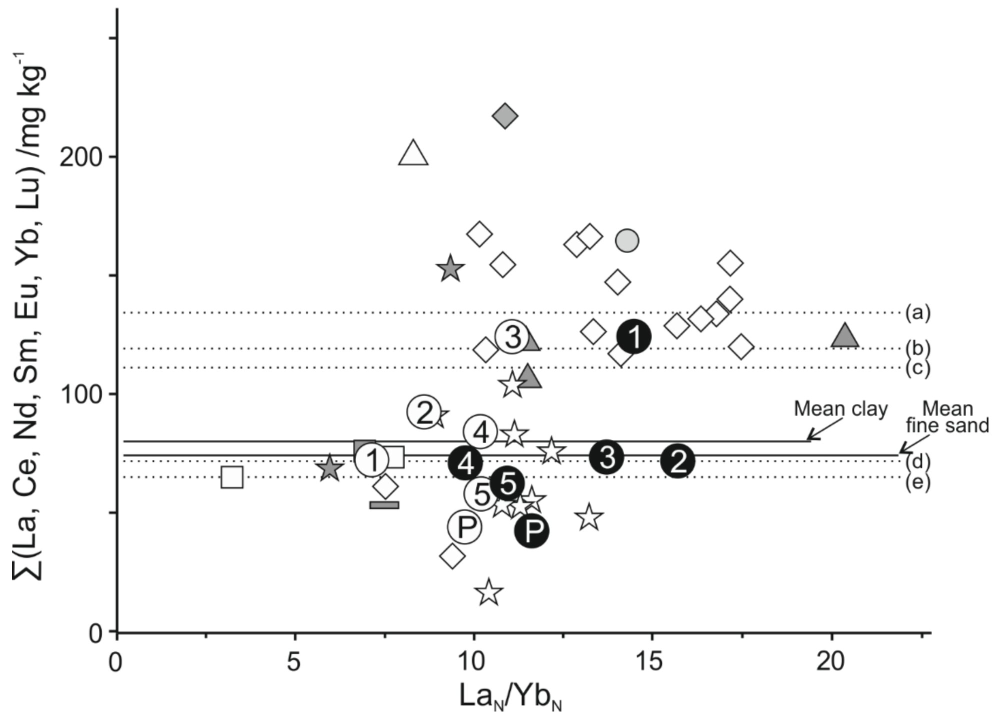

Figure 6. Plot of La_N/Yb_N against Σ(La, Ce, Nd, Sm, Eu, Yb, Lu) for soil fine sand and soil clay fractions (mean profile values) and all values for rocks from the Guadalquivir catchment (igneous, sedimentary and metasedimentary rocks; Larrea *et al.*, 1992, 1994, 1995; Martínez-Ruiz, 1994; Carracedo *et al.*, 1997; Pin *et al.*, 2002; Pascual *et al.*, 2008; Jiménez-Espinosa *et al.*, 2016), Sahara–Sahel materials (Moreno *et al.*, 2006) and Spanish topsoil (Locutura *et al.*, 2012). Symbols used are the same as in Figure 5; the numbers in the circles correspond to soil profile number and P to point bar sediment (PM). The horizontal lines within the figure correspond to the mean values of Σ(La,Ce,Nd,Sm,Eu,Yb,Lu) from: (a) acid igneous rocks (135 mg kg^{-1}), (b) intrusive rocks (119 mg kg^{-1}), (c) metasedimentary rocks (112 mg kg^{-1}), (d) alkaline igneous rocks (72 mg kg^{-1}) and (e) sedimentary carbonatic rocks (65 mg kg^{-1}); soil clay fraction (80 mg kg^{-1}) and soil fine sand fraction (75 mg kg^{-1}).

The ratio of Sm_N/Yb_N functions in a similar way to La_N/Yb_N (Figure 7). The fine sand had larger values than the clay. When La_N/Yb_N was plotted against Sm_N/Yb_N the points were aligned as expected because they have a common denominator, and La and Sm correlate well with each other (Figure 3). However, three families of points can be defined which fit significant straight lines: (i) igneous rocks, (ii) sedimentary and metamorphic rocks (metasedimentary) and (iii) our fine sand and clay samples. To fit a straight line to any of these families of points could be considered to show a lithological relation. Furthermore, the family of points of fine sand and clay is between the lines of the igneous and sedimentary+metamorphic rocks, indicating that both materials could act as parent materials. However, in this case, in contrast to Σ(La, Ce, Nd, Sm, Eu, Yb, Lu), the straight line is closer to the igneous rocks, including its slope value.

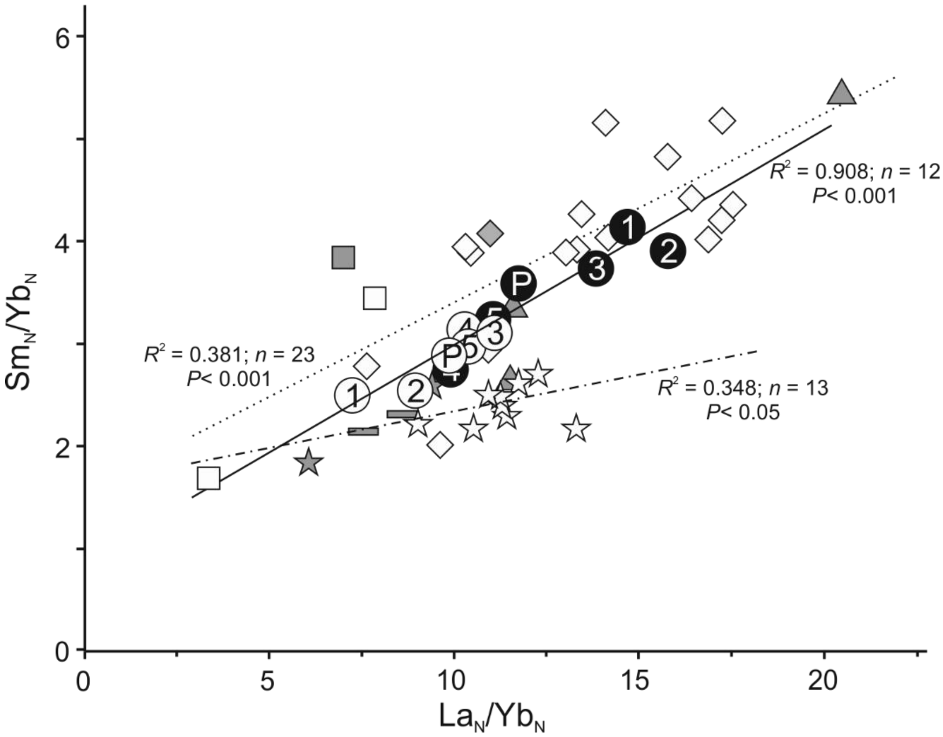

Figure 7. Plot of La_N/Yb_N against Sm_N/Yb_N for soil fine sand and clay fractions (mean profile values) and all values for rocks from the Guadalquivir catchment (igneous, sedimentary and metasedimentary rocks; Larrea *et al.*, 1992, 1994, 1995; Martínez-Ruiz, 1994; Carracedo *et al.*, 1997; Pin *et al.*, 2002; Pascual *et al.*, 2008; Jiménez-Espinosa *et al.*, 2016). Symbols used are the same as in Figure 5; the numbers in the circles correspond to soil profile numbers, and P corresponds to point bar sediment (PM). The lines (and adjacent equations) correspond to the straight lines of correlation for the population of samples of soil fine sand and soil clay fractions (continuous), the igneous rocks (dots) and the sedimentary and metasedimentary rocks (dots and dashes).

The Eu/Eu* anomaly had similar values for fine sand and clay (Table 3, Figure 8); in fact, the correlation between $Eu/Eu^*_{fine\ sand}$ and Eu/Eu^*_{clay} was positive and significant (r = 0.560; n = 24; P< 0.01). Furthermore, the anomaly was always negative (<1), a characteristic shared with the materials from the possible source areas (including aeolian) (Figure 8). The relative homogeneity of values between our soil and parent rocks (Figure 8) indicated that this geochemical ratio can be inherited from the sediment source and the weathering processes do not seem to have changed it (Mongelli *et al.*, 2014).

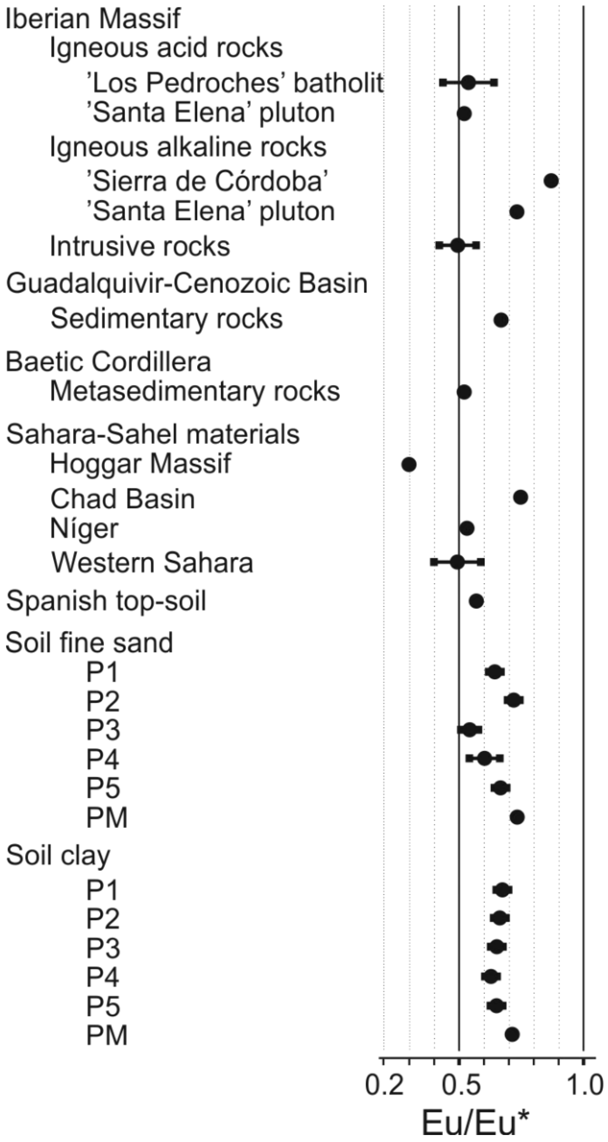

Figure 8. The Eu/Eu* values (mean and, in some cases, standard deviation) for soil fine sand and clay fractions (mean profile) and rocks from the Guadalquivir catchment (igneous, sedimentary and metasedimentary rocks), Sahara–Sahel materials and Spanish topsoil.

So far, we have not confirmed a genetic relation between our soil and the aeolian contributions from the Sahara–Sahel or Spanish soils (Figure 6). We focus now on the surface horizons (Ap) of our soils and the point bar sediment (PM), which, because they occupy the upper levels of the profile are more likely to receive these contributions (Figure 9). Our samples form a group, although differentiated between fine sand and clay because of fractionation of the lanthanides (between

LREE, concentrated in fine sand, and HREE, relatively concentrated in soil clay). Outside the group, the Sahara–Sahel materials occur at the lower edge of the Figure because these are richer in Yb and the genetic relation cannot be confirmed. However, the spot for Spanish soils was included in the cluster of our soil material and this soils could provide materials. Nevertheless, the problem is complex because in the Ap the lanthanide concentration of fine sand decreased (Table 2), whereas it increased in clay (Martín-García *et al.*, 2016).

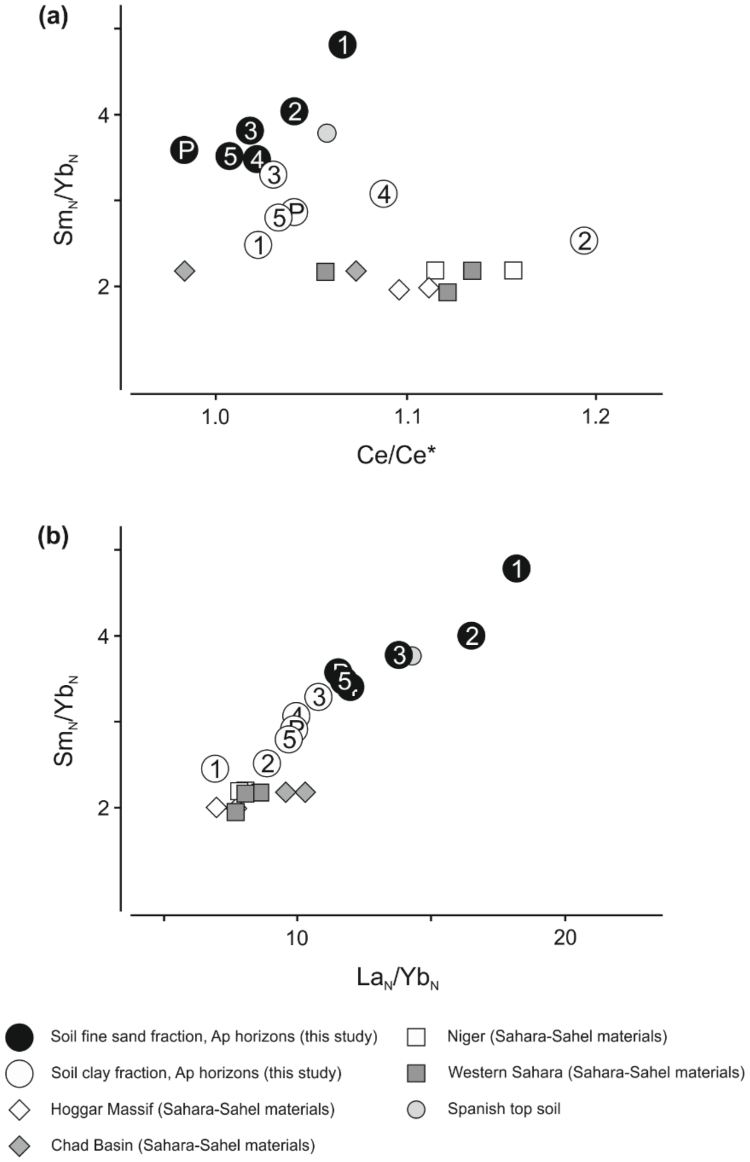

Figure 9 Plot of (a) Ce/Ce* against Sm_N/Yb_N and (b) La_N/Yb_N *versus* Sm_N/Yb_N for soil fine sand and clay fractions from Ap horizons (the numbers in the circles correspond to soil profile numbers) and PM (the letter P in the circle corresponds to point bar sediment PM) and Sahara–Sahel materials (Moreno *et al.*, 2006), and Spanish topsoil (Locutura *et al.*, 2012).

4. Conclusions

The free forms of clay ($FF_{clay\text{-}CDB}$ and $FF_{clay\text{-}Ox}$) showed a relative accumulation of lanthanides, with values >700 mg kg^{-1} (with respect to the mass of free form), thus demonstrating their role as scavengers of lanthanides.

Soil age (pre-Holocene versus Holocene) affects the behaviour of the lanthanides in all the fractions studied: in the fine sand ΣLREE concentration increased in the oldest, as did ΣHREE in the clay and its free forms. Furthermore, significant chronofunctions were formulated between lanthanide concentration and soil age in these cases: from La to Gd in fine sand and from Tb to Lu in the clay. These chronofunction results tend to support the granulometric fractionation cited, and, indirectly, provide data to confirm the presence of a "gadolinium breaking effect".

The concentrations between couples of lanthanides showed high collinearity, particularly in the clay and its free forms ($FF_{clay\text{-}CDB}$ and $FF_{clay\text{-}Ox}$), but only partly in the fine sand. This has permitted the description of a new periodic behaviour, valid for all the fractions analyzed: "the coefficient r_{CLC} significantly decreases with increasing separation between the lanthanide elements in the Periodic Table, estimated by ΔA_r".

The use of lanthanides as fingerprints of provenance using a variety of parameters and geochemical indices (La–Sm–Yb, Σ(La, Ce, Nd, Sm, Eu, Yb, Lu), La_N/Yb_N, Sm_N/Yb_N, Eu/Eu*, Ce/Ce*) concluded that there is a genetic relationship between all of them, although it has not been possible to determine the relative contribution of the different materials to our soils. For example, according to Σ(La, Ce, Nd, Sm, Eu, Yb, Lu) the preferential contribution, i.e. the greatest proximity of values, would be the sedimentary rocks, while, according to La_N/Yb_N vs. Sm_N/Yb_N it would be the igneous rocks.

The Ce fractionates in these soils, being concentrated in the clay fraction and its free forms (especially in $FF_{clay\text{-}CDB}$, where Ce/Ce* is >1) through the process of oxidative scavenging in the iron (hydr)oxides. It behaves more like the heavy lanthanides (HREE) than the light lanthanides (LREE) to which it belongs, showing higher values of r_{CLC} from Gd and Tb, which we attribute to the "gadolinium breaking effect". However, Eu was shown to be inherited from the materials of Guadalquivir catchment.

Acknowledgements: Sample preparation and chemical analysis were conducted by Emma Humphreys-Williams and Stanislav Strekopytov (Imaging and Analysis Centre, Natural History Museum, London). This work was supported by a grant from Ministerio de Economía, Industria y Competitividad de España (‘Tipologías de Suelos Mediterráneos versus Cuarzo. En la frontera del conocimiento edafogenético’; Ref. CGL2016-80308-P). The authors thank Professor Margaret A. Oliver, an anonymous editor and two anonymous reviewers for helpful comments and suggestions that improved the final manuscript. We also thank Robert Abrahams (Bsc) for revising the English language.

References

Aide, M. & Smith-Aide, C. 2003. Assessing soil genesis by rare-earth elemental analysis. Soil Science Society of America Journal, 67, 1470–1476.

Bau, M. 1999. Scavenging of dissolved yttrium and rare earths by precipitating iron oxyhidroxide: Experimental evidence for Ce oxidation, Y-Ho fractionation, and lanthanide tetrad effect. Geochimica et Cosmochimica Acta, 63, 67–77.

Blundy, J. & Wood, B. 2003. Partitioning of trace elements between crystals and melts. Earth and Planetary Science Letters, 210, 383–397.

British Geological Survey (BGS). 2011. Rare Earth Elements (https://www.bgs.ac.uk/downloads/start.cfm?id=1638).

Calero, J., Delgado, R., Delgado, G. & Martín-García, J.M. 2008. Transformation of categorical field soil morphological properties into numerical properties for the study of chronosequences. Geoderma, 145, 278–287.

Calero, J., Delgado, R., Delgado, G. & Martín-García, J.M. 2009. SEM image analysis in the study of a soil chronosequence on fluvial terraces of the middle Guadalquivir (southern Spain). European Journal of Soil Science, 60, 465–480.

Calero, J., Martín–García, J.M., Delgado, G., Aranda, V. & Delgado, R. 2013. A nano-scale study in a soil chronosequence from southern Spain. European Journal of Soil Science, 64, 192–209.

Carracedo, M., Larrea, F.J., Alonso-Olazabal, A. & Gil-Ibarguchi, J.I. 1997. The relationship between the plutonic intrusions and the dyke swarm in the Los Pedroches batholith (Iberian Massif, Spain): Dykes as a paleotectonic and paleostress indicators. Cadernos do Laboratorio Xeolóxico de Laxe, 22, 229–246.

Chang, C., Li, F., Liu, C., Gao, J., Tong, H. & Chen, M. 2016. Fractionation characteristics of rare earth elements (REEs) linked with secondary Fe, Mn, and Al minerals in soils. Acta Geochimica, 35, 329–339.

Chen, L.M., Zhang, G.L. & Jin, Z.D. 2014. Rare earth elements of a 1000-year paddy soil chronosequence: implications for sediment provenances. Parent material uniformity and pedological changes. Geoderma, 230, 274–279.

Chi, R.A., Dai, Z.X., Xu, Z.G., Wu, Y.X. & Wang, C.W. 2006. Correlation analysis on partition of rare earth in ion-exchangeable phase form weathered crust ores. Transactions of Nonferrous Metals Society of China, 16, 1421–1425.

Delgado, R., Martín-García, J.M., Oyonarte, C. & Delgado, G. 2003. Genesis of the terrae rossae of the Sierra Gádor (Andalusia, Spain). European Journal of Soil Science, 54, 1–16.

Gregory, T., Joy, K.H., Strekopytov, S. & Curran, N.M. 2017. Geochemistry and petrology of howardite Miller Range 11100: A lithologically diverse piece of the Vestan regolith. Meteoritics & Planetary Science, 52, 206–224.

Guastoni, A., Nestola, F., Ferraris, C. & Parodi, G. 2012. Xenotime-(Y) and Sn-rich thortveitite in miarolitic pegmatites from Baveno, Southern Alps, Italy. Mineralogical Magazine, 76, 761–767.

Harden, J.W. 1982. A quantitative index of soil development from field descriptions: examples from a chronosequence in central California. Geoderma, 28, 1–28.

Hu, Z., Haneklaus, S., Sparovek, G. & Schnug, E. 2006. Rare earth elements in soils. Communications in Soil Science and Plant Analysis, 37, 1381–1420.

Huang, C. & Gong, Z. 2001. Geochemical implication of rare earth elements in process of soil development. Journal of Rare Earths, 19, 57–62.

Jiménez-Espinosa, R., Jiménez-Millán, J. & García-Tortosa, F.J. 2016. Upper-Pleistocene terrace deposits in Mediterranean climate: geomorphological and source-rock control on mineral and geochemical signatures (Betic Cordillera, SE Spain). Journal of Iberian Geology, 42, 187–200.

Kerr, A. & Rafuse, H. 2012. Rare-earth Element (REE) Geochemistry of the Strange Lake Deposits: Implications for Resource Estimation and Metallogenic Models. Report No 12-1. Newfoundland and Labrador Department of Natural Resources, Geological Survey Branch, St. John's, Canada.

Larrea, F.J., Carracedo, M., Cueto, L.A., Quesada, C., Gil-Ibarguchi, J.I., Fernández, F.J. & Ortega, L.A. 1992; Petrology and geochemistry of Cardeña-Virgen de La Cabeza pluton (batholith of Los Pedroches). Cadernos do Laboratorio Xeolóxico de Laxe, 17, 209–222.

Larrea, F.J., Carracedo, M., Ortega, L.A. & Gil-Ibarguchi, J.I. 1994. The Linares granite (Jaén): cartography, petrology and geochemistry. Cadernos do Laboratorio Xeolóxico de Laxe, 19, 335–346.

Larrea, F.J., Carracedo, M., Ortega, L.A. & Gil-Ibarguchi, J.I. 1995. The Santa Elena stock (Jaén). An intrusion genetically independent from the magmatic association of the Los Pedroches Batolith. Cadernos do Laboratorio Xeolóxico de Laxe, 20, 151–166.

Laveuf, C. & Cornu, S. 2009. A review on the potentiality of rare earth elements to trace pedogenetic processes. Geoderma, 154, 1–12.

Laveuf, C., Cornu, S., Guilerme, L.R.G. & Juillot, F. 2012. The impact of redox conditions on the rare earth element signature of redoximorphic features in a soil sequence developed from limestone. Geoderma, 170, 25–38.

Marques, R., M. Prudencio, M.I., Dias, M.I. & Rocha, F. 2011. Patterns of rare earth and other trace elements in different size fractions of clays of Campanian–Maastrichtian deposits from the Portuguese western margin (Aveiro and Taveiro Formations). Chemie der Erde, 71, 337–347.

Martínez-Ruiz, F. 1994. Geoquímica y mineralogía del tránsito Cretácico-Terciario en las Cordilleras Béticas y en la Cuenca Vasco-Cantábrica. Doctoral dissertation, Universidad de Granada, Granada.

Martín-García, J.M., Sánchez-Marañón, M., Calero, J., Aranda, V., Delgado, G. & Delgado, R. 2016. Iron oxides and rare earth elements in the clay fractions of a soil chronosequence in southern Spain. European Journal of Soil Science, 67, 749–762.

McDonough,W.F. & Sun, S. 1995. The composition of the Earth. Chemical Geology, 120, 223–253.

Meija, J., Coplen, T.B., Berglund, M., Brand, W.A., De Bievre, P., Groning, M. et al. 2016. Atomic weights of the elements 2013 (IUPAC Technical Report). Pure and Applied Chemistry, 88, 265–291.

Mongelli, G., Paternoster, M., Rizzo, G. & Sinisi, R. 2014. Trace elements and REE fractionation in subsoils developed on sedimentary and volcanic rocks: case study of the Mt. Vulture area, southern Italy. International Journal of Earth Sciences, 103, 1125–1140.

Moreno, T., Querol, X., Castillo, S., Alastuey, A., Cuevas, E., Herrmann, L. et al. 2006. Geochemical variations in aeolian mineral particles from the Sahara-Sahel Dust Corridor. Chemosphere, 65, 261–270.

Noack, C.W., Jain, J.C., Stegmeier, J., Hakala, J.A. & Karamalidis, A.K. 2015. Rare earth element geochemistry of outcrop and core samples from the Marcellus Shale. Geochemical Transactions 16, 6, doi: 10.1186/s12932-015-0022-4.

Och, L.M., Müller, B., Wichser, A., Ulrich, A., Vologina, E.G. & Sturm, M. 2014. Rare earth elements in the sediments of Lake Baikal. Chemical Geology, 376, 61–75.

Onac, B.P., Pedersen, R.B. & Tysseland, M. 1997. Presence of rare-earth elements in black ferromanganese coatings from Vântului Cave (Romania). Journal of Cave and Karst Studies, 59, 128–131.

Pascual, E., Donaire, T. & Pin, C. 2008. The significance of microgranular enclaves in assessing the magmatic evolution of a high-level composite batholith: A case on the Los Pedroches Batholith, Iberian Massif, Spain. Geochemical Journal, 42, 177–198.

Pédrot, M., Dia, A., Davranche, M. & Gruau, G. 2015. Upper soil horizons control the rare earth element patterns in shallow groundwater. Geoderma, 239–240, 84–96.

Pin, C., Liñán, E., Pascual, E., Donaire, T. & Valenzuela, A. 2002. Late Neoproterozoic crustal growth in the European Variscides: Nd isotope and geochemical evidence from the Sierra de Córdoba Andesites (Ossa-Morena Zone, Southern Spain). Tectonophysics, 352, 133–151.

Rollinson, H.R. 1993. Using Geochemical Data: Evaluation, Presentation, Interpretation. Prentice Hall, Harlow, England.

Salminen, R. (Ed.) 2005. Geochemical Atlas of Europe. Part 1: Background Information, Methodology and Maps (IUGS/IAGC; http://weppi.gtk.fi/publ/foregsatlas/index.php).

Samonil, P., Danek, P., Schaetzl, R.J., Vasickova, I. & Valtera, M. 2015. Soil mixing and genesis as affected by tree uprooting in three temperate forests. European Journal of Soil Science, 66, 589–603.

Shannon, R.D. 1976. Revised effective ionic radii and systematic studies in interatomic distances in halides and chalcogenides. Acta Crystallographica, A32, 751–767.

Torres-Ruiz, J., Pesquera, A., Gil-Crespo, P.P. & Velilla, N. 2003. Origin and petrogenetic implication of turmaline-rich rocks in the Sierra Nevada (Betic Cordillera, southeastern Spain). Chemical Geology, 197, 55–86.

Wang, G., Li, J., Ravi, S., Van Pelt, R.S., Costa, P.J.M. & Dukes, D. 2017. Tracer techniques in aeolian research: Approaches, applications, and challenges. Earth-Science Reviews, 170, 1–16.

Wen, X.Y., Huang, C.M., Tang, Y., Gong-Bo, S.L., Hu, X.X. & Wang, Z.W. 2014. Rare earth elements: a potential proxy for identifying the lacustrine sediment source and soil erosion intensity in karst areas. Journal of Soils and Sediments, 14, 1693–1702.

Chapter 5:

Intrusions of dust and iberulites in Granada basin (Southern Iberian Peninsula).

Genesis and formation of atmospheric iberulites

Intrusions of dust and iberulites in Granada basin (Southern Iberian Peninsula). Genesis and formation of atmospheric iberulites

J. Párraga[a], J.M. Martín-García[a], G. Delgado[a], A. Molinero-García[a]*, A. Cervera-Mata[a], I. Guerra[b], M.V. Fernández-González[a], F.J. Martín-Rodríguez[a], H. Lyamani[c,d], J.A. Casquero-Vera[c,d], A. Valenzuela[c,d], F.J. Olmo[c,d] and R. Delgado[a]

[a] Department of Soil Science and Agriculture Chemistry. Faculty of Pharmacy, University of Granada

[b] Unidad de Microscopía Electrónica de Barrido de alta resolución y Microanálisis. Centro de Instrumentación Científica

[c] Andalusian Institute for Earth System Research, IISTA-CEAMA, University of Granada, Junta de Andalucía, Granada 18006, Spain

[d] Department of Applied Physics, University of Granada, Granada 18071, Spain

*****Author for correspondence. Email: amolinerogarcia@ugr.es

Published on:

Atmospheric Research, 248 (2021), 105260.

https://doi.org/10.1016/j.atmosres.2020.105260

Impact Factor (JCR):

Journal Impact Factor, JIF (2021): **5.965**; JIF Percentil in Category (Meteorology and atmospheric sciences - Scie): **81.38 (Q1)**

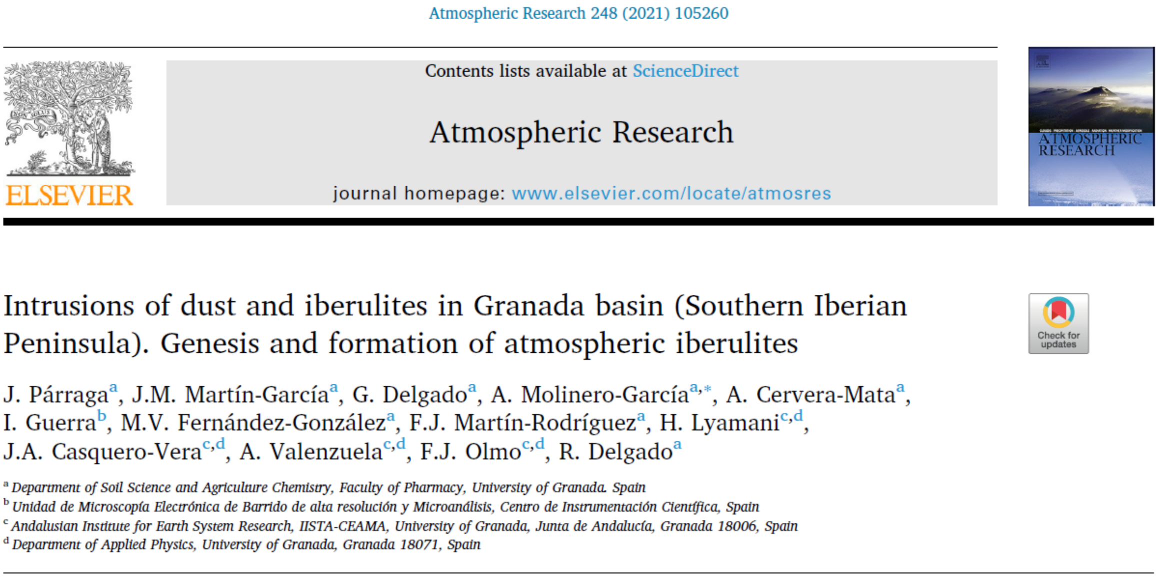

Atmospheric Research 248 (2021) 105260

Contents lists available at ScienceDirect

Atmospheric Research

journal homepage: www.elsevier.com/locate/atmosres

Intrusions of dust and iberulites in Granada basin (Southern Iberian Peninsula). Genesis and formation of atmospheric iberulites

J. Párraga[a], J.M. Martín-García[a], G. Delgado[a], A. Molinero-García[a,*], A. Cervera-Mata[a], I. Guerra[b], M.V. Fernández-González[a], F.J. Martín-Rodríguez[a], H. Lyamani[c,d], J.A. Casquero-Vera[c,d], A. Valenzuela[c,d], F.J. Olmo[c,d], R. Delgado[a]

[a] Department of Soil Science and Agriculture Chemistry, Faculty of Pharmacy, University of Granada. Spain
[b] Unidad de Microscopía Electrónica de Barrido de alta resolución y Microanálisis, Centro de Instrumentación Científica, Spain
[c] Andalusian Institute for Earth System Research, IISTA-CEAMA, University of Granada, Junta de Andalucía, Granada 18006, Spain
[d] Department of Applied Physics, University of Granada, Granada 18071, Spain

Abstract

Fourteen samples of deposited atmospheric dust collected during desert dust intrusions over Granada in the summer of 2010 are studied here. During these atmospheric dust events the PM10 ranged from 25 µg m^{-3} to 200 µg m^{-3}, surpassing occasionally the standard limit (50 µg m^{-3}) established by the European Union Directive as a risk for the human health. The mineralogical composition of the dust samples is very heterogeneous, showing that the origin of collected particles is from north-northwest of Africa and local/regional soils. The analyzed dust samples contain between 1 and 9% of iberulites, polymineral spherical particles with diameter between 34 and 111 µm. New compositional results obtained by mapping chemical elements and mineral compositions of iberulites with VPSEM-EDEX technology allowed as to go further than previous studies and provide new insight on the iberulites genesis. The SEM-microstructure analysis of the iberulites and the compositional results obtained by VPSEM-EDEX technique showed that clay and sulphur components are important in determining their spherical shapes. The analysis also shows that iberulites present a typical vortex at one of the poles and an external covering by nano-clays in laminar clusters, a form of rind and a core internal with sizes less than 10 microns. On the other hand, the micromorphological analysis evidences that the bacteria and its polymeric exudates participate in the iberulite genesis, acting as aggregation agents and contributing to its protection and compensating its fragility. The role of bacteria and its polymeric exudates in the iberulite genesis has not been described previously, and it would explain the flux, transport and survival of tropospheric microorganisms over long distances. These new observations and finding led us to take into account the role of bacteria in iberulite genesis and to reconsider the previous hypothesis regarding the iberulite genesis proposed in previous works.

Keywords: Saharan dust; Iberulites genesis; Rare Earth Elements; Bacterial EPS; Human Health.

Highlights:

- Iberulite, microspherulite with vortex, both mineral and microorganisms assemblage.

- The Clay and the S components are decisive in iberulites spherical shape.
- Bacteria act as an aggregation agent for iberulites.
- Micromorphological evidences the bacteria implication in the iberulite genesis.

Graphical Abstract

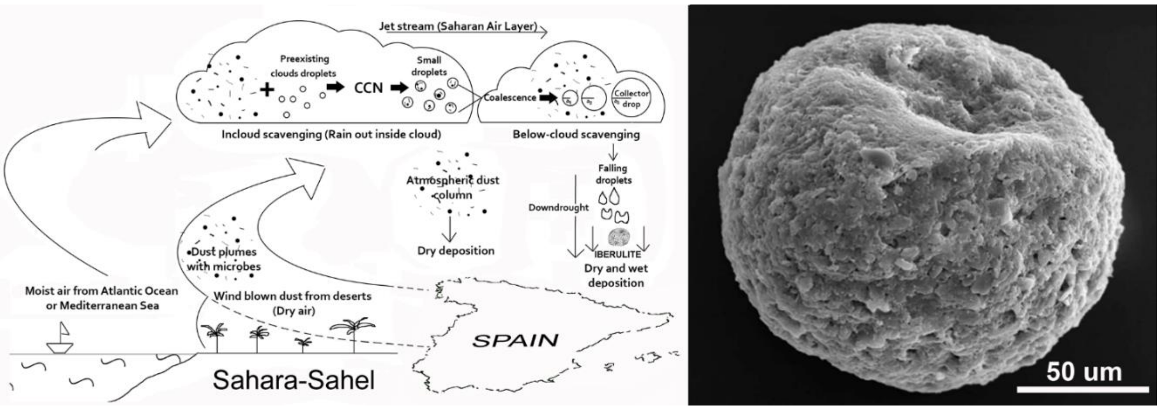

Sequence of iberulite formation vía "cloud processing" with bacterial activity

1. Introduction

Every year between 1 and 3 billion tons of dust are emitted into the atmosphere from arid and semi-arid areas, particularly from the Sahara and Sahel (North Africa), which are responsible for 50-70% of the global dust emissions. Due to its proximity to the African continent, the Iberian Peninsula is frequently affected by desert dust intrusions, especially in the summer season (e.g., Valenzuela et al., 2012a). This dust intrusion phenomenon also affects a large area of Europe, with annual dust mass concentrations between 80 and 120 Tg (e.g., Pey et al., 2013).

During major dust intrusions from North Africa the concentrations of PM10 (particles with an aerodynamic diameter < 10 μm) often exceed the European PM10 air quality standard limits in different European countries (Rodriguez et al., 2001; Reyes et al., 2014), negatively affecting public health (Varga et al., 2014; Oduber et al., 2019). In addition to the effects on human and animal health, the mineral dust also affects climate and ecosystems (e.g., Jeong et al., 2016).

In order to better understand the effects of the dust on climate, atmospheric chemistry, biogeochemical cycles and primary biological production more dust mineralogical studies are still needed (e.g., Engelbrecht et al., 2016). In this sense, the aerosol mineralogy is a difficult property to study due to the difficulties inherent in studying very small objects, such as dust particles, using highly specific techniques including Scanning Electron Microscopy (SEM), Trasmisision Electron Microscopy (TEM) and Energy Dispersive X-Ray Spectroscopy (EDX).

On the other hand, the study of the geographical origin of atmospheric dust is an innovative topic of great interest. Scheuvens et al. (2013) used the mineralogical composition of African dust to detect the origin of transported dust. The rare earth elements (REE: lanthanides and yttrium) are also good dust tracers of geochemical processes and dust origin as they are closely related to the materials of the source area (e.g., Wang et al., 2017). However, there are few REE studies of the atmospheric dust deposited in the Iberian Peninsula. Another method most frequently employed by the scientific community to determine the origin of desert dust is that based on the analysis of the back-trajectories of air masses (e.g., Lyamani et al., 2005; Valenzuela et al., 2012a).

The atmospheric African dust reaching Spain contains up to 47% of giant polymineral particles with diameters between 50 and 200 µm, generated by atmospheric aggregation. These particles were named iberulites by Díaz-Hernández and Párraga (2008). Iberulites were observed in Mallorca (Spain) by Fiol et al. (2001, 2005) and in Tenerife (Canary Islands, Spain) by Cuadros et al. (2015). Furthermore, iberulites were also observed in atmospheric air masses from Saudi Arabia (Posfai et al., 2013) and in Volgograd (Russia) (Kuzmichev et al., 2017). The potential of iberulites to adversely affect human/animals health is due to the fact that they are constituted by potentially harmful micro- and nanometric breathable particles (Vahlsing and Smith, 2012) and they are able to transport biological materials, thus converting them into potential vehicles for pathological infections of humans and animals (Párraga et al., 2013). The microstructure of these aeolian particles is closely related to their genesis in the atmosphere and to processes occurring when they fall to the ground (Díaz-Hernández and Párraga, 2008; Jeong and Nousiainen, 2014; Jeong et al., 2014; Díaz-Hernández and Sánchez-Navas, 2016). Until now, there is little knowledge about the transformation processes as well as about mineralogical and biological compositions of iberulites and, therefore, more studies are needed to improve our knowledge about them.

The main aim of the present work is to explore the mineralogical composition of deposited atmospheric aerosol particles during African dust intrusions over the city of Granada (Spain). We will also study their REE composition, which has not yet been studied during atmospheric dust intrusions over southern Spain. In addition, special emphasis will be put on the identification of source regions of deposited mineral dust using mineralogy and REE composition as well as air mass back-trajectories. Finally, we will study the iberulites during the African dust events and their genesis by bacterial mechanisms, not studied previously.

2. Sampling and methods

2.1 Sampling site

Experimental measurements were obtained in the metropolitan area of Granada (37º 08’ 59” N, 03º 37’ 59” W, 650 m a.s.l.). Granada is a non-industrialized Spanish city with a population of about 250.000, located in the southern Iberian Peninsula, around 50 km from the Mediterranean Sea. Climate is semi-arid to dry ombrotype and meso-Mediterranean thermotype with marked cycles of drought and precipitation every 5 to 10 years. Granada is situated in a natural basin surrounded by mountains (1000 - 3398 m a.s.l.) of siliceous dolomitic limestone. Soils are mainly calcareous Fluvisols, under irrigation or dedicated to olive groves. Due to its proximity to the African continent, Granada is frequently affected by Saharan dust intrusions. The number of African dust intrusions is quite high, especially during summer, with a frequency up to 45% of the days in June-August (e.g., Valenzuela et al., 2012b). Usually, mineral dust particles are transported over Granada at high altitudes of up to 5500 m a.s.l. However, in some cases African dust reaches surface ground level due to dry or wet deposition (e.g., Calvo et al., 2010). The local aerosol sources are mainly the heavy traffic, the domestic heating and the re-suspension of material available on the ground, especially during warm season. The reduced rainfall and the dryness of the terrain can increase the contribution of local mineral dust (e.g., Lyamani et al., 2010).

2.2. Collection of dust, iberulite and soil samples

The sampling station, with collectors of deposited atmospheric dust (DAD) by dry deposition, was located on the roof terrace of a building some 10 m above the ground on a mast 2 m higher than the terrace (Díaz-Hernández and Parraga, 2008). The terrace was covered with coarse gravel (20-40 mm diameter), which, to a large extent, prevent the resuspension of the dust deposited there. The station has been in operation since 2004. Sampling was carried out weekly. Deposited dust concentration was determined by weight. In the present study, 14 DAD samples collected during atmospheric dust intrusions over Granada in the summer of 2010 are analyzed in more detail (Table 1). It should be noted that we opted to analyze DAD samples from the summer of 2010 because this year was the year with the most dust intrusions in the southern Iberian Peninsula, according to the CALIMA network (www.calima.ws/2010.pdf).

Table 1. Granulometric characteristics. Deposited dust[a] and iberulites.

		Granulometric fraction (% volumen)			Iberulites	
Sample	Sampling period	>500 µm	200 - 500 µm	<200 µm	% [b]	Mean apparent diameter (µm)
JP01	01/06/2010 - 03/07/2010	1.7	1.3	97.0	1.6	53
JP02	05/07/2010 - 12/07/2010	0.5	4.6	94.9	9.2	61
JP03	13/07/2010 - 20/07/2010	1.8	9.7	88.5	3.1	57
JP04	21/07/2010 - 27/07/2010	0.9	4.6	94.5	4.7	77
JP05	28/07/2010 - 02/08/2010	3.8	7.4	88.8	1.5	94
JP06	03/08/2010 - 10/08/2010	1.1	6.8	92.1	2.7	59
JP07	11/08/2010 - 17/08/2010	0.9	3.8	95.3	1.9	48
JP08	18/08/2010 - 24/08/2010	3.0	11.0	86.0	1.6	48
JP09	25/08/2010 - 31/08/2010	2.0	6.3	91.7	1.1	49
JP10	01/09/2010 - 08/09/2010	2.3	4.9	92.8	2.7	34
JP11	09/09/2010 - 15/09/2010	1.7	7.8	90.5	0.9	51
JP12	16/09/2010 - 29/09/2010	3.8	5.4	90.8	4.4	53
JP13	30/09/2010 - 14/10/2010	2.0	3.4	94.6	0.7	59
JP14	15/10/2010 - 31/10/2010	2.3	3.7	94.0	0.8	111

[a] Data obtained by laser granulometry (this study)

[b] Percentage of iberulites in particles observed

The quantity and size of iberulites (Table 1) were estimated from digital images (program Analysis-getIT), counting around 500 dust particles from each sample. These particles were isolated from the fine fraction (<200 µm) (obtained by sieving the dust) in the object field of a stereomicroscope (Olympus B061) using a sleeved needle.

In order to study bacteria, soil samples (calcareous Fluvisol) were collected during summer 2010 close to the station (37.15º N, 3.63º W) with horizon Ap (0-20 cm) being selected. For the mean mineralogical compositions of the most common soils in Granada we used the data reported by Márquez (2012), who studied a soil of the same type and close to our studied soil, with an Ap horizon of sandy loamy texture (35.6% sand, 47.8% silt and 16.6% clay), 1.70% organic carbon, 0.19% N, pH (water) 7.3, 21% $CaCO_3$ and totally saturated in exchange cations.

2.3. Suspended particulate matter

The measurements of the concentration (in µg m^{-3}) of atmospheric particulate matter PM10 were taken at the EMEP (cooperative programme for the monitoring and evaluation of the long range transmission of air pollutants in Europe) background station in Viznar, 10 km from the city. The PM10 dataset registered at this background station are very useful for the detection of long range transported aerosol particles such as Saharan mineral dust. Also, these data can give us more insight about the impact of the different African dust intrusions on background aerosol concentration over Granada metropolitan area. As the station is an EMEP station, site selection criteria, sampling, analysis and data quality control protocols are pre-established (EMEP, 2001).

2.4. Methodology. Analysis of deposited dust and iberulites

A more detailed description of the sampling methodology, sample treatment and analytical procedures used here is given by Díaz-Hernández and Párraga (2008) and Párraga et al. (2013). A brief description of the methods and instrumentation used in this study is provided here. In this work we also included new analytical methods for the determination of some REE contents and news in the study of the mineralogical composition by X-ray diffraction (XRD) and Electron Microscopy techniques.

The size distribution of particles collected in DAD samples was obtained by Wet dispersion laser diffraction (Mastersizer 2000, Malvern Instruments Ltd., UK). For the analysis of the mineralogical composition of DAD samples we used XRD technique. The diffraction patterns were obtained by Brucker AXS D8 ADVANCE instrument using Cu Kα radiation by continuous scan between 3 and 70º 2θ with velocity of 2º min^{-1}. The obtained diffractograms were interpreted using the XPowder Program (Martín, 2004). Percentages of mineral contents were estimated using intensity factors of Schultz (1964), Barahona (1974) and Delgado et al. (1982). The presence of palygorskite was investigated with the peak at 0.63 nm (basal distances d_{200}; 15% intensity). For identification of dust origin the obtained mineral compositions are presented in the triangle Carbonates (calcite + dolomite) – Tectosilicates (quartz + K-feldspar + plagioclases) – Phylllosilicates + Fe oxides (hematite + goethite) (Calero et al., 2009).

On other hand, the REE contents in DAD samples were determined by ICP-MS method (inductively coupled plasma mass spectrometry) with quadrupole ion filter ICPMS NEXION 300D PERKIN-ELMER, USA. For ICP-MS analysis, the collected samples were previously disaggregated in HNO_3 and HF. The REE were grouped into: Light (LREE: La, Ce, Pr, Nd), Medium (MREE: Sm, Eu, Gd, Tb, Dy) and Heavy REE (HREE: Ho, Er, Tm, Yb, Lu). Note that Y was not considered in this classification. REE concentrations were chondrite-normalized (using standard CI chondrite of McDonough and Sun, 1995), with Y represented between Ho and Er (Korotev, 2009). After that, we calculated the geochemical indices $HREE_N/LREE_N$ and $MREE_N/LREE_N$ and the anomalies Ce/Ce*, Eu/Eu* and Y/Y* ($Ce/Ce^* = Ce_N/(La_N \times Pr_N)^{1/2}$; $Eu/Eu^* = Eu_N/(Sm_N \times Gd_N)^{1/2}$; $Y/Y^* = Y_N/(Ho_N \times Er_N)^{1/2}$, where the suffix “$_N$” indicates that the chondrite-normalized value was used) (Mourier et al., 2008; Laveuf and Cornu, 2009).

For the analysis of the morphology (external morphology and internal microstructure) and elemental composition of iberulites collected in DAD samples we used Scanning electron microscopy (secondary and backscattered electrons) and electron microanalysis methods (SEM Hitachi S-510, VPSEM Zeiss SUPRA40VP and Rontec–EDX) as well as image analysis (IA). For VPSEM-EDX mapping, the DAD samples were embedded in Epon resin and the iberulites were cut with a diamond microtome to expose their interiors. The mineralogical compositions of these cut iberulites were determined using maps of chemical elements by comparisons with mineral standards. For thin sections (70-90 nm) of iberulites, high resolution transmission electron microscopy (HRTEM) technique was used (STEM PHILIPS CM20, Holland). For VPSEM observation of bacteria in deposited dust samples, iberulites and soil, the samples were first fixed with 2.5% glutaraldehyde in 0.1 M cacodylate buffer, and subsequently fixed with 1% osmium tetroxide, dehydrated with alcohol, dried using the critical point method and finally they were coated with carbon (Kuo, 2007). Other samples were simply covered with carbon.

All equipment detailed in this section belongs to Centro de Instrumentación Científica (CIC), University of Granada.

2.5 Detection of desert dust events and identification of their origin

For detecting the African desert dust intrusions over the Iberian Peninsula, CALIMA uses the models SKIRON, BSC-DREAM, NAAPs and HYSPLIT4 backtrajectory analyses (Draxler et al., 2003), as well as synoptic meteorological charts, satellite images, and surface data (particulate matter recorded at air quality monitoring background stations). The air mass backward trajectories calculated by HYSPLIT were used to detect the source regions of desert dust observed over our study area during 2010 by the method described by Valenzuela et al. (2012b). This method assumes that the dust particles are confined to the mixed layer at the potential source region, and that the air mass is loaded by desert dust when the air mass altitude is lower than or close to the altitude of the mixed layer at potential source.

3. Results and discussion

3.1 Concentrations of PM10

The evolution of mean daily concentrations of atmospheric PM10 during the study period is shown in Fig. 1. These atmospheric PM10 concentrations ranged from 25 µg m^{-3} to 200 µg m^{-3} during the analysed period. Some PM10 concentrations were greater than 50 µg m^{-3}, the standard limit established by the European Union Directive (2008/50/EC). The highest PM10 values were observed from 7th to 13th August, reaching the maximum value of 200 µg m^{-3} on 10 August. African dust intrusions are common in the Granada basin between May and October, although there may also be events in February-March (Rodriguez et al., 2001; De la Rosa et al., 2010; Valenzuela et al., 2012b). Fourteen desert dust intrusions over our study area during the summer 2010 have been confirmed by the CALIMA network (www.calima.ws). In fact, high PM10 values observed during the analyzed period were associated with Saharan Dust Outbreaks (shaded areas in Fig. 1b) as confirmed by CALIMA (www.calima.ws). According to the

CALIMA network, 2010 was the year with the greatest number of Saharan Dust events, with 32 dust events, during the period 2004-2015. The total number of Saharan Dust events in the southeast of the Iberian Peninsula between 2004 and 2016 was 314 African dust intrusions, giving 1349 days of Saharan events (www.calima.ws). In addition, the air mass backward trajectories calculated by HYSPLIT show that the source regions of desert dust at our study area during the summer 2010 were Western Sahara, northwestern Mauritania and southwestern Algeria.

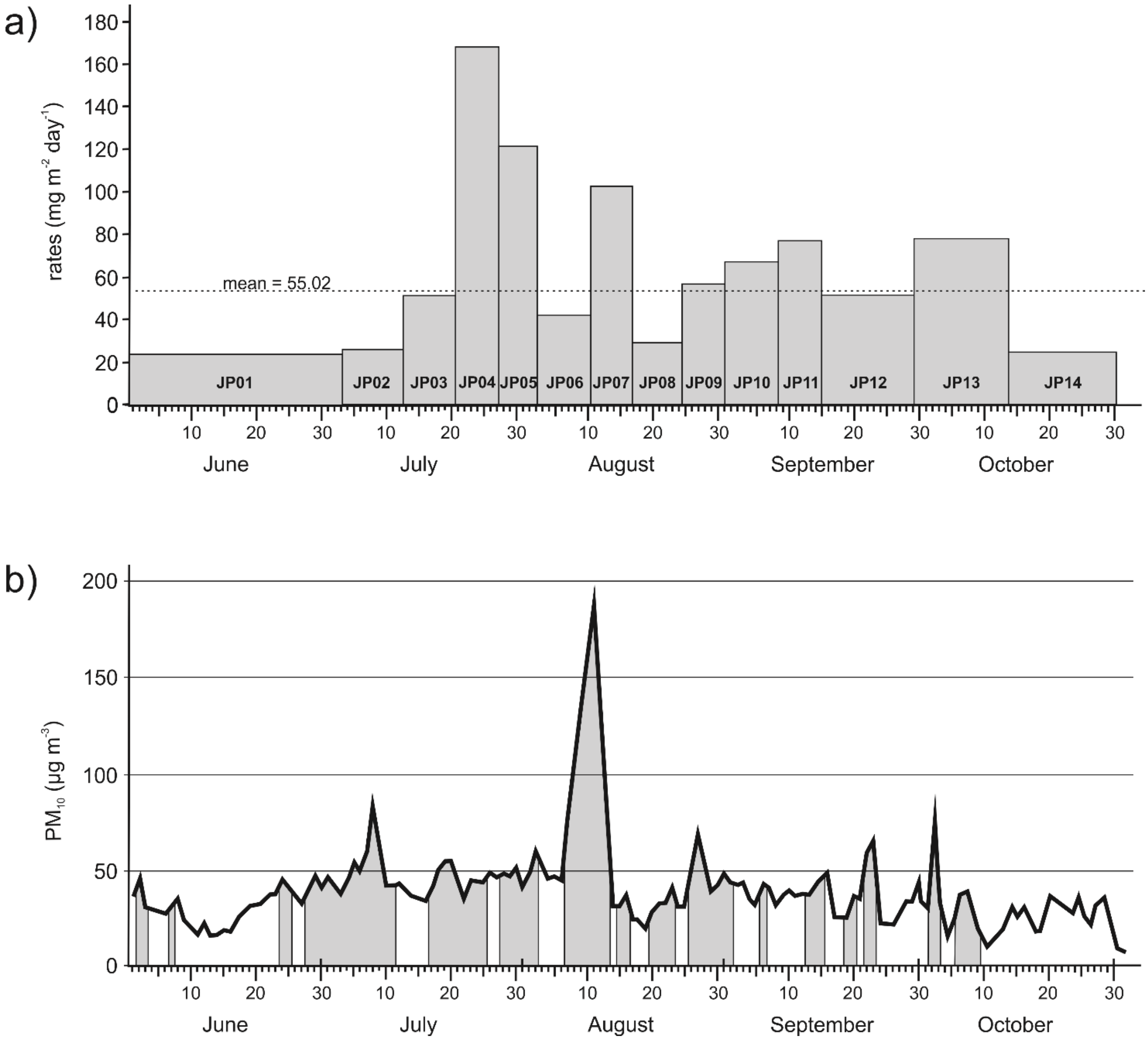

Fig. 1. a) Deposition rates (mg m-2 day-1) of the 14 samples (JP01 to JP14) from June to October 2010. b) PM10 concentrations during summer 2010. Shaded areas show days of Saharan Dust Outbreaks according to CALIMA.

3.2 Deposition and granulometry analyses of deposited dust and iberulites

The deposition rate (Fig. 1) shows a high variability ranging from 23 mg m^{-2} day^{-1} (for JP01 sample) to 168 mg m^{-2} day^{-1} (for JP04 sample). The mean deposition rate was 57 mg m^{-2} day^{-1} during the analyzed period. As can be seen, high deposition rates were registered in July-August and low ones in June and last October. No direct relationship could be observed between PM10 concentration (Fig. 1b) and deposition rate (Fig. 1a), since PM10 concentration only include particles with diameter lower than 10 μm and collected samples include particles with size larger than 10 μm. In fact, the maximum deposition rate was observed during 21-27 July while the highest PM10 concentration was registered from 6 to 13 August 2010.

The collected deposited dust consisted mainly of particles with diameter less than 200 µm (mean = 92.3%) (Table 1). Particles with diameter between 200 and 500 µm represented 5.8% (on average) of the total volume concentration, while those of diameter greater than 500 µm only accounted for 2% of the total concentration. The data from Table 1 show that the granulometry presents a small variation between dust events (coefficient of variation <200 µm = 3.4%). However, some selected granulometric curves (Fig. S1) show that, although the mean size is always fine sand (between 50 and 200 µm) the mean size values are relatively different (between 51.79 µm for JP04 sample and 100.31 µm for JP08 sample).

In all 14 dust samples analyzed, iberulites were found. However, the quantity of iberulites as a percentage of the total dust sample mass concentration varied considerably (coefficient of variation = 88.5%), from very low (0.7% in JP13 sample) to a more elevated contribution (9.2 % in JP02 sample), with a mean value of 2.6% (Table 1). The mass fractions of iberulites obtained in this study are much lower than those observed in the same study zone in 2001 and 2005, which ranged from 16 to 47% (Díaz-Hernández and Párraga 2008).

The mean apparent diameter of the iberulites collected was also variable, varying from 34 µm (sample JP10) to 111 µm (sample JP14), with a mean value of 61 µm (coefficient of variation = 32.8%). Electron microscopy analysis confirmed these measurements (see the corresponding section), and also showed that the constituent particles of the iberulites can reach sizes smaller than 1 µm. The mean diameter of the iberulites obtained in this study (61 µm) differs from that reported by Díaz-Hernández and Párraga (2008), 90 µm, and is in the size range (40 - 300 µm) reported by Fiol et al. (2001, 2005).

3.3 Mineralogical analyses of dust samples

The mineralogical composition of the DAD analyzed in this study is very heterogeneous (Table 2). These mineral phases are usually found in the dust samples previously studied in Granada and its metropolitan area (Díaz-Hernández and Párraga, 2008; Díaz-Hernández et al., 2011; Rodríguez-Navarro et al., 2018), and in other locations in the Iberian Penninsula and Balearic Islands (Queralt et al., 1993; Ávila et al., 1997; Fiol et al., 2001, 2005; Fornós et al., 2004). However, palygorskite, detected in African dust over Iberian Peninsula by Queralt et al. (1993), Ávila et al. (1997), Fiol et al. (2005), Fornós et al. (2004), Díaz-Hernández et al., (2011) and Rodríguez-Navarro et al. (2018) (Table 3) was not detected in the dust samples studied here by XRD nor by VPSEM-EDX method (see the corresponding section).

Table 2. Mineralogy (XRD) (%) of atmospheric dust sampled.

Sample	CM	1.0-1.5Ph	Il	Pa	Ka	Ch	Qz	FdK	Pl	Ca	Do	FeOx	Gy
JP01	31	2	22	5	2	3	13	<1	1	19	27	6	<1
JP02	40	5	17	9	9	1	29	<1	-	8	13	8	1
JP03	32	9	19	<1	4	1	16	tr	3	15	27	6	tr
JP04	48	6	26	5	11	1	16	2	<1	13	17	2	1
JP05	32	3	25	<1	4	4	25	tr	1	16	18	4	<1
JP06	56	8	31	10	7	2	14	1	-	9	15	2	1
JP07	44	9	19	6	10	1	21	2	3	8	16	5	<1
JP08	15	3	7	-	5	<1	64	tr	-	4	17	tr	<1
JP09	49	10	27	6	6	1	18	tr	2	15	15	<1	<1
JP11	43	9	19	8	7	1	26	<1	<1	10	20	<1	<1
JP12	37	5	28	<1	4	2	20	<1	-	11	25	5	<1
JP13	37	4	18	8	7	3	13	<1	<1	12	35	<1	<1
JP14	49	3	31	8	7	2	14	<1	<1	8	18	9	tr
Mean (SD)	39 (11)	6 (3)	22 (7)	5 (4)	6 (3)	2 (1)	22 (14)	1	1	11 (4)	20 (6)	4 (3)	1

CM: Clay Minerals *sensu* Schultz (1964) (all phyllosilicates except chlorite); 1.0-1.5Ph: mineral phases with reflections d_{00l} between 1.0 and 1.5 nm spacing (mainly mixed layers and smectites; without chlorite); Il: illite; Pa, paragonite; Ch: Chlorite; Ka: kaolinite; Qz: quartz; FdK: K feldspar; Pl: plagioclases; Ca: calcite; Do: dolomite; FeOx: iron oxides; Gy: gypsum.
Sample JP10 not included in this Table due to low quantity of dust.

The mineral composition is variable (Table 2), dominated by phyllosilicates, quartz and dolomite. Gypsum presented very low content (<3 %), possibly as an atmospheric neoformation product of the attack of atmospheric H_2SO_4 on some primary minerals as smectites and calcite (Díaz-Hernández and Párraga, 2008).

Due to the small quantities collected in dust samples, iberulites could not be analysed by XRD. However, the mineral composition of iberulites reminds the composition of the dust, according to the results from electron microscopy and microanalysis (see Section 3-5).

In the triangle Carbonates – Tectosilicates – Phylllosilicates + Fe oxides (Fig. 2) the samples studied here occupy a relatively small zone, characterized by higher contents of Phyllosilicates + Iron forms and a composition of Carbonates and Tectosilicates that maintain their relative proportions, except for JP08 sample, which was rich in Tectosilicates. When atmospheric dust samples from the bibliography (Queralt et al., 1993; Ávila et al., 1997; Fiol et al., 2001, 2005; Formós et al., 2004; Díaz-Hernández y Párraga, 2008; Díaz-Hernández et al., 2011; Rodríguez-Navarro et al., 2018) as well as the data of the regional soils (Sierra Nevada, Sierra Gádor and Granada) (Delgado et al., 2003; Martín-García et al., 2004; Márquez, 2012) are also considered, the following finding can be highlighted (Fig. 2):

1) Mineral composition of the different dust samples shows a large dispersion, although always below the line of 55% carbonates, which again evidence the mineral heterogeneity of the atmospheric dust samples. However, it cannot be discarded that the different methods used for mineral composition analysis (Table 3) could contribute to this dispersion. Ávila et al. (1997) and Queralt et al. (1993) applied XRD-Chung's method, Díaz Hernández and Párraga (2008) employed X Powder-RIR method, Fiol et al. (2005) and Fornós et al. (2004) used the XRD method of direct measurement of areas (or heights), and Jeong et al. (2014) applied the counting grains method in micrograph obtained by microscope. The comparison of different mineralogical analysis methods is beyond the scope of the present study.
2) No significant mineralogical differences were detected between the types of dust events: red rain, dry deposition or wet deposition.

3) The mean mineralogical compositions of the silt and coarse sand fractions of the most common soils in Granada and surrounding area (Márquez, 2012) were similar to the compositional sub-triangle of the dust samples of Granada and metropolitan areas. However, the mineralogical composition of soil clay fraction was close to the apex Phyllosilicates+Iron forms. These results point to regional soils as one of possible sources of atmospheric dust collected in our samples.

4) The mineral compositions of silt and sand fractions of the other soils of the region (also included in the ternary plot) such as those of Sierra Nevada (Martín-García et al., 2004) or Sierra de Gádor (Delgado et al., 2003), being preferentially decarbonated, were only comparable with our dust samples in their relative proportions of Phyll-Fe/ Tectosilicates. Our samples contain higher contents of Phyllosilicatos+FeOx than the other soil samples (approx. 20% higher). The clay content in soil samples was richer in Phyllosilicates+FeOx than found in our collected samples.

Scheuvens et al. (2013) established different “fingerprints” of African dust origin, based on XRD’s mineralogical analysis. According to these authors, mineral dust detected in DAD samples studied here was originated from the Atlas mountains and the coastal region of the Western Sahara and Western Mauritania (Atlas - west coast), since IIlite/kaolinite ratio was >1.6, chlorite/kaolinite ratio was in the range 0.0-1.0, and carbonate content (calcite + dolomite) was intermediate to abundant (frequently >30 %), Table 3. Only samples JP01 and JP08 do not satisfy these criteria (Table 2). These results are in good agreement with the results obtained by air mass back trajectories analysis.

According to Scheuvens et al. (2013), the mineral dust, analyzed in the bibliography (Table 3), could have the same origin as the mineral dust studied here or it could come from Southern Algeria and Northern Mali. The presence of paragonite (sodium mica) in our samples (Table 2), a mineral species that is not found in African soil samples but that is abundant in Betic materials from Southern Spain (Martín-García et al., 1997) and the higher content of dolomite with regard to calcite in our samples (Table 3) point to the contribution of Betic materials from Southern Spain region to our collected dust samples This would be a new evidence of contributions from the south of Spain diluting the African dust and another possible reason for palygorskite not being detected. In the other Spanish dusts in the bibliography, paragonite has only been described in Sierra Filabres (Queralt et al., 1993) and some samples from Granada (Díaz-Hernández et al., 2011), coinciding (in accordance with our results) with calcite/dolomite ratios <1 (Table 3).

Furthermore, we calculated the mineralogical ratios-fingerprints of Scheuvens et al. (2013) for some Spanish soils (Entisols of Sierra Nevada, Martin-García et al., 2004, Luvisols and Cambisols of Sierra de Gádor, Delgado et al., 2003) that are possible sources of mineral dust collected in our samples (Table 3). In the case of Entisols, the mineralogical ratios presented the following mean values: IIlite/kaolinite silt + clay = 11,4 (>1,6), chlorite/kaolinite clay = 0,7 (0.0-1.0) while for Luvisols and Cambisols the mean ratios values were: IIlite/kaolinite< 50 µm = 37,6 (>1,6), chlorite/kaolinite< 50 µm = 0,4 (0.0-1.0). These results fit the Scheuvens et al. (2013)'s requirements for 'foothills of Atlas mountains and western coastal region' dust source. This casts doubt on our use of the ratios of Scheuvens et al. (2013) and provides further proof that our dusts could originate from Spanish soils.

The presence of smectite and "mixed-layer" in our samples (Table 2) does not indicate provenance either, since these are minerals found in both soils and atmospheric dust (amongst others, by Jeong et al., 2016). Nonetheless, the presence of smectite is of interest due to its being a constituent of iberulites (Díaz-Hernández and Párraga, 2008).

Table 3. Mineralogical indices of atmospheric dust and soil samples.

	Location	Reference	Sample	Type of event	Period/year of event	Il/Ka[1]	Ch/Ka[1]	Palygorskite (%)[1]	Carbonates (%)[1]	Ca/Do
Atmospheric dust samples		this study	JP01 to JP14	DD	2010					
Mean (n=13)						4.25 (2)	0.38 (2,3,4)	nd (4,5,6)	32 (1,2,3)	0.58
SD						2.67	0.42		9	0.21
Max						11.00 (2)	1.50 (1,4)	nd (4,5,6)	47 (1,2,3)	1.00
Min						1.40 (1,2,4)	0.09 (2,4)	nd (4,5,6)	21 (1,2,3)	0.23
Other atmospheric dust samples from Iberian peninsula and Balearic Islands										
	Catalonia	Avila et al. (1997)	WS	RR	1984-1992	5.39 (2)	(5)	7.3 (1,2)	12 (3,4)	1.40
			MA	RR	1984-1992	11.26 (2)	(5)	10.1 (1,2)	17 (3,4)	2.19
			CA	RR	1984-1992	2.76 (2)	(5)	8.3 (1,2)	2 (5)	1.33
	Mallorca	Fiol et al. (2001)		WD	1988-1992	0.21 (1,4,5)	(5)	nd (4,5,6)	34 (1,2,3)	3.61
		Fiol et al. (2005)		WD	1989-1999	0.52 (1,3,4)	(5)	1.0 (3)	36 (1,2,3)	2.78
		Fornós et al. (2004)		RR	2004	1.07 (1,2,3,4)	(5)	6.0 (1,2)	25 (1,2,3)	4.83
		Fornós et al. (2004)		DD	2004		(5)	9.4 (1,2)	31 (1,2,3)	2.38
	Sierra Filabres	Queralt et al. (1993)		WD	1989-1990	5.93 (2)	1.47 (4)	3.7 (3)	2 (5)	0.60
	Granada	Díaz-Hernández and Párraga (2008)	dust	DD	2001-2005	2.40 (2)	(5)	nd (4,5,6)	51 (1,2,3)	0.20
			iberulite	DD	2001-2005	1.75 (1,2,4)	(5)	nd (4,5,6)	22 (1,2,3)	3.46
		Díaz-Hernández et al. (2011)	F1	DD	1992	0.89 (1,2,3,4)	0.46 (2,3,4)	(3)	26 (1,2,3)	0.91
			F2	DD	1992	1.06 (1,2,4)	0.46 (2,3,4)	(3)	30 (1,2,3)	0.61
			F3	DD	1992	0.33 (1,3,4,5)	0.38 (2,3,4)	(3)	22 (1,2,3)	2.65
		Rodríguez-Navarro et al. (2018)	bulk	RR	2017	3.36 (2)	(5)	11 (1,2)	23 (1,2,3)	4.50
			silt	RR	2017	1.68 (1,2,4)	0.32 (2,3,4)	10.7 (1,2)		
			clay	RR	2017	2.07 (2)	(5)	6.3 (1,2)		
Soils										
Entisols	Sierra Nevada	Martín-García et al. (2004)	coarse sand					nd (4,5,6)	nd (5)	
			fine sand					nd (4,5,6)	nd (5)	
			silt			18.34 (2)	1.00 (2,4)	nd (4,5,6)	nd (5)	
			clay			4.47 (2)	0.68	nd (4,5,6)	nd (5)	
Terrae rossae	Sierra Gádor	Delgado et al. (2003)	coarse sand					nd (4,5,6)	15 (3,4)	1.68
			fine sand					nd (4,5,6)	5 (3,5)	0.10
			silt			6.63 (2)	0.36 (2,3,4)	nd (4,5,6)	nd (5)	
			clay			6.95 (2)	0.16 (2,4)	nd (4,5,6)	nd (5)	
Mean soils	Granada	Márquez (2012)	coarse sand					nd (4,5,6)	24 (1,2,3)	1.14
			fine sand					nd (4,5,6)	24 (1,2,3)	1.27
			silt					nd (4,5,6)	19 (3,4)	2.10
			clay			3.18 (2)	0.49 (2,3,4)	nd (4,5,6)	10 (3,4)	7.50

DD: dry deposition; RR: red rain; WD: wet deposition; Il: illite; Ch: Chlorite; Ka: kaolinite; Ca: calcite; Do: dolomite; nd, not detected.

[1] Scheuvens et al. (2013) fingerprints. Numbers in brackets indicate the potential source areas in northern Africa: 1, Tunisia and northern Algeria (PSA1); 2, foothills of Atlas mountains and western coastal region (PSA2); 3, southern Algeria and northern Mali (PSA3); 4, central Libya (PSA4); 5, western Chad including Bodélé depression (PSA5); 6, southern Egypt and northern Sudan (PSA6).

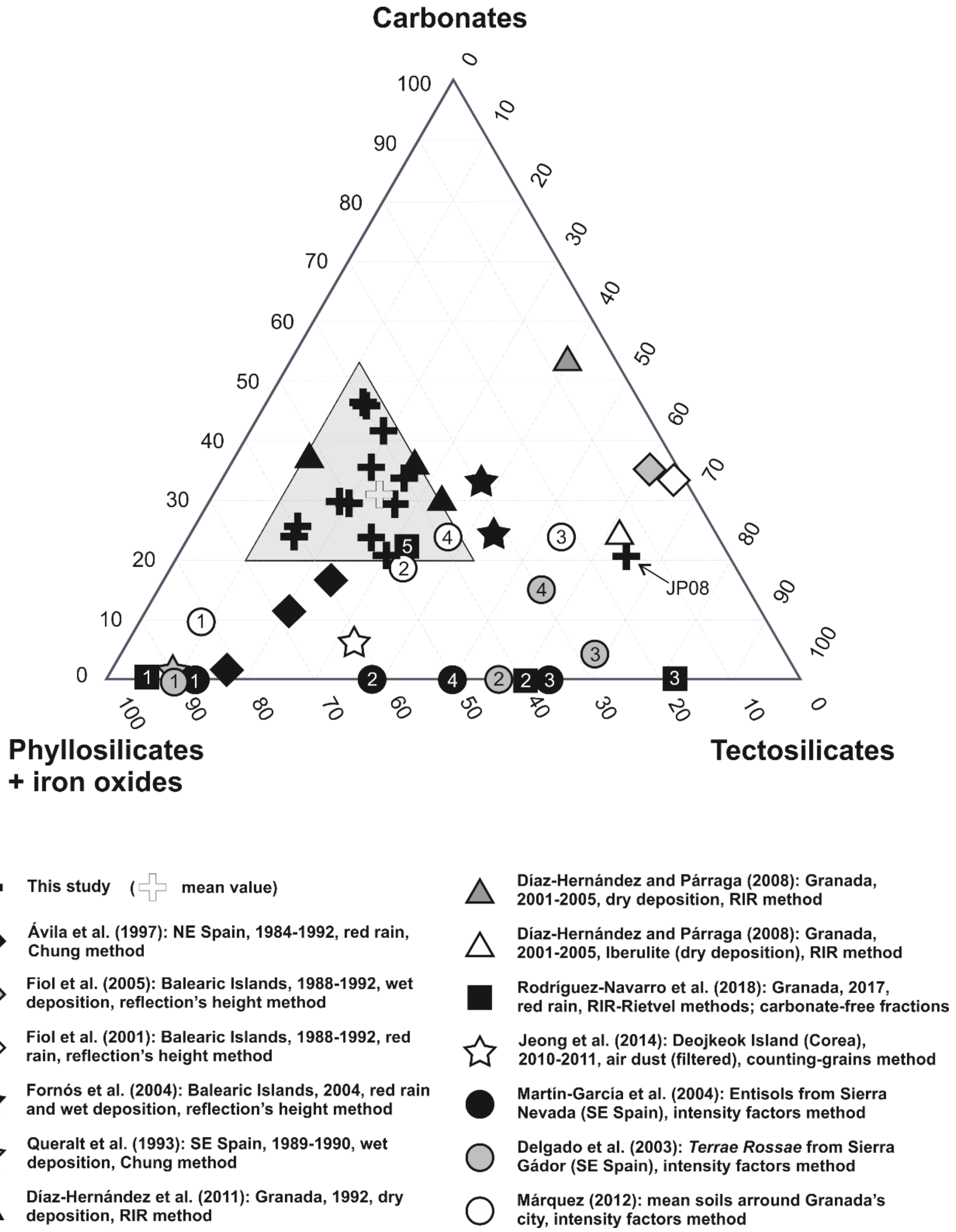

Fig. 2. Ternary plot of Phyllosilicates + iron oxides – Carbonates – Tectosilicates (% from XRD analysis) of the samples analyzed in this study and other samples of dust deposited in the Iberian Penninsula and Balearic Islands. Tectosilicates = quartz + feldspars; carbonates = calcite + dolomite. Numbers within symbols indicate granulometric fractions: 1, clay (<2 µm); 2, silt (2 – 50 µm); 3, fine sand (50 – 250 µm; 4, coarse sand (250 – 2000 µm); 5, bulk sample. The shaded triangle is for samples from Granada and metropolitan area including samples from this study (except sample JP08) and others from the bibliography.

3.4 Rare Earth Elements (REE)

Table S1 shows the contents of rare earth elements in dust samples collected at Granada during summer 2010. Chondrite-normalized profiles (Fig. 3) present values greater than 1 (higher quantities than in the reference meteorite) and confirm the enrichment in LREE, shown by a steep negative slope (with increasing atomic number) which becomes less pronounced after Eu and almost flat in the HREE region, although some samples show an upward slope between Tm and Lu. This result is in good agreement with the values of the ratios $MREE_N/LREE_N$, between 0.09 and 0.13, and $HREE_N/LREE_N$, between 0.15 and 0.21 (Table 4).

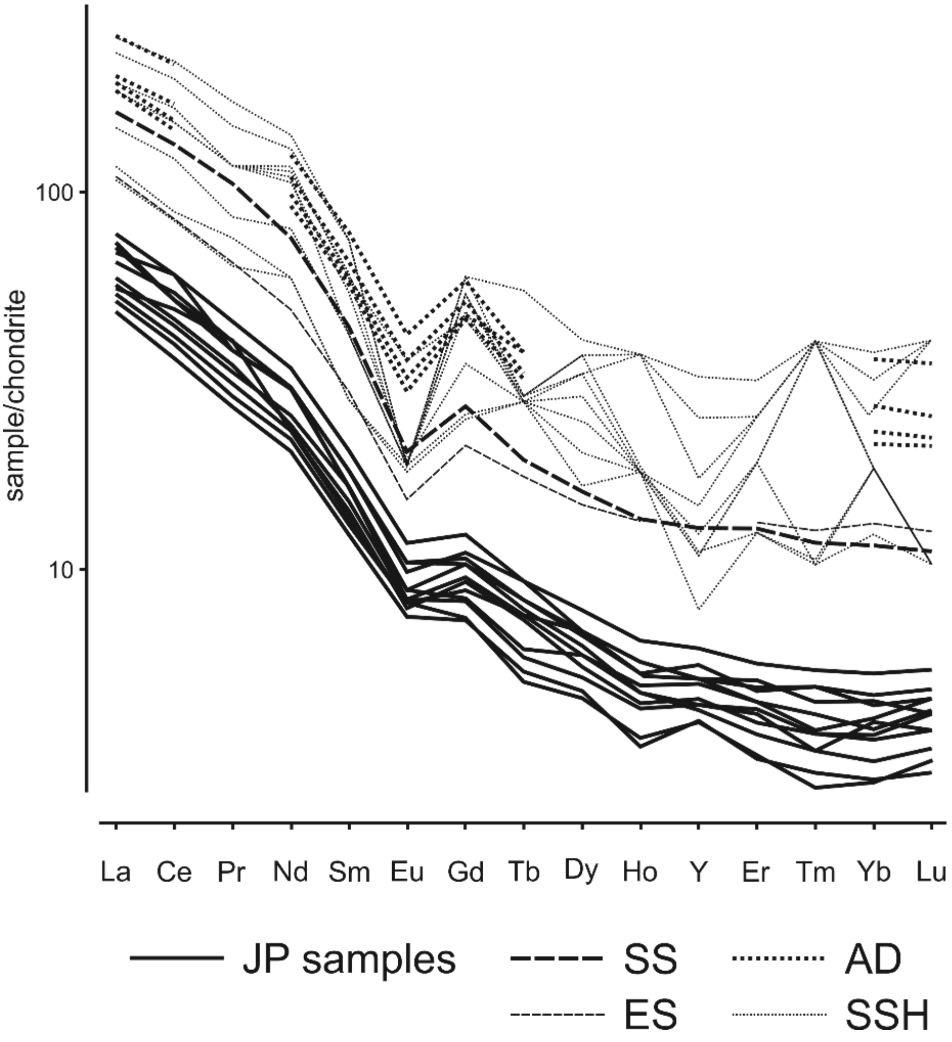

Fig. 3. Chondrite normalization of REE contents of samples of atmospheric dust and other materials. Spanish soils (SS), African dust (AD), European soils (ES), SSH (Sahara-Sahel corridor).

Table 4. Geochemical indices of REE from samples of atmospheric dust studied and other materials.

Reference		$\text{HREE}_N/\text{LREE}_N$	$\text{MREE}_N/\text{LREE}_N$	Ce/Ce*	Eu/Eu*	Y/Y*
Atmospheric dust (this study)						
JP01		0.11	0.18	0.99	0.74	nd
JP02		0.13	0.19	1.03	0.77	1.09
JP03		0.11	0.18	0.99	0.80	1.20
JP04		0.13	0.19	1.02	0.74	1.04
JP05		0.13	0.19	1.00	0.79	1.11
JP06		0.11	0.18	1.01	0.74	1.09
JP07		0.12	0.18	1.17	0.77	1.02
JP08		0.09	0.15	1.02	0.82	1.21
JP09		0.11	0.17	1.00	0.77	1.08
JP10		0.13	0.20	1.03	0.70	1.01
JP11		0.12	0.18	1.09	0.70	0.95
JP12		0.13	0.21	1.02	0.69	1.02
JP13		0.12	0.20	1.02	0.68	nd
JP14		0.13	0.20	0.97	0.66	nd
Spanish Top-soil (Locutura et al., 2012)		0.10	0.17	1.01	0.58	0.98
European Top-soil (Salminen et al., 2005)		0.17	0.22	1.01	0.61	nd
Materials from Sahara-Sahel corridor (Moreno et al., 2006)						
Hoggar Massif	HM1	0.24	0.19	1.05	0.32	0.82
	HM2	0.23	0.22	1.06	0.27	0.94
	$\text{mean}_{\text{Macizo Hoggar}}$	0.24	0.21	1.06	0.30	0.88
Chad	CB1	0.19	0.24	1.02	0.83	0.65
	CB2	0.19	0.25	0.93	0.68	0.72
	$\text{mean}_{\text{Cuenca del Chad}}$	0.19	0.25	0.98	0.76	0.69
Niger	MON	0.25	0.22	1.11	0.34	0.68
	HAR	0.26	0.24	1.06	0.72	0.65
	$\text{mean}_{\text{Níger}}$	0.26	0.23	1.09	0.53	0.67
Western Sahara	WS1	0.17	0.24	1.08	0.47	0.58
	WS2	0.20	0.29	1.01	0.68	0.51
	WS3	0.24	0.18	1.07	0.31	0.57
	$\text{mean}_{\text{Sahara Oeste}}$	0.20	0.24	1.05	0.49	0.55
$\text{mean}_{\text{Sahara-Sahel}}$		0.22	0.23	1.04	0.51	0.68
African dust (Muhs et al., 2010)						
<2 µm					0.61	
2-5 µm					0.61	
5-10 µm					0.57	
10-20 µm					0.59	

nd: not determined

In addition, all our samples show a pronounced negative europium anomaly (Fig. 3), with values of Eu/Eu* between 0.66 and 0.82 (Table 4). The highest Ce/Ce* anomaly value (1.17) was obtained in JP07 sample while the highest Y/Y* anomaly values (1.20 and 1.21) were observed in JP03 and JP08 samples, respectively). The rest of the samples show anomalies close to unity, mainly positive.

Rare earth elements were used also as ‘fingerprints’ of dust provenance comparing our dusts with their potential source materials (Tables S1 and 4; Figs. 3 and 4). For comparison we used the REE values reported for the arable layer of Spanish Soils (Locutura et al., 2012) (SS), the arable layer of European Soils (Salminen et al., 2005) (ES), African Dusts (Muhs et al., 2010) (AD), resuspended soils and aeolic materials from the Sahara-Sahel corridor (Moreno et al., 2006) (SSH), and regional materials derived from metasedimentary rocks (Sierra Nevada) (Torres-Ruiz et al., 2003) and igneous rocks (Los Pedroches batolit) (Pascual et al., 2008).

As can be seen in Table S1, the lanthanides of SS, ES, AD and SSH follow the same pattern as that of our dust samples, namely ΣLREE>ΣMREE>ΣHREE. Chondrite normalization (Fig. 3) showed enrichments in LREE with steep slopes near the HREE region, finishing with an almost flat profile in HREE region for the SS and ES soil samples and a sawtooth profile for SSH samples. However, in SSH samples, materials HM1, HM2, MON and WS3 stood out for the upward slope in the last part of the HREE region (Lu higher than its adjacent Yb), as occurred in some of our atmospheric dusts.

The mean content of ΣREE in our dust samples (67.61 ppm, Table S1) was lower than that of the upper horizons of the SS (164.86 ppm), ES, AD and SSH samples. The lower ΣREE content in our dust samples may be due to their granulometry (mainly fine sand - >50 µm, <250 µm-; Table 1, Fig. S1), coarser than SS, ES and SSH, since the REE are usually concentrated in the fine silt fractions (2 to 50 µm) and clay fractions (<2 µm) (Prudêncio et al., 1993; Aide and Smith-Aide, 2003; Marques et al., 2011).

The geochemical index $HREE_N/LREE_N$ of our dust samples (in the range 0.09 – 0.13; Table 4) is more similar to the reported for SS samples (0.10) and fairly close to the reported for ES and WS1 samples (both 0.17). MREEN/LREEN reported for SS (0.17), HM1 (Hoggar Massif) (0.19) and WS3 (Western Sahara) (0.18) are within the range of values obtained for our dust samples (0.15 – 0.21).

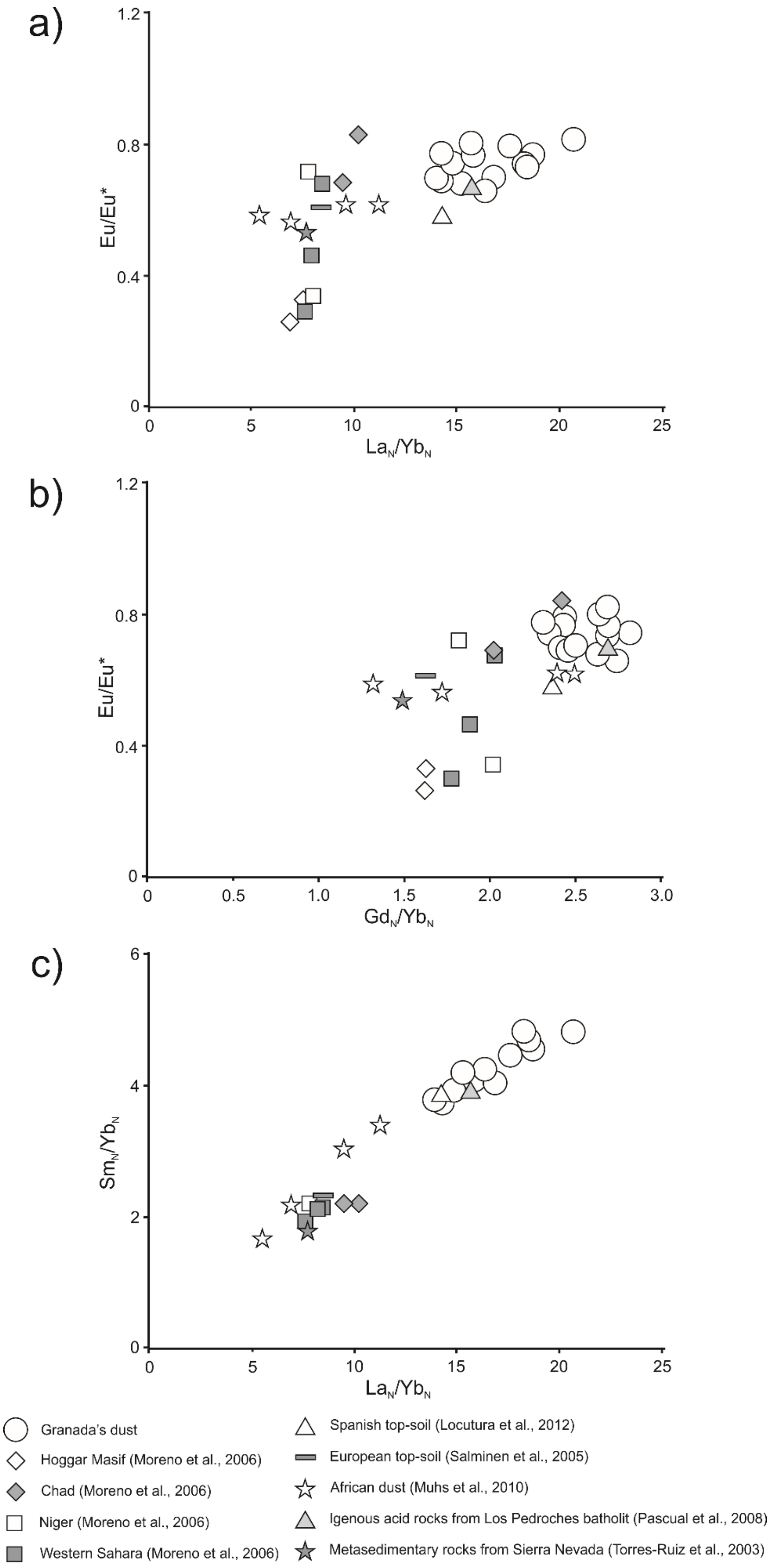

Fig. 4. Diagrams of geochemical indices in atmospheric dust (this study) and other materials. a) LaN/YbN vs. Eu/Eu*, b) GdN/YbN vs. Eu/Eu* and c) LaN/YbN vs. SmN/YbN.

The geochemical anomaly of cerium (Table 4), which is not significant in most of our dust samples (close to 1.00), is similar to that reported for SS and ES samples (both 1.01), and to that of the samples CB1 (Chad) (1.02) and WS2 (Western Sahara) (1.01). In some samples, the cerium anomaly is more pronounced, e.g. in sample JP07 (1.17) and in MON (Niger) of SSH (1.11). The Eu/Eu* anomaly is always negative (<1) in all samples and the yttrium anomaly of our samples is almost similar to that reported for SS (0.98) and HM2 (Hoggar Massif) (0.94).

Consequently, in view of these findings, one cannot discard the contribution of materials from the arable layer of Spanish or European soils or from those of the Sahara Sahel and African Dust to our collected dust samples. This influence is displayed graphically, based on different geochemical indices (Fig. 4). The points representing the composition of our atmospheric dust from Granada are located in a compact group. In diagram La_N/Yb_N *vs* Eu/Eu* (Fig. 4a) the group is segregated from the rest of the materials, although the closest are the Spanish soils, materials CB1 and CB2 (from Chad), some samples of the dust from Africa described by Muhs et al. (2010) and the igneous rock from Los Pedroches (Pascual et al., 2008). In diagram Gd_N/Yb_N *vs* Eu/Eu* (Fig. 4b) the area occupied by the group of atmospheric dust from Granada is next to a sample from the Chad basin and close to the atmospheric dust from Africa, the Spanish soils, a sample from the western Sahara and, again, to the igneous rocks. In diagram La_N/Yb_N *vs* Sm_N/Yb_N (Fig. 4c) area occupied by the group of dust samples from Granada includes the representative point of Spanish soil.

3.5 Electronic micromorphology and EDX analysis of iberulites

The SEM-EDX and VPSEM-EDX results of the morphology, internal microstructure and chemistry of iberulites detected in samples collected in Granada in summer 2010 are shown in Figs. 5 and 6. The characteristics described in Figs. 5 and 6 are may be related to the formation of iberulites. Iberulite morphology is due, amongst other processes, to the interaction of waterdrops and dust particles and their subsequent evaporation during its atmospheric transport (Fiol et al., 2001; Díaz-Hernández and Párraga, 2008) which gives rise to their pseudospherical shape and their different zones (Figs. 5a and 5c): 1) core zone, internal zone, with coarser particles; and 2) rim with finer particles and vortex, an orifice at one of the poles. This morphology determines their behaviour in the air and in the ground surface after their deposition, which may have environmental and public health implications. The porous internal structure of the iberulites (Figs. 5c and 5i) makes them relatively well-equipped to stay longer in the air compared to particles with the same volume but of much greater weight. Furthermore, their external covering by clay, in laminar clusters (Fig. 5f), gives them a certain resistance to disaggregation within the clouds, the wind and the impact with the ground and enables them to travel long distances.

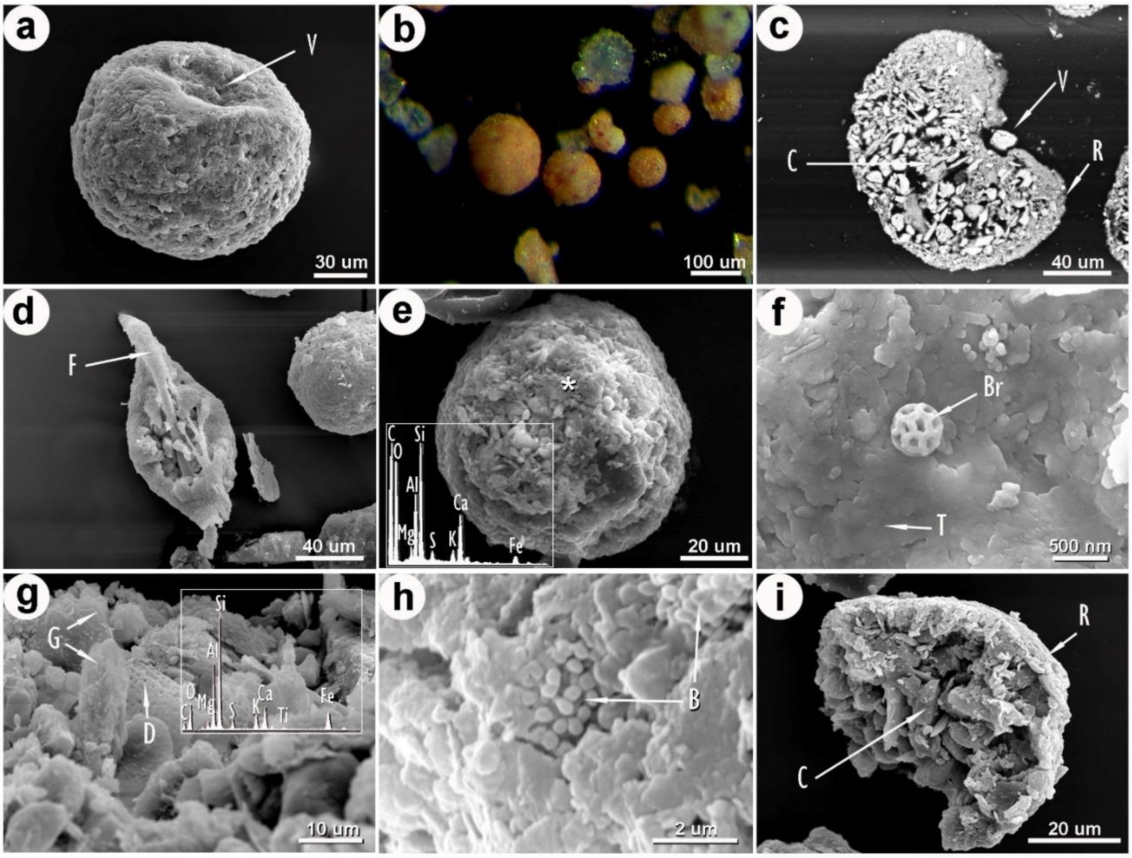

Fig. 5. SEM (conventional) and stereomicroscope photographs, and EDX spectra of iberulites (samples from deposited dust, summer 2010). These are aggregates (mainly quasi-spherical) of mineral particles, thus classified as spherulites. **a)** SEM image of the upper part of an iberulite (V = vortex). **b)** Stereomicroscopy photograph of a field of iberulites. **c**) SEM image of sectioned iberulite. (C = corex; R = rind; V = vortex) **d**) SEM image of a spindle shaped iberulite formed on a filamentous vegetable particle (F). **e)** SEM Image of spherical cap opposite the vortex with EDX microanalysis in the location marked with (*). **f)** Detail of the laminar rind surface, which can be considered as tactoids (T). Presence of a brochosome (Br). **g)** Detail of the surface of the opposite hemisphere to the vortex and microanalysis. Crystal habit of some suggests sulphate crystals, as

gypsum (G). Remains of the siliceous frustule of a centric diatom (*Aulacoseiraceae*-like) (D. **h)** Surface with successive layers of clay and carbonates. Microsites with groups (colonies) of bacteria (B). **i)** Fragmented iberulite (C = core; R = rind).

When iberulites fall on a surface (ground, vegetation, roofs, paved areas) their microstructure again has an important role, since, despite the protective external covering of the rind, they can break easily, as most of their volume consists of an internal aggregate of particles with little cohesion between them, thus affording little resistance (Fig. 5i). But as we will see in the following section, the exudates bacterial make the cements sticky between mineral particles in iberulites which increase their resistance to disaggregation (Fig. 7e).

Thus, iberulites act as stores and diffusers of particles of all sizes representing a significant volume of the event. The data of Jeong et al. (2014) can illustrate this fact since giant aggregates of particles (>10 microns) from the Gobi Desert, sampled during a storm in 2012, accounted for only 20% of the total number of particles of the event as opposed to 89% of the total particles by volume.

These smaller constituent particles of iberulites, which are transported in great quantities by them and released from the iberulites during their disaggregation, can potentially be inhaled by people (as many of these particles have diameter less than 10 microns, Figs. 5 and 6) with concomitant effects on health (Párraga et al., 2013; Oduber et al., 2019). On the other hand, when these particles transported by the iberulites spread out after their impact with the ground surface they can affect the biogeochemical cycles of both land and sea (as reported by Jeong et al., 2016), modifying their chemistry by contributing materials different to those of the location.

The EDX microanalysis with SEM (Figs. 5e, 5g) of the iberulite surface (without sectioning) provided information on chemical and mineral composition. The principal constituents detected were: O, Si, Al, Ca, Fe, K, Mg, Na, Ti and S. This elemental composition is substantiated by the XRD mineralogy (Section 3.3), as we described tectosilicates (quartz and feldspars) and phyllosilicates (micas, kaolinite, smectites, mixed phases and chlorite) which contain O, Si, Al, K, Fe, K, Mg, Na, Ti; calcium and calcium magnesium carbonates (calcite and dolomite):

O, Ca, Mg; iron oxides (hematite and goethite): O, Fe; and sulphates (gypsum): Ca, S.

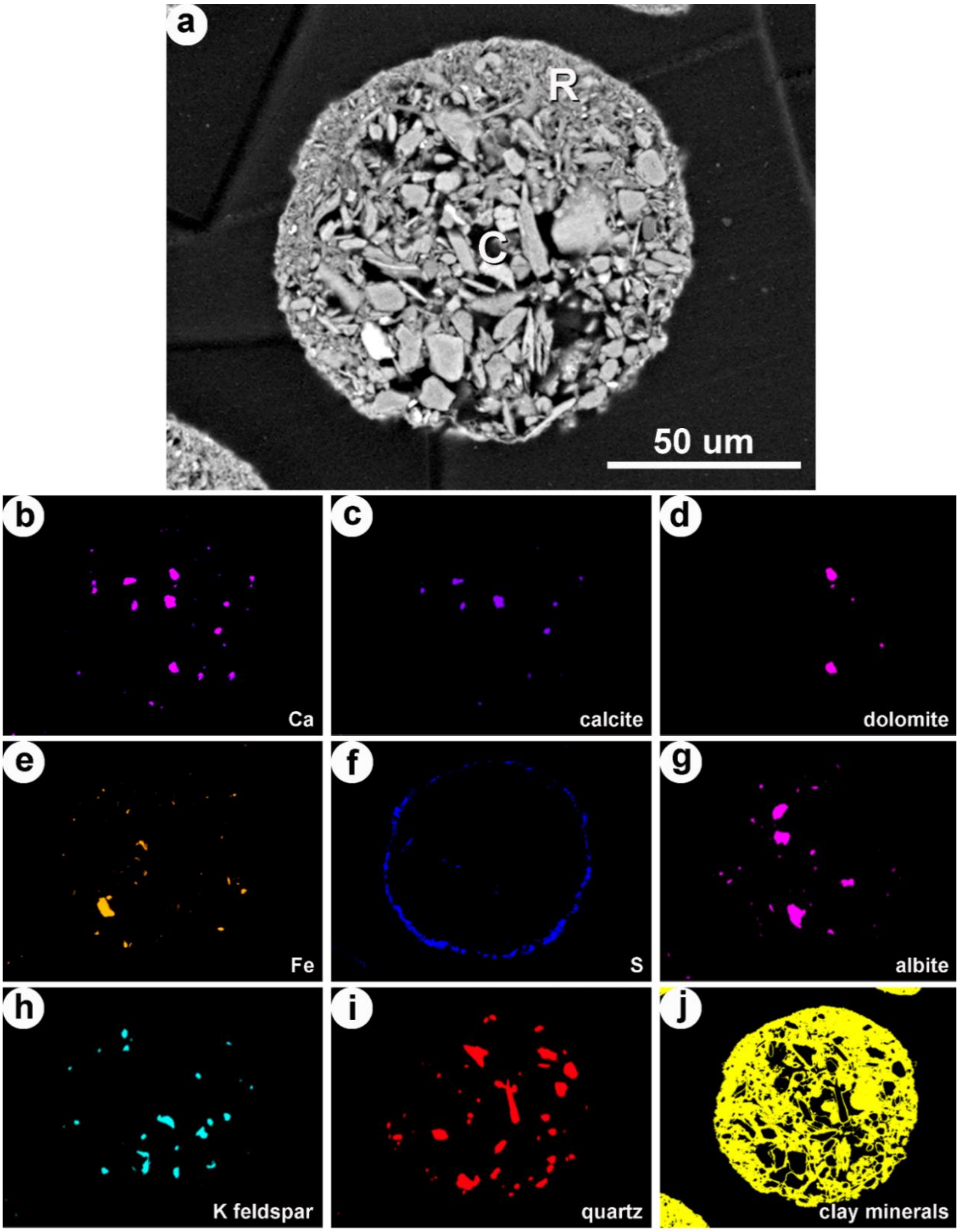

Fig. 6. VPSEM-EDX study of sectioned iberulite (sampled in summer 2010) with spatial distribution of components. a) Retro-dispersed electron image; shape almost perfectly circular, diameter approx. 120 microns; core (C) and rind (R) can be observed; the vortex must be situated in direction N-NW in the image, as shown by thickening of rind (R). Maps of: b) Ca, c) calcite, d) dolomite, e) Fe, f) S, g) albite, h) k feldspar, i) quartz and j) clay minerals.

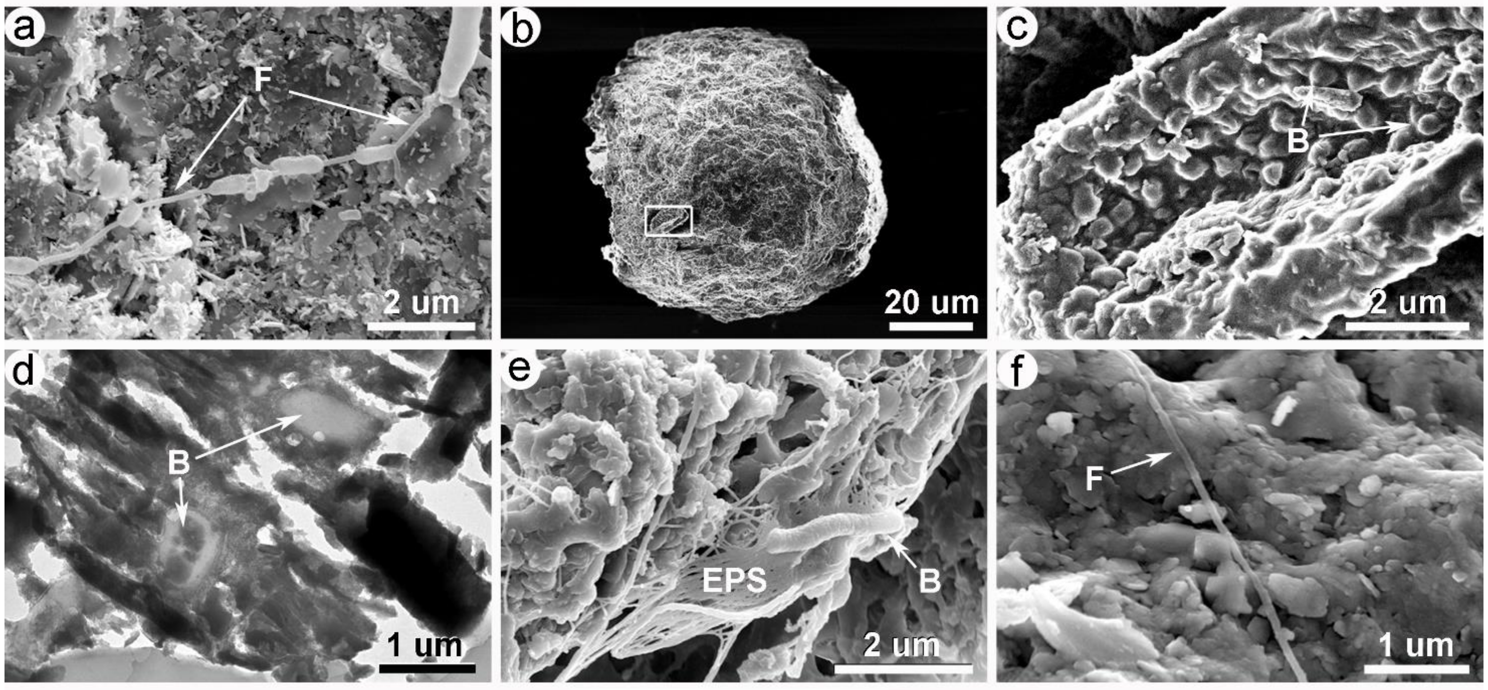

Fig. 7. Presence of bacteria and products of their activity (SEM and HRTEM images). **a)** Presence of chain of bacteria with filament (F) in upper horizon of a soil close to the sampling zone. **b)** Iberulite with unknown biological specimen adhering to it (shown by rectangle). **c)** Detail of b). Colonization of previous biological specimen by nanobacteria (B). **d)** HRTEM image of intact microbial cells (B) embedded in the clayey matrix of a polished section of an undyed iberulite. **e)** Aggregate of mineral particles in sample of atmospheric dust collected in “wet deposition” – “red rain”. Bacterial biofilms (EPSs) cementing particles. **f)** Detail of surface of iberulite collected in “dry deposition”. Very fine (pilum or flagellum) bacterial filament (F) which traverses and stabilizes the surface of the iberulite (similar to the “filaments” connecting the bacteria in microphotograph a). Images b), c) and d) are from samples collected by dry-deposition in summer 2015; image e), summer 2016 by wet-deposition; image f), summer 2010. All samples were taken in the sampling site.

New compositional results were obtained by mapping chemical elements and mineral compositions with VPSEM-EDX (Fig. 6). The map of Ca (Fig. 6b) detected the particles containing significant amounts of this element, belonging to calcite (40% Ca in theoretical formula: $CaCO_3$) and dolomite (21.7% Ca in $CaMg(CO_3)_2$). The points ("calcium spots") are distributed randomly and are typically located in the core of the iberulite (Figs. 6b, 6c, 6d). However, some calcium spots may be from the gypsum grains (29.4% Ca in $CaSO_4 \cdot 2H_2O$) present on the surface of the rind (Fig. 5g). The Fe map (Fig. 6e) shows the particles with relatively high Fe contents, belonging to the iron oxides present: hematite (70% Fe in Fe_2O_3) and goethite (63% Fe in FeOOH). Fe is spread throughout the inside of the iberulite in particles of various sizes. The S map (Fig. 6f), at the sensitivity used to capture the signal of this element, shows an evident ring, around 5 µm thick, which perfectly delineates the shape of the iberulite, although a few signal maxima are also observed inside iberulite. This S must be from other sources than gypsum, which is only present at <1% (Table 2).

The maps of albite ($NaAlSi_3O_8$), potassium feldspar ($KAlSi_3O_8$) and quartz (SiO_2) (Figs. 6g, 6h, 6i) show that these components are spread throughout the core of the iberulite. Another component, denoted as clay (Fig. 6j), corresponds to an elemental composition of 59.5% O, 22.9% Si, 10.3% Al, 2.2% Fe, 1.4% Mg, 1.2% K and 0.2% Ti. These are phyllosilicate phases which are abundant in our dust samples (Table 2): illite, smectite, mixed layers, paragonite or chlorite. Clay minerals define the spherical morphology (circular in 2D) of the iberulite, which help to fill it from the inside outwards and clearly dominate the exterior zone ("rind").

These findings highlighting the spatial distribution of the component elements and minerals (Fig. 6), graphically and concisely, go further than previous studies (Díaz Hernández and Párraga, 2008; Cuadros et al., 2015) and provide more evidence for the hypotheses on the formation of iberulites. The chemical elements Ca and Fe, and the mineral phase particles calcite, dolomite, iron oxides, quartz, albite and potassium feldspar (Fig. 6) are distributed within the core of the iberulite. On the other hand, the "clay minerals" (Fig. 6j) do explain the nature of the iberulite and its spherical shape as they constitute both the greater part of the particle grouping in its interior and the mass of its rind. If the quantity of clay is estimated from the area occupied in Fig. 6 it would be around 50%, close to phyllosilicates content in the dust (around 40% in most cases) measured by XRD (Table 2).

Another components involved in defining the morphology of the iberulite are sulphur phases, S, which mark out a ring and act as a covering or casing (Fig. 6f). However, the S must be from a different source than the gypsum as its content is less than 1% (Table 2), although gypsum was detected on the surface of the rind (Fig. 5g). We believe, firstly, that S from Fig. 6f are elemental sulphur particles (100% S), supported by the noticeable shine of some of the particles in the rim of Fig. 6, and, secondly this is sulphur that has been incorporated into the expandable 2:1 phyllosilicates. In any case, the S in the iberulites seems to originate from the atmospheric processing.

Several studies (Kulshrestha et al. 2003; Korhonen et al. 2003; Díaz-Hernández and Párraga 2008) have revealed that mineral dust particles get often coated with sulphate (and other soluble material) by SO_2 oxidation to SO_4 during in cloud scavenging by heterogeneous nucleation.

In our case, the H_2SO_4 could have two origins: a) condensation of gaseous sulfuric acid on iberulite rind; b) absorption of atmospheric SO_2 into liquid water droplets and dust particles in clouds and on nanoclays clusters in the rind of iberulite (see Figure 8, point 5; Figure 6f). The high surface to volume ratio that clay minerals have together with the influence of the liquid-solid interface, allows nucleation proceeds via direct vapor deposition onto the high surface of nanoclays clusters.

Rodriguez et al (2011) attribute to industrial emissions in North Africa (Morocco, Algeria, Tunisia and Libya) that the major sources of SOx are emissions from crude oil refineries and power plants. Lastly, the intense ship traffic in Mediterranean Sea means that shipping emissions are currently increasing. Impacts from shipping emissions on SO2 atmospheric concentrations were reported over European sea areas (Russo et al. 2018).

3.6 Characteristics of biological activity of iberulites and its importance on their formation

SEM and HRTEM images of the iberulites shown in Figs. 5 and 7 reveal the presence of many biological species in iberulites, including strands of vegetable matter which act as nucleating agents of the dust particles for later formation of the iberulite (Fig. 5d). We also found remains of centric diatoms, of around 20 µm, probably of the Family *Aulacoseiraceae* (Class: *Coscinodiscophyceae*, Order: *Aulacoseirales*), Fig. 5g. The most abundant microorganism associated with African dust intrusion over Granada in 2010 were *Proteobacteria* (74% of the total) and *Firmicutes* (19% of the total), with minor presence of *Bacteriodites* and *Actiniobacteria* (<1% of the total) (Figs. 5h, 7c, 7d, 7e) (Sánchez de la Campa et al. 2013). We even found brochosomes (Fig. 5f), superhydrophobic protein-secreting particles with diameter in the range 0.2-20 µm produced by the Malphigian tubules of grasshoppers (Cicadellidae), one of the most diverse and abundant families of insects (Rakitov and Gorb, 2013). The presence of biological remains in iberulites has already been detected by Fiol et al. (2005), Díaz-Hernández et al. (2012) and Párraga et al. (2013), even though they were not reported to participate in the iberulite genesis.

As shown in Fig. 5h, bacteria tend to appear in colonies clustered together in microsites, which are often situated in micro-depressions on the surface of the iberulite. However, they are sometimes found within the matrix (Fig. 7d). A striking feature, never observed before, is the grouping together of bacterial bodies with mineral grains by means of extremely fine filaments (Fig. 7f) and even biofilms (Fig. 7e). These filaments/biofilms could be flagellae, pili, extracellular polymeric substances (EPS, biofilms) or exudates produced by the bacteria. They are preferentially observed on the iberulite surface, being involved in the formation of microbial aggregates adhered to mineral surfaces. The results indicate that the bacteria might contribute to the protection and stability of the iberulite, reinforcing it and contributing to its internal configuration. Thus, bacteria act as aggregation agent.

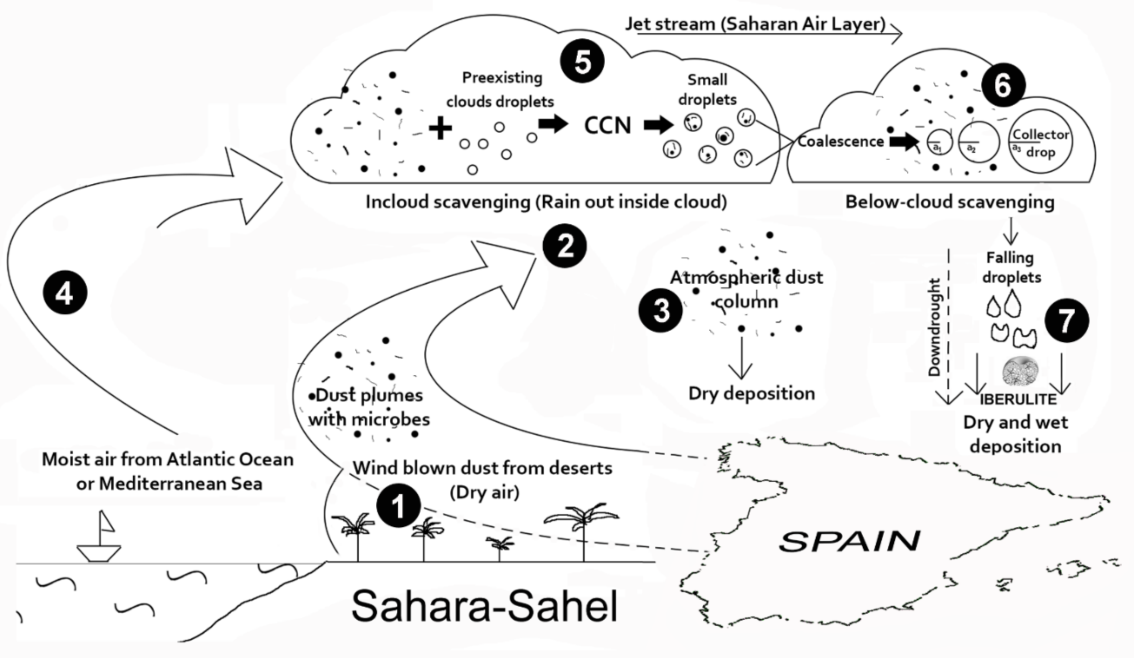

Fig. 8. Sequence of iberulite formation via "cloud processing" with bacterial activity. **1)** The wind picks up dust (mineral particles and bacteria) from the unvegetated surfaces of soils and sediments of African arid and semi-arid zones. Part of this dust may be from Spain. **2)** Ejection of fine particles and bacteria to altitude. **3)** Columns of suspended atmospheric dust which may fall (dry deposition). **4)** Saturated air rises into the atmosphere from the surface of marine water masses. **5)** Water droplets, dust particles and microbes coincide within the clouds. Formation of water droplets from cloud condensation nuclei –CCN-. **6)** Water droplets become collector droplets. Note increase in radius "a". Below-cloud scavenging. Simultaneous bacterial growth. **7)** Falling of droplets and formation of iberulite with bacterial assistance. Role of EPS cements between particles (Fig. 7.e) and stabilization of surface (Fig. 7.f).

These new observations and results have led us to take into account the role of bacteria in iberulite genesis and to reconsider the previous hypothesis regarding the iberulite genesis proposed by Díaz-Hernández and Párraga (2008) and Cuadros et al. (2015). The new proposed iberulite genesis scheme is described in detail in Fig. 8. Mineral particles (and possibly soil organic matter) and their associated bacteria (Fig. 7a) are incorporated from soils without vegetation cover into the atmosphere by wind action (Fig. 8-1 and 8-2). The atmospheric dust (mineral, bacteria and soil organic matter) from the surface (Fig. 8-2) could fall again to surface by dry deposition (Fig. 8-3) or be involved in the cloud formation processes (Fig. 8-5). In the former mechanism the dust aerosol particles (microbes, mineral and other particles) act as cloud condensation nuclei or collides with pre-existing water droplets within the cloud (Fig. 8-5) leading to the formation of small droplets which increase in size through coalescence to become collector drops (Fig. 8-6). Attaining a critical radius these collector drops leave the cloud, becoming larger “falling droplets” (Fig. 8-7) which, through gravity, interact with the atmospheric dust column, with an increase in radius and velocity (and therefore in Reynolds number) and abandon the cloud, once again collecting mineral particles and microorganisms (bacteria, virus, nanoplankton, diatoms, etc.) and finally becoming mature iberulites (with size between 34 and 111 µm). As these iberulites are extremely porous with low density (bulk density 0.65 g cm^{-3} and porosity about 50%) (Díaz-Hernández and Párraga, 2008) they can spend longer time in the atmosphere than mineral particles of similar size. Moisture is present throughout this process due to the iberulites being composed of abundant hygroscopic clay minerals with high water retention (Fig. 6j) and originating from drops of water. Consequently, bacterial growth and their production of exudates (EPS) such as biofilm or filaments (Fig. 7e) is facilitated. These bacteria and their products are either incorporated into the mass of the iberulite (Fig. 7d) or remain on the surface (Fig. 7e, 7f) and thus contribute to the formation and stabilization of the iberulite as a body and compensate its fragility.

Many of these bacteria are viable and resistant to the exposition to the ultraviolet radiation because they are carried within the clayey matrix of iberulite (Fig. 7d) and can survive for a long time in the hostile atmosphere (Yamaguchi et al., 2012; Favet et al., 2013; Sanchez de la Campa et al., 2013).

In Fig. 7d (ultra-thin section of iberulite), we have detected nanoparticles containing EDX spectrum iron (less than 100 nm) inside the bacteria, in the cell wall and outside, that can induce bacterial growth and biofilm formation (Borcherding et al., 2014).

In Figs. 7e and 7f we have appreciates exudates of EPS and a filament of bacterial origin, confirming that there is microbial activity within the structure of iberulite.

This biological material can thus travel through the atmosphere, even between continents because the dust and iberulites can be transported from the Sahara-

Sahel within the Saharan Air Layer (SAL) which rises to about 500 mb (altitude around 6 km) to South America (Amazonia), the North Atlantic-Caribbean area and Europe (Díaz-Hernández and Párraga, 2008).

This marks the end of the cycle of iberulite formation which started with the deflation of bacteria and soil particles from the ground and ended with the growth of these bacteria inside the iberulite and their return to the ground surface (Fig. 8).

4. Conclusions

The paper show that the dust samples collected in Granada in 2010 (14 samples) are mineralogically heterogeneous, both qualitatively and quantitatively, such that a single sample is not sufficient for determination the origin of the sampled particles. The mineralogical composition analysis showed that the sampled particles were originated from the north-northwest of Africa (Atlas – west Sahara – Mauritania) and local/regional soil sources. The use of REE as fingerprints does not rule out the contribution of diverse materials such as African aeolian dusts or Spanish soils to our dusts.

The phenomena of particle aggregation are frequent in the atmosphere with no patterns of structural organization. The complex shapes of these polymineral aggregates are irregular.

All of these shapes are different from iberulites, a new type of quasi-spherical giant atmospheric particle formed under special conditions in periods corresponding to higher levels of dust deposition. A distinct feature of iberulites is the vortex, which is related with their formation mechanism and the distribution of mineral grains.

Thus, we can redefine an iberulite (bioaerosol) as “a microspherulite of clayey mud, mechanically generated and formed in the troposphere by complex mineral grains-bacteria-water-gas interactions. It is a coassociation with axial geometry, made up of well-defined mineral grains, together with biological constituents, bacterial and non-crystalline compounds (extracelular polymeric substances, EPS) structured on a coarse-grained core internal (with sizes less than 10 microns) and a relatively more sulphurated pinkish clayey ring (nano-clays in laminar clusters) with only a typical vortex at one of the poles and an average size of 100µm. “

Iberulites were present in all dust samples analyzed in this study with mass fraction between 0.7 and 9.2%. The SEM-microstructure analysis also shows that the clay and the S components are decisive in determining its spherical shape. On the other hand, the chemical elements Ca and Fe and the mineral phase particles (calcite, dolomite, iron oxides, quartz, albite and potassium feldspar) are distributed in the mass of the iberulite without relevance for its spherical configuration. The micro-morphological analysis evidences the role of bacteria in iberulite formation, which, through bacterial growth in the clouds and the descent to earth, together with the production of EPS conjunct the mineral particles and stabilize the pseudospheres externally. Bacterial can be an important agent in aggregation, which has not been found or considered previously in the formation of iberulite. It is a new viewpoint. With these new observations and results have led us to take into account the role of bacteria in iberulite formation and to reconsider the previous hypothesis regarding the iberulite formation proposed by previous works.

Finally, iberulites can be shuttles for the intercontinental transport of microorganisms, which can grow inside it, being protected from UV radiation and having an environment rich in nutrients. The iberulites are the tangible evidence of the fluid-dynamic theory applied to the interaction of water drops, gases and dust particles in the atmosphere, giving rise to shapes with a vortex, that until now, they had been explained in laboratory studies.

Acknowledgments

This work was supported by the Spanish Agencia Estatal de Investigación (AEI) through projects CGL2016-80308-P, CGL2016-81092-R and CGL2017-90884-REDT, and by the European Union’s Horizon 2020 research and innovation program through project ACTRIS-2 (grant agreement No 654109). Also, we are thankful to EMEP (European Monitoring and Evaluation Programme) for providing the air quality data from background station.

References

Aide, M., Smith-Aide, C., 2003. Assessing soil genesis by rare-earth elemental analysis. Soil Sci. Soc. Am. J. 67, 1470-1476.

Ávila, A., Queralt-Mitjans, I., Alarcón, M., 1997. Mineralogical composition of African dust delivered by red rains over northeastern Spain. J. Geophys. Res. Atmos. 102(D18), 21977-21996.

Barahona, E., 1974. Arcilla de ladrillería de la provincial de Granada. Evaluación de algunos ensayos de materias primas. Tesis Doctoral. Univ. Granada. 398p.

Bergametti, G., Foret, G., 2014. Dust deposition. In Mineral dust: a Key Player in the Earth System (eds. P. Knippertz and J.-B.W. Stuut) Springer, Dordrecht, pp.179-200.

Borcherding, J., Baltrusaitis, J., Chen, H., Stebounova, L., Wu, C. M., Rubasinghege, G., Comellas, A. P., 2014. Iron oxide nanoparticles induce Pseudomonas aeruginosa growth, induce biofilm formation, and inhibit antimicrobial peptide function. Environ. Sci. Nano, 1(2), 123-132.

British Geological Survey (BGS), 2011. “Rare Earth Elements” (BSG, 2011; https://www.bgs.ac.uk/downloads/start.cfm?id=1638).

Calero, J., Delgado, R., Delgado, G., Martín-García, J.M., 2009. SEM image analysis in the study of a soil chronosequence on fluvial terraces of the middle Guadalquivir (southern Spain). Eur. J. Soil Sci. 60, 465–480.

CALIMA. Dirección General de Calidad y Evaluación Ambiental del Ministerio de Agricultura, Alimentación y Medio Ambiente, España. Link: http://www.calima.ws/

Calvo, A.I., Olmo, F.J., Lyamani, H., Alados-Arboledas, L., Castro, A., Fernández-Raga, M., Fraile, R., 2010. Chemical composition of wet precipitation at the background EMEP station in Víznar (Granada, Spain) (2002–2006). Atmos. Res. 96(2-3), 408-420.

Cuadros J., Díaz-Hernández J.L., Sánchez-Navas, 2015. Role of clay minerals in the formation of atmospheric aggregates of Saharan dust Atmos. Environ. 120, 160-172.

De la Rosa, J., Sánchez de la Campa, A.M., Alastuey, A., Querol, X., González-Castanedo, Y., Fernández-Camacho, R., Stein, A.F., 2010. Using PM10 geochemicals maps for defining the origin of atmospheric pollution in Andalusia (Southern Spain). Atmos. Environ. 44, 4595-4605.

Delgado R., Barahona E., Huertas F., Linares J., 1982. Los Mollisoles de la Cuenca Alta del Río Dílar (Sierra Nevada). Anales de Edafología y Agrobiología. 41, 59-82.

Delgado, R., Martín-García, J.M., Oyonarte, C., Delgado, G., 2003. Genesis of the terrae rossae of the Sierra Gádor (Andalusia, Spain). Eur. J. Soil Sci. 54, 1-16.

Díaz Hernández, J.L., Párraga, J., 2008. The nature and tropospheric formation of iberulites: Pinkish mineral microspherulites. Geochim. Cosmochim. Acta. 72, 3883-3906.

Díaz-Hernández, J. L., Martín-Ramos, J. D., López-Galindo, A., 2011. Quantitative analysis of mineral phases in atmospheric dust deposited in the south-eastern Iberian Peninsula. Atmos. Environ. 45(18), 3015-3024.

Diaz-Hernandez, J. L., Sanchez-Navas A., 2016. Saharan dust outbreaks and iberulite episodes, J. Geophys. Res. Atmos. 121, 7064–7078.

Díaz-Hernández, J. L. , Sánchez-Soto, P. J., Serrano-Delgado, A., 2012. Biological nanostructures associated to iberulites: a SEM study. Curr. Microsc. Contrib. Adv. Sci. and Techn. 154-161

Directive, 2008. 50/EC of the European Parliament and the Council of 21 May 2008. Relating to ambient air quality and cleaner air for Europe. OJL 152, 11.6.2008, p.1-44.

Draxler, R. R., Rolph, G. D., 2003: HYSPLIT (HYbrid single- particle Lagrangian integrated trajectory) Model access via NOAA ARL READY Website (http://www.arl.noaa.gov/ready/hysplit4.html), NOAA Air Resources Lab., Silver Spring, MD, USA.

EMEP, 2001. EMEP manual for sampling and chemical analysis. EMEP/CCCReport 1/95, Revision 1/2001, NILU, Norge.

Engelbrecht, J.P., Moosmüller, H., Pincok, S., Jayanty, R.K.M., Lersch, T., Casuccio, G., 2016.Technical note: Mineralogical, chemical, morphological, and optical interrelationships of mineral dust re-suspensions. Atmos. Chem. Phys. 16, 10809-10830.

Favet, J., Lapanje, A., Giongo, A., Kennedy, S., Aung, Y. Y., Cattaneo, A., Schnetger, B., Davis-Richardson, A.G., T Brown C., Kort R., Brumsack HJ, Schnetger B., Chappell A., Kroijenga J., Beck A., Schwibbert K., Mohamed AH., Kirchner T., Dorr de Quadros P., W Triplett E., Broughton W.J., Gorbushina, A., 2013. Microbial hitchhikers on intercontinental dust: catching a lift in Chad. ISME J. 7(4), 850.

Fiol, L., Guijarro, J.A., Forno´s, J.J., 2001. Las lluvias de barro en el Mediterráneo Occidental: el caso de Mallorca. Rev. Climatol. 1, 7-20.

Fiol, L., Fornós, J. J., Gelabert, B., Guijarro, J. A., 2005. Dust rains in Mallorca (Western Mediterranean): Their occurrence and role in some recent geological processes. Catena. 63(1), 64-84.

Fornós, J. J., Fiol, L. A., Pastor, J.A.G., 2004. Episodis significatius de pluges de fang ocorregudes els mesos de febrer i març de 2004 a Mallorca (Mediterrània occidental). Significative dust rain on february and march of 2004 episodes in Mallorca (Western Mediterranean). Bolletí de la Societat d'Història Natural de les Balears. 47, 43-50.

Jeong, G. Y., Kim, J. Y., Seo, J., Kim, G. M., Jin, H. C., Chun, Y., 2014. Long-range transport of giant particles in Asian dust identified by physical, mineralogical, and meteorological analysis. Atmos. Chem. Phys. 14, 505-521.

Jeong, G. Y., Nousiainen, T., 2014. TEM analysis of the internal structures and mineralogy of Asian dust particles and the implications for optical modeling. Atmos. Chem. Phys. 14, 6619-6661.

Jeong G. Y., Achterberg, E. P., 2014. Chemical and mineralogy of clay minerals in Asian and Saharan dust and the implications for iron supply to the oceans. Atmos. Chem. Phys. 14, 12415-12428.

Jeong, G. Y., Park, M. Y., Kandler, K., Nousiainen, T., Kemppinen, O., 2016. Mineralogical properties and internal structures of individual fine particles of Saharan dust. Atmos. Chem. Phys. 16(19), 12397-12410.

Korhonen, H., Napari, I., Timmreck, C., Vehkamäki, H., Pirjola, L., Lehtinen, K. E. J., Lauri, A., Kulmala, M., 2003. Heterogeneous nucleation as a potential sulphate-coating mechanism of atmospheric mineral dust particles and implications of coated dust on new particle formation. J. Geophys. Res. 108(D17).

Korotev, R.L., 2009. “Rare earth plots” and the concentrations of rare earth elements (REE) in chondritic meteorites. Web site: http://meteorites.wustl.edu/goodstuff/ree-chon.htm.

Kulshrestha, M. J., Kulshrestha, U. C., Parashar, D. C., Vairamani, M., 2003. Estimation of SO4 contribution by dry deposition of SO2 onto the dust particles in India. Atmos. Environ. 37(22), 3057-3063.

Kuo, J., 2007. Electron Microscopy. Methods and Protocols, second ed. Humana Press, Inc. Totowa, New Jersey.

Kuzmichev, A.A., Azarov, V.N., Kuzmichev A.V., 2017. The research of contamination regularities of historical buildings and architectural monuments by methods of computer modeling. MATEC. Web of conferences. 129, 05002.

Laveuf, C., Cornu, S., 2009. A review on the potentiality of Rare Earth Elements to trace pedogenetic processes. Geoderma. 154, 1-12.

Locutura, J., Bel-lan, A., García, C.A., Martínez, S., 2012. Atlas Geoquímico de España. Madrid: Instituto Geológico y Minero de España.

Lyamani, H., Olmo, F.J., Alados-Arboledas, L., 2005. Saharan dust outbreak over southeastern Spain as detected by sun photometer Atmos. Environ. 39(38), 7276-7284.

Lyamani, H., Olmo, F.J., Alados-Arboledas, L., 2010. Physical and optical properties of aerosols over an urban location in Spain: seasonal and diurnal variability. Atmos. Chem. Phys., 10, 239-254.

Marques, R., Prudencio, M.I., Dias, M.I., Rocha, F., 2011. Patterns of rare earth and other trace elements in different size fractions of clays of Campanian–Maastrichtian deposits from the Portuguese western margin (Aveiro and Taveiro Formations). Chem Erde-Geochem. 71, 337-347.

Márquez Crespo, R., 2012. El cuarzo de la fracción arena fina en suelos de la provincia de Granada. Universidad de Granada.

Martin, J. D., 2004. XPowder A software package for Powder X-Ray diffraction analysis, Granada, Spain. ISBN 978-84-16478-87-3.

Martín-García, J.M., Delgado, G., Sánchez-Marañón, M., Párraga, J.F., Delgado, R., 1997. Nature of dioctahedral micas in Spanish red soils. Clays Clay Miner. 32, 107–121.

Martín-García, J.M., Aranda, V., Gámiz, E., Bech, J., Delgado, R., 2004. Are Mediterranean mountains Entisols weakly developed? The case of Orthents from Sierra Nevada (Southern Spain). Geoderma. 118, 115-131.

McDonough, W.F., Sun, S., 1995. The composition of the Earth. Chem. Geol. 120, 223–253.

Moreno, T., Querol, X., Castillo, S., Alastuey, A., Cuevas, E., Herrmann, L., Mounkaila, M., Elvira, J., Gibbons, W., 2006. Geochemical variations in aeolian mineral particles from the Sahara-Sahel Dust Corridor. Chemosphere. 65, 261-270.

Mourier, B., Poulenard, J., Chavel, C., Faivre, P., Carcaullet, C., 2008. Distinguishing subalpine soil types using extractable Al and Fe extractions and REE geochemistry. Geoderma. 145, 107-120.

Muhs, D. R., Budahn, J., Skipp, G., Prospero, J. M., Patterson, D., Bettis III, E. A., 2010. Geochemical and mineralogical evidence for Sahara and Sahel dust additions to Quaternary soils on Lanzarote, eastern Canary Islands, Spain. Terra Nova, 22(6), 399-410.

Oduber, F., Calvo, A.I., Blanco-Alegre, C., Castro, A., Nunes, T., Alves, C., Sorribas, M., Fernández-González, D., Vega-Maray, A.M., Valencia-Barrera, R.M., Lucarelli, F., Calzolai, G., Alonso-Blanco, E., Fraile, B., Fialho, P., Coz, E., Prevot, A.S.H., Pont, V., Fraile, R., 2019. Unusual winter Saharan dust intrusions at Northwest Spain: Air quality, radiative and health impacts. Sci. Total Environ. 669, 213-228.

Párraga, J., Delgado, G., Martín-García, J.M., Olmo, F.J., Delgado, R., 2013. Iberulitos: partículas atmosféricas “gigantes” potencialmente inhalables. Actualidad Médica. 98, 86-91.

Pascual, E., Donaire, T., Pin, C., 2008. The significance of microgranular enclaves in assessing the magmatic evolution of a high-level composite batholith: A case on the Los Pedroches Batholith, Iberian Massif, Spain. Geochem. J. 42, 177-198.

Pey, J., Querol, X., Alastuey, A., Forastiere, F., Stafoggia, M., 2013. African dust outbreaks over the Mediterranean Basin during 2001–2011: PM10 concentrations, phenomenology and trends, and its relation with synoptic and mesoscale meteorology. Atmos. Chem. Phys. 13, 1395-1410.

Posfai, M., Axisa, D., Tompa, E., Freney, E., Bruintjes, R., Buseck P., 2013. Interactions of mineral dust with pollution and clouds: An individual-particle TEM study of atmospheric aerosol from Saudi-Arabia. Atmos. Res. 122, 347-361.

Prudêncio, M.I., Braga, M.A.S., Gouveia, M.A., 1993. REE mobilization, fractionation and precipitation during weathering of basalts. Chem. Geol. 107, 251–254.

Queralt-Mitjans, I., Domingo, F., Sole-Benet, A., 1993. The influence of local sources on the mineral content of bulk deposition over an altitudinal gradient in the Filabres Range (SE Spain). J. Geophys. Res. Atmos. 98(D9), 16761-16768.

Rakitov, R., & Gorb, S. N., 2013. Brochosomal coats turn leafhopper (Insecta, Hemiptera, Cicadellidae) integument to superhydrophobic state.

Proceedings of the Royal Society B: Biological Sciences, 280(1752), 20122391.

Reyes, M., Díaz, J., Tobias, A., Montero, J.C., Linares, C., 2014. Impact of Saharan dust particles on hospital admissions in Madrid (Spain). Int. J. Environ. Health. Res. 24(1), 63-72.

Rodriguez, S., Querol, X., Alastuey, A., Kallos, G., Kakaliagou, O., 2001. Saharan dust contributions to PM10 and TSP levels in Southern and Eastern Spain. Atmos. Environ. 35, 2433-2447.

Rodríguez González, S., Alastuey, A., Alonso-Pérez, S., Querol, X., Cuevas Agulló, E., Abreu Afonso, J., Viana, M., Pandolfi, M., de la Rosa, J., 2011. Transport of desert dust mixed with North African industrial pollutants in the subtropical Saharan Air Layer. Atmos. Chem. Phys. Discuss. 11, 8841-8892.

Rodriguez-Navarro, C., Di Lorenzo, F., Elert, K., 2018. Mineralogy and physicochemical features of Saharan dust wet deposited in the Iberian Peninsula during an extreme red rain event. Atmos. Chem. Phys. 18(13), 10089–10122.

Rollinson, H.R., 1993. Using Geochemical Data: Evaluation, Presentation, Interpretation. Harlow: Prentice Hall.

Russo, M. A., Leitão, J., Gama, C., Ferreira, J., Monteiro, A., 2018. Shipping emissions over Europe: a state-of-the-art and comparative analysis. Atmos. Environ. 177, 187-194.

Salminen, R. (Chief-editor), Batista, M. J., Bidovec, M., Demetriades, A., De Vivo, B., De Vos, W., Duris, M., Gilucis, A., Gregorauskiene, V., Halamic, J., Heitzmann, P., Lima, A., Jordan, G., Klaver, G., Klein, P., Lis, J., Locutura, J., Marsina, K., Mazreku, A., O'Connor, P. J., Olsson, S.Å., Ottesen, R.-T., Petersell, V., Plant, J.A., Reeder, S., Salpeteur, I., Sandström, H., Siewers, U., Steenfelt, A., Tarvainen, T., 2005. Geochemical Atlas of Europe. Part 1: Background Information, Methodology and Maps. Espoo, Geological Survey of Finland. Available at: http://weppi.gtk.fi/publ/foregsatlas/index.php

Sánchez de la Campa, A. M., García Salamanca, A., Solano, J., De la Rosa, J., Ramos, J.L., 2013. Chemical and microbiological characterization of atmospheric particulate matter during an intense african dust even in southern Spain. Environ. Sci. Technol. 47(8), 36360-3638.

Scheuvens, D., Schütz, L., Kandler, K., Ebert, M., Weinbruch, S., 2013. Bulk composition of northern African dust and its source sediments. A compilation. Earth. Sci. Rev. 116, 170-194.

Schultz L.G., 1964. Quantitative interpretation of mineralogical composition from X-ray and chemical data for the Pierre Shale. US Geol. Surv. Prof Pap., 391 C., 31 pp.

Torres-Ruiz, J., Pesquera, A., Gil-Crespo, P.P., Velilla, N., 2003. Origin and petrogenetic implication of turmaline-rich rocks in the Sierra Nevada (Betic Cordillera, southeastern Spain). Chem. Geol. 197, 55-86.

Vahlsing, C., Smith, K. R., 2012. Global review of national ambient air quality standards for PM10 and SO_2 (24 h). Air Qual. Atmos. Health. 5(4), 393-399.

Valenzuela, A., Olmo, F.J., Lyamani, H., Antón, M., Quirantes, A., Alados-Arboledas, L., 2012a. Analysis of the columnar radiative properties retrieved during African desert dust events over Granada (2005–2010) using principal plane sky radiances and spheroids retrieval procedure. Atmos. Res. 104-105, 292-301.

Valenzuela, A., Olmo, F.J., Lyamani, H., Anton, M., Quirantes, A., Alados-Arboledas, L., 2012b. Classification of aerosol radiative properties during African desert dust intrusions over southeastern Spain by sector origins and cluster analysis. J. Geophys. Res. Atmos. 117. D06214 doi:10.1029/2011JD016885. 2012b.

Varga, G., Üjvári, G., Kovács, J., 2014. Spatiotemporal patterns of Saharan dust outbreaks in the Mediterranean Basin. Aeolian Res. 15, 151-160.

Wang, G., Li, J., Ravi, S., Van Pelt, R.S., Costa P.J.M., Dukes D., 2017. Tracer techniques in aeolian research: Approaches, applications, and Challenges. Earth Sci. Rev. 170, 1–16.

Yamaguchi, N., Ichijo, T., Sakotani, A., Baba, T., Nasu, M., 2012. Global dispersión of bacterial cells on Asian dust. Sci. Rep. 2, 525.

Supplementary material

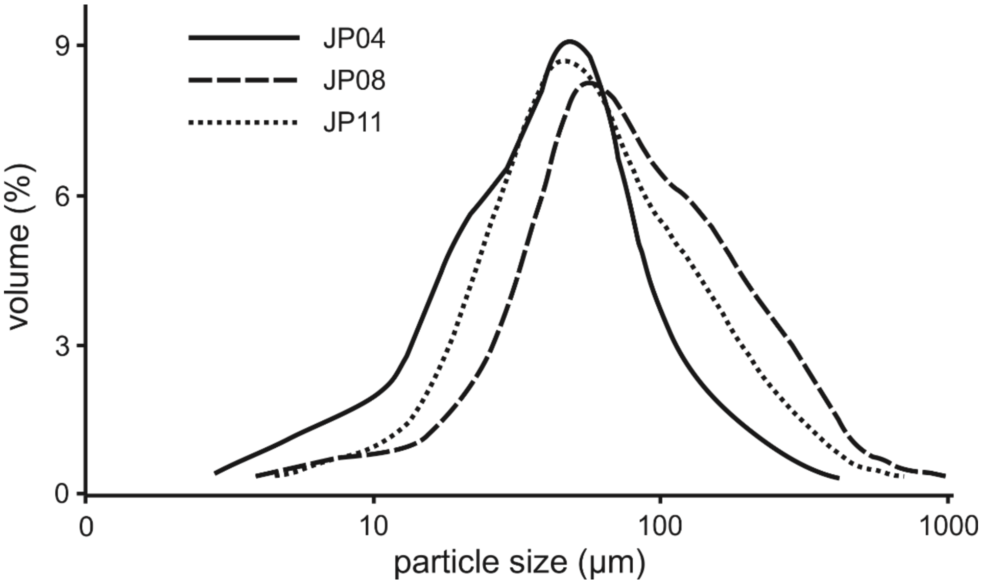

Fig. S1. Selected granulometric curves (laser diffraction).

Table S1. Contents of rare earth elements (ppm) in collected dust samples and comparison with literature.

Reference	sample	La	Ce	Pr	Nd	Sm	Eu	Gd	Tb	Dy	Ho	Y	Er	Tm	Yb	Lu	ΣREE	ΣLREE	ΣMREE	ΣHREE
This study	JP01	17.04	32.79	3.77	14.01	2.73	0.58	2.09	0.29	1.62	0.28	nd	0.73	0.10	0.63	0.11	76.77	67.61	7.31	1.85
	JP02	15.37	31.41	3.52	13.38	2.52	0.58	2.09	0.28	1.64	0.29	8.62	0.77	0.12	0.73	0.12	72.83	63.69	7.12	2.02
	JP03	11.39	21.86	2.49	9.40	1.80	0.42	1.44	0.18	1.10	0.19	6.13	0.49	0.07	0.44	0.07	51.34	45.14	4.94	1.26
	JP04	18.31	36.70	4.16	15.64	3.02	0.66	2.43	0.34	1.90	0.35	9.73	0.89	0.13	0.84	0.13	85.50	74.81	8.35	2.34
	JP05	12.95	25.30	2.88	10.89	2.11	0.49	1.68	0.22	1.42	0.23	7.02	0.62	0.09	0.56	0.09	59.53	52.02	5.92	1.59
	JP06	16.41	32.31	3.68	13.94	2.68	0.58	2.12	0.28	1.52	0.26	7.67	0.68	0.10	0.61	0.10	75.27	66.34	7.18	1.75
	JP07	16.00	36.99	3.66	13.54	2.58	0.58	2.06	0.28	1.62	0.28	7.88	0.76	0.12	0.69	0.11	79.27	70.19	7.12	1.96
	JP08	13.23	29.62	3.75	10.50	1.92	0.45	1.44	0.19	1.15	0.18	6.09	0.50	0.06	0.44	0.07	63.49	57.09	5.15	1.25
	JP09	13.46	27.14	3.19	10.97	2.06	0.46	1.63	0.21	1.25	0.23	6.57	0.57	0.08	0.49	0.08	61.82	54.76	5.61	1.45
	JP10	12.55	25.78	2.95	10.64	2.12	0.45	1.82	0.27	1.33	0.25	6.87	0.65	0.08	0.61	0.09	59.59	51.92	5.99	1.68
	JP11	17.52	35.95	3.66	13.36	2.63	0.55	2.19	0.33	1.68	0.31	7.95	0.80	0.11	0.71	0.10	79.90	70.49	7.38	2.03
	JP12	12.14	23.88	2.66	10.00	2.04	0.43	1.76	0.26	1.32	0.24	6.64	0.62	0.08	0.58	0.09	56.10	48.68	5.81	1.61
	JP13	13.96	27.86	3.11	11.81	2.38	0.49	2.02	0.29	1.45	0.26	nd	0.67	0.09	0.62	0.09	65.10	56.74	6.63	1.73
	JP14	13.45	25.21	2.91	10.68	2.18	0.44	1.89	0.27	1.44	0.25	nd	0.62	0.10	0.56	0.09	60.09	52.25	6.22	1.62
	mean (SD)	14.56 (2.19)	29.49 (4.96)	3.31 (0.49)	12.05 (1.88)	2.34 (0.36)	0.51 (0.08)	1.90 (0.29)	0.26 (0.05)	1.46 (0.22)	0.26 (0.04)	7.38 (1.12)	0.67 (0.11)	0.10 (0.02)	0.61 (0.11)	0.10 (0.02)	67.61 (10.44)	59.41 (9.30)	6.48 (0.97)	1.72 (0.30)
Hoggar Massif[1] (SSH)	HM1	56.00	121.00	14.00	58.00	9.00	1.00	10.00	1.00	9.00	2.00	39.00	4.00	1.00	5.00	1.00	249.00	30.00	13.00	249.00
	HM2	61.00	137.00	16.00	64.00	11.00	1.00	12.00	2.00	10.00	2.00	50.00	5.00	1.00	6.00	1.00	278.00	36.00	15.00	278.00
Chad[1] (SSH)	CB1	45.00	94.00	11.00	48.00	6.00	2.00	9.00	1.00	7.00	1.00	19.00	3.00	1.00	3.00	0.25	198.00	25.00	8.25	198.00
	CB2	28.00	54.00	7.00	28.00	4.00	1.00	5.00	1.00	4.00	1.00	17.00	2.00	0.25	2.00	0.25	117.00	15.00	5.50	117.00
Niger[1] (SSH)	MON	47.00	104.00	11.00	53.00	8.00	1.00	10.00	1.00	9.00	1.00	23.00	4.00	1.00	4.00	1.00	215.00	29.00	11.00	215.00
	HAR	46.00	99.00	11.00	50.00	8.00	2.00	9.00	1.00	8.00	1.00	22.00	4.00	1.00	4.00	1.00	206.00	28.00	11.00	206.00
Western Sahara[1] (SSH)	WS1	35.00	75.00	8.00	37.00	6.00	1.00	7.00	1.00	6.00	1.00	17.00	3.00	0.25	3.00	0.25	155.00	21.00	7.50	155.00
	WS2	25.00	51.00	6.00	27.00	4.00	1.00	5.00	1.00	5.00	1.00	12.00	2.00	0.25	2.00	0.25	109.00	16.00	5.50	109.00
	WS3	56.00	124.00	14.00	62.00	9.00	1.00	11.00	1.00	8.00	2.00	27.00	4.00	1.00	5.00	1.00	256.00	30.00	13.00	256.00

Spanish Top-soil[2] (SS)		38.83	81.27	9.80	34.96	6.49	1.12	5.40	0.71	3.91	0.73	20.01	2.01	0.29	1.85	0.27	164.86	17.63	5.15	164.86
European Top-soil[3] (ES)		25.86	52.25	6.02	22.41	4.28	0.85	4.20	0.64	3.58	0.72	22.74	2.10	0.31	2.09	0.31	106.54	13.56	5.52	106.54
African dust[4] (AD)	<2 µm	61.00	133.00		57.10	11.50	2.31	11.40	1.35		1.62				3.69	0.54				
	2-5 µm	48.40	104.00		49.70	9.64	2.00	10.20	1.16		1.41				3.45	0.52				
	5-10 µm	44.20	90.20		42.90	8.43	1.64	9.19	1.19		1.58				4.33	0.62				
	10-20 µm	46.60	94.90		45.70	8.96	1.77	9.48	1.34		1.95				5.81	0.85				

LREE: light rare earth elements (La, Ce, Pr, Nd); MREE: medium rare earth elements (Sm, Eu, Gd, Tb, Dy); HREE: heavy rare earth elements (Ho, Er, Tm, Yb, Lu); nd: not determined

[1] Materials from Sahara-Sahel corridor (Moreno et al., 2006)

[2] Locutura et al. (2012)

[3] Salminen et al. (2005)

[4] Muhs et al. (2010)

Chapter 6:

Provenance fingerprints of atmospheric dust collected at Granada city (Southern Iberian Peninsula).

Evidence from quartz grains

Provenance fingerprints of atmospheric dust collected at Granada city (Southern Iberian Peninsula). Evidence from quartz grains

A. Molinero-García[a], J.M. Martín-García[a]*, M.V. Fernández-González[a] and R. Delgado[a]

[a] Departamento de Edafología y Química Agrícola, Universidad de Granada, Campus Cartuja, 18071, Granada, Spain

*Author for correspondence. Email: jmmartingarcia@ugr.es

Published on:

CATENA, 208 (2022), 105738. https://doi.org/10.1016/j.catena.2021.105738

Impact Factor (JCR):

Journal Impact Factor, JIF (2021): **6.367**; JIF Percentil in Category (Geosciences, Multidisciplinary - Scie): **91.79 (Q1-D1)**

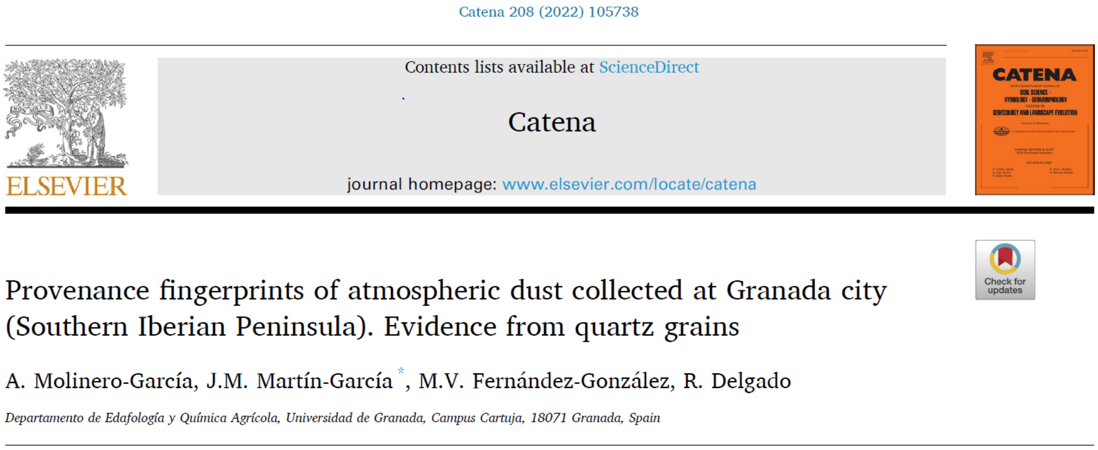

Catena 208 (2022) 105738

Contents lists available at ScienceDirect

Catena

journal homepage: www.elsevier.com/locate/catena

Provenance fingerprints of atmospheric dust collected at Granada city (Southern Iberian Peninsula). Evidence from quartz grains

A. Molinero-García, J.M. Martín-García *, M.V. Fernández-González, R. Delgado

Departamento de Edafología y Química Agrícola, Universidad de Granada, Campus Cartuja, 18071 Granada, Spain

Abstract

Dust in the Earth´s atmosphere is increasing, particularly in southern Spain. The study of dust properties allows for a hypothesis on the origin and provenance of dust. This study characterised atmospheric dust deposited in the city of Granada (south of Spain) during three spring periods (samples 4PA, 16PA, and 28PA, collected in 2012, 2013, and 2014, respectively). The aim was to ascertain dust characteristics and genesis using a set of methodological techniques. The backward trajectories study separated the samples into two groups: scarce Saharan influence (sample 16PA, 6% of backward trajectories are from, or have passed through, Africa) and greater influence (samples 4PA and 28PA, 26% and 33%, respectively). This grouping was verified by the rest of the properties analysed, namely, PM10 concentration, deposition rates, grain size, mineralogy, and elemental composition (minor, including rare earth elements). In addition, mineral quartz showed differences in particle morphology and surface microtextures. The mineralogical and geochemical studies of our samples have proved similarities with other dust collected in Granada and soils from the Iberian Peninsula. The principal component analysis of the quartz shape parameters insists on the differentiation of these groups. We propose the morphoscopy of quartz grains (a significant component of atmospheric dust) as a fingerprint of provenance.

Graphical Abstract

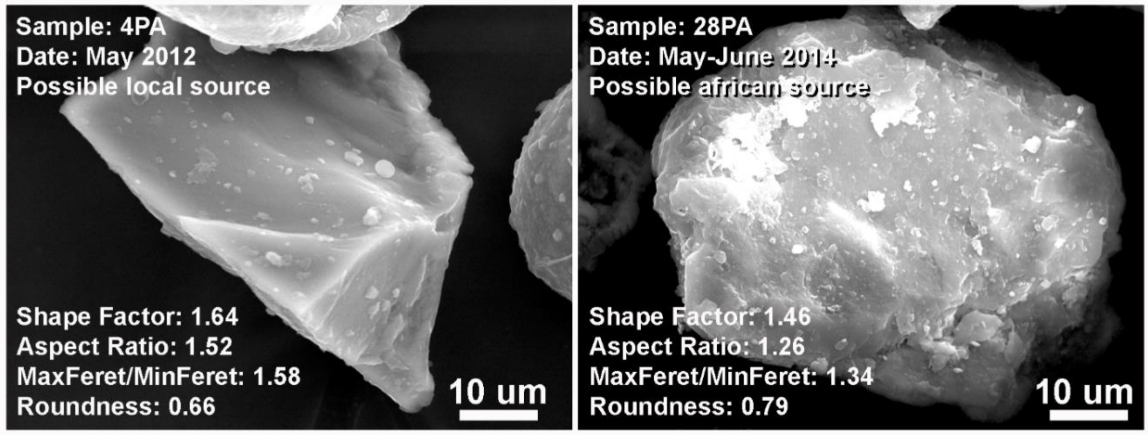

SEM Images of atmospheric quartz particles. Provenance may justify differences in shape parameters.

Keywords: quartz; shape parameters; atmospheric dust; provenance fingerprint; dust mineralogy; dust geochemistry.

Highlights:

- The composition, morphology, and provenance of spring atmospheric dust are heterogeneous.
- Atmospheric dust features depend on their provenance.
- SEM morphology of atmospheric quartz particles is a provenance fingerprint.
- Quartz morphoscopy is a new technique to understand atmospheric dust provenance.

1. Introduction

Atmospheric dust is one of the most abundant aerosols globally and an essential component of the Earth's environmental system (Nickovic et al., 2012; Muhs et al., 2014; Schepanski, 2018). The Sahara Desert is the world's largest source of atmospheric dust (50%–70% of total emissions worldwide), contributing between 1 and 3 billion tons per year (Prospero et al., 2002; Engelstaedter et al., 2006; Huneeus et al., 2011; Russo et al., 2020). African dust intrusion should be considered in the Iberian Peninsula because of the proximity of the Sahara Desert (e.g. Valenzuela, 2012).

Granada city (south of the Iberian Peninsula) has one of Spain's highest atmospheric pollution levels. The primary pollutants are particulate matter (PM) and NOx (Ministry for Ecological Transition and Demographic Challenge, 2019). PM <10 µm (PM10) concentration in Granada frequently exceeds both the limit value recommended by the World Health Organization (WHO) (20 µg m^{-3}) and the one-day limit value (50 µg m^{-3}) established by the European Union Directive (2008/50/EC) — the limits were exceeded 54 days per $year^{-1}$ in the period 2010–2020 (Junta de Andalucía, 2021a). Granada's location (a depression surrounded by mountains) favours the development of thermal inversions and weak winds, which boost PM values. PM is a major problem and an environmental risk to health that has concerned the Spanish government since it was classified as a carcinogen to humans (Group 1) (WHO, 2013a; WHO, 2018).

According to the Environmental Protection Agency, PM (also called particle pollution) is a mixture of solid particles and liquid droplets found in the air. PM can be produced by wind erosion of arid and semiarid soil surfaces (Menut et al., 2013) and transported to areas far from their origin. Soils play a critical role in dust production mechanisms (Marticorena, 2014; Wang et al., 2018; Wang et al., 2021). The mineral fraction of aerosols is determined by the mineral composition of the soil they are from (Nickovic et al., 2012; Journet et al., 2014).

Annual atmospheric dust deposition rates are variables in the surrounding areas of Spain, ranging from 137×10^3 to 3340×10^3 g m^2 (Goudie and Middleton, 2001). These values fluctuate throughout the year. There is a strong interannual variability in the deposition rates (Rodriguez et al., 2015). In some Spanish places, the spring period shows high deposition rates (Gelado et al., 2012; Engelbrecht et al., 2014; Cerro et al., 2020); hence, this study has value. Backward trajectories (e.g. Lyamani et al., 2005; Valenzuela et al., 2012), grain size (e.g. Goudie and Middleton, 2001), mineralogy (e.g. Hojati et al., 2012; Scheuvens et al., 2013) and chemical composition (e.g. Xie et al., 2018; Cerro et al., 2020) analyses have been conducted to ascertain the properties and genesis of atmospheric dust, highlighting its provenance. Image analysis (IA) applied to mineral dust SEM images has been widely used (Kalashnikova and Sokolik, 2004; Scheuvens and Kandler, 2014). These techniques are necessary for the characterisation of atmospheric dust.

The specific process of mineral genesis in the atmosphere is notable. Baker et al. (2014) affirmed that atmospheric transport alters the chemical composition of mineral particles, generating layers on mineral dust particle surfaces. Díaz-Hernández and Párraga (2008) and Párraga et al. (2021) have demonstrated the formation of iberulites in the atmosphere by the coalescence of particles transported by the wind. Likewise, these authors have proved atmospheric mineral neoformation, namely, halite (NaCl) or gypsum ($CaSO_4 \times 2H_2O$), due to dissolution and precipitation processes on atmospheric mineral particle surfaces. Costa et al. (2013) and Vos et al. (2014) have reported the formation of an amorphous silica layer on the surfaces of aeolian quartz grains due to high-energy aeolian collisions.

Quartz is a primary constituent of the Earth’s crust and surface environment (Strunz and Tennyson, 1982; Drees et al., 1989). It is also a significant component of atmospheric dust (Kumar and Rajkumar, 2014; Menéndez et al., 2014; Blondet et al., 2019; Candeias et al., 2020). Moreover, morphological characteristics (e.g. microtextures) analysed by Scaning Electron microscopy (SEM) have been widely used in provenance studies of geological materials (Mahaney, 2002; Delgado et al., 2003; Vos et al., 2014; Kemnitz and Lucke, 2019). However, few studies have analysed atmospheric quartz using SEM-IA (e.g. Kandler et al., 2007).

This study analyses the atmospheric dust collected during three consecutive spring periods (2012, 2013, and 2014) in Granada (south of the Iberian Peninsula), a southern European area of interest. Atmospheric dust characterisation is investigated using a wide variety of complementary techniques, namely, backward trajectory studies, laser granulometry (grain size), X-ray diffraction (XRD) mineralogy, and inductively coupled mass spectrometry (ICP-MS), for minor element composition. This set of techniques is novel in research on possible provenance fingerprints. Our study is the first, according to our review of the literature, to attempt a morphological study (shape parameters by SEM-EDX-IA) and surface microtextures study (SEM) of atmospheric quartz grains. The shape parameters of quartz particles were used as indicators of atmospheric dust provenance.

2. Sampling and methods

2.1. Sampling site

The sampling site was the Cartuja University campus (Granada) near the Andalusian Institute of Geophysics (IAG) (37° 11’ 23.5” N, 3° 35’ 43.7” W) at 775 m.a.s.l.

Granada is encased in a natural basin surrounded by limestone-dolomitic and siliceous mountains (Vera, 2004) in the southeast of the Iberian Peninsula (~ 50 km from the Mediterranean coast). It is affected by air masses from both the African continent and Atlantic Ocean. It has an average annual temperature of 15.4 ºC and a total average annual precipitation of 365 mm (AEMET, 2020).

According to the Köppen climate classification, the climate is a transition between the temperate Mediterranean and dry semiarid.

2.2. Air Particulate Matter <10 µm (PM10) concentration

Particulate matter <10 µm (PM10) concentration data were obtained through the *Red de Vigilancia de la Calidad del Aire de Andalucía* (Table 1) (Junta de Andalucía, 2021b). The measurement stations used (close to the sampling area) were Palacio de Congresos, Granada Norte, and Ciudad Deportiva. PM10 samples were collected on quartz filters by a Digitel Aerosol Sampler (model DPA14) operated at an average flow rate of 2.3 m^3 h^{-1} (55.2 m^3 day^{-1}).

Table 1. General characteristics of dust samples and PM10[1] concentration.

Sample	Period	Deposition rate ($mg\ m^{-2}\ day^{-1}$)	PM10 ($\mu g\ m^{-3}$)	African backward trajectories (%)
4PA	26/04/2012 - 31/05/2012	114	23.33	26
16PA	10/05/2013 - 13/06/2013	159	22.00	6
28PA	16/05/2014 - 18/06/2014	108	25.33	33

[1] According to Junta de Andalucía (2021b)

2.3. Hybrid single-particle Lagrangian integrated trajectory (HYSPLIT) backwards trajectories

The origin of the air masses reaching Granada city was determined by the transport and dispersion HYSPLIT model. The model is an open, online resource provided by the National Oceanic and Atmospheric Administration Air Resources Laboratory (http://www.arl.noaa.gov/ready.html) (Draxler, 2011). It is the most extensively used model for determining atmospheric transport and dispersion (Reche et al., 2018). HYSPLIT backward trajectories were obtained using archived data from the Global Data Assimilation System with a 120-h run time at 500, 1500, and 3000 m.a.s.l. Daily backward trajectories were determined for each sampling period. The number of days (expressed as a percentage) in which air mass intrusions are from (or have passed through) Africa was calculated.

2.4. Atmospheric dust sampling

The samples (dry and wet deposition) were collected in three periods of 30–35 days by a standard sedimentable particles sampler (model MCV PS) consisting of a metallic structure (tripod form) that connects a collecting funnel (upper part) with a tank (lower part) where the sample was collected. Deposition rates were calculated after drying the samples at 35 °C by weighing each sample (g) and considering the surface (m^2) of the standard dust collector. The study focused exclusively on three late spring periods (from 2012 to 2014; Table 1) because they showed the maximum dust deposition rates (Figure 1) and a sufficient quantity of dust to perform the set of techniques.

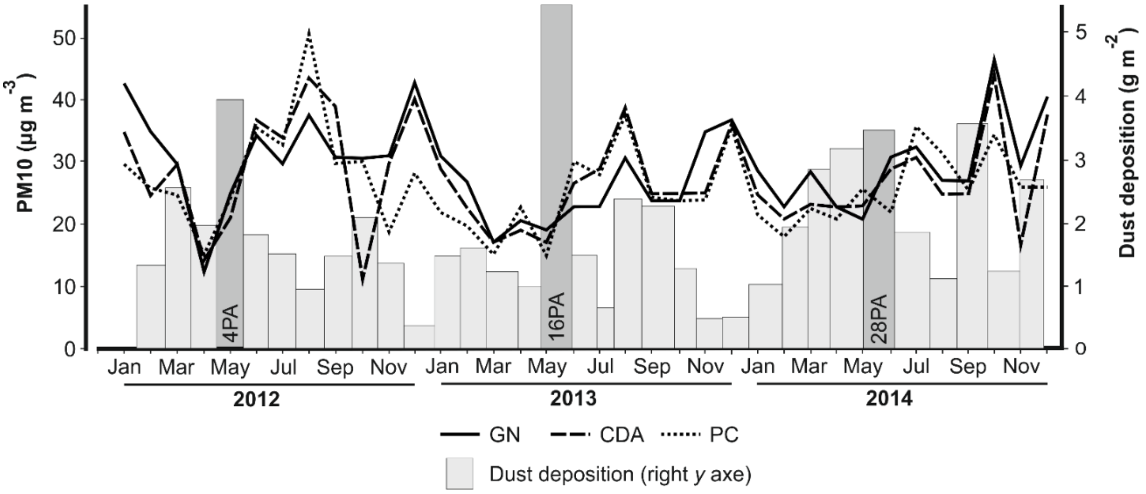

Figure 1. PM10 monthly concentration (µg/m^3) (data from *Red de Vigilancia de la Calidad del Aire*; Junta de Andalucía, 2021b) and dust deposition (g/m^2) between 2012 and 2014. Boxes show the study sample periods. CDA, Ciudad Deportiva Armilla station; GN, Granada Norte station; PC, Palacio Congresos station.

2.5. Atmospheric dust samples study

2.5.1. Particle size distribution

We determined (range 0.02–2000 µm) by wet dispersion laser diffraction method (Mastersizer 2000, Malvern Instruments Ltd., UK). The results were grouped (in µm) as follows: <1, 1–2.5, 2.5–10, <10 (PM10), 10–100, 100–1000 and 1000–2000. Statistical analysis was performed using the free software GRADISTAT (v. 9.1) (http://www.kpal.co.uk/gradistat.html) (Blott and Pye, 2001).

2.5.2. Mineralogical composition

Qualitative and semi-quantitative analysis by X-ray diffraction (XRD) with a Brucker AXS D8 Advance equipment (Cu-Kα radiation, between 3 and 70º 2θ; speed 2º min-1) was performed. The diffractograms were interpreted using the Xpowder software (Martín-Ramos, 2004). The presence of palygorskite was tested at the 0.63 nm peak (d_{200}; 15% intensity). Percentages of minerals were estimated using intensity factors from Schultz (1964), Barahona (1974), and Delgado et al. (1982).

Mineralogical compositions are represented in the triangle Carbonates (calcite + dolomite) —Tectosilicates (quartz + K-feldspar + plagioclase) — Phyllosilicates + Fe oxides (hematite + goethite) (Calero et al., 2009).

2.5.3. Quartz grains study

A morphological study (including microtextures) was performed in approximately 50 quartz grains per sample (a total of 156 quartz grains). Samples were sprinkled on double-sided carbon adhesive tape attached to an aluminium sample stubholder. Next, they were metallised with carbon using a Polaron CC7650 metalliser, and images were obtained by SEM (Hitachi S-510). EDX microanalysis (Rontec) coupled with SEM was used to guarantee the quartz nature of the grains.

First, SEM images were used to detect the quartz surface microtextures. A template (spreadsheet) was created to assess the presence or absence of microtextures (heuristic appreciation), following Mahaney (2002), Vos et al. (2014), and Sweet and Brannan (2016).

Second, SEM images were subjected to IA using ImageJ Software free software (https://imagej.net/) (Abramoff et al., 2004). Particles were separated from the background using image-processing techniques (Kumara et al., 2012). The following shape parameters were calculated: area, perimeter, maximum feret (maxferet), minimum feret (minferet), major and minor axis (ellipse), shape factor, aspect ratio (AR), maxferet/minferet, and roundness. The AR was calculated by fitting an ellipse to the projected particle area and dividing the major by the minor axis (Kandler et al., 2007). Roundness is defined as the ratio of four times the area by one pi times the square of the major axis ($4 \times \text{area} / \pi * \text{major\_axis}^2$). Shape factor is the ratio of the perimeter of a squared particle by four times pi times the projected area ($\text{perimeter}^2 / 4 * \pi * \text{area}$). This dimensionless parameter was used as an indicator of particle complexity. The shape factor describes how ‘jagged’ a particle is, by definition, equal to 1 for a circle (Reid et al., 2003).

Statistical analysis was performed using IBM SPSS Statistics (v. 22) software to perform principal component analysis and crosstabs.

2.5.4. Minor elements concentration

Minor element content (including rare earth elements [REE]) was determined by inductively coupled plasma mass spectrometry (ICP-MS) with a quadrupole ion filter NEXION 300D PERKIN-ELMER, USA (detection limits <0.0001 mg kg^{-1}). The samples were previously disaggregated in HNO_3 and HF.

Minor element concentrations were normalised to chondrite (standard CI chondrite of McDonough and Sun, 1995). REEs were grouped as follows: light (LREE: La, Ce, Pr, Nd), medium (MREE: Sm, Eu, Gd, Tb, Dy), and heavy (HREE: Ho, Er, Tm, Yb, Lu); Y was not considered in this classification. In graphic representations, Y is placed between Ho and Er (Korotev, 2009). Geochemical indices $HREE_N/LREE_N$ and $MREE_N/LREE_N$ were calculated (Mourier et al., 2008; Laveuf and Cornu, 2009); the suffix “N” indicates that the value normalised to chondrite is used.

3. Results and discussion

3.1. PM10 concentration

PM10 concentrations between January 2012 and December 2014 fluctuated between 11 and 51 µg m^{-3} throughout the study period (Figure 1). In the spring sampling periods (May–June), PM10 values vary between 22.00 and 25.33 µg m^{-3} (Table 1). The 16PA sample showed the lowest value. The PM10 daily legal limit (50 µg m^{-3}: European Union Directive, 2008/50/EC) was exceeded on 05/18/2012 at the Palacio de Congresos station (sampling period 4PA), on 6/06/2014 at all stations (sampling period 28PA), and on 06/11/2014 at the Ciudad Deportiva station (sampling period 28PA) (Junta de Andalucía, 2021b). These high concentrations are beyond PM10 daily legal limits and indicate a health risk (WHO, 2013b).

3.2. HYSPLIT backward trajectories

HYSPLIT backward trajectories at the Granada sampling location showed a predominant North and East Atlantic provenance similar to that of Reche et al. (2018) (origin from the east coast of the United States or northern Europe). The influence of the African continent was lower (Figure 2, Table 1), which is similar to other studies (Cerro et al., 2020). The 16PA sample had little influence from the African continent (6% of backward trajectories were from, or had passed through, Africa), and in 4PA and 28PA, the African influence was greater (26% and 33%, respectively). These percentages are consistent with those provided by the Ministry of Ecological Transition and Demographic Challenge (2021). Rarely, air mass circulation was observed in the Mediterranean area.

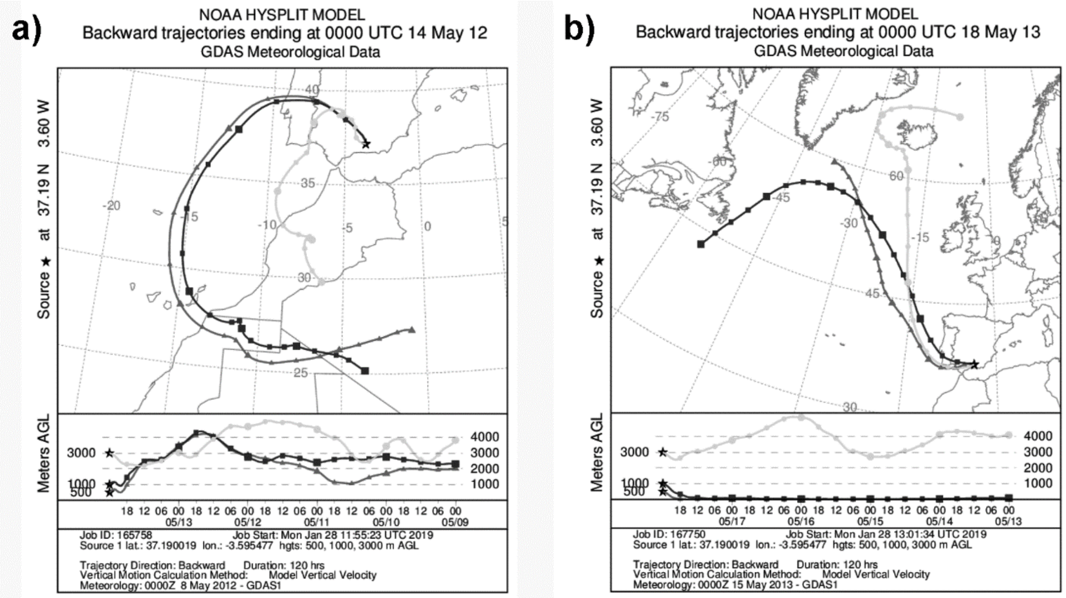

Figure 2. Examples of backward trajectories in the sampling periods: a) 14 May 2012 (4PA sample) from north of Africa, and b) 18 May 2013 (16 PA sample) from the Atlantic Ocean.

3.3. Atmospheric dust deposition rates

16PA showed the highest deposition rate (159 mg m^{-2} day^{-1}; Table 2); the 4PA and 28PA rates were lower and similar between them (114 and 108 mg m^{-2} day^{-1}, respectively; the similarity between 4PA and 28PA is noticeable but differs from 16PA, as observed in backward trajectories). The deposition rates in this study were within the ranges observed by other authors in the Granada area (Díaz-Hernández and Miranda-Hernández, 1997; Díaz-Hernández and Párraga, 2008; Díaz-Hernández et al., 2011; Morales-Baquero et al., 2013; Párraga et al., 2021) and similar to the spring period sample collected by Díaz-Hernández and Párraga (2008) (Table 2).

Table 2. Deposition rate of dust samples.

	Location	Reference	Period	Deposition rates (mg m^{-2} day^{-1})	
				range	mean
This study	Granada	4PA	26-April to 31-May 2012		114
	Granada	16PA	10-May to 13-June 2013		159
	Granada	28PA	16-May to 18-June 2014		108
Spain (Iberian Peninsula)	Granada	Díaz-Hernández and Miranda-Hernández (1997)	whole year 1992	10-158	63
	Granada	Díaz-Hernández and Párraga (2008)	summer 2001,2002 and 2004	1-82	53
	Granada	Díaz-Hernández and Párraga (2008)	1- to 2-April 2005	113	
	Granada	Díaz-Hernández et al. (2011)	whole year 1992	12-160	71
	Granada (Sierra Nevada)	Morales-Baquero et al. (2013)	December 2000-December 2002	1-132	30
	Granada	Párraga et al. (2021)	June to October 2010	23-168	55
	Barcelona	Lequy et al. (2018)	May 2011 to December 2012	20-320	50
	Barcelona	Ávila et al. (1997)	1983-1994		15
Spain (Canary Islands)	Gran Canaria	Menéndez et al. (2007)	October 2002 – October 2003	24-432	108
	Gran Canaria	Menendez et al. (2009)	2003 – 2007	38-120	
Europe (continent)	France (French Forest)	Lequy et al. (2013)	December 2009 – March 2012		5
	France (Alps)	Goudie and Middleton (2001)	30 years ice core		1
	Switzerland (Alps)	Goudie and Middleton (2001)	50 years ice core		1
Europe (Mediterranean islands and seas)	France (Corsica)	Díaz-Hernández and Miranda-Hernández (1997)	whole year 1984		38
	France (Corsica)	Lequy et al. (2013)	December 2009 – March 2012		33
	France (Corsica)	Lequy et al. (2013)	December 2009 – March 2012	11-72	34
	France (Corsica)	Bergametti and Fôret (2014)	February 1985 – April 1986		31
	Italy (Sardinia)	Goudie and Middleton (2001)	1990 – 1995	16-36	
	Greek (Crete)	Díaz-Hernández and Miranda-Hernández (1997)	1988 – 1994	27-90	52
	Greek (Crete)	Bergametti and Fôret (2014)	1988 – 1994	30-63	
	Greek (Crete)	Goudie and Middleton (2001)	January 1988 – September 1990	27-274	
	Aegean Sea	Goudie and Middleton (2001)	1988 – 1992	31-100	
East Mediterranean sites	Turkey	Bergametti and Fôret (2014)	August 1991 – December 1992		36
	Israel (coastline)	Goudie and Middleton (2001)	February 1994, December 1994, February 1995, April 1995		197
	Israel coast (40-100 miles off the coast)	Goudie and Middleton (2001)	February 1994, December 1994, February 1995, April 1995		99
	Israel	Díaz-Hernández and Miranda-Hernández (1997)	March 1976 – February 1977	55-110	
African sites	Libya	Bergametti and Fôret (2014)	June 2000 – May 2021		332
	Sur Chad	Goudie and Middleton (2001)	1966 - 1967		299
	SW Niger	Goudie and Middleton (2001)	1985 - 1989		575
	Nigeria (North)	Díaz-Hernández and Miranda-Hernández (1997)	1976 - 1979	378-493	
	Gulf of Guinea	Goudie and Middleton (2001)	January – March 1988 and March – April 1990	9-32	

However, deposition rates are always higher than the average bibliography rates because of the spring months (this study), which have the highest deposition rates (Díaz-Hernández et al., 2011; Torfstein et al., 2017; Cerro et al., 2020). Our deposition rates (Table 2) contrast with the mean values from 1) Spain (usually lower and similar to Gran Canaria), 2) Europe (lower), and 3) Africa (higher). Lequy et al. (2018) demonstrated a decrease in the influence of Saharan dust in European areas far from it. In addition, lower latitudes show climate dryness and an absence of vegetal cover on soils, promoting aeolian particle erosion–deposition.

3.4. Particle size distribution

The main grain size fractions in the study samples were coarse and very coarse silt (16–62 µm; 53.41% and 43.02% for 16PA and 28PA, respectively; Table 3); the clay fraction also showed low percentages (2.02% and 2.73% for 16PA and 28PA, respectively). These data were also observed by Menéndez et al. (2007; 2014) for atmospheric dust collected from the Canary Islands. The grain size <16 µm (medium silt, very fine, and fine silt and clay) showed higher percentages in 28PA, which could indicate a greater influence of Saharan transport according to Menéndez et al. (2009) and a health problem (WHO, 2013b). The coarser fractions (sand) originate from a proximal local source.

Table 3. Laser Granulometry and statistical parameters of atmospheric dust samples[1].

	16PA	28PA
Grain size (%)		
Medium and coarse sand (250-2000 µm)	0.00	5.46
Fine sand (125-250 µm)	3.57	7.51
Very fine sand (62-125 µm)	25.64	20.79
Coarse and very coarse silt (16-62 µm)	53.41	43.02
Medium silt (8-16 µm)	8.59	9.94
Very fine and fine silt (2-8 µm)	6.77	9.93
Clay <2 µm	2.02	2.73
PM10 (<10 µm)	12.32	17.17
Statistical parameters (arithmetic; µm)		
Mean	48.25	84.16
Sorting (σ)	34.81	157.30
Skewness (*Sk*)	0.89	4.96
Kurtosis (*K*)	3.27	34.38

[1] 4PA sample quantity was insufficient to do Laser Granulometry

All statistical parameters (mean, sorting, skewness, and kurtosis) showed differences between samples (Table 3). A strong positive skewness is shown in 28PA and was also observed in the Canary Islands (Menéndez et al., 2007) and Tenerife (Criado and Dorta, 2003); notably, this is evidence of suspension transport (Nickling, 1983). However, 16PA showed a skewness close to zero (Table 3).

3.5. Mineralogical composition

Mineralogy (XRD) is heterogeneous in terms of mineral species and quantities (Table 4). These minerals were detected: phyllosilicates (mainly illite followed by kaolinite and in less abundance mixed layers with reflection between 1.0-1.5 nm d_{00l} -1.0-1.5 nm phyllosilicates-, paragonite, palygorskite, and chlorite), tectosilicates (quartz and minor contents of K-feldspar and plagioclases), carbonates (calcite and dolomite), iron oxides (hematite and goethite), amphibole, gypsum, sylvite, and halite. Total phyllosilicates were the most abundant (43%–58%), followed by total carbonates (16%–30%) and quartz (16%–20%). Calcite was at least twice the amount of dolomite. The rest of the mineral phases were a minority; some, namely, palygorskite, amphibole, or gypsum, were present in only one sample and <1% quantities. Except for sylvite and amphibole, all mineral species detected have been described in the atmospheric dust of Granada and its metropolitan area (Díaz and Párraga, 2008; Díaz- Hernández et al., 2011; Rodríguez-Navarro et al. 2018; Párraga et al., 2021). The presence of amphiboles is a remarkable result because of its negative impact on human health when inhaled (IARC, 2012).

In the triangle Carbonates — Tectosilicates — Phyllosilicates + Fe oxides (Figure 3), the samples (4PA, 16PA, and 28PA) take up a small area characterised by high contents of phyllosilicates + iron oxides (43%–60%) and low and similar values of carbonates and tectosilicates. 4PA separates from 16PA and 28PA because of the lower percentage of phyllosilicates + iron oxides.

The atmospheric dust samples collected in Granada (Díaz-Hernández et al., 2011; Rodríguez-Navarro et al., 2018; Párraga et al., 2021) were similar to those of the study samples (Figure 3). Díaz-Hernández and Párraga (2008)'s samples were separated because of their low contents of phyllosilicates and iron oxides.

Table 4. Mineralogy (XRD) of atmospheric dust samples.

	4PA	16PA	28PA
Phyllosilicates			
1.0-1.5 nm phyllosilicates		1	1
Illite	23	26	27
Paragonite		7	9
Chlorite	2	1	1
Kaolinite	18	23	17
Palygorskite		<1	
Total phyllosilicates	43	58	55
Tectosilicates			
Quartz	20	16	16
K-feldspar		1	2
Plagioclases	2	<1	
Total tectosilicates	22	17	18
Carbonates			
Calcite	20	12	16
Dolomite	10	4	4
Total carbonates	30	16	20
Others			
Iron oxides	tr	2	1
Amphibole			<1
Gypsum	<1		
Silvite	2	5	3
Halite	3	2	3

tr: traces

The quantification method must be considered to compare the mineralogical composition (XRD) (Párraga et al., 2021). However, linearity and a positive relationship between carbonates and tectosilicates (R^2 = 0.585 and n = 8; relationships not described thus far) were detected in all atmospheric dust samples collected in Granada (including those in this study).

Moreover, fine fractions (<50 µm) of southern Iberian Peninsula soils (Delgado et al., 2003; Martín-García et al., 2004; Márquez, 2012; Comino et al., 2020- Vega Soil Clay; Comino et al., 2020- Red Soil Clay), a possible source of atmospheric dust, are close (but with higher contents of phyllosilicates + iron oxides) to 16PA and 28PA (Figure 3).

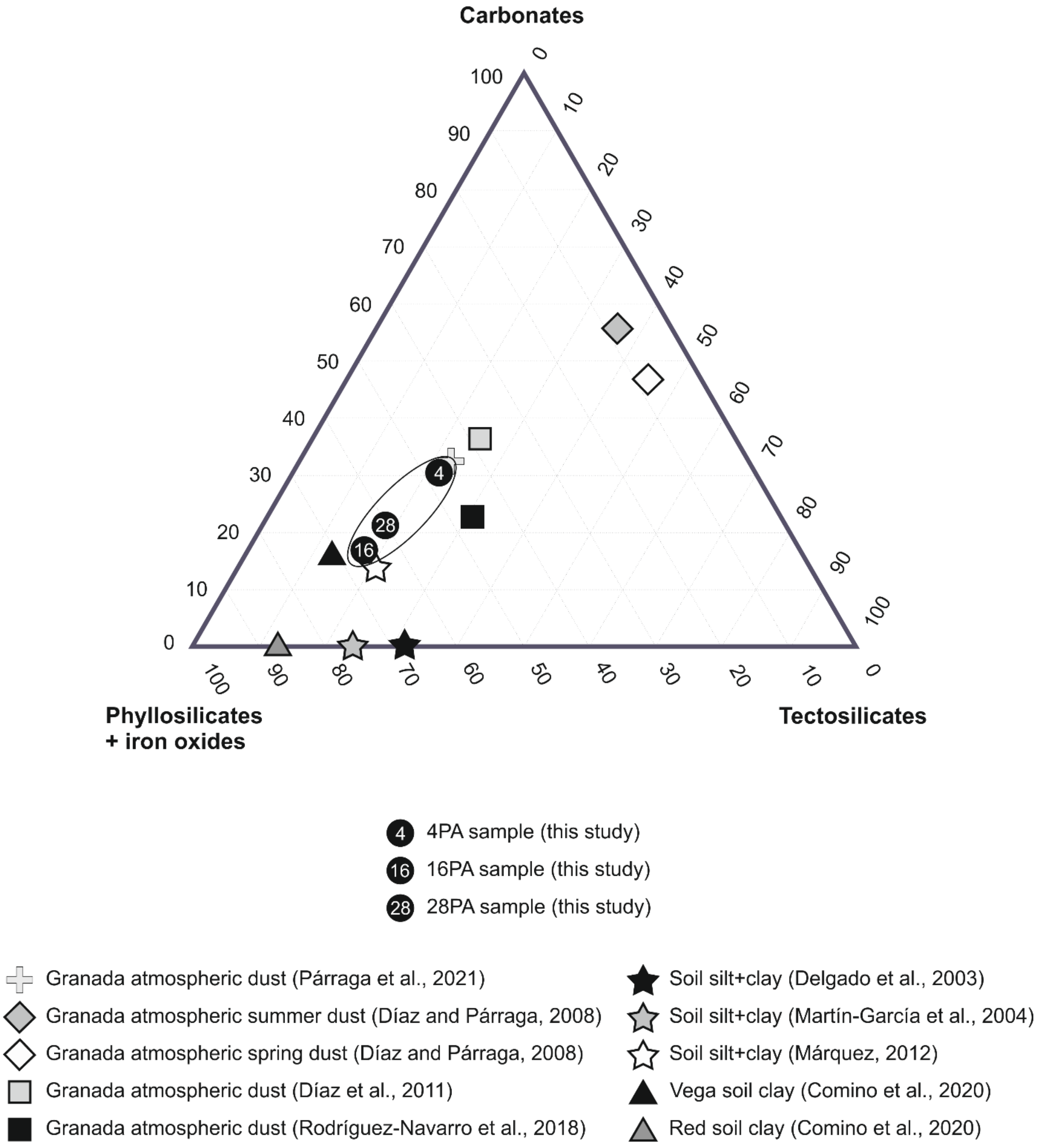

Figure 3. Triplot Carbonates – Phyllosilicates + Iron oxides – Tectosilicates of atmospheric dust samples. The study samples are surrounded by an ellipse.

3.6. Quartz grains study

Quartz grains observed by SEM-EDX were morphologically heterogeneous (Figure 4). They are mainly monocrystalline (Figure 4b, d) and some polycrystalline (Figure 4a, c, e, f; sometimes small crystal aggregates). Well-rounded and polished grains of aeolian origin were observed (Figure 4c). Fresh-looking subangular-angular grains, without aeolian evolution, were also found (Figure 4b, d).

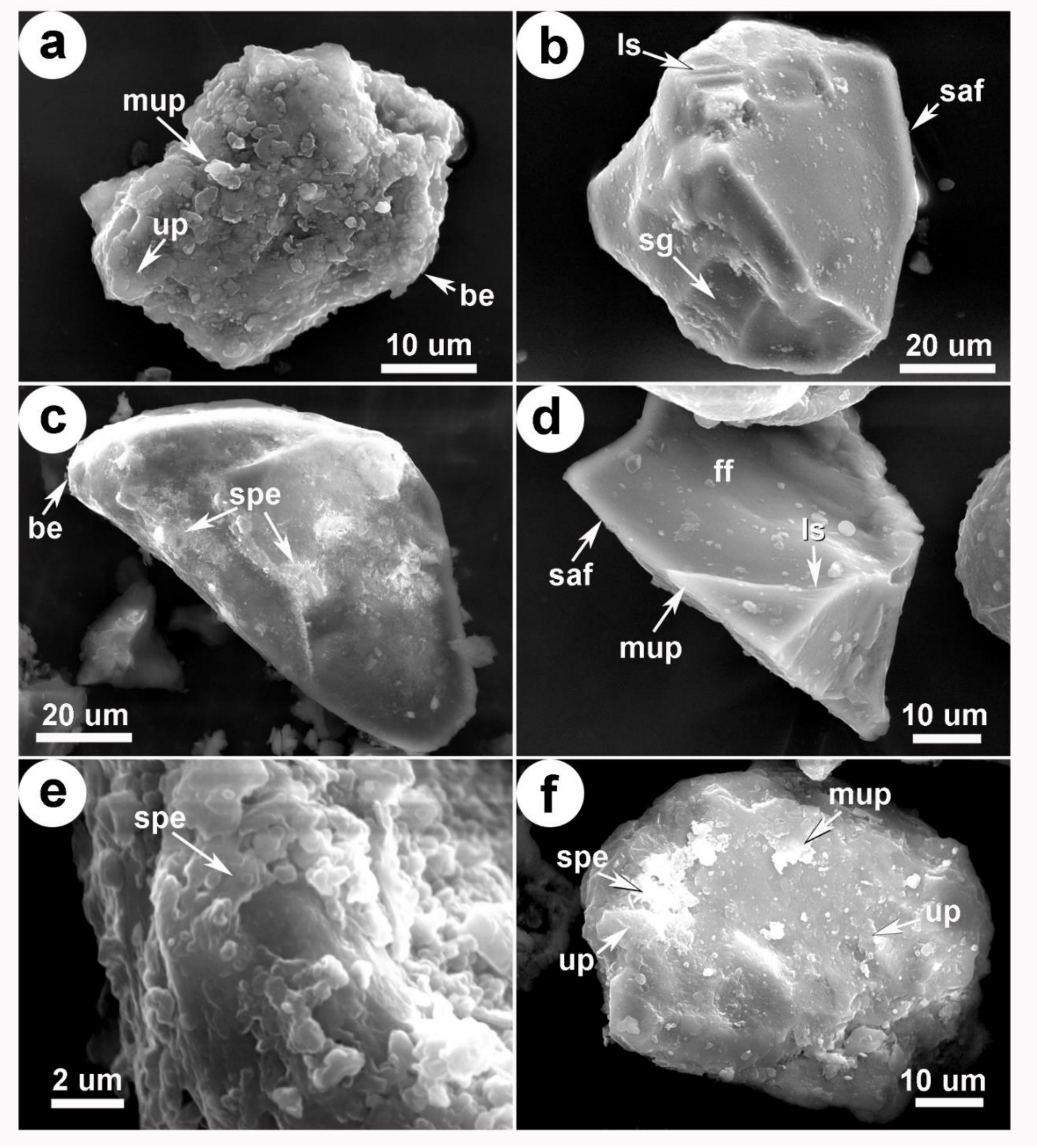

Figure 4. SEM images of quartz grains: a) 4PA sample. Medium relief polycrystalline grain (43 µm maximum diameter), subrounded, whit typical aeolian microtextures, namely, upturned plates (up), bulbous edges (be), and mechanically upturned plates (mup); b) 4PA sample. Medium relief monocrystalline grain (59 µm long) in which crystal faces are recognised. Clear surface, subrounded perimeter with mechanical microtextures, namely, sharp angular features (saf), linear steps (ls), and straight grooves (sg); c) 16PA sample. Low relief polycrystalline grain (102 µm long). Typical aeolian microtextures, namely, rounding, bulbous edges (be), silica pellicle (spe), and polished surface, are observed; d) 4PA sample. Low relief monocrystalline grain (59 µm

long). Mechanical microtextures, namely, saf, mup, ls, and fracture face (ff), are observed. All these mechanical microtextures denote a fresh-looking aspect (little aeolian evolution); e) 28PA sample. Enlargement of a surface quartz grain showing silica pellicle (spe); f) 28PA sample. Low relief polycrystalline grain (63 µm long) showing silica pellicle (spe) and typical mechanical aeolian microtextures, namely, upturned plates (up) and mechanically upturned plates (mup).

The most frequent mechanical microtextures (Table 5) were ‘edge rounding’ (approximately 90% of the grains; Figure 4a,b,c,f), ‘bulbous edges’ (23%–50%; Figure 4a,c,f), ‘upturned plates’ (14%–60%; Figure 4a,f) and ‘mechanically upturned plates’ (38%–49%; Figure 4a,f). These microtextures are typical of aeolian environments (Costa et al., 2013; Vos et al., 2014) because the impact between particles generates an amorphous silica pellicle (Figure 4a,f). The chemical precipitation microtextures (verified by EDX) were ‘silica flower’ and ‘silica pellicle’ (Figure 4c). The dissolution microtextures were ‘corrosion gulf’ and ‘solution pits’. According to Baker et al. (2014), atmospheric transport alters the chemical composition of mineral particles, and pellicles can be found in aeolian grains. Geochemical activity was imprinted on the surface of the grains. The ‘solution pits’ microtextures detected in 16PA (33%) are associated with inheritance from pedological processes (Vos et al., 2014). Medium relief was dominant in this study, followed by low and high relief. According to Vos et al. (2014), low relief is the most abundant in aeolian environments, followed by medium relief.

The chi-square χ^2 statistical study showed significant differences between samples for ‘bulbous edges’ ($P < 0.05$), ‘upturned plates’ ($P < 0.001$), and ‘solution pits’ ($P < 0.001$). The first two are characteristics of aeolian environments, and their occurrence frequencies are higher in 4PA and 28PA (Table 5). Solution pits are characteristic of pedogenic environments, and 16PA has the highest occurrence frequency (Table 5), further proof of the two sample groups.

Quartz grain shape parameters corroborate the differences between samples (4PA and 28PA similar and different from 16PA; Table 6). Differences were notable for area, perimeter, maxferet, minferet, maxferet/minferet, major axis

Table 5. Occurrence frequency (%) of quartz microtextures[1] from atmospheric dust samples.

		4PA	16PA	28PA
Mechanical				
	Edge rounding	92	88	90
	Sharp angular features	22	32	12
	Conchoidal fractures	4	2	2
	Arc-shaped steps	6	9	0
	Linear steps	6	4	8
	Fracture faces	8	16	4
	V-shaped percussion cracks	4	2	2
	Breakage blocks	6	4	6
	Straight grooves	6	9	6
	Curved grooves	4	2	2
	Mecanically upturned plates	48	49	38
Mechanical				
	Bulbous edges	36	23	50
	Upturned plates	60	14	48
	Subparallel linear fractures	4	2	0
Chemical				
	Solution pits	0	33	2
	Corrosion gulf	30	18	12
	Silica flowers	20	11	23
	Silica pellicle	14	21	17
Combined mechanical and chemical				
	Low relief	36	21	40
	Medium relief	52	67	46
	High relief	10	12	13

[1] According to Mahaney (2002), Vos et al. (2014) and Sweet and Brannan (2016).

Table 6. Shape parameters obtained by Image Analysis (IA) from SEM quartz´s micrographs.

	4PA (n=49)		16PA (n=56)		28PA (n=51)	
	mean	SD	mean	SD	mean	SD
Area (μm^2)	1253.78	707.88	3495.99	2119.16	1037.04	697.66
Perimeter (µm)	154.49	43.41	269.97	92.29	141.31	50.02
Maximum Feret (µm)	50.08	13.98	81.92	28.82	45.23	16.02
Minimum Feret (µm)	33.53	10.89	57.04	18.27	29.52	11.26
Maximum Feret / Minimum Feret	1.55	0.34	1.46	0.31	1.60	0.44
Major axis (µm)	47.21	12.85	76.53	27.70	42.82	15.17
Minor axis (µm)	31.74	10.40	53.77	17.24	28.06	10.77
Shape Factor	1.66	0.33	1.81	0.31	1.73	0.30
Aspect Ratio	1.56	0.41	1.45	0.36	1.61	0.51
Roundness	0.68	0.14	0.72	0.14	0.67	0.17

SD, Standar deviation.

(ellipse), and minor axis (ellipse) parameters (Table 6). AR values were consistently higher than 1, and 16PA had the lowest value. 16PA´s shape factor parameter shows the highest value, indicating a greater irregularity of its particles, according to Reid et al. (2003).

Principal component analysis of the shape parameters found two components (PC1 and PC2), which explained 91.20% of the sample variability. Again, 16PA differed from 4PA and 28PA (Figure 5). The PC1 component collects parameters related to quartz grain size (area, perimeter, maxferet, minferet, major axis, minor axis), which differentiates 16PA from 4PA and 28PA.

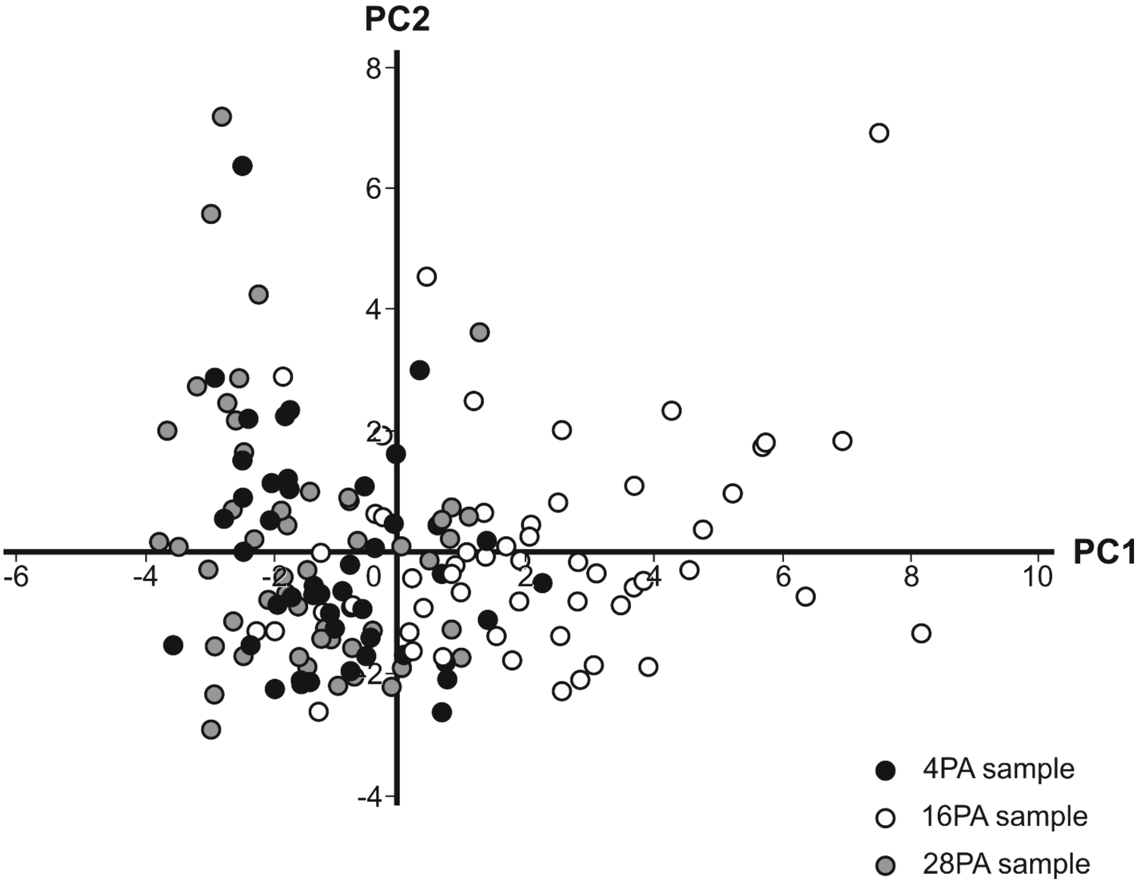

Figure 5. Principal component analysis biplot (PC1 *vs*. PC2).

3.7. Minor elements composition

Zn, Sr, Ba, Mn, and Cr were the most abundant minor elements (>100 ppm in at least one of the three samples studied; Table 7). 16PA always shows the lowest values (except for Mo, Cd, Sn, Sb, and Pb) and differs from 4PA and 28PA (similar in most cases). These results are consistent with the trends already observed. The samples showed high content of Pb and Sr compared with that in the bibliography data (Scheuvens et al., 2013).

Table 7. Minor elements (ppm) of atmospheric dust samples.

	4PA	16PA	28PA		4PA	16PA	28PA		4PA	16PA	28PA
Be	0.50	0.10	0.77	**Mo**	1.95	1.97	4.01	**U**	0.81	0.45	1.00
Sc	2.28	1.04	4.06	**Cd**	0.13	0.14	0.60	**Li**	9.18	5.51	16.48
V	28.88	13.49	35.48	**In**	0.09	0.07	0.08	**Rb**	24.27	14.94	37.52
Cr	33.27	22.60	106.80	**Sn**	12.07	15.02	7.90	**Cs**	1.49	0.78	2.03
Mn	148.52	85.87	239.20	**Sb**	18.89	11.95	11.52	**Sr**	318.79	155.10	357.58
Co	12.19	8.98	20.96	**Ba**	201.13	90.34	170.49	**Ga**	4.36	2.21	6.59
Ni	17.29	15.23	57.07	**Tl**	0.16	0.08	0.20	**Nb**	2.51	1.90	7.88
Cu	84.18	58.48	70.79	**Pb**	36.06	74.79	32.39	**Ta**	0.11	0.01	0.41
Zn	410.30	247.62	319.97	**Bi**	0.51	0.36	0.43	**Zr**	11.70	10.75	52.18
As	3.49	0.61	3.79	**Th**	3.48	1.20	4.62	**Hf**	0.42	0.33	1.32

Figure 6 shows the two groups of samples. 4PA and 28PA are almost coincident and parallel to 16PA, except for Pb, Th, and As.

Additionally, REE composition presents the following characteristics (Table 8): 1) REEs follow the Earth’s crust abundance order (Ce> La> Nd> Y> Pr> Sm> Gd> Dy> Er> Yb> Eu> Ho> Tb> Tm> Lu); however, there are exceptions in the HREE, where the order changed between some contiguous elements (Lu> Tm sample 28PA; Tb> Ho sample 4PA; Yb> Er sample 4PA and 16PA). 2) LREEs are the most abundant, followed by MREE and HREE. 3) 16PA has lower ∑REE than 4PA and 28PA (which present similar values), confirming the existence of two groups again. 4) The normalised chondrite profiles show (Figure 7) 4.1) normalised values that are always higher than 1 (amounts higher than reference meteorite), except for Lu (0.98) in 16PA. This sample shows exceptionally low values, close to 1 in several elements (Figure 7); 4.2) enrichment in LREE, demonstrated by a strong negative slope (with atomic number growth), which decreases from Eu and becomes flatter in the HREE. This is shown by the $\mathrm{MREE_N}/\mathrm{LREE_N}$ (0.14 to 0.17) and $\mathrm{HREE_N}/\mathrm{LREE_N}$ (0.11 and 0.14) ratio values (Table 8); 4.3) the study samples have a noticeable negative europium anomaly. In addition, the positive anomalies of erbium (28PA), ytterbium (4PA, 16PA, and 28PA), and yttrium (16PA) are perceptible (Figure 7).

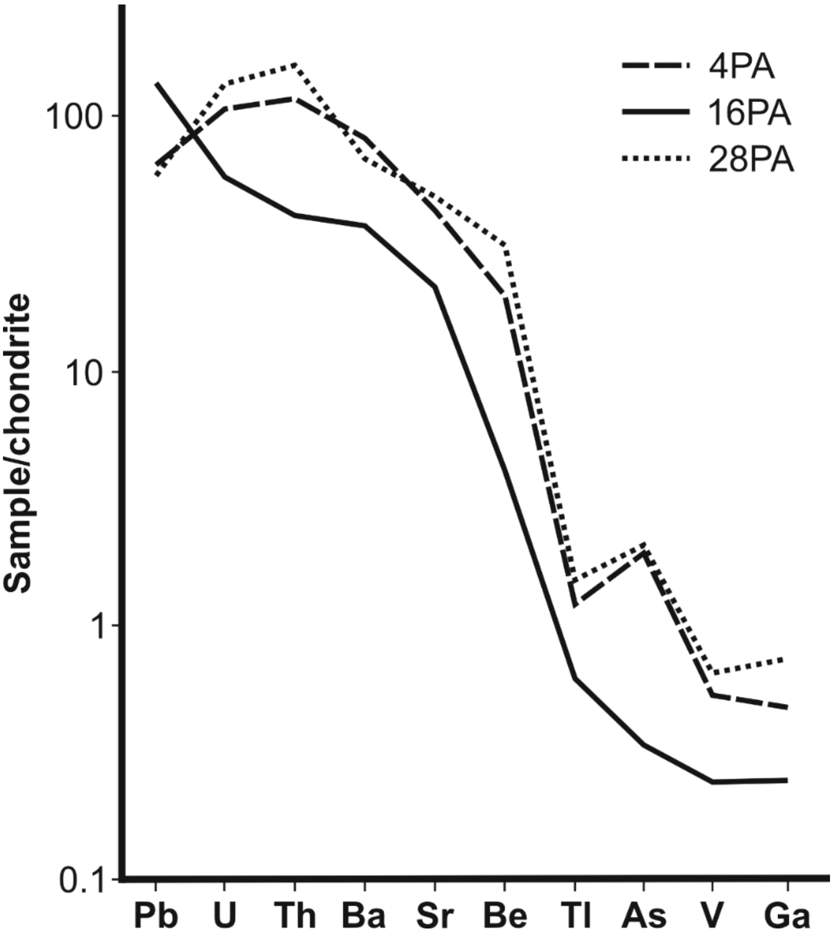

Figure 6. Chondrite normalised diagram of selected minor elements.

We compared this study of REE contents with the literature (Table 8 and Figure 7) and the following was observed: 1) Lower ΣREE in this study´s samples because they have a coarser grain size (Table 3) than SSH (silt size), LE (5-20 µm), and AD (<20 µm). This finding supports that of Xie et al. (2014), that is, grain size exerts an evident influence on REE compositions. Thus, REE are concentrated in the silt (2 to 50 µm) and clay (<2 µm) fine fractions (Prudêncio et al., 1993; Aide and Smith-Aide, 2003; Marques et al., 2011). Granada dust (GD, Párraga et al., 2021) has the closest ΣREE to this study's samples because the two have a similar grain size (fine sand). 2) European soil, Spanish soil (SS), and continental crust (EC1 and EC2) normalised chondrite profiles are closer to our study's samples than the materials from Africa (Figure 7). 3) Our samples' $HREE_N/LREE_N$ and $MREE_N/LREE_N$ ratio values are generally lower than those in literature; the exceptions are GD (0.12) and SS (0.13) for $HREE_N/LREE_N$ and SS (0.17) for $MREE_N/LREE_N$ (Table 8).

Table 8. Rare earth elements content (ppm) and selected geochemical ratios in atmospheric dust samples and other materials from bibliography.

	This study			Other materials[1]							
	4PA	16PA	28PA	SSH	LE	GD	AD	EC1	EC2	SS	ES
La	8.49	3.64	12.82	44.33	25.81	14.56	50.05	31.00	30.00	38.83	25.86
Ce	19.32	7.06	26.51	95.44	53.27	29.49	105.53	63.00	64.00	81.27	52.25
Pr	2.12	0.81	2.92	10.89	6.57	3.31		7.10	7.10	9.80	6.02
Nd	7.07	3.17	10.38	47.44	25.81	12.05	48.85	27.00	26.00	34.96	22.41
Sm	1.46	0.61	2.21	7.22	4.97	2.34	9.63	4.70	4.50	6.49	4.28
Eu	0.22	0.07	0.36	1.22	1.03	0.51	1.93	1.00	0.88	1.12	0.85
Gd	1.23	0.46	1.82	8.67	4.47	1.90	10.07	4.00	3.80	5.40	4.20
Tb	0.15	0.05	0.21	1.11	0.67	0.26	1.26	0.70	0.64	0.71	0.64
Dy	0.76	0.27	1.24	7.33	4.46	1.46		3.90	3.50	3.91	3.58
Ho	0.13	0.06	0.24	1.33	0.97	0.26	1.64	0.83	0.80	0.73	0.72
Y	3.47	1.83	5.84	25.11	27.99	7.38		21.00	22.00	20.01	
Er	0.38	0.17	0.83	3.44	2.84	0.67		2.30	2.30	2.01	2.10
Tm	0.06	0.03	0.09	0.75	0.47	0.09		0.30	0.33	0.29	0.31
Yb	0.41	0.25	0.65	3.78	2.96	0.61	4.32	1.96	2.20	1.85	2.09
Lu	0.04	0.02	0.09	0.67	0.46	0.10	0.63	0.31	0.32	0.27	0.31
∑REE	41.83	16.66	60.37	233.64	134.75	67.61	233.91	148.10	146.37	187.64	125.62
∑LREE	37.00	14.68	52.63	198.11	111.46	59.41	204.43	128.10	127.10	164.86	106.54
∑MREE	3.82	1.45	5.84	25.56	15.60	6.48	22.89	14.30	13.32	17.63	13.56
∑HREE	1.01	0.53	1.89	9.97	7.69	1.72	6.59	5.70	5.95	5.15	5.52
$\text{HREE}_N/\text{LREE}_N$	0.11	0.13	0.14	0.22	0.28	0.12	0.17	0.18	0.19	0.13	0.21
$\text{MREE}_N/\text{LREE}_N$	0.16	0.14	0.17	0.22	0.24	0.19	0.24	0.20	0.18	0.17	0.22

[1] SSH, Sahara-Sahel corridor (Moreno et al., 2006); Libya-Egypt materials (Abed et al., 2009); GD, Granada dust (Párraga et al., 2021); AD, African dust (Muhs et al., 2010); EC1, mean composition of continental crust (Rudnick and Gao, 2003); EC2, mean composition of continental crust (Taylor and McLennan, 1985); SS, Spanish top soil (Locutura et al., 2012); ES, European top soil (Salminen et al., 2005).

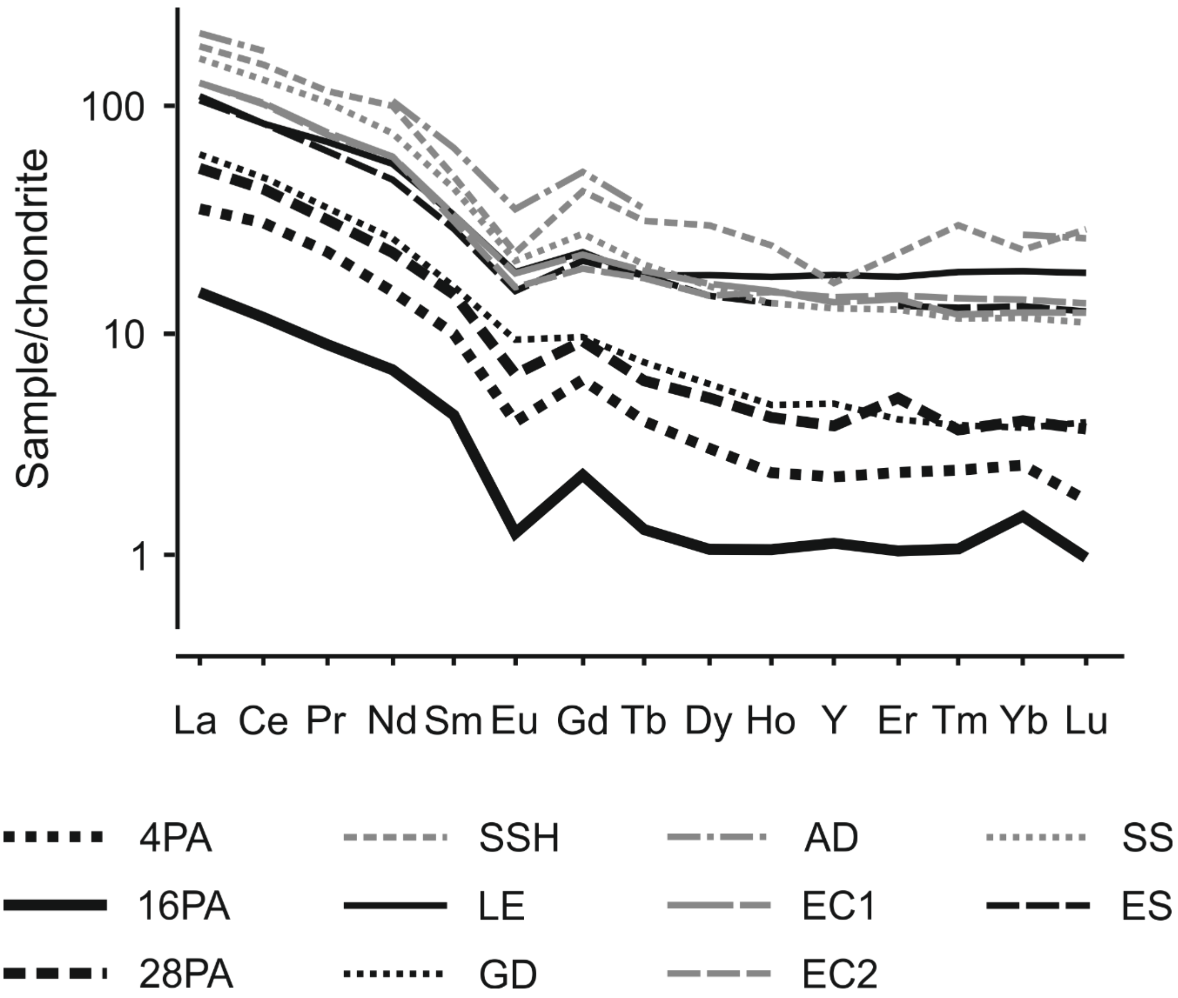

Figure 7. Chondrite normalisation of REE contents of atmospheric dust samples and other materials from the bibliography. See Table 8 for abbreviation explanations.

3.8. Provenance fingerprints of atmospheric dust. Quartz evidence

The results obtained can be regarded as atmospheric dust provenance fingerprints.

4PA and 28PA showed the highest backward trajectory percentages from North Africa, the highest PM10 concentrations (expressed in µg m^{-3} and as a percentage), and the lowest deposition rates (Table 1). However, 16PA shows the lowest backward trajectory percentage from Africa, the lowest PM10 concentration, and the highest deposition rate. These results indicates a greater Sahara Desert influence on 4PA and 28PA. The decrease in deposition rates when PM10 increases could be due to the inefficiency of removal processes of small-diameter particles (<2.5 µm) (Bergametti and Fôret, 2014), allowing them to remain suspended in the atmosphere for longer and enabling long-distance travel. However, large particles (mainly >10 µm) settle quickly (Bergametti and Fôret, 2014), which suggests a local origin. The weak correlation of PM10 and dust deposition rates may be also caused by the wet and dry deposition events differences of the studied period. Besides, the urban and rural pollution, a main component of the PM10 fraction, could contribute to this poor correlation (Querol et al., 2001; Rodriguez et al., 2011).

The greater abundance of quartz microtextures, namely, bulbous edges and upturned plates (Table 5), prints a greater aeolian character to 4PA and 28PA (Costa et al., 2013). By contrast, the presence of solution pits in 16PA quartz grains indicates a greater participation of local origin. Martín-García et al. (2004, 2015) discovered solution pits microtexture in quartz from southern Spain soils.

Quartz grain shape parameters (Table 6, Figure 5) indicate the differences between the samples. The lower PC1 values (in principal component analysis) for the 4PA and 28PA samples (Figure 5) show a smaller area, perimeter, maxferet, minferet, major axis, minor axis. The atmospheric dust AR values provided by Scheuven and Kandler (2014) for atmospheric dust from Africa varied between 1.57 and 1.90, consistent with the 4PA (1.56) and 28PA (1.61) values. However, 16PA was outside the range (1.45). The quartz grain AR values provided by Kandler et al. (2007) for African dust collected in Tenerife (Spain) were 1.60, remarkably close to 4PA (1.56) and 28PA (1.61) (Table 6). All previous results support a greater African influence on 4PA and 28PA. According to Coz (2008), the highest AR values correspond to greater transport distances, suggesting that 4PA and 28PA can undergo greater atmospheric transport than 16PA. For quartz grains, the shape factor, 4PA (1.66), and 28PA (1.73) values (Table 6) are within the African dust range (1.53–1.76) provided by Chou et al. (2008); 16PA would be out of the range (1.81).

The XRD mineralogy (Table 4) allows us to interpret the African origin of atmospheric dust by Scheuvens et al. (2013)'s indices (Table 9). In this manner, 4PA and 28PA could be influenced by the Libya central zone (PSA4) because they have iIlite/kaolinite between 0.2 and 1.9, chlorite/kaolinite between 0.0 and 2.6, carbonate content (calcite + dolomite) from low to intermediate (1%–30%),

Table 9. Mineralogical indices (and Saharan provenance) of atmospheric dust samples.

Sample	Reference	Type of event	Date/Period/Year of event	Il/Ka	Ch/Ka	Palygorskite (%)	Carbonates (%)	Ca/Do
4PA	This study	DD+WD	26-April to 31-May 2012	1.28 (1,3,4)	0.11 (2,4)	nd (4,5,6)	30 (1,2,3,4)	2
16PA	This study	DD+WD	10-May to 13-June 2013	1.13 (1,3,4)	0.04 (2,4)	<1 (1,2,3)	16 (1,2,3,4)	3
28PA	This study	DD+WD	16-May to 18-June 2014	1.59 (1,4)	0.06 (2,4)	nd (4,5,6)	20 (1,2,3,4)	4
Atmospheric dust samples from Granada								
	Díaz-Hernández and Párraga (2008)	DD	sumer 2001, 2002 and 2004	2.25 (2)	(5)	nd (4,5,6)	52 (1,2,3)	0.23
		DD	1- to 2-April 2005	3.00 (2)	(5)	nd (4,5,6)	46 (1,2,3)	0.07
	Díaz-Hernández et al. (2011)	DD	whole year 1992	0.89 (3,4)	0.46 (2,3,4)	tr (1,2,3)	26 (1,2,3,4)	0.91
		DD	whole year 1992	1.06 (1,3,4)	0.46 (2,3,4)	tr (1,2,3)	30 (1,2,3,4)	0.61
		DD	whole year 1992	0.33 (3,4,5)	0.38 (2,3,4)	tr (1,2,3)	22 (1,2,3,4)	2.65
	Rodríguez-Navarro et al. (2018)	RR	21 to 23 February 2017	3.36 (2)	(5)	11 (1,2)	23 (1,2,3,4)	4.50
	Párraga et al. (2021)	DD	June to October 2010	4.25 (2)	0.38 (2,3,4)	nd (4,5,6)	32 (1,2,3)	0.58

Abbreviations: Il, illite; Ka, kaolinite; Ch, Chlorite; Ca, calcite; Do, dolomite; DD, dry deposition; WD, wet deposition; RR, red rain; nd, non-detected; tr, traces.

Source areas according to Scheuvens et al. (2013): (1) PSA1, Tunisia and northern Algeria including the ‘zone of chotts’; (2) PSA2, Foothills of Atlas mountains and western coastal region; (3) PSA3, Southern Algeria and northern Mali; (4) PSA4, Central Libya; (5) PSA5, Western Chad including the Bodélé depression; (6) PSA6, Southern Egypt, northern Sudan.

and palygorskite absence. However, 16PA could be influenced by African dust from Libya (PSA4), southern Algeria, northern Mali (PSA3), and the foothills of the Atlas mountains and the western coastal region (PSA2). Applying the indices of Scheuvens et al. (2013) to other atmospheric dust collected in Granada, these would show influence from 1) those of Párraga et al. (2021) from the foothills of the Atlas mountains and western coastal region (PSA2) (although with an absence of palygorskite); 2) those of Rodríguez-Navarro et al. (2018) from the foothills of the Atlas mountains and western coastal region (PSA2) (except for Ch/Ka index); 3) those of Díaz-Hernández and Párraga (2008), summer and spring samples, both from the foothills of the Atlas mountains and western coastal region (PSA2) and from western Chad including the Bodélé depression (PSA5); and 4) those of Díaz-Hernández et al. (2011) from southern Algeria and northern Mali (PSA3). The application of the Scheuvens et al. (2013) indices reveals that atmospheric dust samples from Granada (including those in this study) are not homogeneous in terms of influence from the African continent.

Furthermore, XRD mineralogy (Table 4) demonstrates that minority mineral species provide valuable information on the genesis and origin of atmospheric dust: 1) amphibole was detected in 28PA (minimal quantities). Amphibole presence is noticeable due to its genesis and implications for human health, which are remarkably notable (IARC, 2012). This mineral has not been described in African atmospheric dust samples (Scheuvens et al., 2013). However, it has been described (in few studies) in Spanish atmospheric dust and was associated with local pollution from natural sources (Menéndez et al., 2007) and with anthropogenic pollution from road traffic (wear of brake pads or clutch discs) (Amato et al., 2011). Jeong (2008) and Lequy et al. (2013) have detected amphiboles in Asian and northern French atmospheric dust, respectively. The authors concluded that amphiboles originated from local soils. In this study, amphiboles in 28PA could be due to local anthropic contamination from construction materials (e.g. corrugated fibre cement roofing) and dust from the traffic of urban areas (Amato et al., 2011); 2) gypsum, detected in 4PA, described both in atmospheric dust from the Sahara (Scheuvens et al., 2013) and neo-formed in the atmosphere from the weathering of other minerals (Díaz-Hernández and Párraga, 2008); 3) sylvite, detected in all samples and reported for the first time, according to our review of the literature, in atmospheric dust collected in Granada, which may have a natural origin associated with the erosion of sylvite-bearing rocks and soils present in the Granada Basin (SE Spain) (López-Quirós et al., 2016), or an origin associated with marine aerosols (Blondet et al., 2019); 4) palygorskite, already described in Granada (Díaz-Hernández et al., 2011; Rodríguez-Navarro et al., 2018) and only detected in 16PA, indicates a potential source from Tunisia and northern Algeria (including the 'zone of chotts' [PSA1]), the foothills of the Atlas mountains and western coastal region (PSA2) or southern Algeria and northern Mali (PSA3) (Scheuvens et al., 2013); 5) paragonite, detected in 16PA and 28PA, is an abundant mineral in geological materials from southern Spain (Martín-García et al., 1997) and in Rif's materials from Morocco (Rodríguez-Ruiz et al., 2019) and has been described in Granada atmospheric dust (Díaz-Hernández et al., 2011; Párraga et al., 2021). Paragonite presence could indicate an influence from northern Africa (Morocco) and south of the Iberian Peninsula.

Moreover, mineralogical similarities (Figure 3) between atmospheric dust and soil fine fractions from the south of the Iberian Peninsula could be a provenance indication. 16PA is the closest (in the mineralogical triangle) to the soil samples (higher phyllosilicates + iron oxides content). Atmospheric dust samples located far from soil samples (Figure 3) show more phyllosilicates + iron oxides and fewer carbonates + tectosilicates. This finding could indicate that local soils contribute as the main focus of phyllosilicates + iron oxides, and carbonates + tectosilicates could be from a different source.

Geochemistry can also provide evidence for provenance. Once again, the two groups differ: 16PA (usually lower contents) differs from 4PA and 28PA (Tables 7 and 8, Figures 6 and 7).

In this study, the samples showed higher Pb and Sr contents than those of most atmospheric dust from the Scheuvens et al. (2013) database: Sr is only surpassed in one case (by dust deposited in the Azores), and Pb is only exceeded in 7% of database cases (by dust collected in Italy and Beirut/Lebanon). The relatively high Sr contents can be explained by the proximity to Montevives and Escúzar, celestine mines ($SrSO_4$) located 20 km from Granada city. The relatively high Pb values must be attributed to anthropogenic influence (road traffic) (Parvainen et al., 2020), indicating a local influence on the study samples.

The ∑REE in this study showed values lower than those in the bibliography materials (Table 8, Figure 7). The lower ∑REE content, as discussed, is due to the higher particle sizes. Thus, the ∑REE content in atmospheric dust, linked to its grain size, can be an indicator of the transport distance.

4. Conclusions

A multitechnical study has enabled characterisation of the spring atmospheric dust (2012–2014) in Granada's strategic area (frontier of the European continent with Africa). PM10 concentration, deposition rates, grain size, XRD mineralogy, SEM quartz microtextures, SEM-IA quartz shape parameters, and minor element contents (including REE) showed differences among spring sampling periods, possibly due to differences in their provenance.

African influence has been shown by the following properties of atmospheric dust: a) apparently greater contents of PM10; b) greater presence of microtextures, namely, bulbous edges and upturned plates, on the surface of quartz grains; and c) for quartz´s shape parameters, minor values for area, perimeter, maximum feret, minimum feret, major axis, minor axis, and shape factor, and higher values for AR.

The mineralogy has confirmed different origins for atmospheric dust collected in Granada: the Northwest African continent (e.g. presence of palygorskite has been described in Tunisia, Algeria, Atlas mountains, western coastal region, and northern Mali), local sources, and minerals crystallised in the atmosphere during dust transport (sylvite and gypsum). Geochemistry has evinced a local influence through the relatively high Sr and Pb contents attributable to celestine mines ($SrSO_4$) located close to Granada city and pollution from road traffic, respectively. The low ∑REE content in the 16PA sample is an indicator of the short distance travelled.

In summary, the applied techniques can be used as provenance fingerprints. Quartz particle morphoscopy has been revealed as a new technique for understanding atmospheric dust provenance.

Acknowledgments

This work was supported by a grant from Ministerio de Economía, Industria y Competitividad de España ("Mediterranean Soil Typologies versus Quartz. At the frontier of pedogenic knowledge"; Ref. CGL2016-80308-P).

References

Abramoff, M.D., Magalhaes, P.J., Ram, S.J., 2004. Image Processing with ImageJ. Biophotonics Int. 11 (7), 36–42.

AEMET, 2020. Estadísticos básicos climatológicos del periodo 1981-2010. Agencia Estatal de Meteorología, Ministerio de Transición Ecológica y el Reto Demográfico. Retrieved from: http://www.aemet.es/es/serviciosclimaticos/datosclimatologicos

Aide, M., Smith-Aide, C., 2003. Assessing soil genesis by rare-earth elemental analysis. Soil Sci. Soc. Am. J. 67, 1470–1476.

Amato, F., Pandolfi, M., Moreno, T., Furger, M., Pey, J., Alastuey, A., Bukowiecki, N., Prevot, A.S.H., Baltensperger, U., Querol, X., 2011. Sources and variability of inhalable road dust particles in three European cities. Atmos. Environ. 45 (37), 6777–6787.

Avila, A., Queralt-Mitjans, I., Alarcón, M., 1997. Mineralogical composition of African dust delivered by red rains over northeastern Spain. J. Geophys. Res. Atmos. 102 (D18), 21977–21996.

Baker A.R., Laskina O., Grassian V.H., 2014. Processing and Ageing in the Atmosphere, in: Knippertz, P., Stuut, J.B. (Eds.), Mineral Dust. Springer, Dordrecht, pp. 75–92.

Barahona, E., 1974. Arcilla de ladrillería de la provincial de Granada. Evaluación de algunos ensayos de materias primas (Doctoral dissertation). Universidad de Granada, Granada.

Bergametti G., Forêt G., 2014. Dust Deposition, in: Knippertz, P., Stuut, J.B. (Eds.), Mineral Dust. Springer, Dordrecht, pp. 179–200.

Blondet, I., Schreck, E., Viers, J., Casas, S., Jubany, I., Bahí, N., Zouiten, C., Dufréchou, G., Freydier, R., Galy-Lacaux, C., Martínez-Martínez, S., Faz, A., Soriano-Disla, M., Acosta, J.A., Darrozes, J., 2019. Atmospheric dust characterisation in the mining district of Cartagena-La Unión, Spain: air quality and health risks assessment. Sci. Total Environ. 693, 133496.

Blott, S.J., Pye, K., 2001. GRADISTAT: a grain size distribution and statistics package for the analysis of unconsolidated sediments. Earth Surf. Process. Landf. 26(11), 1237–1248.

Calero, J., Delgado, R., Delgado, G., Martín-García, J.M., 2009. SEM image analysis in the study of a soil chronosequence on fluvial terraces of the middle Guadalquivir (southern Spain). Eur. J. Soil Sci. 60 (3), 465–480.

Candeias, C., Vicente, E., Tomé, M., Rocha, F., Ávila, P., Alves, C., 2020. Geochemical, mineralogical and morphological characterisation of road dust and associated health risks. Int. J. Environ. Res. Public Health 17 (5), 1563.

Chou, C., Formenti, P., Maille, M., Ausset, P., Helas, G., Harrison, M., Osborne, S., 2008. Size distribution, shape, and composition of mineral dust aerosols collected during the African Monsoon Multidisciplinary Analysis Special Observation Period 0: Dust and Biomass-Burning Experiment field campaign in Niger, January 2006. J. Geophys. Res. Atmos. 113, D00C10.

Comino, F., Cervera-Mata, A., Aranda, V., Martín-García, J.M., Delgado, G., 2020. Short-term impact of spent coffee grounds over soil organic matter composition and stability in two contrasted Mediterranean agricultural soils. J. Soils Sediments 20 (3), 1182–1198.

Costa, P.J.M., Andrade, C., Mahaney, W.C., Da Silva, F.M., Freire, P., Freitas, M.C., Janardo, C., Oliveira, M.A., Silva, T., Lopes, V., 2013. Aeolian microtextures in silica spheres induced in a wind tunnel experiment: Comparison with aeolian quartz. Geomorphology 180, 120–129.

Coz, E., 2008. Caracterización química y morfológica del aerosol ambiental en las fracciones PM10 y PM2.5 mediante microscopía electrónica de barrido en episodios de contaminación atmosférica de origen diverso (Doctoral dissertation). Universidad Carlos III, Madrid.

Criado, C., Dorta, P., 2003. An unusual ‘‘blood rain’’ over the The Canary Islands (Spain). The storm of January 1999. J. Arid Environ. 55, 765–783.

Delgado, R., Barahona, E., Huertas, F., Linares, J., 1982. Los Mollisoles de la Cuenca Alta del Río Dílar Sierra Nevada. Anales de Edafología y Agrobiología 41, 59–82.

Delgado, R., Martín-García, J.M., Oyonarte, C., Delgado, G., 2003. Genesis of the terrae rossae of the Sierra Gádor (Andalusia, Spain). Eur. J. Soil Sci. 54 (1), 1–16.

Díaz-Hernández, J., Miranda-Hernández, J., 1997. Tasas de deposición de polvo atmosférico en un área semiárida del entorno Mediterráneo occidental. Estudios Geológicos 53 (5-6), 211–220.

Díaz-Hernández, J.L., Martín-Ramos, J.D., López-Galindo, A., 2011. Quantitative analysis of mineral phases in atmospheric dust deposited in the South-Eastern Iberian Peninsula. Atmos. Environ. 45 (18), 3015–3024.

Díaz-Hernández, J.L., Párraga, J., 2008. The nature and tropospheric formation of iberulites: pinkish mineral microspherulites. Geochim. Cosmochim. Acta 72 (15), 3883–3906.

Draxler, R.R., 2011. HYSPLIT Model (HYbrid Single-Particle Lagrangian Integrated Trajectory). Retrieved from: https://www.ready.noaa.gov/HYSPLIT.php

Drees, L.R., Wilding, L.P., Smeck, N.E., Senkayi, A.L., 1989. Silica in soils: quartz and disordered silica polymorphs, in: Dixon, J.B., Weed, S.B. (Eds.), Minerals in Soil Environments. Soil Science Society of America, Madison, WI, pp. 913–965.

Engelbrecht, J.P., Menéndez, I., Derbyshire, E., 2014. Sources of PM2. 5 impacting on gran Canaria, Spain. Catena 117, 119–132.

Engelbrecht, J.P., Moosmüller, H., Pincok, S., Jayanty, R.K.M., Lersch, T., Casuccio, G., 2016. Technical note: Mineralogical, chemical, morphological, and optical interrelationships of mineral dust re-suspensions. Atmos. Chem. Phys. 16, 10809–10830.

European Union Directive, 2008. 50/EC of the European Parliament and the Council of 21 May 2008. Relating to ambient air quality and cleaner air for Europe. OJ L 152, 11.6.2008, pp. 1–44.

Gelado-Caballero, M.D., López-García, P., Prieto, S., Patey, M.D., Collado, C., Hérnández-Brito, J.J., 2012. Long-term aerosol measurements in Gran Canaria, Canary Islands: Particle concentration, sources and elemental composition. J. Geophys. Res. Atmos. 117, D03304.

Goudie, A.S., Middleton, N.J., 2001. Saharan dust storms: nature and consequences. Earth-Sci. Rev. 56 (1-4), 179–204.

Hernández, J.D., Hernández, J.M., 1997. Tasas de deposición de polvo atmosférico en un área semiárida del entorno Mediterráneo occidental. Estudios Geológicos, 53 (5-6), 211–220.

Hojati, S., Khademi, H., Cano, A.F., Landi, A., 2012. Characteristics of dust deposited along a transect between central Iran and the Zagros Mountains. Catena, 88 (1), 27-36.

Huneeus, N., Schulz, M., Balkanski, Y., Griesfeller, J., Prospero, J., Kinne, S., Bauer, S., Boucher, O., Chin, M., Dentener, F., Diehl, T., Easter, R., Fillmore, D., Ghan, S., Ginoux, P., Grini, A., Horowitz, L., Koch, D., Krol, M.C., Landing, W., Liu, X., Mahowald, N., Miller, R., Morcrette, J.J., Myhre, G., Penner, J., Perlwitz, J., Stier, P., Takemura, T., Zender, C.S., 2011. Global dust model intercomparison in AeroCom phase I. Atmos. Chem. Phys. 11, 7781–7816.

IARC, 2012. Working Group on the Evaluation of Carcinogenic Risks to Humans. Arsenic, Metals, Fibres and Dusts. Lyon (FR): International Agency for Research on Cancer (IARC) Monographs on the Evaluation of Carcinogenic Risks to Humans, No. 100C. Asbestos (chrysotile, amosite, crocidolite, tremolite, actinolite and anthophyllite). Retrieved from: https://www.ncbi.nlm.nih.gov/books/NBK304374/

Jeong, G.Y., 2008. Bulk and single-particle mineralogy of Asian dust and a comparison with its source soils. J. Geophys. Res. Atmos. 113, D02208.

Journet, E., Balkanski, Y., and Harrison, S.P., 2014. A new data set of soil mineralogy for dust-cycle modeling, Atmos. Chem. Phys. 14, 3801–3816.

Junta de Andalucía, 2021a. Monthly air quality reports (1997-present). Retrieved from: https://www.juntadeandalucia.es/medioambiente/portal/landing-page-%C3%ADndice/-/asset_publisher/zX2ouZa4r1Rf/content/informes-mensuales-de-calidad-del-aire/20151?categoryVal=

Junta de Andalucía, 2021b. Red de Vigilancia de la Calidad del Aire de Andalucía. Retrieved from: https://www.juntadeandalucia.es/temas/medio-ambiente/emisiones/calidad.html

Kalashnikova, O.V., Sokolik, I.N., 2004. Modeling the radiative properties of nonspherical soil-derived mineral aerosols. J. Quant. Spectrosc. Ra. 87 (2), 137–166.

Kandler, K., Benker, N., Bundke, U., Cuevas, E., Ebert, M., Knippertz, P., Rodríguez, S., Schütz, L., Weinbruch, S., 2007. Chemical composition and complex refractive index of Saharan Mineral Dust at Izaña, Tenerife (Spain) derived by electron microscopy. Atmos. Environ. 41 (37), 8058–8074.

Kemnitz, H., Lucke, B., 2019. Quartz grain surfaces–A potential microarchive for sedimentation processes and parent material identification in soils of Jordan. Catena 176, 209–226.

Korotev, R.L., 2009. “Rare Earth Plots” and the Concentrations of Rare Earth Elements (REE) in Chondritic Meteorites. Retrieved from: http://meteorites.wustl.edu/goodstuff/ree-chon.htm

Kumar, R.S., Rajkumar, P., 2014. Characterization of minerals in air dust particles in the state of Tamilnadu, India through FTIR, XRD and SEM analyses. Infrared Phys. Technol. 67, 30–41.

Kumara, G.H.A.J.J., Hayano, K., Ogiwara, K., 2012. Image analysis techniques on evaluation of particle size distribution of gravel. Int. J. Geomate 3 (1), 290–297.

Laveuf, C., Cornu, S., 2009. A review on the potentiality of Rare Earth Elements to trace pedogenetic processes. Geoderma 154, 1–12.

Lequy, E., Legout, A., Conil, S., Turpault, M.P., 2013. Aeolian dust deposition rates in Northern French forests and inputs to their biogeochemical cycles. Atmos. Environ. 80, 281–289.

Lequy, E., Avila, A., Kaci, M.B.N., Turpault, M.P., 2018. Atmospheric deposition of particulate matter between Algeria and France: Contribution of long and short-term sources. Atmos. Environ. 191, 181–193.

López-Quirós, A., Barbier, M., Martín, J.M., Puga-Bernabéu, Á., Guichet, X., 2016. Diagenetic evolution of Tortonian temperate carbonates close to evaporites in the Granada Basin (SE Spain). Sediment. Geol. 335, 180–196.

Lyamani, H., Olmo, F.J., Alados-Arboledas, L., 2005. Saharan dust outbreak over southeastern Spain as detected by sun photometer. Atmos. Environ. 39 (38), 7276–7284.

Mahaney, W.C., 2002. Atlas of sand grain surface textures and applications. Oxford University Press, New York.

Marques, R., Prudêncio, M.I., Dias, M.I., Rocha, F., 2011. Patterns of rare earth and other trace elements in different size fractions of clays of Campanian–Maastrichtian deposits from the Portuguese western margin (Aveiro and Taveiro Formations). Chem Erde. 71, 337–347.

Márquez, R., 2012. El cuarzo de la fracción arena fina en suelos de la provincia de Granada (Doctoral dissertation). Universidad de Granada, Granada.

Marticorena, B., 2014. Dust Production Mechanisms, in: Knippertz, P., Stuut, J.B. (Eds.), Mineral Dust. Springer, Dordrecht, pp. 93–120.

Martín-García, J.M., Aranda, V., Gámiz, E., Bech, J., Delgado, R., 2004. Are Mediterranean mountains Entisols weakly developed? The case of Orthents from Sierra Nevada (Southern Spain). Geoderma 118, 115–131.

Martín-García, J.M., Delgado, G., Sánchez-Marañón, M., Párraga, J.F., Delgado, R., 1997. Nature of dioctahedral micas in Spanish red soils. Clays Clay Miner. 32, 107–121.

Martín-García, J.M., Márquez, R., Delgado, G., Sánchez-Marañón, M., Delgado, R., 2015. Relationships between quartz weathering and soil type (Entisol, Inceptisol and Alfisol) in Sierra Nevada (southeast Spain). Eur. J. Soil Sci. 66 (1), 179–193.

Martin-Ramos, J.D., 2004. Using XPowder: A software package for Powder X-Ray diffraction analysis, Granada, Spain.

McDonough, W.F., Sun, S., 1995. The composition of the Earth. Chem. Geol. 120, 223–253.

Menéndez, I., Derbyshire, E., Engelbrecht, J., von Suchodoletz, H., Zoeller, L., Dorta, P., Carrillo, T., Rodríguez De Castro, F.C.B., 2009. Saharan dust and the aerosols on the Canary Islands: past and present in: Cheng, M., Liu, W., (Eds.), Airbone Particulates. Nova Science Publishers, New York, pp. 39–80.

Menéndez, I., Díaz-Hernández, J.L., Mangas, J., Alonso, I., Sánchez-Soto, P.J., 2007. Airborne dust accumulation and soil development in the North-East sector of Gran Canaria (Canary Islands, Spain). J. Arid Environ. 71 (1), 57–81.

Menéndez, I., Pérez-Chacón, E., Mangas, J., Tauler, E., Engelbrecht, J. P., Derbyshire, E., Cana, L., Alonso, I., 2014. Dust deposits on La Graciosa Island (Canary Islands, Spain): texture, mineralogy and a case study of recent dust plume transport. Catena 117, 133-144.

Menut, L., Pérez, C., Haustein, K., Bessagnet, B., Prigent, C., Alfaro, S., 2013. Impact of surface roughness and soil texture on mineral dust emission fluxes modeling. J. Geophys. Res. Atmos. 118 (12), 6505–6520.

Ministry for Ecological Transition and Demographic Challenge, 2019. Evaluación de la calidad del aire en España 2018, p. 208 (in Spanish). Retrieved from: https://www.miteco.gob.es/es/calidad-y-evaluacion-ambiental/temas/atmosfera-y-calidad-del-aire/informeevaluacioncalidadaireespana2018_tcm30-498764.pdf

Ministry for Ecological Transition and Demographic Challenge, 2021. Histórico de informes de episodios naturales (in Spanish). Retrieved from: https://www.miteco.gob.es/es/calidad-y-evaluacion-ambiental/temas/atmosfera-y-calidad-del-aire/calidad-del-aire/evaluacion-datos/fuentes-naturales/anuales.aspx

Morales-Baquero, R., Pulido-Villena, E., Reche, I., 2013. Chemical signature of Saharan dust on dry and wet atmospheric deposition in the south-western Mediterranean region. Tellus B Chem Phys Meteorol. 65 (1), 18720.

Mourier, B., Poulenard, J., Chavel, C., Faivre, P., Carcaullet, C., 2008. Distinguishing subalpine soil types using extractable Al and Fe extractions and REE geochemistry. Geoderma 145, 107–120.

Muhs, D.R., Budahn, J., Skipp, G., Prospero, J.M., Patterson, D., Bettis III, E.A., 2010. Geochemical and mineralogical evidence for Sahara and Sahel dust additions to Quaternary soils on Lanzarote, eastern Canary Islands, Spain. Terra Nova 22 (6), 399–410.

Muhs, D.R., Prospero, J.M., Baddock, M.C., Gill, T.E., 2014. Identifying Sources of Aeolian Mineral Dust: Present and Past, in: Knippertz, P., Stuut, J.B. (Eds.), Mineral Dust. Springer, Dordrecht, pp. 51–74.

Nickling, W., 1983. Grain-size characteristics of sediment transported during dust storms. J. Sediment. Petrol. 53 (3), 1011–1024.

Nickovic, S., Vukovic, A., Vujadinovic, M., Djurdjevic, V., Pejanovic, G., 2012. High-resolution mineralogical database of dust-productive soils for atmospheric dust modeling. Atmos. Chem. Phys. 12 (2), 845–855.

Párraga, J., Martín-García, J.M., Delgado, G., Molinero-García, A., Cervera-Mata, A., Guerra, I., Fernández-González, M.V., Martín-Rodríguez, F.J., Lyamani, H., Casquero-Vera, J.A., Valenzuela, A., Olmo, F.J., Delgado, R., 2021. Intrusions of dust and iberulites in Granada basin (Southern Iberian Peninsula). Genesis and formation of atmospheric iberulites. Atmos. Res. 248, 105260.

Parviainen, A., Papaslioti, E.M., Casares-Porcel, M., Garrido, C.J., 2020. Antimony as a tracer of non-exhaust traffic emissions in air pollution in Granada (S Spain) using lichen bioindicators. Environ Pollut. 263, 114482.

Prospero, J., Ginoux, P., Torres O., Nicholson S.E., 2002. Environmental characterization of global sources of atmospheric soil dust identified with the NIMBUS 7 total ozone mapping spectrometer (TOMS) absorbing aerosol product. Rev. Geophys. 40 (1), 1002.

Prudêncio, M.I., Braga, M.A.S., Gouveia, M.A., 1993. REE mobilization, fractionation and precipitation during weathering of basalts. Chem. Geol. 107, 251–254.

Querol, X., Alastuey, A., Rodriguez, S., Plana, F., Ruiz, C. R., Cots, N., Massagué, G., Puig, O., 2001. PM10 and PM2.5 source apportionment in the Barcelona Metropolitan area, Catalonia, Spain. Atmos. Environ. 35 (36), 6407–6419.

Reche, I., D'Orta, G., Mladenov, N., Winget, D.M., Suttle, C.A., 2018. Deposition rates of viruses and bacteria above the atmospheric boundary layer. ISME J. 12 (4), 1154–1162.

Reid, E.A., Reid, J.S., Meier, M.M., Dunlap, M.R., Cliff, S.S., Broumas, A., Perry, K., Maring, H., 2003. Characterization of African dust transported to Puerto Rico by individual particle and size segregated bulk analysis. J. Geophys. Res. Atmos. 108 (D19), 8591.

Rodríguez, S., Alastuey, A., Alonso-Pérez, S., Querol, X., Cuevas, E., Abreu-Afonso, J., Viana, M., Pérez, N., Pandolfi, M., De la Rosa, J., 2011. Transport of desert dust mixed with North African industrial pollutants in the subtropical Saharan Air Layer. Atmos. Chem. Phys. 11 (13), 6663–6685.

Rodríguez, S., Cuevas, E., Prospero, J. M., Alastuey, A., Querol, X., López-Solano, J., García, M.I., Alonso-Pérez, S., 2015. Modulation of Saharan dust export by the North African dipole. Atmos. Chem. Phys. 15, 7471–7486.

Rodriguez-Navarro, C., Di Lorenzo, F., Elert, K., 2018. Mineralogy and physicochemical features of Saharan dust wet deposited in the Iberian Peninsula during an extreme red rain event. Atmos. Chem. Phys. 18 (13), 10089–10122.

Rodríguez-Ruiz, M., Abad, I., Bentabol, M.J., 2019. Permo-triassic clastic rocks from the Ghomaride complex and Federico units (Rif Cordillera, N Morocco): An example of diagenetic-metamorphic transition. Minerals 9 (12), 738.

Russo, A., Sousa, P.M., Durão, R.M., Ramos, A.M., Salvador, P., Linares, C., Díaz, J., Trigo, R.M., 2020. Saharan dust intrusions in the Iberian Peninsula: Predominant synoptic conditions. Sci. Total Environ. 717, 137041.

Schepanski, K., 2018. Transport of mineral dust and its impact on climate. Geosciences 8 (5), 151.

Scheuvens, D., Kandler, K., 2014. On Composition, Morphology, and Size Distribution of Airborne Mineral Dust, in: Knippertz, P., Stuut, J.B. (Eds.), Mineral Dust. Springer, Dordrecht, pp. 15–49.

Scheuvens, D., Schütz, L., Kandler, K., Ebert, M., Weinbruch, S., 2013. Bulk composition of northern African dust and its source sediments—A compilation. Earth-Sci. Rev. 116, 170–194.

Schultz L.G., 1964. Quantitative interpretation of mineralogical composition from X-ray and chemical data for the Pierre Shale. US Geol. Surv. Prof Pap., 391 C.

Strunz, H., Tennyson, C., 1982. Mineralogical Tables. Akademie-Verlaggesellschaft. Geest & Portig, Leipzig.

Sweet, D.E., Brannan, D.K., 2016. Proportion of glacially to fluvially induced quartz grain microtextures along the Chitina river, SE Alaska, USA. J. Sediment. Res. 86 (7), 749–761.

Torfstein, A., Teutsch, N., Tirosh, O., Shaked, Y., Rivlin, T., Zipori, A., Stein, M., Lazar, B., Erel, Y., 2017. Chemical characterization of atmospheric dust from a weekly time series in the north Red Sea between 2006 and 2010. Geochim. Cosmochim. Acta 211, 373–393.

Valenzuela, A., Olmo, F.J., Lyamani, H., Antón, M., Quirantes, A., Alados-Arboledas, L., 2012. Analysis of the columnar radiative properties retrieved during African desert dust events over Granada (2005–2010) using principal plane sky radiances and spheroids retrieval procedure. Atmos. Res. 104-105, 292-301.

Vera, J.A. (editor), 2004. Geología de España. SGE-IGME, Madrid.

Vos, K., Vandenberghe, N., Elsen, J., 2014. Surface textural analysis of quartz grains by scanning electron microscopy (SEM): From sample preparation to environmental interpretation. Earth-Sci. Rev. 128, 93–104.

Wang, R.D., Li, Q., Zhang, C.L., Wang, Z.T., Guo, Z.L., Chang, C. P., Li, J.F., 2021. Comparison of dust emission ability of sand desert, gravel desert (Gobi), and farmland in northern China. Catena 201, 105215.

Wang, X., Wen, H., Shi, J., Bi, J., Huang, Z., Zhang, B., Zhou, T., Fu, K., Chen, Q., Xin, J., 2018. Optical and microphysical properties of natural mineral dust and anthropogenic soil dust near dust source regions over northwestern China. Atmos. Chem. Phys. 18 (3), 2119.

WHO, 2013a. IARC: Outdoor air pollution a leading environmental cause of cancer deaths. Press release n° 221. Retrieved from: https://www.iarc.who.int/wp-content/uploads/2018/07/pr221_E.pdf

WHO, 2013b. Health effects of particulate matter. Policy implications for countries in eastern Europe, Caucasus and central Asia. Retrieved from: https://www.euro.who.int/__data/assets/pdf_file/0006/189051/Health-effects-of-particulate-matter-final-Eng.pdf

WHO, 2018. Ambient (outdoor) air pollution. Retrieved from: https://www.who.int/news-room/fact-sheets/detail/ambient-(outdoor)-air-quality-and-health

Xie, Y., Meng, J., Guo, L., 2014. REE geochemistry of modern eolian dust deposits in Harbin city, Heilongjiang province, China: Implications for provenance. Catena 123, 70-78.

Xie, Y., Yuan, F., Zhan, T., Kang, C., Chi, Y., 2018. Geochemical and isotopic characteristics of sediments for the Hulun Buir Sandy Land, northeast China: implication for weathering, recycling and dust provenance. Catena 160, 170-184.

Chapter 7: General conclusions

The main conclusion of this PhD Thesis is that the sand granulometric fraction (50-2000 µm) and its main component, mineral quartz, are indicators of genesis and origin in soils and atmospheric dust materials of the Mediterranean area.

This can be specified through the following specific conclusions:

- Fine sand is a granulometric fraction of great pedogenic interest, with the advantage of its easiness of extraction and analysis. Our results demonstrate the usefulness of fine sand (50-250 µm) in discussing the origin of the different minerals it contains, pedogenic alteration and the provenance of soil materials, even enabling us to establish chronofunctions between properties of fine sand and soil age.
- The characterisation of quartz grains (coarse sand) by applying SEM-CL (scanning electron microscope cathodoluminescence), SEM-EDX (scanning electron microscopy–energy dispersive X-ray spectroscopy) and LA-ICP-MS (laser ablation inductively coupled plasma mass spectrometry) is an effective methodological approach to characterise the provenance/origin of quartz grains in the sand fraction of soils. Six types of quartz grains have been distinguished in the soil sand fraction of Guadalquivir River terraces: metamorphic quartz (type 1), undeformed granitic quartz (type 2), strongly altered granitic quartz (type 3), recrystallised (deformed) granitic quartz (type 4), sandstone quartz (type 5) and hydrothermal quartz (type 6). The origin of these quartz types has been established: Iberian Massif, Betic Cordilleras and Cenozoic Guadalquivir Basin. The quartz type contents in pre-Holocene soils (P1, P2 and P3) are more variable than in Holocene soils (P4 and P5) and parent material (PM), which are more homogeneous. This difference could be attributed to changes in the source area over time, which affected the materials that form the soils.
- The study of lanthanide contents in soil granulometric fractions (fine sand, clay and free form of clay) has demonstrated that soil age (pre-Holocene versus Holocene) affects the behaviour of the lanthanides (in all the fractions studied). Furthermore, some chronofunctions were formulated between lanthanide concentration and soil age in fine sand and clay fraction. The concentrations between couples of lanthanides showed

strong collinearity, particularly in the clay and its free forms, but only partly in the fine sand. This enabled the identification of a new relation, depending on their position in the periodic table that is valid for all the fractions analyzed. The use of lanthanides as fingerprints of provenance using a variety of properties and geochemical indices suggested a genetic relation between all of them, although it has not been possible to determine the relative contribution of the different materials to our soils.

- Atmospheric dust deposited in the Southern Iberian Peninsula under African intrusion conditions is mineralogically heterogeneous, both qualitatively and quantitatively. Mineralogical composition analysis showed that the samples originated from both the north-northwest of Africa (Atlas – west Sahara – Mauritania) and local/regional soil sources. The use of REE as fingerprints does not exclude the contribution of diverse materials such as African aeolian dust or Spanish soils to the Southern Iberian Peninsula. Iberulites were present in all dust samples analyzed. They are a co-association with axial geometry, made up of well-defined mineral grains, together with biological constituents, bacterial and non-crystalline compounds (extracelular polymeric substances, EPS) structured on a coarse-grained core internal (with sizes less than 10 µm) and a relatively more sulphurated clayey ring with only a typical vortex at one of the poles and an average size of 100 µm. They can be shuttles for the intercontinental transport of microorganisms.
- Granulometry, mineralogy and geochemistry of the spring atmospheric dust deposited during three consecutive years in the Granada area showed influence from both local and African sources. African influence has also been shown by the following quartz grains properties: a) greater presence of bulbous edges and upturned plates microtextures on the surface of quartz grains; and b) for quartz´s shape parameters, minor values for area, perimeter, maximum feret, minimum feret, major axis, minor axis and shape factor, and higher values for aspect ratio. Quartz particle morphoscopy has been revealed as a new technique for understanding atmospheric dust provenance.

Conclusiones generales

La principal conclusión de esta Tesis Doctoral es que la fracción granulométrica arena (50-2000 µm) del suelo y su principal componente, el mineral cuarzo, son indicadores de génesis y origen en suelos y materiales atmosféricos del área Mediterránea.

Esto se puede detallar mediante las siguientes conclusiones específicas:

- La arena fina es una fracción granulométrica de gran interés pedogenético con la ventaja de su facilidad de extracción y análisis. Nuestros resultados demuestran la utilidad de la arena fina (50-250 µm) para discutir el origen de los diferentes minerales que contiene, la alteración pedogenética y la procedencia de los materiales del suelo, pudiendo incluso establecer cronofunciones entre las propiedades de la arena fina y la edad del suelo.
- La caracterización de granos de cuarzo (arena gruesa) mediante la aplicación de SEM-CL (microscopía electrónica de barrido con detector de catodoluminiscencia), SEM-EDX (microscopía electrónica de barrido con microanálisis por dispersión de energías de rayos-X) y LA-ICP-MS (espectrometría de masas de plasma acoplado por inducción con sistema de ablación láser) es un enfoque metodológico efectivo para caracterizar su procedencia/origen. En la fracción arena de suelos de las terrazas del río Guadalquivir se han distinguido seis tipos de granos de cuarzo: cuarzo metamórfico (tipo 1), cuarzo granítico no deformado (tipo 2), cuarzo granítico fuertemente alterado (tipo 3), cuarzo granítico recristalizado (deformado) (tipo 4), cuarzo de arenisca (tipo 5) y cuarzo hidrotermal (tipo 6). Se ha establecido el origen de estos tipos de cuarzo: Macizo Ibérico, Cordilleras Béticas y Cuenca Cenozoica del Guadalquivir. Los contenidos, de estos tipos de cuarzo, son más variables en los suelos preholocénicos (P1, P2 y P3) que en los suelos holocénicos (P4 y P5) y el material parental (PM). Esta diferencia podría atribuirse a cambios en el área fuente a lo largo del tiempo, lo que afectó a los materiales que forman los suelos.
- El estudio de los contenidos de lantánidos en las fracciones granulométricas del suelo (arena fina, arcilla y formas libres de la arcilla) ha demostrado que la edad del suelo (preholoceno versus holoceno) afecta al comportamiento de los lantánidos (en todas las fracciones

estudiadas). Además, se han formulado algunas cronofunciones entre la concentración de lantánidos y la edad del suelo en las fracciones arena fina y arcilla. Las concentraciones entre parejas de lantánidos demostraron una fuerte correlación, particularmente en la arcilla y sus formas libres, y parcialmente en la arena fina. Esto permitió identificar una nueva relación, dependiendo de su posición en la tabla periódica, que es válida para todas las fracciones analizadas. El uso de los lantánidos como huellas dactilares de procedencia, utilizando una variedad de propiedades e índices geoquímicos, sugirió una relación genética entre todos ellos, aunque no ha sido posible determinar la contribución relativa de los diferentes materiales a nuestros suelos.

- El polvo atmosférico depositado en el sur de la Península Ibérica, bajo condiciones de intrusión africana, es mineralógicamente heterogéneo, tanto cualitativa como cuantitativamente. El análisis de la composición mineralógica demostró que las muestras procedían tanto del norte-noroeste de África (Atlas - Sahara occidental - Mauritania) como de fuentes de suelo locales/regionales. El uso de las REE como huellas dactilares no descartó la aportación de materiales diversos como el polvo eólico africano o los suelos del sur de la Península Ibérica. Los iberulitos estuvieron presentes en todas las muestras de polvo analizadas. Estos, son una co-asociación de geometría axial, constituida por granos minerales bien definidos, junto con constituyentes biológicos, compuestos bacterianos e incluso sustancias poliméricas extracelulares (EPS), estructurados sobre un núcleo interno de grano grueso (<10 µm) y un anillo arcilloso relativamente más sulfurado. Presentan un solo vórtice en uno de sus polos. Su tamaño promedio es de 100 µm y pueden ser lanzaderas para el transporte intercontinental de microorganismos.
- La granulometría, mineralogía y geoquímica del polvo atmosférico primaveral depositado durante tres años consecutivos en la zona de Granada, mostró influencia tanto de fuentes locales como africanas. La influencia africana también ha sido mostrada por las siguientes propiedades de los granos de cuarzo: a) mayor presencia de las microtexturas ‘bulbous edges’ y ‘upturned plates’ en la superficie de los

granos de cuarzo; y b) para los parámetros de forma del cuarzo (shape parameters), valores menores de área, perímetro, feret máximo, feret mínimo, ‘major axis’, ‘minor axis’ y ‘shape factor’, y valores mayores para ‘aspect ratio’. La morfoscopia de las partículas de cuarzo se ha revelado como una nueva técnica para comprender la procedencia del polvo atmosférico.